The Dissertation Committee for Joshua Jesse Adams
certifies that this is the approved version of the following dissertation:

Integral Field Spectroscopy as a Probe of Galaxy Evolution

Committee:

Gary J. Hill, Supervisor

Karl Gebhardt, Supervisor

Niv Drory

Neal Evans

Volker Bromm

Integral Field Spectroscopy as a Probe of Galaxy Evolution

by

Joshua Jesse Adams, B.S. M.A.

Dissertation

Presented to the Faculty of the Graduate School of

The University of Texas at Austin

in Partial Fulfillment

of the Requirements

for the Degree of

Doctor of Philosophy

The University of Texas at Austin

August 2011

Acknowledgments

I thank my parents, Ned and Donna Adams, for giving me the resources to pursue my ambitions, teaching me a solid work ethic, and exemplifying the prudent values that lead to worthy ambitions.

Joshua Jesse Adams

The University of Texas at Austin
August 2011

Integral Field Spectroscopy as a Probe of Galaxy Evolution

Publication No. ____________________

Joshua Jesse Adams, Ph.D.
The University of Texas at Austin, 2011

Supervisors: Gary J. Hill and Karl Gebhardt

Optical spectroscopy and modeling are applied to four independent problems related to the structure and evolution of galaxies. The problems cover a broad range of look-back time and galaxy mass. Integral field spectroscopy with low surface brightness sensitivity is the tool employed to advance our understanding of the distribution, interplay, and evolution of the stars, dark matter, and gas. First, I review development and commissioning work done on the VIRUS-P instrument. I then present a large sample of galaxies over redshifts 1.9<z<3.8 selected solely through their Lyman-α flux. This work is done as a pilot survey to the Hobby-Eberly Telescope Dark Energy eXperiment (HETDEX). I create a redshift catalog of 397 galaxies discovered over 169 arcsec^2 taken over 113 nights. Second, I study a high redshift (z=3.4) radio galaxy halo by mapping the Lyman-α velocity field. The signal extends far beyond the optical and radio extents of the system. Plausible, but non-unique, models are made to explain the Lyman-α signal that require a very large reservoir of neutral hydrogen ($\geq 10^{12} M_{\odot}$). Third, I study the dark matter halo profile in a nearby late-type dwarf galaxy in the context of the "core-cusp" controversy. N-body simulations predict such galaxies to have cuspy dark matter halos, while HI rotation curves and more recent hydrodynamical simulations indicate that such halos may instead be strongly cored. I measure the spatially resolved stellar velocity field and fit with two-integral Jeans models. A cuspy halo is preferred from the stellar kinematics. The mass models from stellar and gaseous kinematics disagree. The gas models assume circular motion in an infinitely thin disk which is likely unrealistic. The stellar kinematics presented are the first measurements of a collision-less tracer in such galaxies. Fourth, I attempt to measure diffuse Hα emission, fluoresced by the metagalactic UV background, in the outskirts of a nearby gas rich galaxy. I do not make a detection, but the deep flux limit over a large field-of-view places the most sensitive limit to-date on the UV background's photoionization rate of $\Gamma(z = 0) < 1.7 \times 10^{-14}$ s^{-1} at 5σ certainty.

Contents

Chapter 1

VIRUS-P commissioning and design science

1.1 The VIRUS-P instrument

The Visible Integral field Replicable Unit Spectrograph Prototype (VIRUS-P) saw first light on October 21, 2006 at the McDonald Observatory's 2.7m Harlan J. Smith telescope. The instrument delivered the first integral field spectroscopy (IFS) capability to the observatory and provides the largest field-of-view of any extant integral field spectrograph. IFS instruments have had a growing impact on observational extragalactic astronomy over the last two decades. Beginning with optical 4m telescopes, Densepak (Barden & Wade 1988) was installed on Kitt Peak's Mayall and TIGER (Bacon 1994) on the Canada-France-Hawaii Telescope. SPIRAL (Kenworthy et al. 1998; Saunders et al. 2004) raised the resolution capabilities to R=2200 on the Anglo-Australian Telescope, and UIST (Ramsay Howat et al. 2004) opened up the NIR on the UK Infrared Telescope. SAURON (Bacon et al. 2001) delivered the largest-to-date number of resolution elements at 1500 with modest (R=1415) resolution on the William Herschel Telescope and became a workhorse for survey science. Sparsepak (Bershady et al. 2004) on the Wisconsin-Indiana-Yale-NOAO Telescope and PMAS-PPAK (Verheijen et al. 2004; Roth et al. 2005; Kelz et al. 2006) on the Calar Alto large telescope featured multiple modes and improved efficiencies. Finally, 8-10m class telescopes have reached IFS capabilities with GMOS (Allington-Smith et al. 2002) and NIFS (McGregor et al. 2003) on Gemini, VIMOS (Le Fèvre et al. 2003) and SINFONI (Eisenhauer et al. 2003; Bonnet et al. 2004) on the Very-Large-Telescope (VLT), and OSIRIS (Larkin et al. 2003) on Keck. The next generation of IFS will feature MUSE (Henault et al. 2003) and KMOS (Sharples et al. 2004) on the VLT and VIRUS on the HET. VIRUS-P was made primarily to test the design for VIRUS and the upcoming HETDEX survey over the $3400\text{Å} < \lambda < 5700\text{Å}$ range at R$\sim$850. However, VIRUS-P was designed with more flexibility to operate up to 6800Å and up to R$\sim$4400. During the first several years, I used VIRUS-P primarily to complete the HETDEX Ly-α emitter pilot survey. In the later years, I turned the instrument to several independent projects that will be described in the following chapters. In this section, I will summarize the commissioning work undertaken to support the large science output of VIRUS-P. A more detailed description is available in Hill et al. (2008b).

VIRUS-P is designed to accept a f/3.65 input which leads to a seeing-matched spatial resolution for the HET. When mounted on the 2.7m, VIRUS-P has very coarse spatial sampling. This makes the astrometric calibrations problematic. I circumvented this problem by writing general use software that uses the fixed offset guiding camera to predict and measure the positions of each IFS fiber. This work required in-lab measurements of the relative fiber positions in the bundle, a determination of the necessary distortion terms over the integral field and guider focal planes from data on open clusters, and monitoring of the solution stability with time and instrument stowing. The solutions I derive with the $4\farcs1$ diameter fibers have $0\farcs3$ accuracy. So long as the IFS fiber head is not removed from its focal plane mount and the guider camera is not dismounted, I have measured solutions to have drifts $<0\farcs5$ under all operating temperatures. Since the commercial guide cameras generally fail every few months, this has become an ongoing support task to measure the astrometry for every new instrument alignment.

Over the course of early data collection, I identified several key deficiencies in the instrument and assisted in finding their solutions. First, the instrument has been through three charge-coupled devices (CCD). The first, Texas L3O CCD (known as SO1), was used till December 2006 but had poor cosmetics and poor quantum efficiency. The second, Ohio State L3L CCD (known as SO2), was used till June 2007 but had unacceptably high read noise ($\sim$6 e^-). Both further suffered from having warped surfaces that compromised the optical quality and ultimately the achievable sensitivity. Phillip MacQueen and Joe Tufts led the engineering efforts to reach operation with the final, Fairchild Instrument (FI1) CCD on September 2007. I also worked to identify the light path of some unexpected ghosts stray light in the spectrograph. This led to extra baffling and a second-order blocking filter being created and installed. Finally, a focal reducer with poor UV transmission was replaced in September of 2008.

A large block of time was given to making a customized, general user software reduction package for VIRUS-P in collaboration with Karl Gebhardt and Guillermo Blanc. The software is known as `vaccine` and available under version control. All VIRUS-P observers use this software. Three types of operation form the package. First, there are general and common CCD reduction steps. Second, there are spectroscopy steps specific to multi-object spectroscopy as are found in the commonly used `dohydra` or `p3d` packages, such as tracing fibers and making wavelength solutions. Finally, extra care was put into the background subtraction. Since the Ly-α emitter pilot survey relies on low S/N detections with a large number of empty resolution elements, the noise properties must be very well known. The common step in background subtraction of wavelength resampling is unacceptable as it introduces correlated noise. Our solution was to integrate a b-spline fitting algorithm into the background subtraction to reach statistically perfect results with well defined errors. Some previous spectroscopy pipelines have used this step, but no IFS packages have before.

Finally, a great deal of work was given to testing the instrument's volume phase holographic gratings. Four gratings are currently available for the instrument: VP1 at R$\sim$850 able to cover the instrument's whole wavelength range, VP2 at R$\sim$2700 again able to cover the full wavelength range, VP3 at R$\sim$4000 operating in the blue, and VP4 at R$\sim$4300 operating in the red. The details of the grating testing follow.

1.2 Volume phase holographic grating performance

1.2.1 Introduction to grating testing

HETDEX will discover spectroscopically 800,000 new Lyman-alpha Emitting galaxies (LAEs) for use as probes of baryonic acoustic oscillation in the early universe which can be used to measure the strength of dark energy and its possible evolution in a currently unmeasured epoch(Hill et al. 2008a). This 120 night survey will use 150 modified copies of the exising VIRUS-P instrument placed on the 9.2m HET. The overall instrument design is described in Hill et al. (2008b), the camera design and performance in Tufts et al. (2008a), and tests of the fiber optic bundles in Murphy et al. (2008). We here detail tests and optimizations that have been performed on the VPH gratings that act as the dispersion elements in these spectrographs at transmission order m=1. Our results push the technology to high efficiency at bluer wavelengths than has been previously published as we need to operate to 3400Å. Besides the test results, we present details of the automated test bench we have created for repeatable and speedy measurements of the large quantity of gratings that HETDEX will eventually require. A test of more limited on-telescope performance verifies our test bench results. We also discuss two observed stray light paths that involve the grating. One is the Littrow reflection that is already known, but the second is a higher dispersion, redder pattern that is new to the literature.

1.2.2 Gratings

We have acquired three VPH gratings for potential use in the VIRUS-P instrument. All three are sandwiched between fused silica plates of glass yielding a total size of 140x140x17mm^3. The optically active surface for our purposes is a centered circle of diameter 130mm. All three gratings share a modulation frequency of 831 lines/mm and have unslanted fringes. We know neither the dichromated gelatin layer thicknesses nor the amplitudes of refractive index modulation, so we cannot estimate efficiencies with the Kogelnik approximation (Kogelnik 1969). The two gratings provided by Wasatch photonics are a holographic master and copy ideally sharing all properties we will hereafter call H1 and C1. The copy is made by a method unknown to us, but which promises lower unit cost as desirable for the multiplexing nature of the VIRUS design. The third grating was provided by Kaiser Optical Systems Inc. (KOSI). Rigorous coupled wave analysis (Gaylord & Moharam 1985) (RCWA) was performed by KOSI for their design as shown in Fig. 1.1.

1.2.3 Test bench

Components

We have built an automated optical test bench to measure the wavelength dependent efficiency of diffraction gratings under general conditions. The very simple design is inspired by the tunable spectrograph concept sketched in Barden et al. (1998).

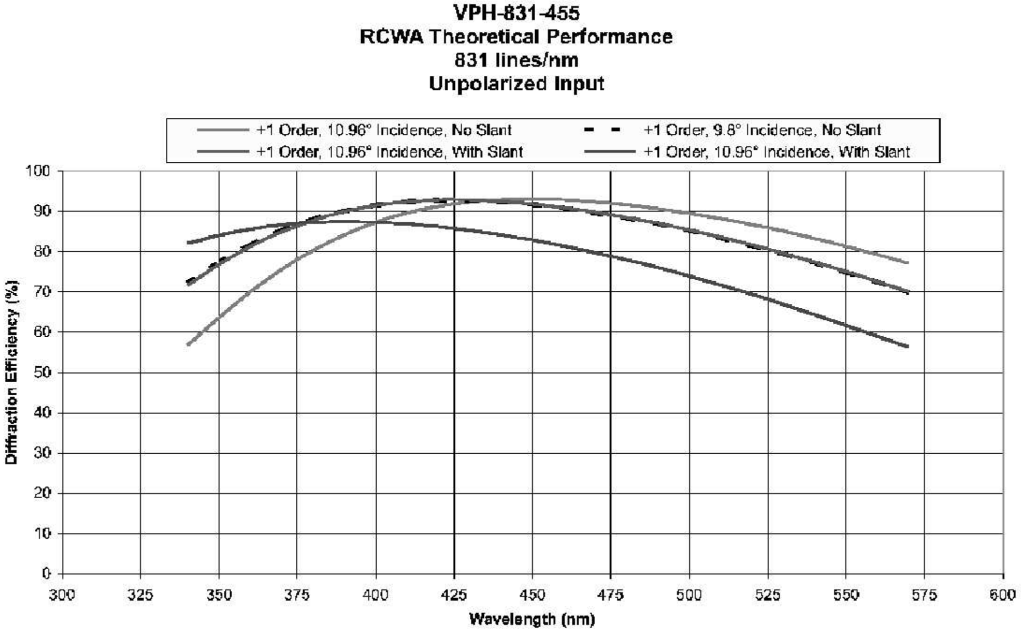

Figure 1.1 RCWA performed by KOSI for their grating.

Figure 1.2 shows our design. A commercial monochromator is coupled to a fiber optics bundle. A filter wheel lies just prior to the output slit with a set of filters to block out second order light for any configuration. The monochromator can use a 100W quartz tungsten halogen (QTH) or 30W deuterium lamp as input. The deuterium lamp gives us access to the 3400-4500Å UV range which is crucial to the survey science. We use large, matched input and output slits of size 0.76mm in our monochromator to improve signal strength in the bench tests. This translates at 5000Å to a bandpass of 21Å in our measurements. The monochromatic light leaves the fiber bundle and becomes collimated by a 50mm diameter fused silica singlet. An adjustable iris then cuts down the beam to the desired size. All measurements presented here used a 19mm diameter collimated beam. The collimated beam next transmits through our grating. The grating rests in a mount whose back surface has been aligned as normal to the input beam to within 0.1°. This grating mount sits on a stepper motor rotation stage of 0.01° accuracy. The beam travels from the grating to a focusing lens identical to the collimating lens. This lens brings the image to a focus in the middle of a 10mm diameter Fabry, or pupil, fused silica lens. The Fabry lens improves measurement stability by imaging the exit pupil of the fiber bundle onto the final component, a silicon single element 5mm diameter photodiode. The spot delivered to the photodiode is of size 0.56mm across the monochromator bandpass per a ray tracing model and safely an order of magnitude smaller than the photodiode surface. Laboratory tests verify this by showing that the measured efficiency is constant to within 1% until the output angle at measurement, β, deviates from that demanded by the simple grating equation by more than ±0.5°. All elements acting after the grating are on a second stepper motor rotation stage which rotates with accuracy 0.001° around the same axis as the grating rotation stage. All operations, from monochromator control to motor movements to detector readout, are controlled through a computer and custom written software. This simple design

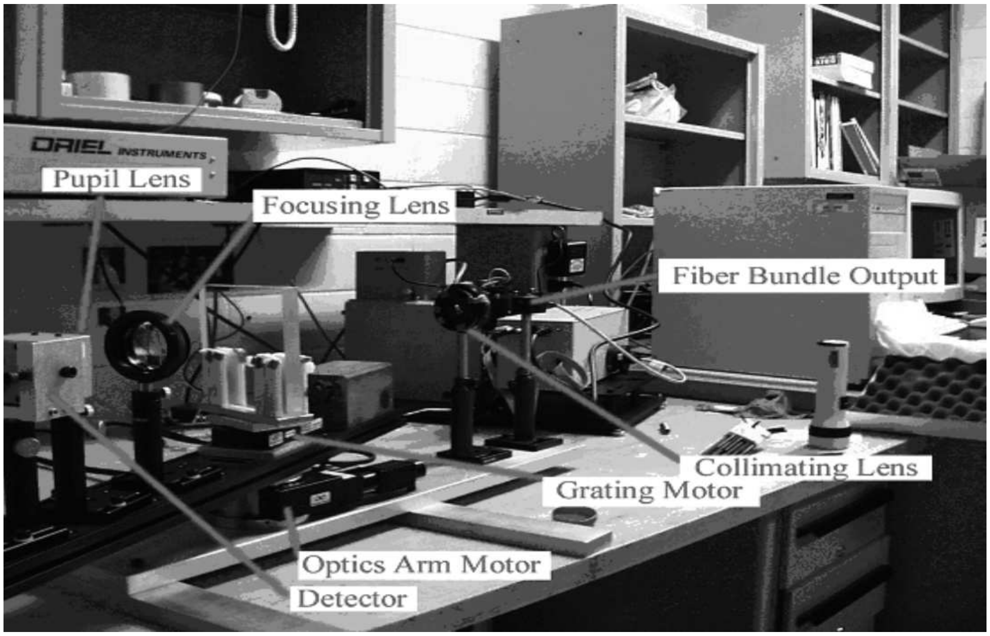

Figure 1.2 The grating test bench optical layout. The setup has been removed from its light box for display.

allows us to measure diffraction grating efficiency as a function of wavelength, input angle, and diffraction order. We are also capable of scanning through angles outside of Bragg diffraction for scattered or reflected light.

Operating procedure

We begin a measurement with both α and β set to 0° and the mount absent a grating. We step through all wavelengths of interest with the monochromator. Each measurement consists of a light reading with the light path open followed by a dark reading with a shutter in the monochromator closed. The subtraction of these two removes any bias and background. This step establishes the amount of light being delivered through the system without the grating. The diffraction grating is then inserted, and measurements are taken through all wavelengths and angles of interest. The ratio of the dark subtracted grating measurement to the dark subtracted normalization measurement gives the grating efficiency. At the end of all scans, the normalization measurements are again checked to evaluate lamp stability. In all measurements presented, the post-measurement normalization intensity was within 2% or better of the pre-measurement normalization itensity at all wavelength.

1.2.4 Results

Efficiency with input angle

The wavelength of peak efficiency at a particular α can be easily estimated through the Bragg condition. However, the efficiency envelope at other wavelengths has no easy estimation. This envelope is often asymmetric with the dropoff less severe at wavelengths redward of the Bragg condition. RCWA can make these predictions, but imperfections in the manufacturing process can further degrade performance. For our instrument, we desire high efficiency in the survey wavelength range of 3400-5700Å, with emphasis on the bluer region. Our prototype spectrograph is tunable in α, so off-design performance at higher wavelengths is of interest for our side science applications. However, this performance does not drive our design. Figures 1.3, 1.4, and 1.5 show the measured performance through a variety of α's. We are still falling below RCWA predictions, so we believe further development work may improve final grating performance. Interestingly, the RCWA curve at $\alpha = 9.8°$ best matches the data measured for the $\alpha = 9.0°$ curve. This is well outside our possible alignment error in α, and we cannot explain this discrepancy. The Wasatch H1 grating reaches a roughly equal peak efficiency as the KOSI grating, but the efficiency envelope dropoff is stronger. Notably at 3400Å, the extra loss is 10%. The copy has extra loss over the master, although this effect is not severe at the bluest wavelengths. The extra loss in the copy is 10% at the region of peak efficiencies near 4500Å.

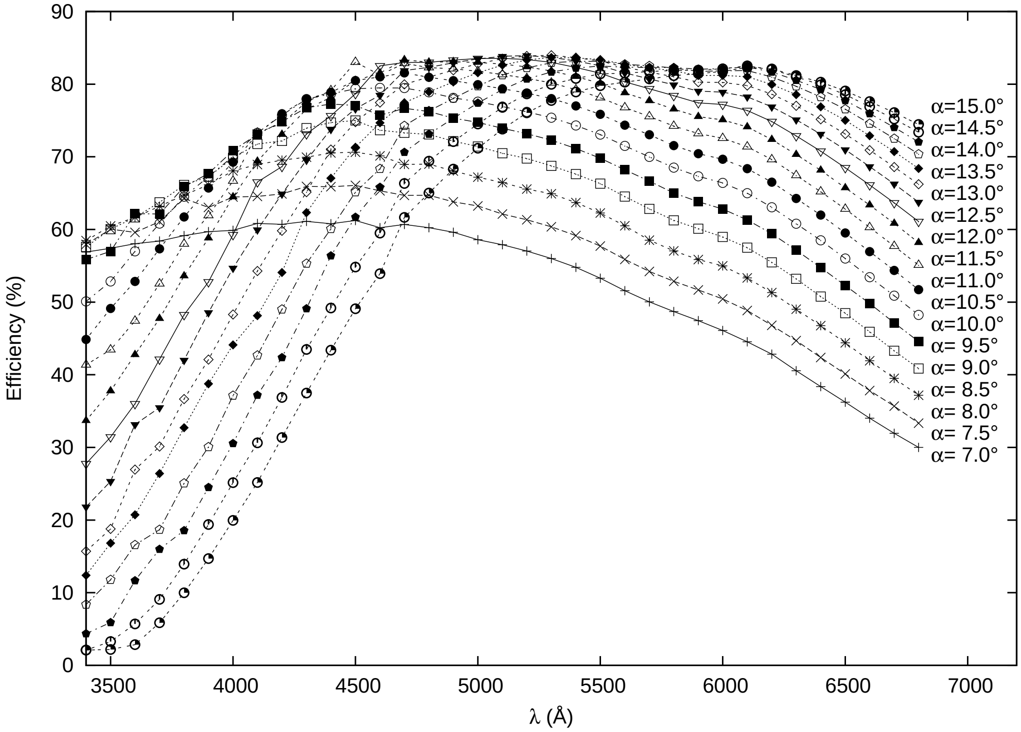

Figure 1.3 The laboratory measurement of the KOSI grating first order efficiency as a function of input angle and wavelength.

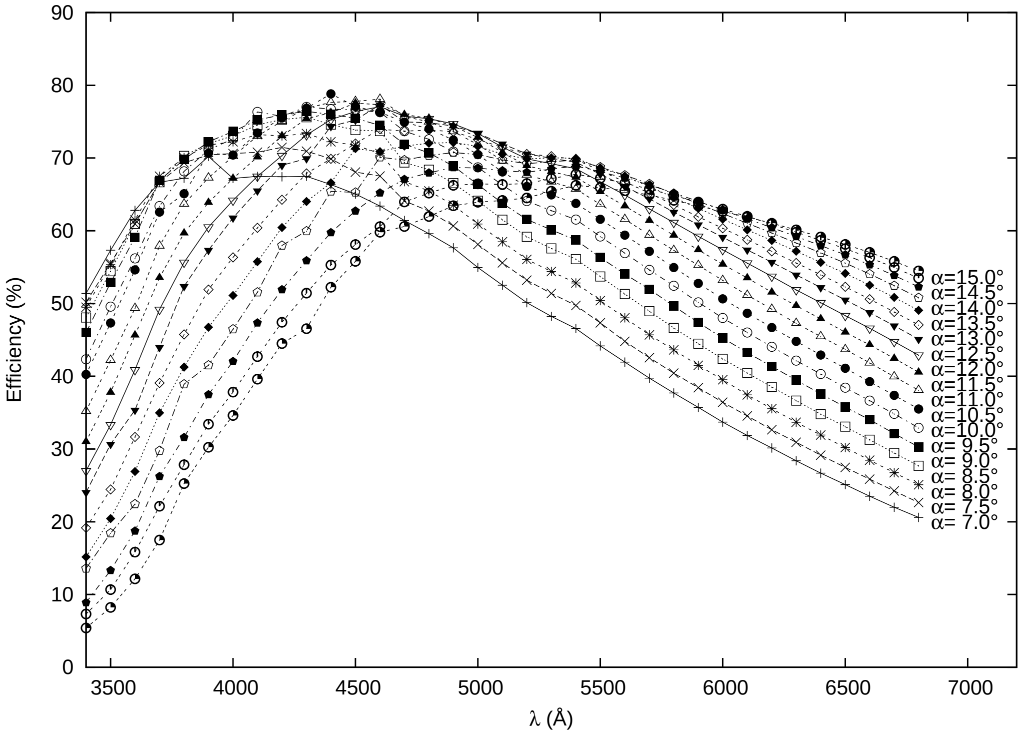

Figure 1.4 The laboratory measurement of the H1 first order efficiency as a function of input angle and wavelength.

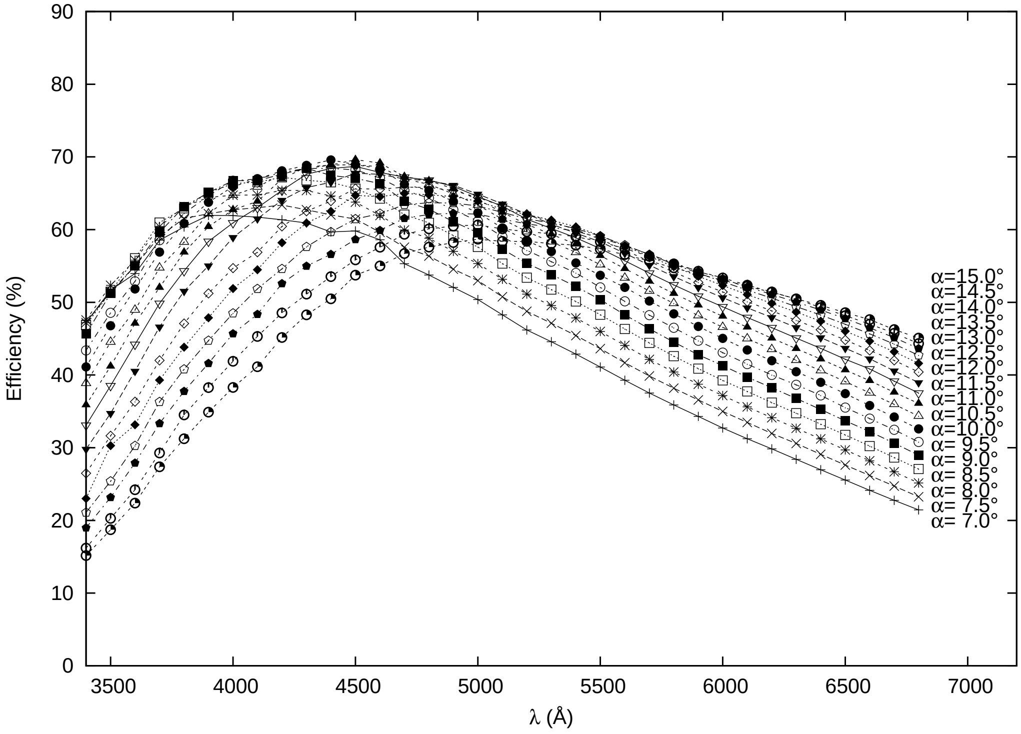

Figure 1.5 The laboratory measurement of the C1 first order efficiency as a function of input angle and wavelength.

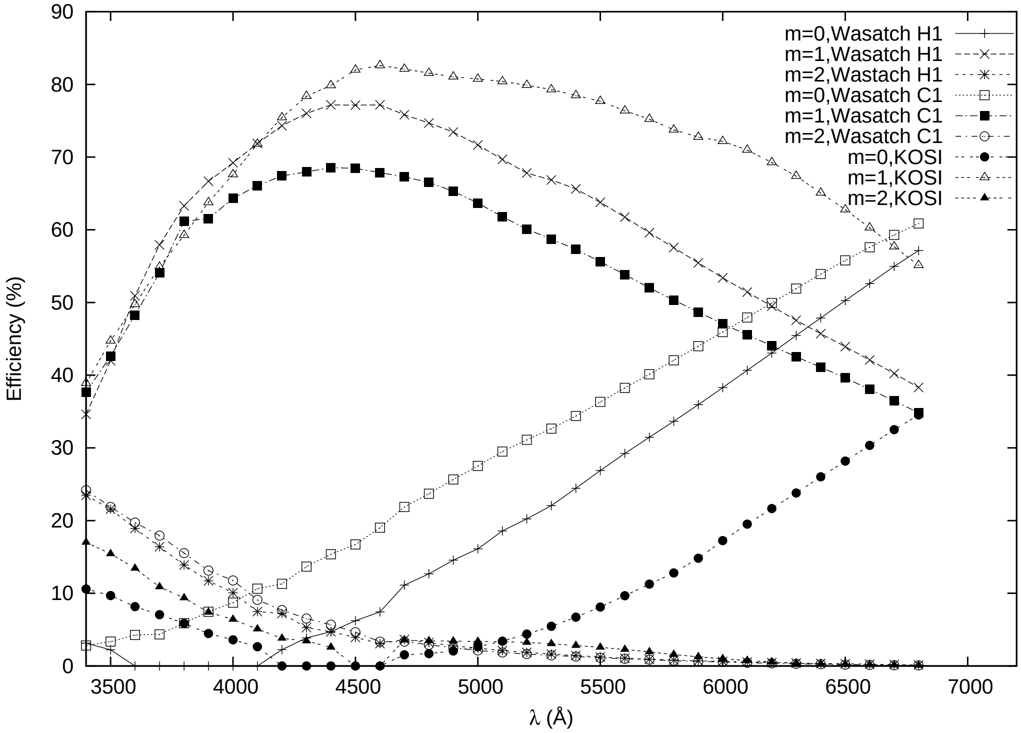

Figure 1.6 The laboratory measurement of diffraction orders 0,1,and 2 for $\alpha = 10.5°$.

Efficiency with diffraction order

We can investigate the types of efficiency loss by looking at diffraction orders other than m=1. This is shown in Fig. 1.6. At the bluest wavelengths, the main thief from m=1 is the m=2 order. At off-design redder wavelengths, the main thief is the m=0 order. There is obvious correlation between a rising strength in the m=0 or m=2 orders and a drop in the m=1 order for all gratings. This serves as validation for our measurements.

Laboratory verification

A scan outside of the usual, simple grating equation will reveal two important features: any non-ideal scattered light being caused by the grating and an input light source that is not properly monochromatic. We give such scans at two wavelengths in Figs. 1.7 and 1.8. We have zoomed in our plot to low signal levels. The m=0,1,and 2 orders are where expected and often rise off the charts. Figure 1.7 shows a curious feature near $\beta = -23°$. Here, for both gratings the intensity unexpectedly rises. We have investigated this with cutoff filters and found that this is not a scattered light component. Instead, this is an imperfection in our commercial monochromator. The very red QTH source produces undesired emission through the monochromator around 6800Å. This will affect our measurement by causing an overestimate in the normalization reading. For the case given, the error contributes a fraction of a percent to the final measurement which is below our interest. However, this error becomes more severe for bluer wavelengths as the strength of the source intrinsically becomes dimmer. It is for this reason that we have used the deuterium lamp for all measurements between 3400-4600Åand the QTH lamp only for redder wavelengths. A β scan for the deuterium source in Fig. 1.8 does not show a similar bump as expected for the bluer intrinsic deuterium spectrum. The deuterium scan does show increased measurement noise as the signal is much weaker at these wavelengths, but this error is 2% or lower in all cases.

On-telescope verification

Independently from our test bench, we have measured the efficiency of the KOSI and H1 gratings on the 2.7m McDonald Observatory telescope with the full VIRUS-P instrument. We cannot measure an absolute grating efficiency in this case, but the ratio of the two measurements can be used to validate our lab data. Figure 1.9 shows the result. On telescope, we used a QTH lamp against the dome wall. This

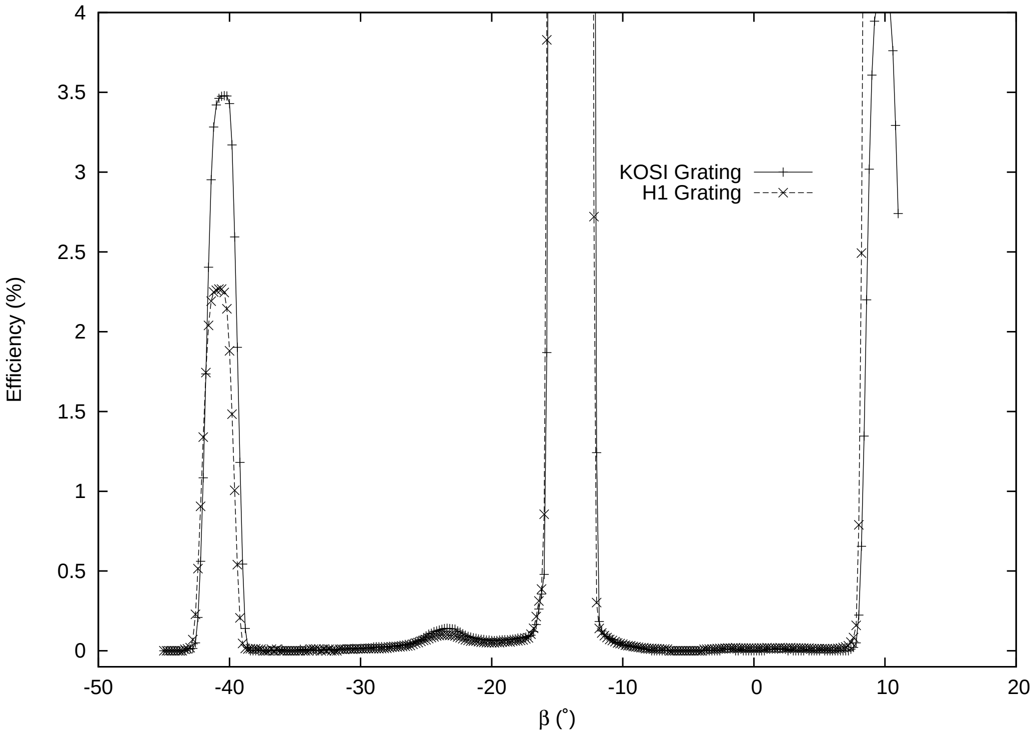

Figure 1.7 A scan across output angle to search for scattered or polychromatic light with the QTH source at $\alpha = 10^\circ$ and λ=5000Å.

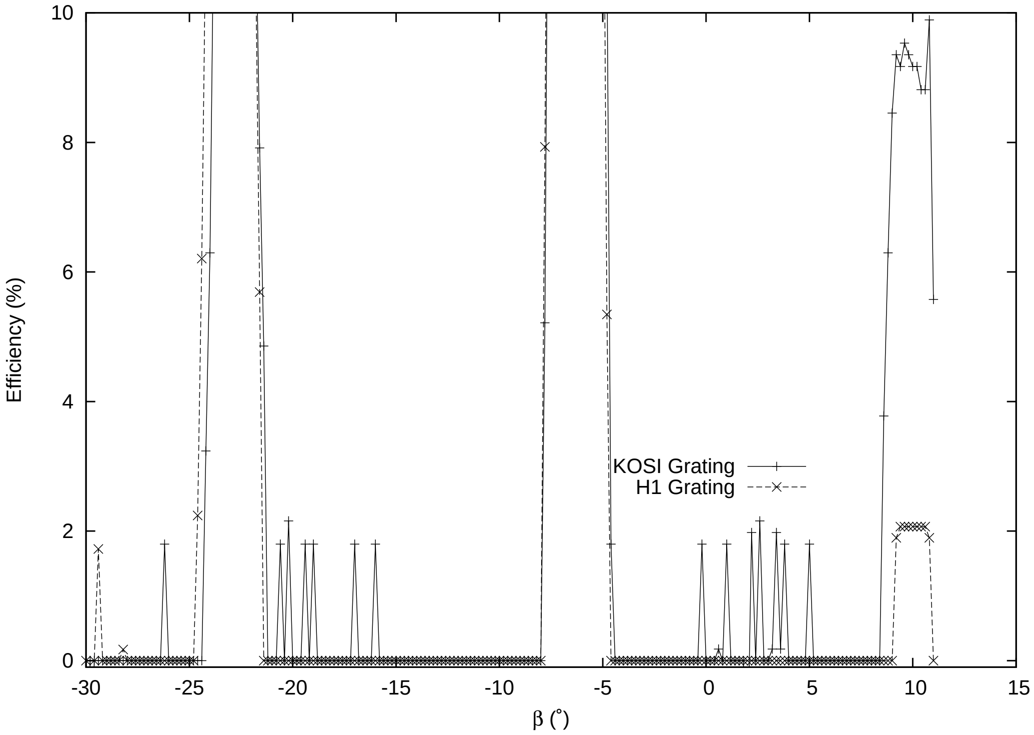

Figure 1.8 A scan across output angle to search for scattered or polychromatic light with the deuterium source at $\alpha = 10^\circ$ and λ=3400Å.

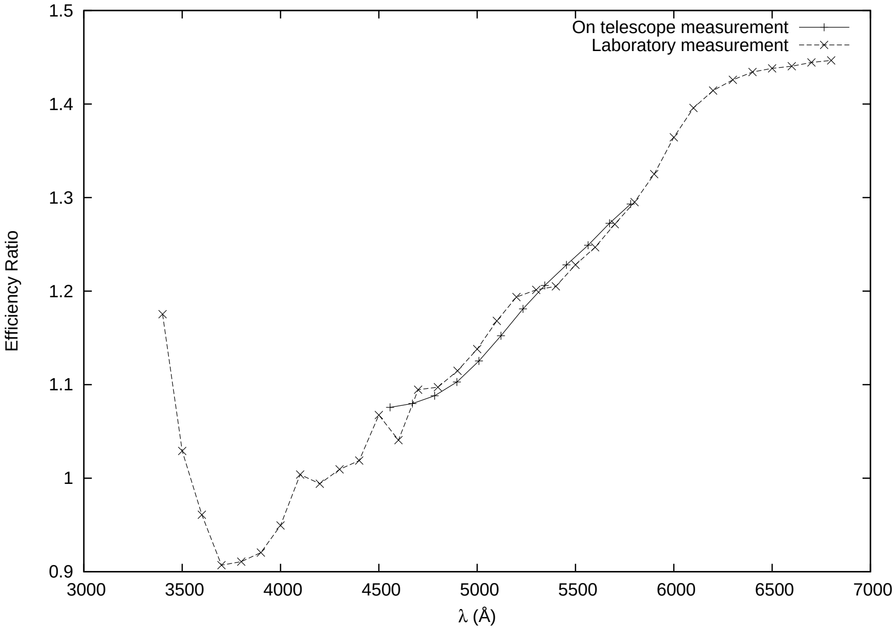

Figure 1.9 The ratio of first order efficiency between the KOSI and H1 gratings as measured on-telescope and in-lab at $\alpha = 10.5^\circ$.

is a very red source, so we cannot directly measure by this method the efficiency of the bluest wavelengths due to lack of flux. However, in the wavelength regions that overlap, we find excellent agreement between the on-telescope and in-lab ratios.

1.2.5 Stray light

Narcissus

During the VIRUS-P pilot survey, we have observed two types of stray light that were not initially expected in the design. When taking data on bright standard stars, we found an apparent emission line displaced from the standard star by eight fibers. Through moving the telescope position, we found that this putative emission line did not stay in a fixed location on the sky, but instead stayed a fixed distance in detector space from the bright, standard star spectra. We identify this as

”narcissus” discussed in Tull et al. (1995) with a slight out-of-plane angle between optical surfaces giving the eight fiber offset. Narcissus occurs in a spectrograph when light traveling the designed path reflects from the CCD, diffracts again through the dispersion element, and returns to the CCD. In the specific case where the dispersion orders of each pass are identical, the stray light is called a ”Littrow ghost” (Burgh et al. 2007). In this case, which we observe, there is no dispersion in the final ghost. Although we are not usually operating with the Littrow wavelength centered in our bandpass, the wavelength is still within our bandpass so the Littrow ghost gets imaged. The stray light will exit the grating at the input angle, α. The measured Littrow ghost in VIRUS-P is within 0.1° of the α we measured through an inclinometer which has a comparable measurement resolution. If not accounted for, this could be a dangerous contaminant to our science goals. For the detection of LAEs, our only signal is from a solitary emission line that looks very similar to this stray light. With the Littrow ghost known, however, we can exclude the detector position around the rare, bright objects in our survey area and avoid sample contamination.

High-dispersion, red contamination

A second source of stray light becomes obvious when we take neon arc lamp frames. Neon has a large number of bright emission lines that should lie redward of our recorded data. The pattern of these red lines is superimposed on the proper neon spectrum, but with double dispersion and double the expected curvature with γ. We installed better baffling around the camera window which cut down but did not eliminate this feature. The stray light path we have found that can cause this behavior is as follows: first order transmissive diffraction, reflection from the camera window, reflection from the grating (can be either reflection from the front surface of the grating's glass, zeroth order reflective diffraction, or zeroth order transmissive

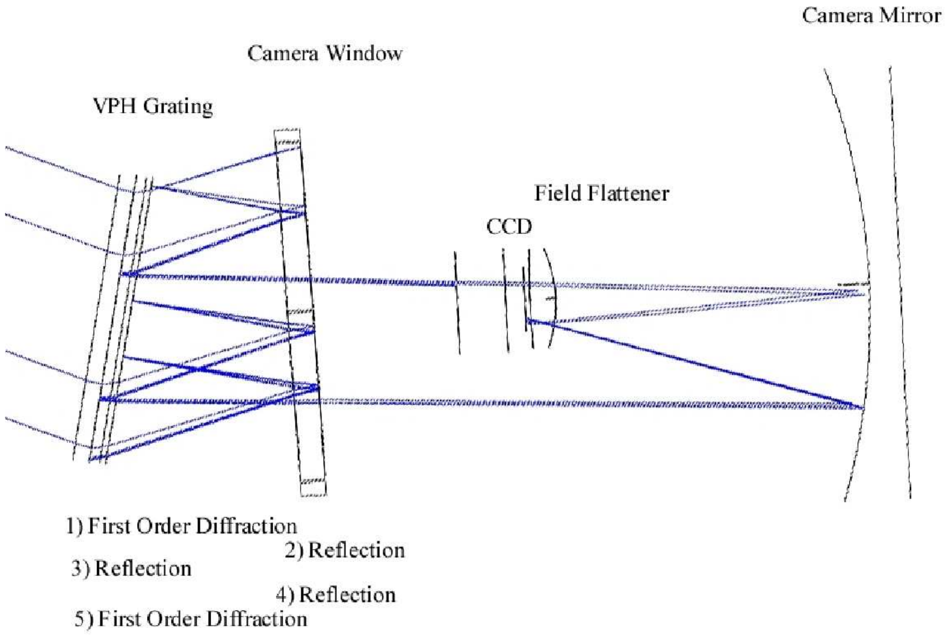

Figure 1.10 The stray light path that images red, high dispersion light.

diffraction followed by reflection from the rear surface of the grating's glass and then another zeroth order transmissive diffraction), another reflection from the camera window, and finally another first order diffraction of the light (can be either a first order reflective diffraction or a zeroth order transmissive diffraction followed by a reflection from the rear glass surface and then a first order transmissive diffraction). Fig. 1.10 shows this stray light path that images red light which normally would strike baffling or the inner wall of the camera chamber. For a simplified, analytic model we can ignore the slight curvature in the camera window's front surface and the wavelength dependent refractive index of the fused silica window and treat all the reflections as from flat surfaces. Doing this, we can derive Eq. 1.1 where α is the input angle for the light entering the grating, β_c is the angle between the normal of the camera window and the normal of the grating, λ_s is the stray light wavelength,

λ_p is the proper wavelength of light that should be imaged on the detector position where the stray light of λ_s is appearing, and σ is the spacing between fringes in the same unit as all the wavelengths.

$$\frac{\lambda_p}{\sigma} = \frac{\lambda_s}{\sigma} + \sin\alpha + (\frac{\lambda_s}{\sigma} - \sin\alpha)\cos(4\beta_c) - \sqrt{1 - (\frac{\lambda_s}{\sigma} - \sin\alpha)^2}\sin(4\beta_c) \qquad (1.1)$$

The wavelength solution from readout data informs us very well of the angle between the camera mirror and the grating normal, which we can also adjust. Assuming the camera window has the exact same axis as the camera mirror gives a poor fit to our observations of the stray, red light. However, we installed the camera and adjusted the camera mirror for optimal image quality which may have tilted the angle between the camera mirror and the normal to the camera window. If we allow an offset of 1.5° between these surfaces, we find the model matches in Table 1.2.5. We estimate the strength of this stray light from the observed arc lamps lines in a similar neon lamp on the Low Resolution Spectrograph (LRS) on the HET. Roughly assuming a similar relative instrument response across wavelength between the LRS and VIRUS-P, we measure the attenuation factors for this light again in Table 1.2.5 with our current best baffling around the camera window. These measurements are high compared to our expectation for three reflections of 10^{-6}. However, it may be that the anti-reflection coatings are not operating at these wavelengths so far off design. This discrepancy remains as mild evidence against the stray light path we have given. Now that we have found this source of stray light, we can create further baffling to attenuate the stray light without affecting the desired signal. In particular, the rear side of the VPH grating has a surrounding surface of glass that is currently unbaffled. This surface in no way contributes to the desired optical path, but does give red light more area in the stray light's second reflection. This improvement will be important scientifically as currently the stray light from the night sky line [OI]λ6300 with higher curvature with γ causes a minor residual in our background subtraction and interferes with automatic LAE detection algorithms.

Table 1.1 The observed red stray light compared to our stray light model. The match is convincing considering the simplifications we made in the reflections from the camera window and that different line curvatures between the proper and stray light spectra make this measurement vary over the chip at the level of the wavelength residual.

α	β_c	λ_s	Model λ_p	Measured λ_p	Attenuation Factor
10.6	10.4	6438.5	4330.6	4377.7	2E-3
11.0	15.1	8377.6	4656.2	4689.6	3E-2
11.0	15.1	8495.4	4893.0	4767.5	4E-2
11.0	15.1	8654.4	5215.1	5196.0	4E-2
11.0	15.1	8780.6	5472.9	5401.5	4E-2

1.2.6 Conclusion

The tunable nature and the broad efficiency envelopes that VPH gratings display over traditional ruled gratings are essential to reaching the low flux limits required by our science. We find that the performance results that have been documented at wavelengths in the middle of the visible spectrum can be pushed down to blue and UV wavelengths successfully without an obvious need for slanted fringes, but that RCWA predictions are not yet being achieved. We expect further iterations of design and sample manufacturing from our vendors, but counting the current results as the worst case for the final design gives us first order efficiency of 60% at 3400Å and 85% at 5000Å. Our test bench, with its computer controlled, automated operation, will be essential for the large quantity characterization that will be required for HETDEX.

Acknowledgements: This work was done in collaboration with Gary J. Hill and Phillip J. MacQueen.

1.3 HETDEX pilot survey for Lyman-α emitters

The Hobby-Eberly Telescope (HET) Dark Energy Experiment (HETDEX) (Hill et al. 2004, 2008a) will survey 60 $\square^\circ$ spread throughout 420 $\square^\circ$ to discover 0.8 million new Lyman-α emitting galaxies (LAEs) over $1.9 < z < 3.5$ and use them to map the expansion history of the universe. A further ~1 million low-z galaxies will have their redshifts determined, primarily in the [OII]3727 transition, over $0 < z < 0.47$. The primary HETDEX science goal is to measure the dark energy equation of state at high redshift by using the three-dimensional power spectrum of LAE positions and redshifts (Jeong & Komatsu 2006; Koehler et al. 2007; Jeong & Komatsu 2009; Shoji et al. 2009). An important secondary goal of HETDEX is to investigate the physical properties of star forming galaxies, through Lyα and [OII] emission, using vastly greater statistics and volumes than currently available. The survey will use an array of 150 integral field spectrographs on the upgraded 10 m HET (Ramsey et al. 1998; Savage et al. 2010) called the Visible Integral field Replicable Unit Spectrograph (VIRUS; Hill et al. 2010).

The HETDEX Pilot Survey (HPS) is the pathfinder to the full HETDEX survey. This pilot survey provides a direct test of equipment, data reduction, target properties, observing procedures, and ancillary data requirements to HETDEX by using one integral field spectrograph, named the VIRUS prototype (VIRUS-P; Hill et al. 2008b), on the 2.7 m Harlan J. Smith telescope at the McDonald Observatory over 111 nights. To do this, the pilot survey uses the novel technique of blindly targeted, wide-field contiguous spectroscopy to find emission line objects over a broad redshift range. While large numbers of narrowband-selected LAEs have been assembled by previous surveys (e.g. Hu & McMahon 1996; Cowie & Hu 1998; Rhoads et al. 2000; Steidel et al. 2000; Ouchi et al. 2003; Hu et al. 2004; Hayashino et al. 2004; Santos et al. 2004; Palunas et al. 2004; Venemans et al. 2005; Gawiser et al. 2006; Gronwall et al. 2007; Nilsson et al. 2007; Ouchi et al. 2008;

Nilsson et al. 2009; Guaita et al. 2010; Tilvi et al. 2010), these surveys are heterogeneous in nature, with different depths and equivalent width (EW) limits. The HPS is designed to produce a homogeneous sample of LAEs over an extremely large volume, 1.03×10^6 Mpc^{3}h$_{70}^{-3}$, that is nearly an order of magnitude larger than the largest existing blind spectroscopic survey, 2.5×10^5 Mpc^{3}h$_{70}^{-3}$ (Cassata et al. 2010), and vastly larger than other blind surveys (Pirzkal et al. 2004; van Breukelen et al. 2005; Xu et al. 2007; Sawicki et al. 2008; Martin et al. 2008). This allows us to evaluate potential redshift evolution of LAE properties and to make comparisons to color-selected high redshift galaxy populations (e.g. Steidel et al. 1996, 1999; Daddi et al. 2004; Kornei et al. 2010). The HPS also enables us to find a large sample of lower redshift galaxies selected through, primarily, their [OII]3727, Hβ, and [OIII] emission and study their properties over a lower redshift ranges (up to z =0.56, 0.19, 0.17, and 0.16 for [OII], Hβ, [OIII]4959, and [OIII]5007 respectively).

The paper is organized as follows. In §1.3.1 we describe the instrumental capabilities of VIRUS-P, the type and quality of data taken, the necessary calibrations, and the imaging compiled to aid source classification. We detail the data reduction steps, with special care given toward tracking systematic errors in §1.3.2. In §1.3.3, we describe the methods used to recover objects to the survey's statistical limits and analyze the effect of noise contamination and the emission-line flux measurements. In §1.3.4, we present our classification methods, relying primarily on imaging counterpart likelihoods and equivalent width measurements. The contamination of the high redshift LAE sample by active galactic nuclei (AGN) is presented as well as example classifications. The final emission-line catalog and its summary properties are given in §1.3.5. Finally, in §1.3.6, we review the analysis and describe its place in future projects.

In this work, we adopt a standard ΛCDM cosmology with H$_0$=70 km s^{-1} Mpc^{-1}, Ω_M=0.3, and Ω_Λ=0.7. All magnitudes are quoted in the AB system

(Oke & Gunn 1983). All wavelengths are corrected to vacuum conditions in the heliocentric frame with an assumed wavelength-independent index of refraction for air at the observatory's altitude of $n = 1.00022$.

1.3.1 Observations

Instrumental configuration

The Visible Integral-field Replicable Unit Spectrograph Prototype (VIRUS-P) was designed for this pilot survey and is described in Hill et al. (2008b) and references therein. The instrument is a fiber-based Integral Field Spectrograph (IFS) fed at f/3.65 on the McDonald Observatory's 2.7m Harlan J. Smith telescope. A small focal reducer sits just prior to the Integral Field Unit (IFU) input in the lightpath of the telescope's f/8.8 focus. Originally, VIRUS-P operation used a focal reducer labeled FR1, but all data taken after September of 2008 used a second focal reducer labeled FR2, which has significantly improved efficiency below 4000Å compared to FR1 (see §1.3.1). Auto-guiding and sky transparency measurements were performed with an off-the-shelf Apogee Alta camera installed into a field position $\sim 9'$ north of the IFS field of view (FOV). The guider has a square $20.25\square'$ FOV and uses a B+V filter with a mean wavelength of 5000Å at a platescale of $0\farcs53$ per pixel.

Two different IFUs have been used over the course of this pilot survey. Fiber bundle IFU-1, used prior to March 2008, spans $1\farcm70 \times 1\farcm77$ with 244 functional and 3 broken 200 μm core diameter ($4\farcs235$ on-sky) fibers. IFU-2 spans $1\farcm61 \times 1\farcm65$ with 246 functional and 0 broken fibers of the same core size. There is no significant difference in throughput between the bundles. Both IFUs are of the densepak type (Barden et al. 1998) with a filling factor near 1/3, requiring at least three dithered positions to fully sample the FOV. This survey utilizes a six position dithering pattern as illustrated in Figure 1.11. The nearly ×2 oversampling delivered by this dithering pattern provides improved spatial registration between detected spectral objects and imaging-based continuum counterparts. The wavelength range on VIRUS-P is adjustable from 3400-6800Å, and a set of volume phase holographic gratings delivering various spectral resolutions are available. For this survey the instrument was set to cover 3500-5800Å at resolutions that range from 4.5-5.5Å full width half maximum (FWHM) over the whole dataset through a 831 lines mm^{-1} grating that delivers a dispersion of 1.1Å pixel^{-1} in the unbinned charge-coupled device (CCD) mode. The spectral resolution over that range weakly and gradually varies with wavelength and between different fibers due to CCD surface shape deviations from planarity, camera design limits, and the residual camera alignment errors. The data are recorded on a 2k×2k CCD with 15 μm pixels in a custom built, LN$_2$ cooled, vacuum-sealed camera (Tufts et al. 2008b) with electronics that deliver between 3.6-4.2 e$^-$ read noise, making the sky background the dominant source of noise at all wavelengths in our 20 minute exposures. The data have been taken with 2×1 binning along the dispersion direction to minimize read noise and still maintain a Nyquist sampling of the instrumental line profile.

Several instrumental properties determine the survey's calibration needs. The instrument's scattered light properties have been discussed in Adams et al. (2008). A weak in-focus ghost of atmospheric OH lines redder than the targeted wavelength range was found to exist at discrete wavelengths. These lines are easily distinguished by their deviations from calibrated wavelength solutions and fiber trace positions. The strength of the scattered light varied over time as alignments changed and baffling was implemented, but the ghost's strength was at maximum 3× the resolution element noise, and more characteristically below the noise in any one fiber. The scattered light affected one resolution element per fiber. Extra masking installed around the grating solved this issue for all data taken after September 2008. All emission-line sources discussed in this paper from observations prior to the installation of the grating mask have been visually inspected to not lie in the

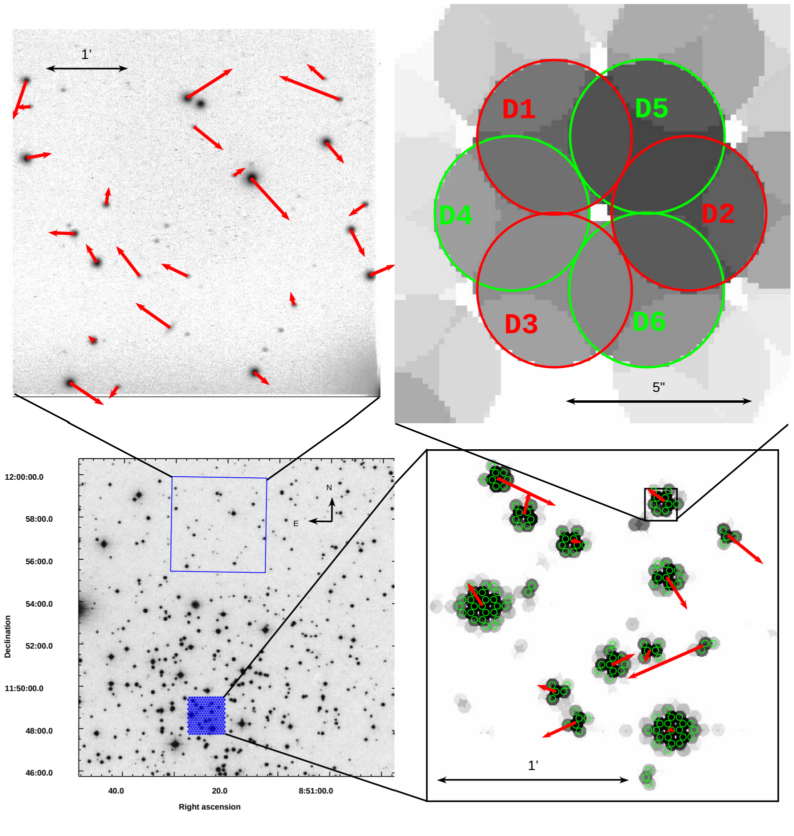

Figure 1.11 The layout of a VIRUS-P observation and the quality of a guider-based astrometric solution. *Bottom left*: The footprints of the spectroscopic science FOV and the northernly offset guider FOV overlayed on a Digital Sky Survey (DSS) image of the open cluster M67. This type of field is used to calibrate the astrometry of the guider and the fibers as discussed in §1.3.1. *Top left*: An expanded view of the VIRUS-P guider field with residuals from the astrometric model. The residuals are shown as red vectors scaled by 60×. The rms is $0\farcs42$. *Bottom right*: An expanded view of the science FOV. The continuum map is generated from the IFS data summed over $4100\text{Å} < \lambda < 5700\text{Å}$. Fibers that have significant flux and border other significant fibers are highlighted with green circles and bunched as point source detections for the astrometric fit. The residuals are shown as red vectors scaled by 60×. The rms is $0\farcs21$. The residuals in the IFU are less than the residuals in the guider as both fields have a similar number of degrees of freedom, but the guider has more datapoints. *Top right*: The expanded view of one fiber moving through the six dither positions. The pattern, marked with D1-D6, gives very nearly an oversampling of two. The small offsets necessary to complete the dither patterns are controlled by sending offsets to the guider.

affected regions.

The lab testing and characterization of the VIRUS-P fibers, with particular attention to transmission and focal ratio degradation, has been investigated in Murphy et al. (2008). A high stability in each fiber's throughput over a night, at minimum, is crucial toward the survey's goals. IFU mounting practices have been established from these tests to yield fiber stability sufficient for our purposes. To facilitate mounting on the HET as well as the Smith telescope, the IFU was made longer than otherwise necessary. Since the IFU demonstrated inferior performance when coiled, the fibers were left uncoiled for most of this pilot survey. When the IFU bundle is properly uncoiled, it is measured on-telescope to be stable over nightly operating conditions to 1% root-mean-squared (rms) for the most affected fibers and 0.3% rms for the median fiber. We will explore the effect of this potential systematic on the data in §1.3.2. There, we will show that the VIRUS-P fiber stability is not an important issue for emission-line detections, but can dominate the uncertainty in continuum estimates.

The mechanical design of VIRUS-P has been presented in Smith et al. (2008). The instrument's mechanical structures are all made from aluminium to achieve a uniform coefficient of thermal expansion between components and to maintain the optical alignment. The gimbal mount connecting VIRUS-P to the telescope allows VIRUS-P to swing into a horizontal position for any pointing of the equatorially-mounted telescope. This ensures that the trace patterns of fibers on the CCD remains constant to high precision over a night. Although a < 0.05 pixel trace shift per night is desired, this could not always be accomplished. A trace could shift by up to 0.3 pixels with temperature under some operating conditions. Consequently, data reduction steps were developed to identify and compensate for this subtle systematic; these are described in §1.3.2. There is not an atmospheric differential corrector installed on the telescope. We discuss the atmopheric effects on emission-line source astrometry in Appendix B and the absolute flux calibration of the data in §1.3.1. All observations were taken with airmasses below two.

Data collection

We obtained regular fall/winter/spring dark time observations from September 2007 to February 2010 on the McDonald 2.7m Harlan J. Smith telescope. These observing runs are summarized in Table 1.2. In total, out of our allocation of 113 nights, 61 were useful for this project. We constructed datacube mosaics in four science fields: the Cosmological Evolution Survey (COSMOS; Scoville et al. 2007), the Hubble Deep Field North (HDFN; Williams et al. 1996) and the surrounding Great Observatories Origins Deep Survey North (GOODS-N Dickinson et al. 2003), the Munich Near-IR Cluster Survey (MUNICS; Drory et al. 2001), and the XMM Large Scale Structure field (XMM-LSS; Pierre et al. 2004). We completed 27, 13, 16, and 4 field pointings, respectively in these fields, by taking three 20-minute exposures at each of the 6 dither positions. Our effective observation area, accounting for mosaic overlap, is 169.23 $\square'$ over the wavelengths ~3500-5800Å with a spectral resolution of ~5Å. This corresponds to survey volumes of 1.03×10^6 $\mathrm{Mpc^3h_{70}^{-3}}$ for LAEs and 4.24×10^4 $\mathrm{Mpc^3h_{70}^{-3}}$ for [OII] sources. As described in §1.3.1 and shown in Figure 1.12, we give the survey's flux and luminosity limits as a function of wavelength under photometric conditions for the case of a spectrally unresolved, point source emission-line object well centered on a fiber.

In addition to the science data, the following calibration data were obtained one or twice each night. Spectrophotometric standard stars from Massey et al. (1988) were observed. Flats near zenith of the dawn and dusk sky were taken. Calibration with dome lamps was explored but abandoned when none were found with sufficient blue-to-red flux balance. Sets of bias frames were taken and used to construct a master bias for each run. HgCd arc lamps were used to illuminate a

Table 1.2. Summary of VIRUS-P Observations

Date	Number of pointings	Fields	Median A_V used	Range of A_V used	Number of emission line detections
2007 Oct 04-09	3	MUNICS S2	0.29	0.18-0.44	21
2007 Nov 05-10	5	MUNICS S2;COSMOS	0.33	0.00-1.48	26
2007 Dec 04-09	6	MUNICS S2;COSMOS	0.24	0.23-0.42	36
2008 Jan 03-10	8	MUNICS S2;COSMOS	0.25	0.00-2.84	71
2008 Feb 01-12	6	MUNICS S2;COSMOS;GOODS-N	0.28	0.00-1.63	27
2008 Apr 01-07	3	COSMOS;GOODS-N	0.30	0.00-0.97	30
2008 Apr 28-May 03	3	GOODS-N	0.39	0.00-2.77	43
2008 Jun 03-09	2	GOODS-N	0.31	0.00-1.69	0
2008 Sep 24-29	2	XMM-LSS	0.36	0.19-0.51	28
2008 Nov 24-30	2	COSMOS	0.13	0.07-0.46	8
2008 Dec 22-27	4	COSMOS;XMM-LSS	0.23	0.13-0.47	40
2009 Jan 21-27	3	COSMOS;XMM-LSS	0.23	0.13-0.67	46
2009 Feb 19-23	4	COSMOS;GOODS-N	0.19	0.00-0.53	27
2009 Mar 20-25	4	COSMOS;GOODS-N	0.34	0.00-0.92	29
2009 Apr 20-25	2	GOODS-N	0.20	0.07-0.48	28
2009 May 20-25	1	GOODS-N	0.21	0.00-1.55	5
2010 Feb 09-11	1	COSMOS	0.30	0.10-0.50	0

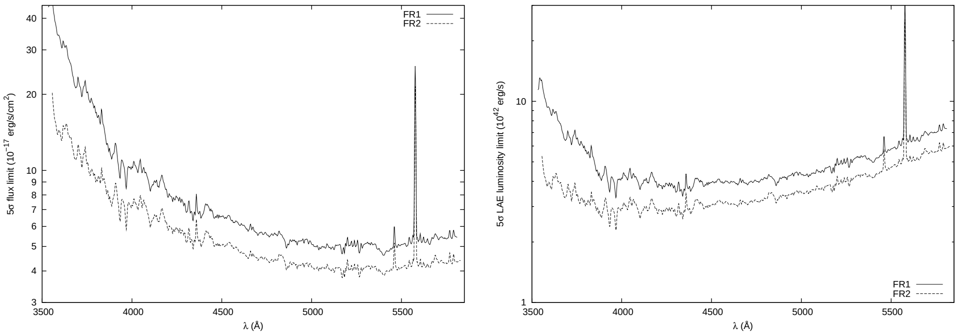

Figure 1.12 *Left* The 5σ detection limit under photometric conditions for an emission-line object perfectly centered in a fiber in three 20 minute exposures. Different source positions can improve or decrease this limit by ~15% which is captured in our completeness calculation. In both figures, curves are given for the two focal reducers, FR1 and FR2. *Right* The 5σ luminosity limit under photometric conditions for objects detected in the Lyα line.

dome screen for wavelength calibration. Custom line lists for the HgCd lamps were made by observing the lamps with the 2.7m's Tull Coudé Spectrograph (Tull et al. 1995) at R=60k. The Coudé wavelength calibration was made from ThAr lines. For most of the observing runs, guider frames were saved at intervals of 2-10 seconds, depending on the guider star brightness and transparency. The collection of guider frames was prevented 13% of the time due to human error and guider equipment failure. For those observations, the flux calibration was done assuming the median of the observed atmospheric transmission (§1.3.1) from the dataset's remaining observations.

Astrometry

The position of a faint source is not well determined by the IFS data alone since most pointings lack sufficiently bright stars to establish an astrometric solution for the frame. Instead, the positions of stars in the offset guider camera were used to determine the fiber positions; this required precise calibration of the relative astrometry between the fiber array and the offset guider. The relative fiber-to-fiber positions of both IFUs were measured in the laboratory and verified to be very regular due to the precise machining. Illumination and direct imaging in the lab showed that IFU-2 has exceptional uniformity in its fiber matrix, and no deviations from the designed pitch of 340 μm could be measured to an accuracy of 1 μm. IFU-1 is somewhat less uniformity in its fiber matrix than IFU-2. We have mapped the centroid of each fiber to within 0.3μm, or $0\farcs007$, at the nominal plate scale.

The transformation from guider field position to science field position was calibrated by on-sky measurements. Whenever the guide camera was replaced, we obtained data under a six dither pattern on open clusters at low airmass. In total, seven astrometric solutions were derived, each yielding the plate scales, offsets, and rotations of two image planes under a standard tangent projection (Greisen & Calabretta 1993). We found adequate fits with constant plate scales determined for each IFU axis yielding twelve degrees of freedom in a non-linear transformation from guider and IFS pixel positions to celestial coordinates. We first determined guider positions by using SExtractor (Bertin & Arnouts 1996) to measure the positions of stars and match to coordinates from the United States Naval Observatory's (USNO) Nomad catalog (Zacharias et al. 2005). Similarly, the continuum intensities of USNO stars in the fibers were measured by summing flux over the wavelength range $4100\text{Å} < \lambda < 5700\text{Å}$; this region was chosen to mimic the guider wavelength response and minimize atmospheric refraction differences. Fibers containing signal significantly above the noise were matched with significant detections in adjacent fibers. Centroids were calculated for each source and again matched to the Nomad catalog. A simplex method (Press et al. 1992) was then used to find the least squares minimum robustly in the presence of the many local minima. We show in Figure 1.11 the fit quality in a representative solution. The range of systematic uncertainty in our seven eras of astrometric solutions was $0\farcs17$-$0\farcs51$ with a median of $0\farcs31$.

We further measured the stability of the astrometry over many months from flux standard stars. We anticipated any drift to be negligible due to the design of plastic pins which located the IFU head against the telescope mounting surface. However, we found substantial month-to-month systematic variations of order $1\farcs8$ rms. The only clear dependence was a declination term with temperature, which we attribute to a thermal expansion of the guider camera mount. However, this expansion cannot explain the bulk of the astrometric scatter. Since we find much smaller astrometric scatter in any one month, the monthly removal and remounting of the IFU input head from the telescope between observing runs is the plausible source of drift. So, we have chosen to estimate an empirical month-by-month offset in the astrometric zeropoint which lowers the median monthly rms to $0\farcs6$ and ranges from $0\farcs0$-$1\farcs0$.

Coarse positional sampling by the large fibers and low S/N limitations forms the final component of the astrometric error budget. In order to quantify this uncertainty, we have simulated the positional recovery for a range of emission line sources. We describe those simulations in §1.3.3. The result is a fit to the random astrometric uncertainty with a functional form of $\sigma_{r,random} = 0\farcs348 + 2\farcs04/(S/N)$.

We can assess the completeness of our error budget by measuring the observed positional offsets of emission-line objects found with high confidence counterparts. As explained in §1.3.4, a comparison of our fiber detections with broadband imaging shows that 55% of our emission-line detections have an isolated counterpart detected with $\geq 90\%$ confidence. Through a comparison, we find a mean offset of $\Delta\alpha = -0\farcs53 \pm 0\farcs05$ and $\Delta\delta = 0\farcs39 \pm 0\farcs05$ between the fiber-based emission-line source positions and the broadband photometric centers. The source of this offset is not certain, but we apply it to all our reported emission-line positions. After correcting for this offset, the counterpart associations were iterated to produce our

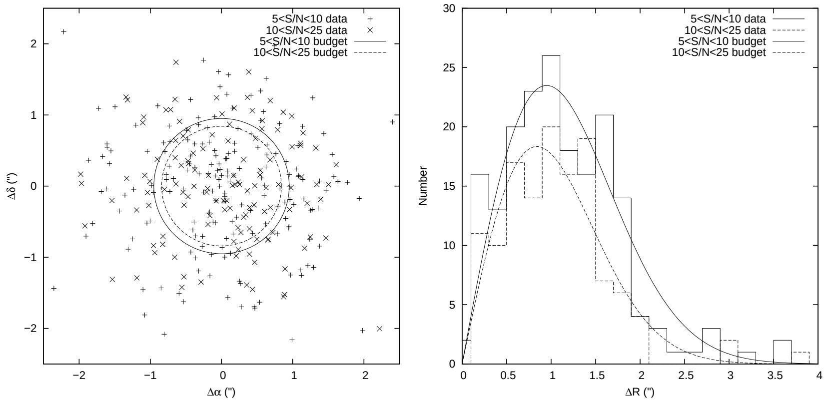

Figure 1.13 *Left*: The positional offsets from catalog emission-line detection positions and broadband counterpart image positions divided into two S/N bins. The residual correction discussed in §1.3.1 has been applied. The 1σ astrometric error budget for each bin is also drawn with radii $0\overset{\prime\prime}{.}95$ for $5 < S/N < 10$ and $0\overset{\prime\prime}{.}84$ for $10 < S/N < 25$. *Right*: A histogram of the same data shown with a Rayleigh distribution. The same dispersions are used to demonstrate the appropriate characterization of the astrometric error as a two-dimensional Gaussian function.

final emission-line positions. In Figure 1.13 we present the distribution of the data offsets to test the error budget. This error budget serves as an important input in the method (§1.3.4) for assigning broadband counterparts in crowded fields to the emission-line sources.

Flux calibration and transparency

The majority of the observations were not taken under photometric conditions, hence a proper flux calibration requires a realtime measurement of the atmospheric transparency. Unlike some modern wide-field imagers, the VIRUS-P field of view is not large enough to contain photometrically calibrated stars in the majority of its arbitrary pointings. However, the offset guider with a larger field of view has a size sufficient for this continuous calibration purpose. We recorded all guide camera exposures sampled at 2-10 seconds that were contemporary with the IFS science exposures. The guider exposure times varied depending on the guide star brightness. Basic bias-subtraction and flat-fielding reductions were implemented on the guider frames. We performed aperture photometry on all stars detected. When available, we used Sloan Digital Sky Survey (SDSS) measurements (Adelman-McCarthy et al. 2008) for our calibrations; otherwise we used the USNO-B1.0 survey (Monet et al. 2003). The SDSS photometric precision is quoted at below 1% for guide stars used, typically V< 19. The USNO-B1.0 photometric precision is typically much worse, ~0.25 magnitudes, and this directly leads to an important uncertainty in line fluxes for objects in the MUNICS and XMM-LSS fields. Accordingly, we have added in quadrature a 15% error, assuming the median of three guide stars per field, to the flux and equivalent width (EW) measurements for the MUNICS and XMM-LSS sources. We treat these errors as random, since multiple and independent sets of stars were used in different mosaic pointings and multiple spectrophotometric standards were observed. A color term was fit from the guider data considering its non-standard, wide-bandpass filter, a new zeropoint was calculated each month to correct for periodic equipment changes and mirror cleanings, and non-photometric extinctions were found for each frame after removing a standard airmass term of 0.186 mag AM^{-1}. Typically, we had two to five stars per field that were bright enough for this purpose. The resultant distribution of zeropoint offsets due to transparency, Δzp, is given in Figure 1.14. By measuring the scatter in the zeropoint offset from all the stars available in each frame, we find a mean uncertainty of 6% in the guider-based photometric correction.

The flux calibration of IFS data was done in a manner similar to that for longslit spectroscopy, but with some additional steps to compensate for fiber sampling patterns. We used the spectrophotometric stars and calibrations of Massey et al. (1988) observed under a six-dither pattern. Airmass extinction coefficients for photometric conditions with a curve specifically modeled for McDonald

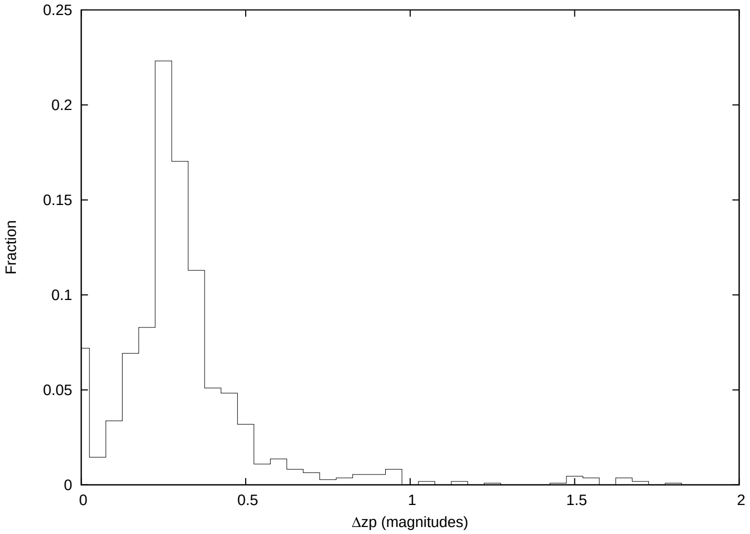

Figure 1.14 The distribution of zeropoint offsets due to non-photometric transparency as measured with the guider camera. This distribution represents the best $60^{\rm th}$ percentile of the observing allocation with the remaining 40% being too poor to guide or requiring dome closure.

Observatory are applied. This extinction curve is similar to the Kitt Peak curve supplied with IRAF. The bright standards allowed us to determine both the source position relative to the fiber grid and the seeing Point Spread Function (PSF), which in turn yields the exact fiber sampling. In contrast, fainter emission-line sources require statistical sampling corrections that are discussed in §1.3.3. In order to determine the percentage of incident flux captured over the six dither positions, we employed the following analysis. We began by considering the spectra for all fibers positioned within a large radial aperture (operationally, $8''$) from the stellar centroid. and adopting a seeing model with a 2D circular, Gaussian PSF. The broadband flux of each fiber was measured by summing over a large wavelength range (operationally, $4000Å< \lambda <5500Å$). The PSF and Gaussian normalization were determined through a nonlinear least squares minimization by assuming the spatial response of each fiber was tophat. The sampling correction was then formed from the ratio of the Gaussian normalization to the sum of the broadband flux measurements. Then, the spectral count rates of the relevant fibers were resampled to a common wavelength scale, co-added, and normalized using the sampling correction. By using such a broad, circular aperture, we ensured that the effects of atmospheric differential refraction on the co-added spectrum were negligible. The final spectral flux calibration curve was then formed from the ratio of the published, absolute flux density to the sampling corrected data count rate. Spectrophotometric standards were taken under a range of conditions, so their comparison required a further correction for transparency as estimated from the guider measurements. Once done, we find an rms between all flux calibration curves of 9.3% and 8.5% for FR1 and FR2. We find no trend with wavelength in this scatter and so validate the assumed gray zeropoint correction for all guider transparencies at these levels of uncertainty. The final catalog will list the random line flux errors, but the whole sample may be considered to also be subject to the ∼10% flux calibration systematic uncertainty just discussed. We do not fold the systematic into the tabulated values as relative comparisons within the sample should not be subject to it.

Several statistics from this flux calibration analysis summarize the survey's performance. First, the range of atmospheric transparencies for recorded data is shown in Figure 1.14. These statistics are biased against periods of weather too poor to attempt observation and represent only the best 60% by time. The median nonphotometric transparency penalty to this survey in the observable periods is 0.28 magnitudes. The total system throughput is shown in Figure 1.15 as the fraction of light recorded after passing through one photometric airmass (zenith), the telescope, the focal reducer, and the VIRUS-P instrument. The curves for the two focal reducers show a dramatic difference: FR2 performs better than FR1 at all wavelengths, but particularly in the blue where FR1 has only half the throughput of FR2.

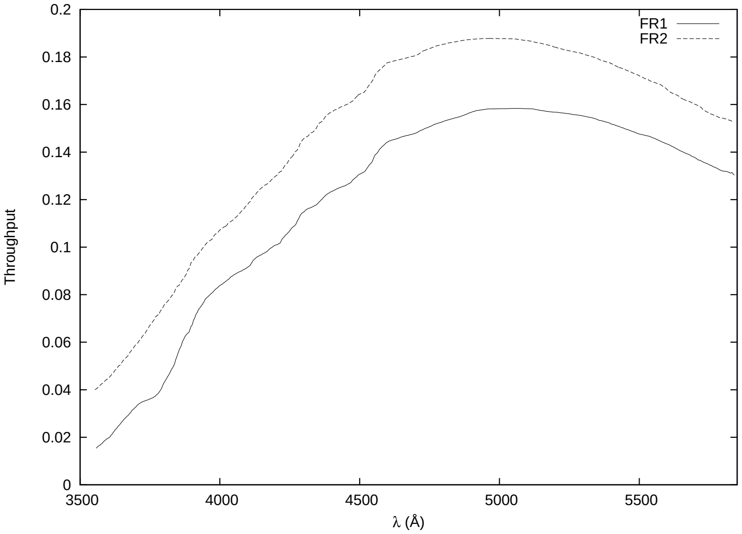

Figure 1.15 The total system throughput of VIRUS-P, the 2.7m telescope, and the atmosphere at an airmass of one. Curves are given for the two eras of focal reducers, FR1 and FR2.

The combination of read noise, system throughput, and sky brightness determine the detection limit for an unresolved emission-line source. Figure 1.12 shows the 5σ limit in a detection element (defined as $\pm 2\times$ the instrumental dispersion or $\pm 1.9\times$ binned pixels), which is nominally the survey's photometric limit with some modulation for sources sampled under different fiber positions. The luminosity limit for LAEs is also shown in Figure 1.12. The exact limits will be further explored in §1.3.3 and compensated for with the completeness limit derived in §1.3.3. Finally, in Figure 1.16 we give the sensitivity maps at 4500Å for spectrally unresolved point sources, taking into account mosaic overlap, bright objects, dead fibers in IFU-1, guider measured extinctions, and the range in airmass over the dataset. Small gaps in the map are due to the slightly different sizes of IFU-1 and IFU-2, and the failure to complete the desired six dither pattern in one COSMOS pointing by only completing a three dither pattern. Finally, five fields were chosen to overlap with previous fields for cases where transparency in the first pass yielded poor depth.

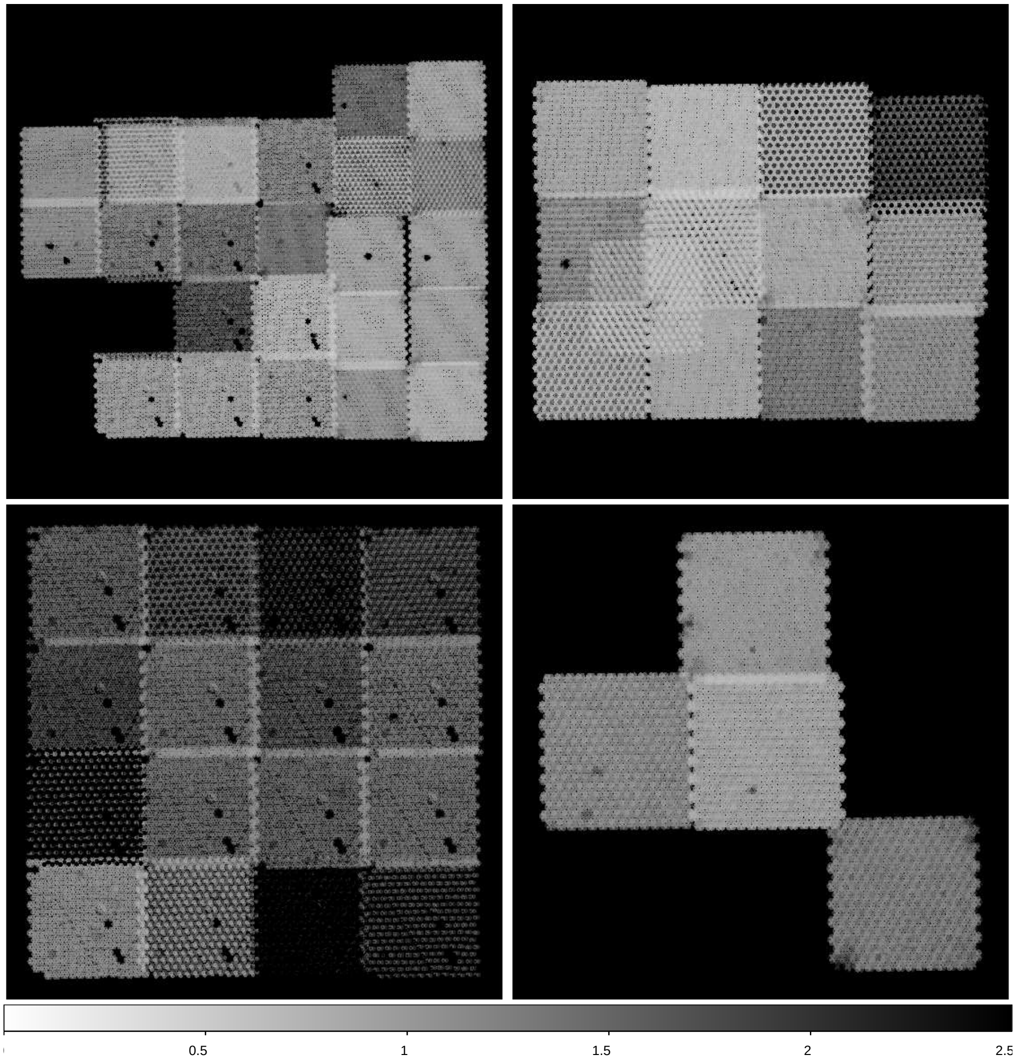

Figure 1.16 Sensitivity maps (1σ per detection element) at 4500Å in 10^{-17} erg s^{-1} cm^{-2}. The three broken fibers in fiber bundle IFU-1 are evident. *Top left*: COSMOS, *Top right*: GOODS-N, *Bottom left*: MUNICS, *Bottom right*: XMM-LSS.

Ancillary imaging

This survey discovers and spectroscopically measures LAEs in one pass, as opposed to narrowband surveys that often require spectroscopic confirmation on a subsample. The depth and bandpass restrictions of VIRUS-P, however, still make discrimination between LAEs and low-z contaminants challenging. For both LAEs and [OII] emitters at many redshifts, we expect to have only one strong emission line in the VIRUS-P bandpass. Respectively, [OIII]λ5007, [OIII]λ4959, and Hβ will be lost at $z > 0.158$, $z > 0.170$, and $z > 0.193$, and the survey's spectral resolution does not resolve the [OII] doublet. Furthermore, the variation observed in local galaxies for strong line ratios (Kennicutt 1992) never guarantees that two statistically significant lines will be detected. By necessity, we resort to an EW cut, as used extensively in LAE narrowband surveys, to classify single emission-line detections. We discuss the EW cut further in §1.3.4. However, the VIRUS-P spectra are not sufficiently sensitive for continuum detections for the majority of the emission-line detections. To reach the necessary limits, we must supplement the spectra with deep imaging.

This dataset's fields are located in regions of the sky with existing deep images and catalogs (Drory et al. 2001; Fernández-Soto et al. 1999; Capak et al. 2004, 2007; Ilbert et al. 2009). The XMM-LSS field does not have a published catalog but is covered by the Canada-France-Hawaii Telescope Legacy Survey[1] (CFHTLS) wide field W1. The deep MUNICS images, which were not part of the original publications, consist of B$_J$, g', i', and z' data taken with the Large Area Imager for Calar Alto (LAICA) on the Calar Alto Observatory 3.5m, with zeropoints made by matching stellar photometry to the published catalog. Instead of using the litera-

---

[1] Based on observations obtained with MegaPrime/MegaCam, a joint project of CFHT and CEA/DAPNIA, at the Canada-France-Hawaii Telescope (CFHT) which is operated by the National Research Council (NRC) of Canada, the Institut National des Science de l'Univers of the Centre National de la Recherche Scientifique (CNRS) of France, and the University of Hawaii. This work is based in part on data products produced at TERAPIX and the Canadian Astronomy Data Centre as part of the Canada-France-Hawaii Telescope Legacy Survey, a collaborative project of NRC and CNRS.

ture catalogs, we have chosen to produce our own SExtractor catalogs on the images and error maps; this ensured a consistent analysis for the fields and pushed the S/N to a lower threshold for a more complete emission-line association. We list select properties of the relevant broadband data in Table 1.3. The table also gives the Galactic extinction values (Schlegel et al. 1998) we applied to the continuum and emission-line fluxes under the extinction curve fit of O'Donnell (1994).

Care was taken in the photometry to ensure our photometric colors were robust. Two measures of seeing FWHM are relevant: the one for the particular band where a Kron (Kron 1980) aperture is measured (FWHM_{Kron}) and another larger value to which the other photometric bands will be matched (FWHM_{match}). For each field, we formed a detection image by stacking the deeper available bands without matching each band's seeing (see Table 1.3). The detection parameters of SExtractor were then set to find a minimum of three neighboring pixels detected with 1σ significance over sky without filtering. Since we will only be using sources with 3σ significance in their photometry, the exact detection weights and filters have little importance. Also, the return of spurious continuum sources from the low significance thresholds is acceptable for our application. A chosen band with good depth for each field, labeled here as i, was compared to the detection image using SExtractor dual image mode, in order to measure flux densites in a blending corrected Kron aperture, $\hat{f}_{\nu,i,Kron}$. The Kron ellipse dimensions a and b were also measured. Blending correction was crudely accomplished with the SExtractor `AUTO` flux measurements and the flag `MASK_TYPE` set to `CORRECT`. Under this setting, SExtractor sums the flux from the opposite side of the Kron aperture whenever it encounters pixels covered by multiple Kron apertures. In the remaining bands, labeled here as j, each frame was matched in seeing to FWHM_{match} and run in dual detection mode to measure the flux density in a circular aperture of diameter $1.4\times\mathrm{FWHM}_{match}$, $\hat{f}_{\nu,j,circ}$. The term $f_{corr} = (1 - e^{-0.5ab/\sigma^2_{Kron}})$ then forms a cor-

Table 1.3. Ancillary broadband imaging properties

Field	Central α (J2000)	Central δ (J2000)	E(B-V)	Filters	FWHM *	Stack †	Band$_K$ ‡	Depth **	VIRUS-P area ($\square'$)
COSMOS	10:00:30	+02:15:04	0.018	u*,B$_J$,V$_J$,r',i',z'	1.33	B$_J$r'i'	V$_J$	26.5	71.6
GOODS-N	12:36:51	+62:12:51	0.012	U$_J$,B$_J$,V$_J$,R$_J$,I$_J$,z'	1.26	B$_J$R$_J$I	V$_J$	26.6	35.5
MUNICS-S2	03:06:41	+00:01:15	0.083	B$_J$,g',i',z'	0.99	B$_J$g'i'	g'	25.8	49.9
XMM-LSS	02:21:20	-04:30:00	0.027	u*,g',r',i',z'	0.97	g'r'i'	g'	25.8	12.3

[*] The worst seeing FWHM in $''$ to which all bands are matched.

[†] Filters combined to form the detection image.

[‡] The band chosen for Kron aperture measurement.

[**] The 5σ limit in AB magnitudes for a point source in a $2''$ aperture for the band with the Kron aperture measurement.

rection factor for the fraction of flux lost to the Kron aperture from a point source under seeing with dispersion σ_{Kron}. The final aperture-corrected flux density in each band j was then estimated from Equation 1.2. Standard error propagation was applied.

$$\hat{f}_{\nu,j} = \frac{\hat{f}_{\nu,i,Kron} \times \hat{f}_{\nu,j,circ}}{\hat{f}_{\nu,i,circ} \times f_{corr}} \tag{1.2}$$

This resultant source catalog was used only in cross-correlation with our VIRUS-P emission-line catalog to identify object counterparts. The method of assigning counterparts is described in §1.3.4. The emission line fluxes are subtracted off from the broadband measurements according to the filter transmission curves as supplied by Brammer et al. (2008) once counterparts are assigned.

1.3.2 Data reduction

The science goals of this survey required the development of a custom reduction pipeline. Several IFS reduction pipelines already exist (e.g. Valdes 1992; Zanichelli et al. 2005; Turner et al. 2006; Sánchez 2006; Sandin et al. 2010) and are well suited to many applications. In particular, we first tried using a predecessor of `p3d` (Sandin et al. 2010; Becker 2002). The crucial limitation of the `p3d` package and all other IFS pipelines at the time, is that they resample the spectrum of each fiber onto a common wavelength scale at some step in the processing. This step correlates errors and complicates the detection statistics. In fact, we found by running simulated, source-less VIRUS-P data through `p3d` that many more resolution elements were flagged to have 5σ significance than was possible from the input Poisson statistics. The use of `p3d` would have either produced too high a contamination fraction or required higher S/N cuts and survey flux limits. This consideration led us to develop a set of scripts and FORTRAN routines collectively called Vaccine. Many of the pipeline steps are standard to all spectroscopic reductions. However, the primary Vaccine requirement to avoid data resampling is done in a manner similar to the Kelson (2003) pipeline developed for longslit spectroscopy and affects the flat fielding and sky subtraction steps.

Preliminaries

The first operation done to each VIRUS-P frame is to measure a single bias value from the overscan regions, subtract it from the frame's data section, and trim the overscan. A master bias then is created from all the overscan-subtracted biases taken during an observing run (typically 100 to 200 frames). Overall, the noise statistics in bias frames were remarkably stable and indistinguishable over weeks. Next, we cleaned the images with a bad pixel mask made by exposing the camera to scattered white light and finding the pixels with relative quantum efficiency outside 10% of the CCD's median. The VIRUS-P CCD has very clean cosmetics: besides the two rows nearest the readout register, this bad pixel mask only contained thirteen total pixels in three patches. Data combination for all co-additions of frames is accomplished using the biweight estimator (Beers et al. 1990); this algorithm was chosen for its robust performance regarding outliers such as cosmic rays. The master bias and individual overscans are subtracted from all calibration, science, and flux standard frames. Calibration frames, consisting of arc frames and twilight flats, are taken at the beginning and end of each observing night. The dawn arcs and flats were preferentially used over those frames taken in dusk, as they were a better match to the temperature of the night-time conditions.

As is common to both IFS and slitlet multi-object spectroscopy, the traces of all fibers are not strictly parallel to the CCD pixels or to each other. The fiber profiles, taken from a flat field calibration, must be traced to define an extraction aperture of each fiber. Moreover, the dispersion axis is not necessarily parallel to each fiber's trace. However, with the camera alignment in VIRUS-P, we found the maximum deviation of this misalignment is 0.2 resolution elements, so we ignored this distinction and defined the dispersion axis along the fiber trace to be perpendicular to the cross-dispersion direction. This assumption effectively broadens, slightly, the resolution in some fibers. The tracing is then made by fitting Gaussian functions to cuts along the cross-dispersion axis at a series of wavelengths for each fiber. The Gaussian centers are fit by a fourth order polynomial across the CCD. This fit was tested against repeated flats and shown to be precise to < 0.1 pixels across the CCD. Trace information is displayed for the user, who can iterate the fit tolerances if required. All further operations are done in the traced coordinates with cross-dispersion apertures of five pixels. Vaccine propagates errors for all operations starting with the read noise and keeps track of the Poisson noise from sources and the background sky.

Wavelength calibration

An automated peak finding algorithm is run on the arc lamp frames, and line identifications are made from a user entered initial wavelength solution. Typically, seven unblended HgCd lines are found with their central pixel locations determined by a Gaussian fit to the line profile. The pixel-to-wavelength mapping is then fit with a fourth order polynomial in the dispersion direction. The first order term of that polynomial is found to vary smoothly for all fibers as a function of the cross-dispersion direction. Hence, for increased accuracy, this first order term is refit as a function of the cross-dispersion distance from the camera optical axis using a fourth order polynomial. Finally, the wavelength polynomial as a function of dispersion direction pixel is refit, this time with the constrained first order term. The residuals of this procedure are typically one hundredth the size of a resolution element and the solutions are stable to a tenth of a resolution element over several weeks.

The heliocentric correction is found for each frame by using a FORTRAN implementation (written by G. Torres[2]) of the IRAF task `bcvcorr` in the `rvsao` package (Kurtz & Mink 1998). The small, <1 km s^{-1} differences in heliocentric velocities for exposures at the same dither position but taken over different nights are ignored and only the mean heliocentric correction between them is applied. All reported wavelengths are in the heliocentric frame. A correction to vacuum conditions is made assuming an index of refraction for air of n=1.0002 for all observed wavelengths.

Flat fielding

Typically fifteen twilight flats were taken each night and combined using the biweight estimator. To ensure high S/N in the twilight flats, each frame was exposed to near but below the CCD's 1% nonlinearity specification which occurs at 50% of full well. Four signals are present in the twilight flats, 1) the solar spectrum, 2) the relative throughputs between fibers, 3) the fiber profile in the cross-dispersion direction, and 4) the relative pixel-to-pixel responses. To remove the first of these we employed a bspline fit (Dierckx 1993) constrained by input from large subsets of fibers. Such a fit is robust against outlier datapoints (i.e. our cosmic rays or faint sources that fill a subset of the data) and fits curvature that a linear interpolation would miss. The advantage of the bspline fit is best leveraged when a spectrum is highly supersampled, and the camera's optical distortions naturally deliver this quality in different fibers, predominantly as a smooth function of cross-dispersion direction. However, the slight (10%) spectral resolution variation across the CCD disfavors a single fit for all the fibers' data. As a compromise, we consider each fiber with its twenty nearest fibers in CCD coordinates. Within these sets the spectral resolution variations at any wavelength are less than 2%. We do not make more complicated corrections for the spectral resolution variation beyond this. The

---

[2] http://tdc-www.harvard.edu/iraf/rvsao/bcvcorr/bcv.f

bspline fit for each fiber, serving as a model of the solar spectrum, is then divided into the original flat field data, resulting in a precision between different sets of frames to <1% rms.

Background subtraction

The majority of VIRUS-P fibers and resolution elements in this blind survey record blank sky. This enables the noise if our sky model to be driven down by stacking measurements over many fibers, so long as the noise is statistical. By using the 50 nearest fibers in the cross-dispersion direction, the statistical noise in the sky can be reduced to only 14% of a single fiber's noise. In this way, the uncertainty in the post-sky-subtracted data can be made very close to that of the pre-sky-subtracted data (as long as the flat-fielding systematics are understood). Our sky background models were formed identically to the flat field models.

We note, however, that this semi-local sky estimation method is only robust for sources that fill a small fraction of the combination window, which on-sky is approximately $\Delta\alpha$=100$''$ by $\Delta\delta$=20$''$. No bright, broadband sources have such sizes in the survey fields. Moreover, in order to further avoid oversubtracting bright sources, we constructed an object mask prior to the bspline fit. Any fibers that yield $>2\sigma$ significance in the continuum, as estimated by combining the data and errors across all VIRUS-P wavelengths, were placed in the object mask.

Data combination

The count rates in the three frames taken at each dither position were first corrected by the airmass-based photometric extinctions and the guider-based transparency measurements and then combined. The three frames and the 5 pixel cross-dispersion aperture delivered fifteen input values to the biweight estimator at each wavelength. The VIRUS-P flux standard frames are passed through Vaccine exactly as the primary science data. Finally, the science spectra (and errors) are scaled by the flux calibration (§1.3.1) to form a set of calibrated, one-dimensional spectra at each fiber and dither position.

Systematic errors

We identify three potential sources of systematic error in VIRUS-P data, one unimportant, and two that require monitoring. First, we discuss why crosstalk between fibers is not important in VIRUS-P data. Next, we identify the effects of throughput variations and the accuracy of flat field cross-dispersion profiles on the error budget as the most prominent systematics. Finally, we describe an empirical, frame-specific estimate of the systematics that must be added to the random errors.

IFS crosstalk occurs when the profile of a fiber in the cross-dispersion direction significantly overlaps that of other fibers projected nearby on the CCD. We make no crosstalk correction in Vaccine for two reasons. First, the fibers are measured to have cross-dispersion profiles of 4 pixels FWHM size. This is a factor of 2 smaller than the center-to-center fiber spacing on the CCD and results in larger relative fiber spacing than in many IFS instruments. As a result of our 5 pixel extraction aperture, sources of equal strength in neighboring fibers imply only a $< 0.5\%$ contamination. Second, the blind field selection of this survey leaves most fibers seeing only uniform sky background and leaves little risk from cross-talk contamination. A fiber aligned on a source will usually be isolated and trade an equal flux from the background sky with its crosstalk neighbors. The flux calibration (§1.3.1) steps use the same cross-dispersion aperture, and therefore correct for the source flux lost by crosstalk.

The stability in the throughput of fibers can cause significant systematic errors in some measurements. As discussed earlier, our fiber throughput is very stable, with 1% rms variation at worst and 0.3% median variation over a night. However, our background sky is 25-40× stronger than the statistical noise limits in each resolution element. As a result, the systematics can overwhelm the statistical errors in spectral apertures of six resolution elements or more during the worst stability conditions. Continuum estimates using large wavelength ranges may thus be severely affected in our survey, and we make no claims on such properties. However, the situation for emission lines is far better. First, the systematics in a detection element (approximately two resolution elements) are at worst 56% of the statistical error and at median are 13% before background subtraction. Second, most of the throughput variation is captured in the background subtraction step. As described in §1.3.3, before we detect emission lines we subtract off a locally estimated continuum value using roughly ninety independent spectral pixels. Since fiber throughput variations manifest uniformly across wavelength, the spurious signal is a small multiple of the sky spectrum and relatively featureless over our bandpass (exempt for the bright [OI] 5577Å sky line which we mask prior to all detections). The systematic error in a post-background-subtraction detection element therefore drops to 5.9% of the statistical error in the extreme case and 1.4% of the statistical error in the median case. We include this systematic uncertainty in both the detection and flux calibration error budgets via the empirical correction described below.

The final known source of systematic error is occasional variability in the cross-dispersion profile that occurs with time and temperature for different fibers. These profile changes can appear as both a trace position shift and a width change, and while small, are important. Between twilight flats spaced eight hours apart and through maximum dome temperature changes of ten Celsius degrees, we have measured trace shifts of up to 0.3 pixels and profile FWHM changes of 0.3Å. Our goal was to limit this systematic to 10% for any pixel in the flat. The FWHM variation already meets this criterion, but the maximum trace shift is too large by a factor of six. Moreover, although the trace shift also appears to be coherent between adjacent fibers on the CCD, it sometimes goes in opposite directions at the opposite ends of the fiber bundle, as if the traces are subject to a “breathing mode.” We have developed a heuristic solution that mitigates this problem. The core idea is to measure the offset over subsets of fibers, alter the flat fields to maintain the fiber-to-fiber and pixel-to-pixel patterns but resample the fiber profile to produce a shifted flat tailored to each exposure.

For each pre-sky-subtracted data frame, the fiber centroids at each wavelength along the cross-dispersion direction are calculated with respect to the corresponding flat. These trace shift estimates are then median smoothed with their twelve nearest fibers on the CCD. Rather than presume a cross-dispersion profile shape, which displays non-Gaussian features, we use sinc interpolation to resample the profile. Linear interpolation fails to recover the strong curvature in this profile. In each fiber and each wavelength, the flat field is resampled at the fiber-specific estimated offset relative to the polynomial trace peak. However, additional smoothing is still required to leave pixel-to-pixel features unaltered. To do this, we run a boxcar smoother of eighty-one pixels along the dispersion direction for both the original flat field and the sinc resampled flat field. The biweight of each forms a pure profile model in the original and resampled frames, and the pixel-to-pixel variations are isolated in a separate image. The total, shifted flat is then formed by multiplying the pure, shifted profile model by the isolated pixel-to-pixel estimate. A final scaling is then applied to maintain the fiber-to-fiber throughputs and total flat normalization, as sinc interpolation does not automatically conserve flux. The use of these shifted flats rather than the original flats results in lower systematic errors and meets the goal of $< 10\%$ flat field profile error.

To capture any remaining systematics we have made a second, independent estimate of the error using the rms of the fifteen measurements that go into the final data combination (§1.3.2). This error estimate is itself noisy, but the ratio between this empirical error and our formal error over all pixels is useful as a diagnostic. We find the median of this ratio per frame is 0-20% above the random noise alone, and the median over all data is 5%. Therefore, we increase the errors by this amount prior to the detection steps. Figure 1.17 shows the distribution of all 87.9 million independent datapoints divided by the error estimates of this dataset. Versions prior to and after continuum subtraction are shown. If the dataset were entirely without signal, if all the systematics were understood, and if all the noise were uncorrelated, the distribution should match the given Gaussian function with a dispersion of unity. Clearly the distribution is asymmetric, distorted on the positive end by signal and the negative end presumably by the previously discussed fiber throughput variations. However, the continuum subtracted data with the fiber throughput variation removed are much more symmetric and show a distribution that is a much better match to the Gaussian width. Emission line objects are detected in the continuum-subtracted data, and the noise model is validated.

1.3.3 Emission line source selection

The controlled selection of emission-line objects is the next step in producing this survey's catalog. The primary task of the detection process is to optimally use the source signal that has been distributed into, potentially, several fibers. The challenge is to push to a high completeness level at low S/N under a contamination constraint. The approach we adopt is to define emission-line detection seed apertures at a low S/N significance, test the combination of the seed apertures and all nearby fibers on sky, and allow the aperture to grow if the significance of the encompassed signal increases. The growth process is iterated. To understand the completeness and contamination rates of this method, we also present simulations with mock data. In similar datasets such as blind longslit spectroscopy (Gilbank et al. 2010) and grism spectroscopy (Meurer et al. 2007), detection algorithms based on data convolution

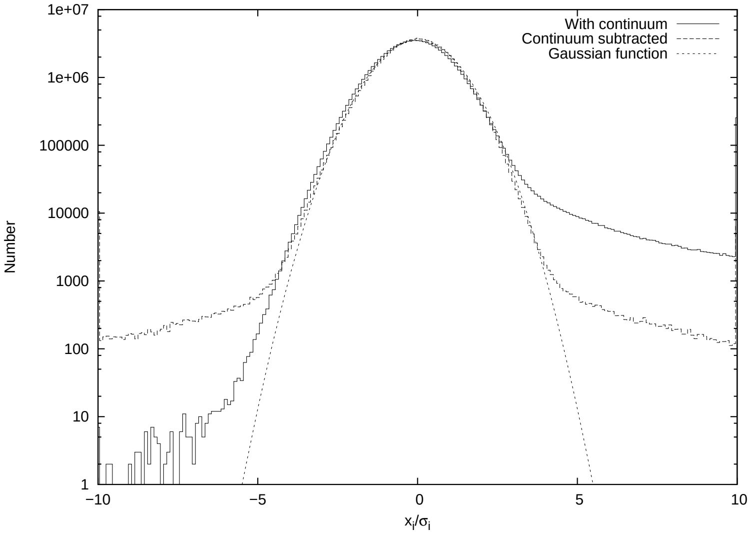

Figure 1.17 A histogram of the ratio between the reduced data and error for all 87.8M indepedent spectral elements in this survey. Most elements only see the sky background with residuals consistent to a normally distributed noise model. A small but obvious fraction of the elements also see bright, positive signal from continuum sources. The normalized Gaussian function shows the expected distribution in the absence of signal and systematics. The influence of the fiber throughput systematic (§1.3.2) likely broadens the distribution. This is most evident on the negative side which becomes nearer the normal distribution after background subtraction. The distribution after continuum subtraction appears much more symmetric and with a better matching width. The data wings at high and low ends represent the fiber positions with strong continuum. The boxcar-based continuum fitting is a rather crude tool that does not characterize all the continuum signal, but the emission line catalog is uncompromised by its use.

have been used. We have tested this approach on our dataset, but found it inferior in completeness to our adopted technique (see §1.3.3).

Detection method

Several terms require definition before we describe the detection method. A fiber position carries a set of neighboring fibers, defined as all other fibers offset by $\leq 3''$ in their center-to-center coordinates. The detection aperture starts with one fiber and, by iteration, is allowed to grow by accepting neighboring fibers. A detection aperture may be composed of multiple fibers and has its own set of neighbors, defined as the union of all neighbors to the current member fibers. The S/N of a potential emission line is calculated in a specific spectral window around the fit central wavelength. We define this detection window as spanning $\pm 2\sigma_{res}$ where σ_{res} is the dispersion of the VIRUS-P resolution element (2.2Å). Within this window, data are summed and errors added in quadrature. Pixels that straddle the window are included by their fractional overlap.

We begin with the fully calibrated spectra, errors, and fiber sky coordinates. First, a local continuum for each fiber is estimated and removed through a 200Å wide biweight boxcar. Second, seed apertures are defined as all pixels that have 1σ positive significance under a 6Å wide boxcar smoothing. Seeds are merged when found in the same fiber and at contiguous wavelengths. Third, a Gaussian model is fit to each seed with variable width, wavelength, and intensity using a data window of 30Å. We anticipate emission-line widths for LAEs to lie below the VIRUS-P spectral resolution, but the detection method is designed to be general to all line widths. We experimented with basing the detection aperture on the Gaussian function's fit width instead of the instrument's resolution, but simulations showed that the broad fits produced an unacceptable level of contamination. Fourth, fits with the seed apertures and each of the neighboring fibers are made. When making fits using multiple fibers, each fiber's emission-line intensity is allowed to vary, but constrained to a common wavelength and width. Fifth, if the inclusion of any prospective neighboring fiber increases the total S/N over a particular threshold, the fiber with the greatest increase is added to the detection aperture. Operationally, we use a threshold of $\Delta S/N = 0.3$. Sixth, these steps are iterated until the apertures no longer grow or the aperture size reaches six fibers. The cut at six fibers is chosen because in the dither pattern, a point source can be equidistant from at most six fibers. Seventh, a final significance cut is made on the potential detections. If the detections had only been made using single, independent apertures, simple counting statistics could be used to meet the $< 10\%$ contamination goal. For example, when applied to the luminosity function of Gronwall et al. (2007), our S/N≥5 cut and no galactic extinction implies that we should see 2.4 LAEs per VIRUS-P pointing under photometric conditions. Similarly, a VIRUS-P pointing (over six dithers) has 756k independent resolution elements, so a S/N≥5 cut would deliver 8% contamination. Unfortunately, the more complicated detection algorithm used here is not so straightforward to assess. While the growth steps will recover some sources that would otherwise be missed, they can also bundle noise from neighboring fibers. We therefore have made simulations of mock noise frames in order to optimize our selection thresholds.

False source tests

To test for false sources, we began by simulating full, two-dimensional spectral data for twenty-five VIRUS-P fields using the observed median sky brightness. The mock data were made with noise realizations from the actual sky background and CCD read noise but were otherwise without sources. The fields were then analyzed for emission-line sources exactly as in §1.3.3 for all detections that reached S/N $\geq$ 3. The number of spurious sources were then compared to the expected number of true LAEs (Gronwall et al. 2007) as a function of S/N cut, aperture, size, and survey depth. Evidence indicates that the LAE luminosity function does not evolve strongly at $z = 3$ and higher redshifts (Ouchi et al. 2008), but there is less certainty about the rate of evolution over the lower redshifts that we also probe (Nilsson et al. 2009; Cassata et al. 2010). The results of this analysis are shown in Figure 1.18. Interestingly, at higher S/N the larger apertures begin to contribute the most contamination. Under the typical survey observing conditions and the majority (∼80%) of source-fiber geometries, the optimal number of fibers to include in a simultaneous detection is two. Point source emission objects, which we anticipate most LAEs to be (Bond et al. 2010), rarely ($< 5\%$) benefit from fiber apertures of four or more. Conversely, the S/N for extended low-z objects is often improved by including more fibers, so we should not avoid large apertures altogether. Finally, it is clear that a common cut of S/N ≥ 5 would deliver an unacceptably high rate of (60%) contamination. The situation can be improved by varying the S/N limit as a function aperture size. The choice we adopt is for an aperture of N fibers to have a S/N cut of $S/N \geq 5 + 0.3 \times (N - 1)$. Under the assumption of a non-evolving LAE luminosity function, we predict a 10%±1.6% contamination of spurious sources to the LAE sample. We project there are 17±3 spurious sources in the data catalog. A sample essentially free of contamination can be produced by using this catalog with a S/N$>$ 6 cut, which by the limited number statistics of these simulations may contain 0^{+5}_{-0} spurious sources.

In addition we have also performed an empirical test for spurious sources by analyzing the inverse of the survey data frames. All sources with a detected continuum were masked (so that we would not find the inverse of absorption features as spurious sources), and our detection algorithm was re-run. This analysis found 7 spurious sources in 28 fields; a rate that is significantly lower than that estimated from the simulations. This suggests our estimate of the systematic error

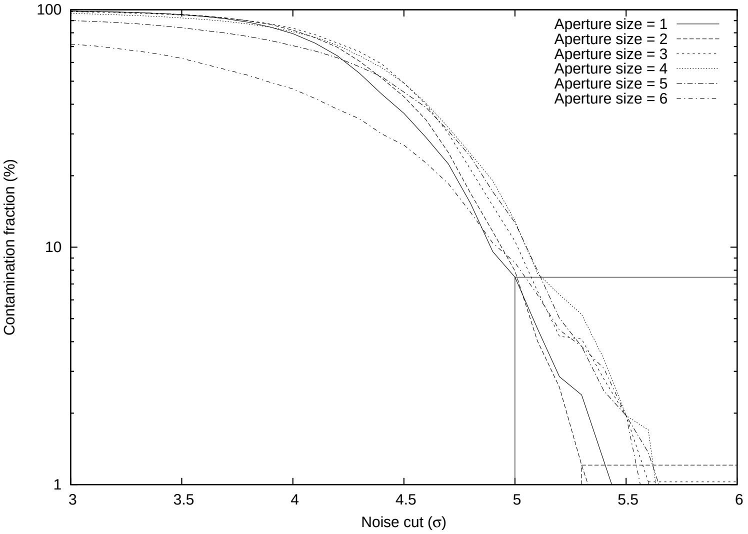

Figure 1.18 The fractional contamination to the LAE sample by S/N cut. The detection method used is described in detail in §1.3.3. The LAE predictions are the same as in §1.3.1. Curves are given for differently sized collections of neighboring fibers. The growth of apertures was allowed whenever the S/N was increased by > 0.3 with the inclusion of another fiber. At a high, constant S/N, the greatest contamination is produced by large apertures. The optimum sized aperture for a point source under all dither-source geometries is two at median. To optimize our selection, we make a staggered series of S/N cuts based on the number of fibers used, N, as S/N$> 5.0+0.3\times(N-1)$. The horizontal and vertical lines show the evaluation points of this cut to the simulation curves. This procedure predicts 10%±1.6% noise contamination.

is conservative and the true contamination fraction likely lies somewhere between 4-10%.

Completeness tests

Not every source at the flux limit of Figure 1.12 will be recovered by the detection scheme. Beyond the usual statistical fluctuations introduced by noise, different source positions and seeing variations will cause the signal to be distributed over a different numbers of fibers and cause varying fractions of light to be lost to the gaps between fibers. While this partial image sampling is an undesirable feature, IFS mitigates these uncertainties compared to serendipitous longslit observations (Rauch et al. 2008; Lemaux et al. 2009; Cassata et al. 2010), where the slit losses can range (nearly uniformly) from 0-100%.

We have simulated our completeness limit using 25 mock fields of full, two-dimensional data with noise generated from the mean McDonald sky spectrum and the CCD read noise. Each simulated image contained 3000 emission-line sources randomly chosen in position and wavelength, but constrained to avoid object blending and spaced by the seeing from the IFU edges. We used the same detection routines as for the real data. For all these simulations, the seeing was held constant at the survey's $1\farcs5$ FWHM median. These mock sources were modelled as spectrally unresolved point sources with fluxes randomly drawn from an unevolving Gronwall et al. (2007) LAE luminosity function over the luminosity range $41.5 < \log L(\mathrm{erg\ s^{-1}}) < 44.5$ where the lower bound was chosen to yield S/N=0.5 over most of the wavelength range. Figure 1.19 compares our simulated emission-line fluxes to the fluxes that were measured. As the S/N decreases, the error in our measurements increases. Moreover, at the faintest limits, there is a slight systematic trend, with the measured fluxes being over-estimated. This is the well-known Eddington (Eddington 1913, 1940) correction which, if ignored, can lead to an under-

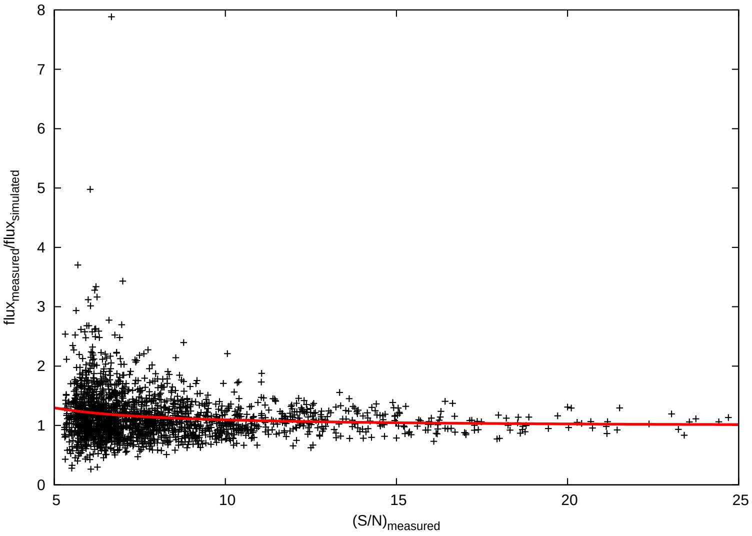

Figure 1.19 The ratio of measured and input fluxes from point source simulation and a least-squares fit (§1.3.3). The curve-of-growth method is used here to measure emission line flux. The upturn at low S/N is expected from the Eddington bias. This ratio can be applied to the LAE flux measurements of Table 1.4 for some applications. The average correction is fit as $\text{flux}_{\text{measured}}/\text{flux}_{\text{true}} = 0.98 + 0.74/(\text{S/N})_{\text{measured}} + 4.27/(\text{S/N})^2_{\text{measured}}$

estimate of a luminosity function's slope. The least-squares fit shown in the figure will be used to statistically correct all our LAE fluxes prior to luminosity function computation. The completeness results are shown in Figure 1.20. We reach 50% and 95% corrected completeness at 5.6σ and 8.3σ respectively. Compared to a step function completeness limit at $S/N > 5$ at the photometric limit of this survey which we consider the ideal goal, the number of detected LAEs is degraded by 13%. The long, low S/N tail helps mitigate the loss of objects to the non-ideal completeness.

Our source simulations also allow us to quantify the statistical astrometric error as a function of S/N. This is an important ingredient to our algorithm for associating VIRUS-P emission-line objects with sources found in broadband imaging (see §1.3.4). If we adopt a Rayleigh dsibtribution for the form of the radial errors, i.e. $\sigma = a + b/(S/N)$, then a maximum likelihood fit for the coefficients yields $a = 0\farcs348$

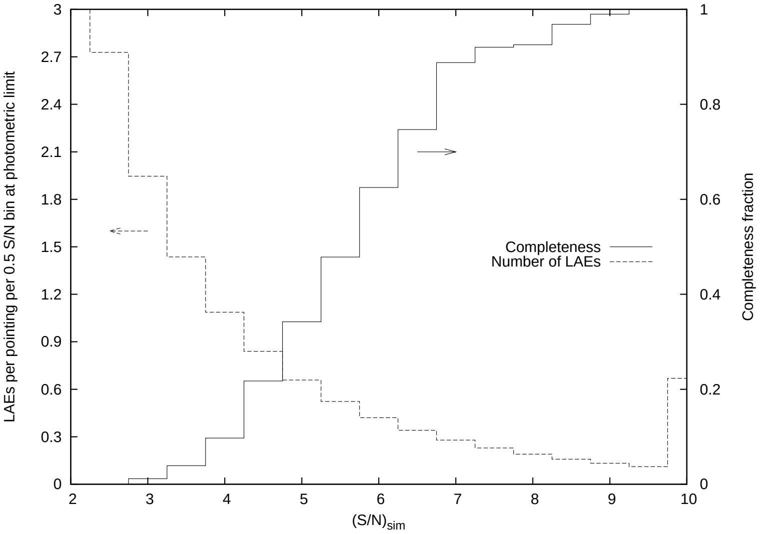

Figure 1.20 The survey's catalog completeness function for multiples of the flux limit. When combined, this function, the survey's photometric wavelength-based flux limit in Figure 1.12, and the actual mosaic pattern with photometric calibration in Figure 1.16 define the limits necessary for volume and luminosity function calculation (Blanc et al. 2010). The number of predicted LAEs per S/N bin assuming photometric conditions and a non-evolving Gronwall et al. (2007) LAE luminosity function is also plotted for reference. The long tail of the completeness curve down past the luminosity function break shows that the incomplete bins are crucial towards maximizing the catalog size.

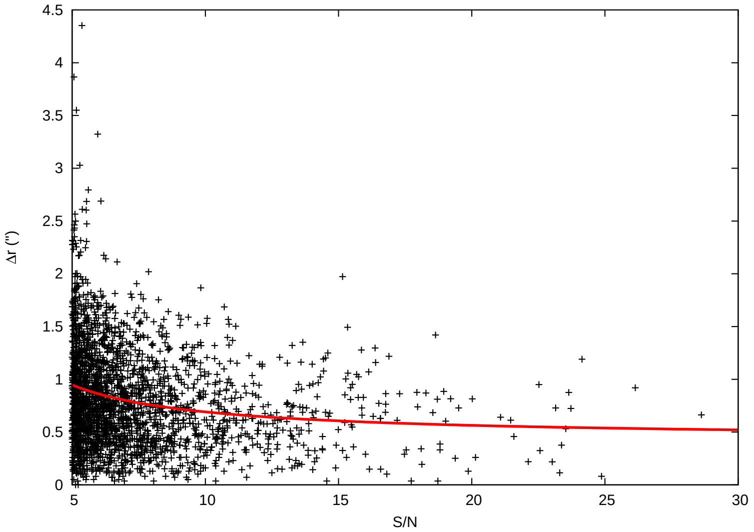

Figure 1.21 The distribution of simulated source positional errors under VIRUS-P sampling patterns with a fit to the dispersion as a function of measured S/N. The maximum liklihood fit to the peak of a Rayleigh distribution gives $\sigma = 0\farcs348 + 2\farcs04/(S/N)$.

and $b = 2\farcs04$. Figure 1.21 shows this relation, with the individual measurements overplotted.

The large VIRUS-P fibers lead to poor spatial resolution. Nevertheless, we have also simulated one mock field of 3000 point sources at and above the survey's flux limit and seeing distribution in an effort to quantify the minimum resolvable source size. To do this, we modeled the seeing FWHM distribution as a Gaussian function centered on $1\farcs5$ with a dispersion of $1''$ but truncated below $1\farcs2$. With the oversampled pattern of dithers, we expect the Nyquist limit to be near the diameter size of a fiber. The same curve-of-growth photometry routines as described in §1.3.3 were used to measure the sizes of simulated point sources. Figure 1.22 shows the distribution of emission line flux and measured size. The distribution is mostly flat with either flux or source S/N. Based on the simulation, we label a threshold of $7\farcs5$ as the resolution limit of our survey. This can be compared to the usual

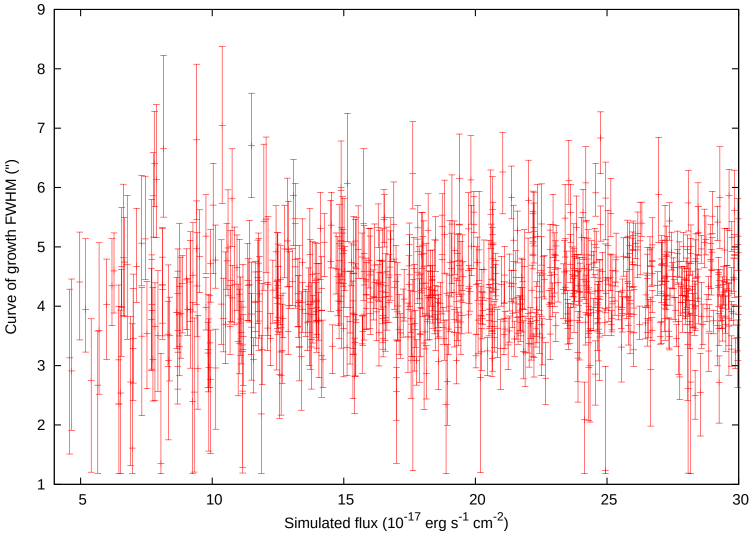

Figure 1.22 The distribution of measured source sizes in simulated data. The simulation input source sizes were drawn from the survey seeing distribution. The large fiber sizes set a large resolution threshold. Based on the 99.7% confidence interval, we only claim significantly resolved measurements for curve-of-growth FWHM sizes $> 6.81''$.

definition for Lyα blobs, i.e. emission over an isophotal area of $> 16\square''$ at a certain surface brightness threshold. The Lyα blob surveys of Matsuda et al. (2004) and Yang et al. (2010) used thresholds of 2.2×10^{-18} erg s^{-1} cm^{-2} arcsec^{-2} and 5×10^{-18} erg s^{-1} cm^{-2} arcsec^{-2}, respectively. Our HETDEX pilot survey should detect many Lyα blobs based on this flux limit, but will only be able to resolve the very largest objects. The full HETDEX survey will have ∼3× better spatial resolution.

Line flux measurement

A source's detection aperture described in §1.3.3 does not contain the total source flux. The imposed S/N cut omits some fraction of the flux in the detection aperture; this fraction is a function of source strength and orientation to the fiber dither pattern. In order to determine an unbiased emission line flux in the presence of these complications, we describe here a curve-of-growth procedure used to measure a source's total line flux after detection. While other total flux estimators are possible, we advocate this method as generally robust against the range of sizes and morphologies encountered in the survey and the rather large astrometric errors and seeing variations inherent in this dataset. The algorithm is similar to curve of growth (CoG) (Stetson 1990) fits previously developed for CCD imaging photometry, but is new to spectrophotometry.

We begin a flux measurement by considering the positions, central wavelengths, and line widths (σ_{det}) obtained from the emission-line detection algorithm described in §1.3.3. A circular aperture is formed around the centroid emission-line position of variable radius. Fibers overlapping this aperture are given fractional weights determined by their enclosed areas. Specifically, we form fifteen apertures linearly spaced between radii $2\farcs2$ and $9\farcs0$. In each aperture, the enclosed fibers have their continuum-subtracted data summed and errors summed in quadrature for wavelengths within $\pm 2\sigma_{res}$ of the detection wavelength. A spectral correction factor is defined as the flux fraction of a Gaussian line profile that falls within the fixed, spectral window defined by Equation 1.3.

$$f_{spec,corr} = \mathrm{erf}(\sqrt{2}\sigma_{res}/\sqrt{\sigma_{res}^2 + \sigma_{det}^2}) \tag{1.3}$$

Note that the fluxes returned by directly summing all fibers in a circular aperture of radius r, $\hat{f}(r)_{raw}$, may oversample or undersample the source flux depending on the data completeness and overlap regions of mosaic. For example, the ideal six dither pattern produces an oversampling of very near two. Let the number of fibers at a particular position lying within one fiber radius, r_{fib}, be $N(\Delta r < r_{fib}, r, \theta)$ in polar coordinates. Equation 1.4 gives the raw flux measured for arbitrary sampling of a source with total flux f_{total} and normalized profile $P(r, \theta)$; $f(r)_{samp} \equiv \int_0^r f_{total} P(r, \theta) r dr d\theta$ is an estimate of the cumulative flux corrected for sampling. This approximation is correct when $N(\Delta r < r_{fib}, r, \theta)$ does not systematically depend on r, which is nominally true for the randomly positioned observations presented here. The approximation is necessary to cleanly estimate an unbiased flux without knowing the exact profile.

$$\begin{aligned}\hat{f}(r)_{raw} = \int_0^r f_{total} N(\Delta r < r_{fib}, r, \theta) \times P(r, \theta) r dr d\theta \approx \\ \hat{f}(r)_{samp} \times \frac{\int_0^r N(\Delta r < r_{fib}, r, \theta) r dr d\theta}{\pi r^2}\end{aligned} \tag{1.4}$$

We fit, by nonlinear least squares minimization, a cumulative two-dimensional Gaussian function, $A_{CoG} \times (1 - e^{-0.5r^2/\sigma^2_{CoG}})$, to the highly correlated distribution $\hat{f}(r)_{samp}$, where we enforce the limits $1'' < \sigma_{CoG} < 10''$. In addition, we create Monte Carlo realizations by varying each fiber's intensity from the best-fit model. The CoG datapoints are highly correlated, so we took care to estimate the errors from the uncorrelated data of each fiber. The final, total flux estimate is given by Equation 1.5, with errors similarly propagated from the raw data and the uncertainty in σ_{CoG}. Figure 1.23 gives curve of growth examples for an [OII] emitter and a LAE.

$$\hat{f}_{total} = A_{CoG} / f_{spec,corr} \tag{1.5}$$

We tested the reliability of the curve-of-growth flux measurement, particularly for correlated errors with the source size, by using the simulated data discussed in §1.3.3. We first measured the flux from the fibers chosen as the detection aperture (§1.3.3), and compared this to the simulated flux. The mean and dispersion of the measured-to-simulated ratio are 0.93 and 0.31; unsurprisingly, the fluxes are systematically underestimated. Next, the set of all fibers within $6''$ of the detected position was used as the flux aperture. This reduced the scatter found by the fixed aperture method, but a systematic error still remained with a mean of 0.94 and dispersion of 0.20. Finally, the curve-of-growth flux measurement was considered. Under this procedure, the bulk systematic flux measurement error vanished, giving a mean of

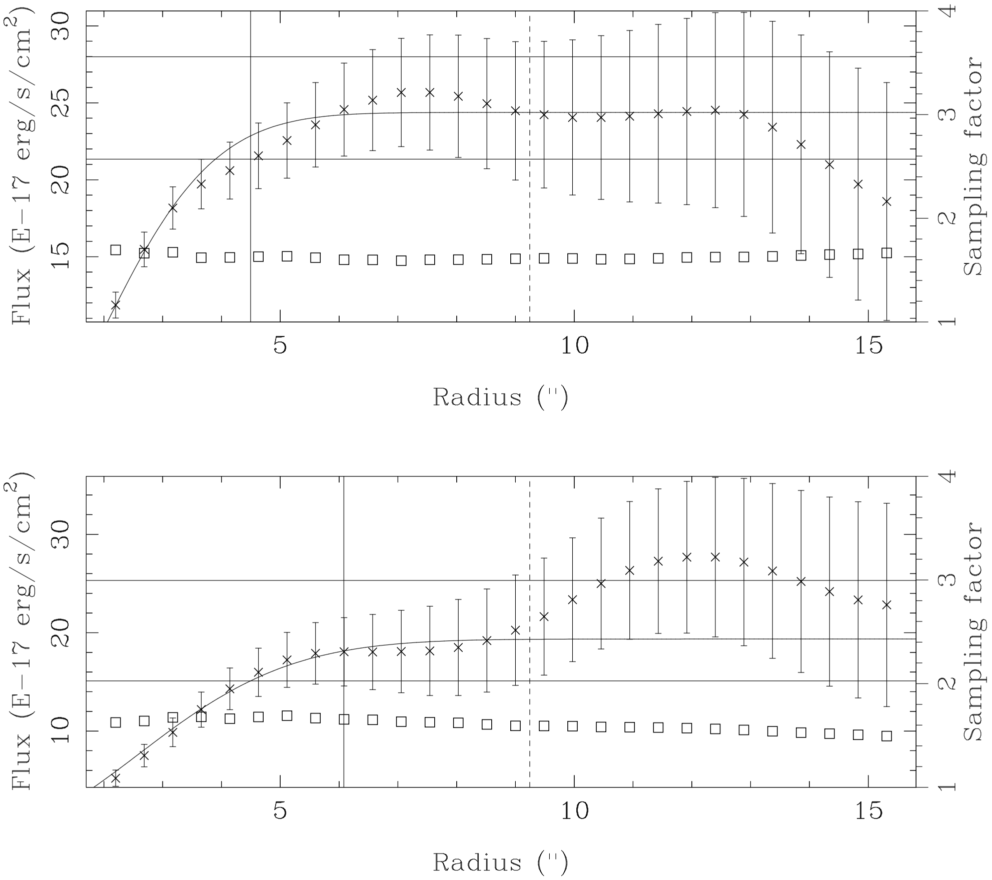

Figure 1.23 The data, fits, and final evaluation for the curve of growth line flux measurements of a LAE (*top*) and an [OII] emitter (*bottom*). In both, the open square symbols display the cumulative sampling factor on the right hand scale. The sampling factor is written in Equation 1.4 as $N(\Delta r < r_{fib}, r, \theta)$ and is the average number of fibers overlaying the surface enclosed in radius r. The points with errors show the estimated cumulative flux on the left hand scale. The vertical dotted lines mark where the fit is truncated. This threshold has been selected with consideration towards being significantly larger than the widest objects found and small enough to limit unnecessary noise. The vertical solid line marks the radius to the fit where 90% of the flux in enclosed. The horizontal solid lines show the 1σ confidence of the fit's normalization. The top fit returns a total flux of $24^{+3.6}_{-3.0} \times 10^{-17}$ erg s^{-1} cm^{-2}. The bottom fit returns a total flux of $19^{+6.0}_{-4.3} \times 10^{-17}$ erg s^{-1} cm^{-2}. The errors are correlated on the displayed scale, but the Monte Carlo fit varies the data from each fiber independently to generate proper errors.

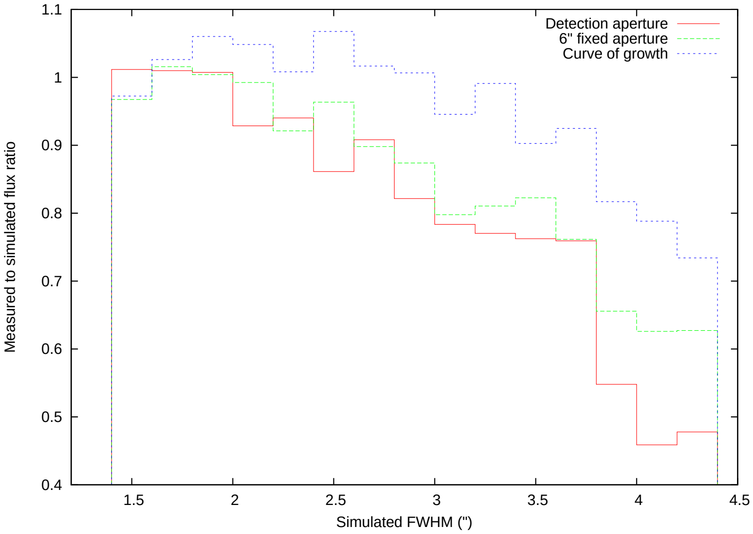

Figure 1.24 Binned ratios of measured and input fluxes for simulated data under a range of source sizes. The curve-of-growth flux estimator is preferred as the least biased for extended sources compared to either the detection set of fibers or a fixed radius set of fibers as the photometry aperture.

1.00 while still maintaining a low dispersion of 0.23. All three flux estimation methods are shown in Figure 1.24 against the simulated source size. A systematic offset with input source size can be seen for all cases, but the curve-of-growth photometry is preferred as the least biased method investigated.

1.3.4 Source classification

An emission-line galaxy catalog is of limited value without secure redshift identifications. Unfortunately, the uncertainty in identifying single emission lines is a common hindrance to high-redshift galaxy surveys (e.g., Stern et al. 2000). We here describe the two steps necessary to robustly assign redshifts to the emission-line catalog. Tables 1.4 and 1.5 present the catalogs. We give the detailed description of these tables in §1.3.5. We further summarize the statistics of commonly found objects and compare the sample to other works where available.

Table 1.4. HETDEX Pilot Survey Emission Line Catalog

HPS Index (1)	α (J2000) (2)	δ (J2000) (3)	$\lambda_{\rm det}$ (Å) (4)	FWHM (km s^{-1}) (5)	S/$N_{\rm det}$ (6)	Flux (10^{-17} cgs) (7)	Spatial FWHM ($''$) (8)	Matching indices (9)
001	02:21:11.16	-04:31:25.0	5219.16	229	8.1	$17.4^{3.5}_{-3.9}$	$4.7^{0.8}_{-0.6}$	..
002	02:21:12.21	-04:32:25.3	5448.72	307	5.6	$12.2^{3.6}_{-4.3}$	$4.3^{0.8}_{-1.0}$	..
003	02:21:14.28	-04:31:38.2	4973.93	422	7.5	$19.9^{4.7}_{-3.1}$	$4.4^{0.8}_{-0.5}$	..
004	02:21:14.86	-04:31:56.6	5261.37	1285	6.3	$42.6^{11.2}_{-12.4}$	$5.1^{0.7}_{-0.9}$	5
005	02:21:15.14	-04:31:54.0	4270.67	1841	33.1	$342.1^{16.5}_{-14.3}$	$4.8^{0.2}_{-0.1}$	4
006	02:21:16.26	-04:29:32.8	4591.58	399	14.8	$32.7^{3.5}_{-3.6}$	$4.6^{0.4}_{-0.2}$	..
007	02:21:16.35	-04:31:14.6	5161.72	293	19.5	$49.4^{2.6}_{-4.4}$	$4.7^{0.2}_{-0.2}$	..
008	02:21:17.25	-04:27:55.7	5820.13	118	6.7	$19.1^{5.0}_{-3.2}$	$6.6^{0.9}_{-0.6}$	..
009	02:21:17.25	-04:30:10.4	5464.33	78	12.1	$14.1^{1.5}_{-2.5}$	$3.6^{0.5}_{-0.4}$	..
010	02:21:17.47	-04:27:30.6	4808.33	357	15.9	$38.9^{3.4}_{-3.6}$	$4.6^{0.2}_{-0.3}$	..
011	02:21:18.48	-04:27:32.2	4590.82	441	6.6	$21.2^{4.7}_{-4.6}$	$5.9^{0.7}_{-0.7}$	..
012	02:21:19.20	-04:30:28.9	4398.59	344	9.9	$26.4^{4.0}_{-3.9}$	$5.7^{0.6}_{-0.5}$	..
013	02:21:19.22	-04:30:39.9	5250.96	378	7.8	$11.7^{2.6}_{-1.9}$	$3.6^{0.7}_{-0.5}$	..
014	02:21:19.47	-04:28:21.9	4863.62	328	21.8	$49.6^{2.4}_{-3.8}$	$5.5^{0.2}_{-0.2}$	..
015	02:21:19.48	-04:29:34.0	4919.31	243	21.7	$36.2^{2.8}_{-2.8}$	$4.9^{0.2}_{-0.3}$	..
016	02:21:19.83	-04:28:08.8	4901.07	397	5.9	$13.7^{5.2}_{-3.1}$	$5.3^{1.2}_{-1.2}$	..
017	02:21:19.85	-04:27:43.4	4588.13	93	5.9	$13.2^{3.9}_{-3.4}$	$5.3^{1.1}_{-0.9}$	..
018	02:21:20.77	-04:30:56.6	5655.44	972	8.2	$45.4^{8.4}_{-7.5}$	$5.6^{0.4}_{-0.6}$	19
019	02:21:20.78	-04:30:56.4	5452.07	438	26.8	$83.6^{4.2}_{-4.0}$	$5.6^{0.1}_{-0.1}$	18
020	02:21:21.27	-04:27:44.6	5788.83	303	8.9	$21.8^{3.9}_{-3.9}$	$5.1^{0.8}_{-0.6}$	..
021	02:21:22.13	-04:30:35.0	5448.33	277	8.6	$8.8^{2.4}_{-1.9}$	$3.3^{0.7}_{-0.8}$	..
022	02:21:22.84	-04:29:25.2	4586.30	603	7.4	$17.7^{5.5}_{-4.3}$	$5.2^{0.8}_{-0.9}$	..
023	02:21:22.88	-04:29:44.3	4540.36	323	9.4	$18.5^{3.2}_{-4.1}$	$4.6^{0.7}_{-0.6}$	..
024	02:21:23.28	-04:29:22.3	4592.57	204	8.8	$14.3^{3.7}_{-2.5}$	$4.0^{0.6}_{-0.5}$	..
025	02:21:23.47	-04:29:09.4	4319.48	810	14.1	$64.3^{10.1}_{-8.8}$	$6.2^{0.5}_{-0.5}$	..
026	02:21:23.78	-04:30:00.2	5336.44	306	34.7	$79.4^{3.9}_{-4.1}$	$4.4^{0.1}_{-0.2}$	..
027	02:21:24.45	-04:30:01.8	5805.02	74	18.1	$34.7^{3.8}_{-3.2}$	$4.5^{0.3}_{-0.3}$	28,29,30
028	02:21:24.47	-04:30:01.3	5636.41	76	7.9	$15.7^{3.7}_{-2.7}$	$4.7^{0.7}_{-0.7}$	27,29,30
029	02:21:24.48	-04:30:00.8	4322.09	204	23.1	$48.0^{3.8}_{-3.3}$	$3.9^{0.2}_{-0.3}$	27,28,30

Table 1.4 (cont'd)

HPS Index (1)	α (J2000) (2)	δ (J2000) (3)	$\lambda_{\rm det}$ (Å) (4)	FWHM (km s^{-1}) (5)	S/N$_{\rm det}$ (6)	Flux (10^{-17} cgs) (7)	Spatial FWHM ($''$) (8)	Matching indices (9)
030	02:21:24.49	-04:30:02.0	5749.30	92	5.8	$10.5^{3.7}_{-3.5}$	$4.6^{0.9}_{-1.2}$	27,28,29
031	02:21:25.54	-04:30:25.3	5435.34	337	13.1	$24.9^{3.3}_{-3.0}$	$3.9^{0.4}_{-0.3}$	..
032	02:21:25.90	-04:29:49.3	5448.11	337	6.7	$11.5^{4.3}_{-3.0}$	$4.6^{0.8}_{-0.8}$	..
033	02:21:26.83	-04:30:05.8	5460.20	343	9.4	$25.4^{3.6}_{-4.6}$	$5.0^{0.5}_{-0.6}$	..
034	02:21:27.15	-04:29:39.2	4569.09	530	7.2	$20.6^{5.3}_{-5.0}$	$4.8^{0.7}_{-0.7}$	..
035	02:21:27.45	-04:30:19.1	4040.56	284	82.7	$752.1^{17.1}_{-9.7}$	$6.9^{0.1}_{-0.1}$	36,37,38,39
036	02:21:27.53	-04:30:18.4	4705.35	91	20.5	$54.3^{3.5}_{-4.2}$	$5.5^{0.3}_{-0.2}$	35,37,38,39
037	02:21:27.56	-04:30:18.4	5269.77	81	93.9	$290.9^{4.8}_{-4.7}$	$5.7^{0.0}_{-0.0}$	35,36,38,39
038	02:21:27.56	-04:30:19.8	5427.20	127	104.5	$392.3^{3.9}_{-5.3}$	$5.8^{0.0}_{-0.0}$	35,36,37,39
039	02:21:27.57	-04:30:18.4	5375.63	128	61.3	$182.9^{3.2}_{-4.4}$	$5.7^{0.1}_{-0.1}$	35,36,37,38
040	02:21:27.69	-04:29:51.9	5457.98	371	9.3	$15.4^{4.3}_{-3.0}$	$3.2^{0.5}_{-0.7}$	..
041	02:21:30.08	-04:30:46.9	4562.73	393	6.3	$14.2^{3.4}_{-5.4}$	$3.9^{1.0}_{-1.3}$	..
042	03:06:30.22	+00:03:51.9	4607.42	216	7.9	$54.0^{9.6}_{-9.3}$	$6.5^{0.6}_{-0.5}$	..
043	03:06:30.67	+00:01:27.1	5601.44	76	7.2	$24.5^{4.5}_{-5.0}$	$5.1^{0.6}_{-0.7}$	44
044	03:06:30.73	+00:01:28.8	4170.97	251	7.2	$43.7^{7.6}_{-8.7}$	$5.7^{0.8}_{-0.6}$	43
045	03:06:31.95	+00:01:46.0	5112.96	359	7.2	$21.1^{4.9}_{-3.7}$	$4.8^{0.7}_{-0.5}$	..
046	03:06:32.73	+00:01:50.1	5112.48	410	18.4	$57.8^{4.8}_{-3.9}$	$4.8^{0.2}_{-0.2}$	..
047	03:06:33.34	-00:01:31.5	5716.24	380	8.9	$32.0^{6.3}_{-5.3}$	$5.3^{0.8}_{-0.4}$	..
048	03:06:33.57	-00:01:31.0	5674.73	330	20.0	$78.9^{7.0}_{-5.2}$	$6.4^{0.2}_{-0.3}$	..
049	03:06:34.23	-00:00:47.1	5100.63	382	7.4	$33.0^{6.5}_{-5.6}$	$6.8^{1.0}_{-0.8}$	..
050	03:06:34.24	+00:00:20.8	5093.97	226	6.2	$13.4^{4.1}_{-3.5}$	$5.5^{0.8}_{-1.2}$	..
051	03:06:34.61	-00:00:49.6	4980.74	428	5.2	$9.1^{5.0}_{-4.0}$	$3.5^{1.4}_{-1.7}$	..
052	03:06:35.18	+00:00:03.2	5310.40	374	19.4	$110.7^{11.2}_{-7.7}$	$8.7^{0.4}_{-0.4}$	..
053	03:06:35.59	+00:00:18.5	5558.78	294	6.8	$13.0^{4.7}_{-3.8}$	$5.0^{1.0}_{-1.0}$	..
054	03:06:35.72	-00:00:55.9	5317.42	352	5.3	$10.8^{3.1}_{-3.6}$	$3.1^{1.0}_{-1.7}$	..
055	03:06:35.85	+00:01:06.7	5262.94	81	6.2	$9.8^{4.0}_{-2.6}$	$2.7^{1.3}_{-1.5}$	..
056	03:06:35.95	-00:00:37.7	5309.58	243	12.1	$33.6^{4.5}_{-4.9}$	$4.4^{0.4}_{-0.4}$	..
057	03:06:36.20	-00:00:39.4	4740.14	272	21.7	$84.0^{7.0}_{-5.2}$	$6.3^{0.3}_{-0.3}$	..
058	03:06:37.22	-00:02:59.9	5112.92	261	13.5	$58.0^{8.2}_{-7.7}$	$5.7^{0.4}_{-0.4}$	..

Table 1.4 (cont'd)

HPS Index (1)	α (J2000) (2)	δ (J2000) (3)	$\lambda_{\rm det}$ (Å) (4)	FWHM (km s^{-1}) (5)	S/N$_{\rm det}$ (6)	Flux (10^{-17} cgs) (7)	Spatial FWHM ($''$) (8)	Matching indices (9)
059	03:06:37.38	+00:03:47.4	5108.04	320	5.7	$18.3^{6.9}_{-5.4}$	$5.5^{1.5}_{-1.0}$	..
060	03:06:37.40	+00:02:04.3	5505.53	226	7.2	$27.3^{7.4}_{-5.5}$	$6.8^{1.0}_{-0.7}$	..
061	03:06:37.74	-00:00:27.8	4971.74	337	5.5	$17.1^{3.7}_{-4.3}$	$4.5^{0.9}_{-0.8}$	..
062	03:06:38.12	+00:00:40.0	3741.83	392	5.5	$67.7^{22.9}_{-21.0}$	$3.4^{1.3}_{-1.0}$	..
063	03:06:38.48	-00:01:29.5	5318.97	366	6.9	$24.2^{7.4}_{-6.5}$	$6.1^{1.1}_{-0.7}$	..
064	03:06:38.68	+00:00:23.8	4743.43	362	10.3	$28.6^{4.4}_{-3.7}$	$4.1^{0.5}_{-0.4}$	..
065	03:06:38.75	-00:00:15.9	4144.91	333	23.5	$243.8^{16.6}_{-14.8}$	$9.0^{0.3}_{-0.4}$	66,68
066	03:06:38.76	-00:00:18.6	5404.62	97	6.8	$24.8^{5.3}_{-3.9}$	$6.0^{0.8}_{-0.7}$	65,68
067	03:06:38.91	-00:02:40.1	4145.52	289	5.7	$45.7^{14.8}_{-13.0}$	$4.7^{1.0}_{-1.0}$	..
068	03:06:38.94	-00:00:22.0	5564.20	410	5.5	$67.0^{11.8}_{-13.8}$	$8.6^{0.9}_{-0.8}$	65,66
069	03:06:38.99	+00:01:25.7	5676.74	295	8.7	$28.8^{4.8}_{-5.1}$	$4.7^{0.5}_{-0.7}$	..
070	03:06:39.48	+00:03:34.8	5317.91	187	8.3	$22.4^{7.3}_{-3.9}$	$3.8^{0.9}_{-0.7}$	..
071	03:06:39.51	+00:03:44.7	4536.81	1840	6.0	$110.7^{22.8}_{-22.0}$	$1.5^{0.9}_{-0.4}$	72,73,74,75,76,77,78
072	03:06:39.53	+00:03:45.3	3791.53	582	8.5	$200.9^{37.5}_{-31.6}$	$4.2^{0.4}_{-0.5}$	71,73,74,75,76,77,78
073	03:06:39.53	+00:03:45.0	4126.75	356	36.4	$437.0^{16.2}_{-12.2}$	$4.8^{0.1}_{-0.1}$	71,72,74,75,76,77,78
074	03:06:39.54	+00:03:44.6	4282.36	885	26.4	$449.6^{21.6}_{-21.3}$	$4.5^{0.2}_{-0.1}$	71,72,73,75,76,77,78
075	03:06:39.54	+00:03:44.2	5490.35	504	66.0	$583.2^{17.4}_{-10.1}$	$3.9^{0.1}_{-0.1}$	71,72,73,74,76,77,78
076	03:06:39.54	+00:03:44.2	5381.88	1187	83.5	$1264.5^{19.6}_{-17.9}$	$3.4^{0.0}_{-0.0}$	71,72,73,74,75,77,78
077	03:06:39.54	+00:03:44.0	5543.38	536	102.9	$1903.5^{20.1}_{-22.0}$	$4.2^{0.0}_{-0.0}$	71,72,73,74,75,76,78
078	03:06:39.56	+00:03:44.7	4807.15	1667	28.2	$484.5^{33.5}_{-22.5}$	$2.9^{0.1}_{-0.1}$	71,72,73,74,75,76,77
079	03:06:40.01	-00:00:02.7	5185.09	433	6.7	$20.6^{4.9}_{-3.6}$	$4.9^{0.8}_{-0.8}$	..
080	03:06:40.02	-00:02:49.7	4927.84	323	7.4	$34.6^{9.5}_{-8.3}$	$4.6^{0.7}_{-0.9}$	..
081	03:06:40.69	+00:01:53.2	4970.84	278	6.4	$12.3^{5.6}_{-3.5}$	$2.8^{1.1}_{-1.6}$	..
082	03:06:40.73	-00:01:32.7	3950.67	743	6.5	$89.8^{23.4}_{-24.2}$	$6.4^{1.0}_{-0.7}$	..
083	03:06:40.96	+00:00:24.0	5112.14	279	10.0	$21.2^{3.1}_{-3.0}$	$3.6^{0.4}_{-0.6}$	..
084	03:06:41.10	-00:02:48.5	5159.92	285	5.8	$31.9^{10.2}_{-5.8}$	$6.6^{1.1}_{-1.5}$	..
085	03:06:41.48	+00:01:10.8	3699.08	2323	7.5	$288.3^{90.6}_{-59.8}$	$3.5^{0.7}_{-0.7}$	86
086	03:06:41.58	+00:01:07.2	4569.91	1880	7.1	$100.4^{20.1}_{-17.3}$	$4.2^{0.8}_{-0.5}$	85
087	03:06:42.58	+00:00:20.1	5056.88	347	9.6	$21.6^{3.1}_{-3.3}$	$4.8^{0.4}_{-0.6}$	..

Table 1.4 (cont'd)

HPS Index (1)	α (J2000) (2)	δ (J2000) (3)	$\lambda_{\rm det}$ (Å) (4)	FWHM (km s^{-1}) (5)	S/N$_{\rm det}$ (6)	Flux (10^{-17} cgs) (7)	Spatial FWHM ($''$) (8)	Matching indices (9)
088	03:06:43.25	+00:00:32.5	4781.86	240	8.0	$44.9^{6.3}_{-7.9}$	$7.3^{0.9}_{-0.8}$	..
089	03:06:44.02	-00:01:27.4	4299.64	408	10.8	$30.2^{5.7}_{-7.0}$	$3.8^{0.7}_{-0.6}$	..
090	03:06:44.11	+00:03:50.0	4766.79	326	6.7	$39.1^{7.2}_{-7.7}$	$5.6^{0.9}_{-0.8}$	..
091	03:06:44.17	+00:00:47.3	4858.31	534	5.6	$16.7^{5.8}_{-5.2}$	$5.9^{1.8}_{-1.2}$	..
092	03:06:44.44	+00:01:46.7	5682.19	363	6.0	$13.2^{4.2}_{-4.3}$	$4.4^{1.0}_{-0.7}$	..
093	03:06:44.77	-00:02:49.3	3966.35	956	6.0	$65.2^{13.9}_{-17.1}$	$7.1^{1.2}_{-1.2}$	..
094	03:06:46.23	+00:02:18.3	5767.11	370	22.7	$134.7^{9.6}_{-11.4}$	$6.0^{0.2}_{-0.4}$	..
095	03:06:46.55	+00:03:06.8	4196.57	370	5.9	$34.6^{12.4}_{-12.2}$	$6.5^{1.0}_{-1.5}$	..
096	03:06:46.68	+00:00:23.6	5186.29	353	10.4	$22.7^{4.1}_{-3.3}$	$5.0^{0.5}_{-0.5}$	..
097	03:06:46.82	+00:02:20.1	5769.89	344	8.9	$78.7^{18.7}_{-12.7}$	$8.8^{1.1}_{-1.0}$	..
098	03:06:48.25	-00:03:01.5	4811.19	397	6.0	$23.8^{6.9}_{-5.3}$	$6.1^{0.9}_{-1.0}$	..
099	03:06:48.36	+00:00:17.0	4868.35	505	8.3	$33.0^{8.3}_{-5.3}$	$7.4^{0.7}_{-0.6}$	..
100	03:06:48.86	-00:00:58.0	5084.20	469	9.4	$25.4^{5.2}_{-4.6}$	$4.2^{0.7}_{-0.5}$	..
101	03:06:48.94	-00:01:01.1	4780.25	367	11.6	$26.2^{5.0}_{-4.2}$	$3.6^{0.6}_{-0.5}$	..
102	03:06:49.19	-00:00:15.3	5309.65	331	6.9	$24.8^{5.1}_{-4.6}$	$5.8^{0.9}_{-0.7}$	..
103	03:06:49.45	+00:01:23.4	5056.51	174	7.5	$15.8^{4.1}_{-3.7}$	$4.1^{0.8}_{-0.6}$	..
104	03:06:49.73	-00:03:15.9	5554.32	189	16.2	$58.9^{4.9}_{-6.9}$	$6.1^{0.3}_{-0.3}$	105,106,107
105	03:06:49.74	-00:03:14.4	4134.79	253	11.1	$56.6^{5.8}_{-9.3}$	$5.5^{0.6}_{-0.5}$	104,106,107
106	03:06:49.76	-00:03:16.1	5500.66	259	6.4	$29.2^{5.8}_{-6.5}$	$6.4^{0.8}_{-0.6}$	104,105,107
107	03:06:49.78	-00:03:15.9	5392.14	280	6.7	$23.7^{6.0}_{-4.4}$	$6.3^{0.7}_{-0.6}$	104,105,106
108	03:06:50.08	+00:02:03.9	5111.31	304	12.4	$39.9^{7.2}_{-4.8}$	$6.4^{0.5}_{-0.4}$	..
109	03:06:50.19	-00:02:14.9	5111.34	487	5.8	$30.7^{9.9}_{-6.2}$	$6.8^{1.4}_{-0.9}$	..
110	03:06:50.47	-00:01:18.9	5262.67	311	12.6	$28.1^{5.7}_{-2.7}$	$3.6^{0.4}_{-0.4}$	..
111	03:06:50.61	+00:01:39.1	5080.69	383	6.2	$15.1^{4.6}_{-5.4}$	$4.4^{1.4}_{-0.8}$	..
112	03:06:51.13	+00:01:30.6	5109.22	460	8.1	$27.9^{7.1}_{-4.0}$	$5.4^{0.7}_{-0.6}$	..
113	03:06:51.41	+00:01:03.9	5263.21	356	7.2	$23.4^{5.4}_{-5.8}$	$6.3^{1.0}_{-1.1}$	..
114	03:06:51.54	-00:01:28.8	5322.09	387	6.1	$11.7^{13.0}_{-10.5}$	$7.2^{6.6}_{-2.4}$	..
115	03:06:51.86	-00:02:35.6	5544.32	124	5.7	$10.7^{3.1}_{-3.3}$	$5.6^{1.1}_{-0.8}$	118
116	03:06:51.91	+00:01:22.6	5405.25	79	7.5	$19.4^{5.2}_{-4.0}$	$4.6^{0.8}_{-0.9}$	117,119

Table 1.4 (cont'd)

HPS Index (1)	α (J2000) (2)	δ (J2000) (3)	$\lambda_{\rm det}$ (Å) (4)	FWHM (km s^{-1}) (5)	S/N$_{\rm det}$ (6)	Flux (10^{-17} cgs) (7)	Spatial FWHM ($''$) (8)	Matching indices (9)
117	03:06:51.92	+00:01:21.9	5514.40	137	6.3	$23.7^{5.8}_{-5.6}$	$5.2^{1.0}_{-0.8}$	116,119
118	03:06:51.94	-00:02:34.7	4126.70	183	9.8	$40.3^{6.5}_{-5.2}$	$6.8^{0.8}_{-0.5}$	115
119	03:06:52.02	+00:01:23.4	4144.88	226	30.2	$207.6^{11.5}_{-9.7}$	$5.6^{0.2}_{-0.2}$	116,117
120	03:06:52.56	+00:00:47.6	5188.15	283	10.2	$37.0^{5.1}_{-6.8}$	$4.5^{0.5}_{-0.4}$	..
121	03:06:52.74	+00:02:09.4	5116.78	84	6.1	$10.0^{4.0}_{-2.9}$	$3.3^{1.0}_{-0.7}$	..
122	03:06:53.28	+00:03:13.9	4495.46	408	6.9	$29.9^{7.3}_{-7.5}$	$5.4^{1.0}_{-0.7}$	..
123	03:06:53.53	-00:02:09.5	5422.37	302	32.5	$80.4^{3.4}_{-3.0}$	$4.7^{0.2}_{-0.1}$	..
124	03:06:53.64	-00:02:32.8	5766.95	401	5.2	$12.7^{7.0}_{-5.4}$	$3.2^{1.8}_{-1.4}$	..
125	03:06:55.10	-00:00:50.3	4143.68	227	20.5	$223.9^{33.1}_{-37.7}$	$7.1^{0.6}_{-0.5}$	..
126	03:06:55.26	+00:00:33.8	4653.11	815	14.2	$167.1^{14.8}_{-13.8}$	$7.5^{0.5}_{-0.3}$	..
127	03:06:55.52	+00:03:33.6	4298.41	380	5.4	$22.1^{10.9}_{-6.8}$	$5.1^{1.4}_{-0.7}$	..
128	03:06:55.80	+00:01:04.2	5025.72	537	8.1	$31.7^{6.6}_{-6.1}$	$4.3^{0.5}_{-0.7}$	..
129	03:06:55.81	+00:02:13.5	4240.25	234	12.7	$50.8^{5.8}_{-7.1}$	$4.7^{0.4}_{-0.4}$	131,134
130	03:06:55.81	+00:00:52.2	4780.23	316	13.0	$55.6^{8.2}_{-5.8}$	$4.5^{0.4}_{-0.4}$	..
131	03:06:55.82	+00:02:12.8	5640.06	332	7.5	$31.5^{6.2}_{-5.8}$	$6.3^{1.0}_{-0.6}$	129,134
132	03:06:55.83	-00:00:23.2	5324.05	176	6.9	$50.1^{15.1}_{-15.9}$	$5.7^{1.4}_{-1.0}$	..
133	03:06:55.84	+00:01:58.6	4608.89	548	5.7	$20.6^{4.0}_{-5.7}$	$3.2^{0.7}_{-0.9}$	..
134	03:06:55.87	+00:02:12.9	5694.38	210	15.8	$52.7^{5.6}_{-5.0}$	$4.9^{0.3}_{-0.3}$	129,131
135	03:06:56.42	+00:03:04.9	4815.23	268	5.6	$17.0^{5.9}_{-4.4}$	$4.8^{1.2}_{-0.9}$	..
136	03:06:57.30	-00:03:02.5	4728.95	363	13.6	$30.2^{4.3}_{-3.3}$	$4.3^{0.4}_{-0.4}$	..
137	03:06:57.43	+00:00:03.1	4659.83	213	11.2	$34.5^{15.1}_{-17.6}$	$6.0^{1.5}_{-1.5}$	..
138	03:06:57.63	-00:01:39.1	4109.87	242	28.1	$94.2^{5.0}_{-5.1}$	$4.7^{0.2}_{-0.2}$	139,140,141
139	03:06:57.63	-00:01:39.6	5520.42	78	23.3	$51.4^{3.9}_{-3.0}$	$4.5^{0.2}_{-0.2}$	138,140,141
140	03:06:57.64	-00:01:40.3	5359.66	80	12.4	$33.6^{2.9}_{-3.9}$	$5.5^{0.4}_{-0.4}$	138,139,141
141	03:06:57.67	-00:01:39.5	5467.60	138	8.2	$15.4^{2.8}_{-2.9}$	$3.6^{0.6}_{-0.6}$	138,139,140
142	03:06:58.84	-00:02:34.5	4352.06	612	5.9	$20.6^{6.8}_{-3.2}$	$3.8^{0.8}_{-0.9}$	..
143	10:00:05.63	+02:16:08.9	4608.30	346	30.2	$67.8^{3.3}_{-2.9}$	$4.1^{0.1}_{-0.1}$	..
144	10:00:05.83	+02:19:47.2	4534.15	324	5.9	$5.5^{2.7}_{-2.5}$	$2.7^{1.8}_{-1.5}$	..
145	10:00:06.26	+02:13:10.9	3859.84	1164	8.6	$84.0^{14.8}_{-8.1}$	$7.5^{0.8}_{-0.8}$	..

Table 1.4 (cont'd)

HPS Index (1)	α (J2000) (2)	δ (J2000) (3)	$\lambda_{\rm det}$ (Å) (4)	FWHM (km s^{-1}) (5)	S/N$_{\rm det}$ (6)	Flux (10^{-17} cgs) (7)	Spatial FWHM ($''$) (8)	Matching indices (9)
146	10:00:06.32	+02:18:03.7	4876.41	301	10.2	$17.7^{4.0}_{-3.1}$	$4.6^{0.6}_{-0.5}$	..
147	10:00:06.89	+02:13:27.7	4534.91	253	30.7	$59.3^{4.1}_{-3.4}$	$5.3^{0.2}_{-0.2}$	..
148	10:00:07.00	+02:19:27.8	5370.35	289	5.3	$8.6^{2.0}_{-2.6}$	$4.5^{1.2}_{-1.0}$	..
149	10:00:07.14	+02:17:06.3	4995.67	449	6.3	$24.3^{5.9}_{-4.6}$	$7.3^{1.1}_{-0.8}$	..
150	10:00:07.15	+02:14:56.8	4742.42	1165	7.6	$29.1^{6.9}_{-6.7}$	$4.7^{0.8}_{-0.6}$	..
151	10:00:07.23	+02:18:46.6	5359.12	297	15.7	$25.7^{4.8}_{-3.4}$	$4.4^{0.3}_{-0.5}$	..
152	10:00:07.29	+02:17:22.9	4723.68	273	22.9	$40.7^{3.7}_{-4.0}$	$6.1^{0.3}_{-0.5}$	..
153	10:00:07.32	+02:12:45.5	4507.81	997	6.8	$31.9^{6.2}_{-6.4}$	$6.5^{0.8}_{-0.7}$	..
154	10:00:07.59	+02:15:18.4	4707.81	254	6.4	$10.6^{2.6}_{-2.8}$	$4.3^{0.9}_{-0.7}$	..
155	10:00:07.68	+02:17:37.1	4941.47	288	6.9	$8.1^{4.9}_{-3.0}$	$3.4^{1.5}_{-0.9}$	..
156	10:00:08.03	+02:15:42.4	4778.44	342	17.7	$29.0^{3.0}_{-3.4}$	$5.2^{0.3}_{-0.4}$	..
157	10:00:08.35	+02:15:23.0	4658.96	324	25.4	$59.6^{3.8}_{-2.7}$	$5.0^{0.2}_{-0.2}$	..
158	10:00:08.52	+02:15:42.6	4073.10	257	14.3	$45.3^{5.3}_{-3.7}$	$6.4^{0.5}_{-0.4}$	159
159	10:00:08.52	+02:15:42.1	5471.22	138	14.8	$19.0^{3.5}_{-1.8}$	$5.4^{0.4}_{-0.4}$	158
160	10:00:08.61	+02:17:38.6	4175.32	663	6.0	$17.1^{10.5}_{-6.4}$	$5.2^{1.5}_{-1.6}$	..
161	10:00:08.73	+02:12:50.0	5168.43	658	15.0	$39.1^{4.1}_{-4.1}$	$5.7^{0.4}_{-0.3}$	..
162	10:00:08.73	+02:15:32.0	4167.83	1063	7.3	$76.4^{14.6}_{-11.5}$	$8.3^{1.3}_{-0.9}$	..
163	10:00:08.82	+02:14:20.4	5117.51	366	18.8	$38.4^{4.3}_{-2.1}$	$5.0^{0.3}_{-0.2}$	..
164	10:00:08.95	+02:17:23.2	4196.31	482	6.6	$25.4^{13.7}_{-12.9}$	$11.0^{3.3}_{-3.3}$	..
165	10:00:09.25	+02:16:28.2	4541.90	231	6.7	$14.2^{3.4}_{-4.1}$	$5.5^{1.0}_{-1.3}$	..
166	10:00:09.29	+02:15:36.9	5116.42	261	15.6	$25.1^{2.1}_{-2.1}$	$4.3^{0.3}_{-0.3}$	..
167	10:00:09.41	+02:12:24.4	5008.85	310	12.2	$21.4^{2.6}_{-2.9}$	$4.8^{0.4}_{-0.3}$	..
168	10:00:09.69	+02:14:54.9	5409.27	480	16.9	$34.9^{2.8}_{-3.0}$	$4.5^{0.2}_{-0.3}$	..
169	10:00:09.75	+02:12:40.7	4704.85	321	25.1	$42.2^{3.0}_{-2.8}$	$4.9^{0.1}_{-0.2}$	..
170	10:00:09.94	+02:15:50.0	4777.21	384	7.4	$12.3^{3.5}_{-2.0}$	$4.1^{0.9}_{-0.7}$	..
171	10:00:10.00	+02:16:59.7	4781.40	307	16.2	$23.4^{3.1}_{-3.0}$	$3.9^{0.4}_{-0.4}$	172
172	10:00:10.01	+02:16:59.8	4962.23	260	6.1	$5.0^{2.3}_{-2.3}$	$2.3^{1.3}_{-1.1}$	171
173	10:00:10.35	+02:13:22.5	5141.95	242	15.3	$20.9^{2.1}_{-2.6}$	$4.5^{0.3}_{-0.4}$	..
174	10:00:11.06	+02:12:26.7	5405.49	474	5.0	$3.2^{2.4}_{-2.4}$	$2.1^{1.9}_{-0.9}$	..

Table 1.4 (cont'd)

HPS Index (1)	α (J2000) (2)	δ (J2000) (3)	$\lambda_{\rm det}$ (Å) (4)	FWHM (km s^{-1}) (5)	S/N$_{\rm det}$ (6)	Flux (10^{-17} cgs) (7)	Spatial FWHM ($''$) (8)	Matching indices (9)
175	10:00:11.27	+02:14:33.2	4779.62	400	18.8	$41.6^{3.0}_{-4.0}$	$5.5^{0.3}_{-0.2}$	..
176	10:00:11.36	+02:17:41.8	5557.45	371	13.9	$29.2^{5.4}_{-3.9}$	$5.1^{0.5}_{-0.4}$	..
177	10:00:11.38	+02:13:48.8	5146.23	277	10.5	$18.3^{2.8}_{-3.2}$	$4.8^{0.4}_{-0.5}$	..
178	10:00:11.39	+02:15:14.1	5484.87	283	5.8	$10.1^{3.5}_{-2.6}$	$4.8^{0.8}_{-0.7}$	..
179	10:00:11.85	+02:13:40.1	5009.81	426	7.2	$7.3^{2.9}_{-1.9}$	$3.4^{1.3}_{-0.9}$	..
180	10:00:12.08	+02:20:02.6	5139.19	372	8.7	$3.7^{2.4}_{-2.1}$	$1.3^{2.3}_{-0.1}$	..
181	10:00:12.11	+02:14:30.9	4752.15	300	18.8	$43.1^{4.2}_{-3.7}$	$6.0^{0.4}_{-0.3}$	..
182	10:00:12.33	+02:14:16.0	4174.25	211	7.4	$25.6^{5.8}_{-5.2}$	$4.9^{0.5}_{-0.8}$	..
183	10:00:12.44	+02:17:53.0	3844.49	1094	8.4	$27.8^{23.1}_{-11.3}$	$5.2^{1.7}_{-1.7}$	..
184	10:00:12.57	+02:17:54.6	5112.92	336	5.4	$6.1^{5.0}_{-3.2}$	$5.2^{3.0}_{-2.4}$	..
185	10:00:12.66	+02:13:07.1	4421.68	282	6.7	$16.8^{4.1}_{-3.4}$	$3.9^{0.9}_{-0.5}$	..
186	10:00:12.71	+02:12:30.0	4421.87	312	20.1	$91.4^{5.3}_{-7.2}$	$5.5^{0.2}_{-0.2}$	187
187	10:00:12.73	+02:12:29.0	5765.58	74	6.2	$13.7^{4.6}_{-2.6}$	$4.5^{0.7}_{-0.9}$	186
188	10:00:13.07	+02:20:22.4	5134.26	437	7.1	$22.8^{6.1}_{-4.1}$	$4.7^{0.9}_{-0.7}$	..
189	10:00:13.11	+02:18:56.3	4195.93	509	5.6	$12.9^{8.7}_{-6.7}$	$5.1^{1.8}_{-1.9}$	..
190	10:00:13.25	+02:16:49.2	3980.38	301	5.3	$19.2^{4.7}_{-5.8}$	$5.2^{1.3}_{-0.5}$	..
191	10:00:13.29	+02:19:59.4	5505.13	312	16.1	$37.2^{3.5}_{-2.4}$	$3.4^{0.4}_{-0.2}$	..
192	10:00:13.57	+02:13:16.6	4893.46	406	9.0	$23.6^{3.9}_{-4.9}$	$5.4^{0.6}_{-0.6}$	..
193	10:00:13.92	+02:14:16.7	5511.98	426	9.4	$17.8^{3.2}_{-2.7}$	$4.7^{0.6}_{-0.5}$	..
194	10:00:14.16	+02:14:28.3	3997.41	667	15.7	$61.0^{4.9}_{-4.3}$	$4.9^{0.3}_{-0.2}$	..
195	10:00:14.61	+02:17:02.9	4536.52	94	15.3	$35.4^{4.8}_{-2.6}$	$5.1^{0.4}_{-0.4}$	..
196	10:00:14.69	+02:16:25.5	4441.28	321	8.5	$24.0^{3.1}_{-4.7}$	$6.3^{0.8}_{-0.5}$	..
197	10:00:14.69	+02:17:47.4	4184.22	536	6.9	$17.8^{7.1}_{-6.0}$	$4.1^{1.2}_{-1.2}$	..
198	10:00:14.93	+02:12:23.4	4715.87	364	9.8	$24.9^{4.0}_{-3.6}$	$4.9^{0.6}_{-0.4}$	..
199	10:00:15.40	+02:14:12.6	4502.45	363	16.8	$35.8^{3.3}_{-4.1}$	$4.7^{0.3}_{-0.3}$	..
200	10:00:15.55	+02:16:17.9	5820.96	222	5.9	$10.8^{3.8}_{-3.2}$	$4.3^{1.0}_{-0.9}$	..
201	10:00:16.14	+02:19:17.1	5607.11	76	10.6	$35.1^{4.5}_{-4.9}$	$5.3^{0.6}_{-0.5}$	..
202	10:00:16.17	+02:18:40.1	5320.35	276	18.3	$30.6^{3.4}_{-4.6}$	$4.8^{0.3}_{-0.4}$	..
203	10:00:16.19	+02:14:00.4	4420.85	332	10.0	$23.9^{2.8}_{-3.2}$	$5.9^{0.4}_{-0.4}$	..

Table 1.4 (cont'd)

HPS Index (1)	α (J2000) (2)	δ (J2000) (3)	$\lambda_{\rm det}$ (Å) (4)	FWHM (km s^{-1}) (5)	S/N$_{\rm det}$ (6)	Flux (10^{-17} cgs) (7)	Spatial FWHM ($''$) (8)	Matching indices (9)
204	10:00:16.23	+02:14:35.4	5012.40	239	21.3	$38.2^{2.5}_{-2.8}$	$4.9^{0.2}_{-0.2}$	..
205	10:00:16.43	+02:20:30.2	4750.98	262	5.2	$22.6^{6.2}_{-6.2}$	$6.0^{0.9}_{-1.1}$	..
206	10:00:16.66	+02:16:19.5	4535.17	242	9.4	$5.9^{3.0}_{-3.5}$	$1.7^{2.0}_{-0.5}$	..
207	10:00:16.71	+02:18:21.5	4509.08	182	6.3	$9.9^{3.5}_{-3.2}$	$4.6^{1.4}_{-1.2}$	..
208	10:00:16.74	+02:12:18.7	4418.58	351	7.7	$28.5^{4.2}_{-4.5}$	$5.6^{0.6}_{-0.7}$	..
209	10:00:16.99	+02:12:38.6	4422.83	302	18.8	$66.6^{6.5}_{-4.4}$	$5.6^{0.4}_{-0.2}$	..
210	10:00:17.09	+02:16:14.1	5455.26	526	5.9	$10.5^{3.4}_{-3.3}$	$3.9^{1.1}_{-0.9}$	..
211	10:00:17.20	+02:17:36.7	5359.13	195	7.0	$11.8^{4.3}_{-4.0}$	$5.7^{1.1}_{-1.4}$	..
212	10:00:17.40	+02:20:42.4	5513.32	78	5.5	$8.2^{2.5}_{-3.0}$	$2.2^{1.2}_{-1.0}$	..
213	10:00:17.44	+02:16:59.0	5226.89	200	7.7	$13.0^{3.5}_{-3.1}$	$5.0^{1.2}_{-0.7}$	..
214	10:00:17.46	+02:19:04.2	5221.86	82	6.4	$8.2^{4.4}_{-3.2}$	$6.0^{2.0}_{-1.8}$	..
215	10:00:17.59	+02:19:33.9	4553.01	166	5.1	$22.3^{5.0}_{-5.0}$	$5.6^{0.9}_{-1.1}$	..
216	10:00:17.77	+02:17:59.9	4768.66	280	34.5	$45.8^{3.1}_{-4.2}$	$4.3^{0.2}_{-0.2}$	..
217	10:00:17.86	+02:20:17.3	5358.95	282	17.8	$68.1^{6.0}_{-5.2}$	$5.5^{0.3}_{-0.4}$	..
218	10:00:18.00	+02:16:31.5	5069.17	264	14.9	$31.9^{2.8}_{-3.5}$	$5.3^{0.4}_{-0.2}$	..
219	10:00:18.10	+02:18:18.7	4185.91	297	44.2	$185.5^{8.1}_{-7.7}$	$7.4^{0.2}_{-0.2}$	220,221
220	10:00:18.20	+02:18:18.3	5458.79	78	14.3	$40.3^{4.9}_{-7.5}$	$6.3^{0.6}_{-0.5}$	219,221
221	10:00:18.23	+02:18:15.7	5623.60	195	28.2	$71.0^{4.7}_{-5.4}$	$7.0^{0.3}_{-0.3}$	219,220
222	10:00:18.24	+02:15:51.0	4793.40	983	22.0	$87.3^{4.7}_{-5.8}$	$4.7^{0.2}_{-0.2}$	..
223	10:00:18.56	+02:14:59.8	4018.61	1102	5.7	$39.0^{11.5}_{-9.4}$	$6.4^{1.0}_{-0.9}$	..
224	10:00:18.82	+02:18:09.8	5598.94	327	12.5	$16.0^{3.8}_{-3.2}$	$4.0^{0.8}_{-0.6}$	..
225	10:00:18.94	+02:14:26.6	4190.38	237	21.8	$54.6^{2.3}_{-3.0}$	$4.9^{0.1}_{-0.2}$	226,227
226	10:00:18.96	+02:14:25.9	5628.37	122	20.8	$31.7^{1.5}_{-2.4}$	$4.1^{0.3}_{-0.3}$	225,227
227	10:00:18.97	+02:14:25.3	5465.05	78	6.8	$11.8^{2.6}_{-1.9}$	$4.9^{0.6}_{-0.7}$	225,226
228	10:00:19.31	+02:20:25.4	5500.26	326	6.6	$20.8^{5.5}_{-4.3}$	$3.8^{0.8}_{-0.7}$	..
229	10:00:19.39	+02:13:12.6	4910.43	625	14.2	$41.6^{4.2}_{-5.0}$	$5.4^{0.5}_{-0.3}$	..
230	10:00:20.43	+02:12:44.8	5317.30	330	11.8	$31.0^{5.4}_{-4.7}$	$5.6^{0.6}_{-0.7}$	..
231	10:00:20.80	+02:19:18.8	4524.17	551	7.0	$30.8^{8.0}_{-7.6}$	$6.3^{1.1}_{-0.7}$	..
232	10:00:21.04	+02:19:29.4	5147.66	326	23.4	$84.2^{5.0}_{-4.1}$	$6.1^{0.3}_{-0.2}$	..

Table 1.4 (cont'd)

HPS Index (1)	α (J2000) (2)	δ (J2000) (3)	$\lambda_{\rm det}$ (Å) (4)	FWHM (km s^{-1}) (5)	S/N$_{\rm det}$ (6)	Flux (10^{-17} cgs) (7)	Spatial FWHM ($''$) (8)	Matching indices (9)
233	10:00:21.36	+02:14:50.7	4888.43	367	32.1	$70.1^{2.5}_{-3.3}$	$5.5^{0.2}_{-0.2}$	..
234	10:00:21.49	+02:13:51.5	5465.91	78	14.1	$24.4^{3.6}_{-3.0}$	$4.5^{0.4}_{-0.4}$	..
235	10:00:21.67	+02:12:23.6	4218.01	453	12.5	$35.5^{5.8}_{-4.9}$	$5.1^{0.5}_{-0.5}$	..
236	10:00:21.92	+02:12:37.6	5618.91	386	5.2	$11.0^{5.4}_{-4.7}$	$4.4^{1.5}_{-1.1}$	237
237	10:00:21.94	+02:12:37.4	4185.31	211	6.2	$19.4^{6.0}_{-4.2}$	$6.1^{1.4}_{-0.6}$	236
238	10:00:22.95	+02:17:55.3	5072.40	413	7.6	$39.6^{7.0}_{-4.9}$	$7.8^{0.8}_{-0.7}$	..
239	10:00:22.96	+02:13:14.0	4419.67	302	52.5	$284.9^{5.1}_{-6.0}$	$5.5^{0.1}_{-0.1}$	240,241,242
240	10:00:22.99	+02:13:13.5	5146.25	83	12.2	$29.7^{2.9}_{-3.1}$	$4.5^{0.5}_{-0.3}$	239,241,242
241	10:00:23.00	+02:13:13.7	4584.53	1069	13.4	$95.0^{8.3}_{-9.2}$	$5.4^{0.3}_{-0.4}$	239,240,242
242	10:00:23.00	+02:13:13.3	5764.11	163	47.9	$140.3^{4.8}_{-3.3}$	$4.4^{0.1}_{-0.1}$	239,240,241
243	10:00:23.05	+02:15:13.9	4921.57	373	8.8	$16.9^{2.4}_{-2.1}$	$4.9^{0.7}_{-0.4}$	..
244	10:00:23.66	+02:13:12.0	3768.03	114	5.1	$10.4^{5.2}_{-4.2}$	$3.5^{1.5}_{-1.3}$	..
245	10:00:23.86	+02:14:41.9	5712.13	272	9.4	$11.3^{2.7}_{-1.9}$	$3.8^{0.5}_{-0.5}$	..
246	10:00:23.93	+02:13:52.9	4850.29	88	6.4	$9.2^{4.8}_{-2.7}$	$4.4^{1.0}_{-0.7}$	..
247	10:00:24.37	+02:13:59.7	4418.51	212	9.0	$19.5^{5.7}_{-2.0}$	$4.9^{0.7}_{-0.5}$	..
248	10:00:26.26	+02:13:27.0	5113.54	279	23.0	$47.7^{2.9}_{-3.3}$	$6.2^{0.2}_{-0.2}$	..
249	10:00:26.74	+02:17:40.0	5194.68	368	5.6	$7.4^{3.1}_{-2.7}$	$5.4^{1.5}_{-1.3}$	..
250	10:00:26.91	+02:13:01.5	5115.86	501	5.1	$7.9^{2.6}_{-3.1}$	$3.7^{1.3}_{-1.2}$	..
251	10:00:27.28	+02:17:31.3	3993.64	884	5.4	$45.0^{13.7}_{-11.6}$	$5.2^{1.0}_{-0.8}$	..
252	10:00:27.48	+02:17:06.6	5366.96	363	21.8	$101.7^{6.4}_{-6.7}$	$6.7^{0.2}_{-0.2}$	..
253	10:00:27.48	+02:15:52.3	5085.05	353	6.8	$20.4^{3.6}_{-4.4}$	$5.6^{0.7}_{-0.6}$	..
254	10:00:27.99	+02:12:57.9	5324.76	187	12.7	$17.3^{2.4}_{-1.5}$	$3.8^{0.4}_{-0.5}$	..
255	10:00:28.21	+02:19:05.5	4605.60	346	7.3	$18.6^{3.8}_{-3.3}$	$6.6^{0.9}_{-1.0}$	..
256	10:00:28.25	+02:17:58.4	4243.48	612	9.0	$31.4^{9.3}_{-6.5}$	$5.4^{0.8}_{-0.6}$	..
257	10:00:28.38	+02:17:36.2	4781.50	184	5.9	$6.0^{2.2}_{-2.8}$	$2.6^{1.1}_{-1.4}$	..
258	10:00:28.50	+02:17:55.9	4631.84	515	12.3	$31.2^{2.8}_{-4.9}$	$5.8^{0.3}_{-0.4}$	..
259	10:00:28.52	+02:14:42.1	5699.80	75	5.2	$7.1^{5.0}_{-3.7}$	$1.5^{2.2}_{-0.3}$	..
260	10:00:28.57	+02:18:58.4	4123.08	416	6.0	$22.7^{4.9}_{-5.4}$	$5.8^{1.1}_{-1.1}$	262
261	10:00:28.57	+02:17:48.4	3763.70	886	9.8	$143.7^{23.2}_{-10.1}$	$8.3^{0.9}_{-0.6}$	..

Table 1.4 (cont'd)

HPS Index (1)	α (J2000) (2)	δ (J2000) (3)	$\lambda_{\rm det}$ (Å) (4)	FWHM (km s^{-1}) (5)	S/N$_{\rm det}$ (6)	Flux (10^{-17} cgs) (7)	Spatial FWHM ($''$) (8)	Matching indices (9)
262	10:00:28.60	+02:18:57.8	5538.09	95	6.9	$7.0^{2.3}_{-2.1}$	$3.9^{0.8}_{-1.0}$	260
263	10:00:29.06	+02:14:09.2	4172.49	511	6.1	$24.1^{8.0}_{-7.7}$	$5.8^{1.2}_{-1.0}$	..
264	10:00:29.20	+02:18:58.5	5062.51	362	11.8	$25.3^{4.1}_{-2.9}$	$5.8^{0.4}_{-0.4}$	..
265	10:00:29.21	+02:15:02.6	4656.10	287	16.5	$72.5^{8.7}_{-6.0}$	$5.2^{0.3}_{-0.3}$	..
266	10:00:29.73	+02:18:50.1	3886.57	242	9.6	$41.9^{5.8}_{-5.7}$	$5.8^{0.6}_{-0.5}$	..
267	10:00:30.37	+02:18:44.2	4540.92	284	6.6	$12.5^{4.0}_{-3.0}$	$5.2^{0.8}_{-0.8}$	..
268	10:00:30.60	+02:17:35.4	4768.98	280	22.0	$40.6^{3.0}_{-2.2}$	$4.3^{0.2}_{-0.2}$	..
269	10:00:30.60	+02:17:43.9	4334.67	377	6.7	$13.9^{4.4}_{-2.9}$	$6.4^{0.9}_{-1.0}$	..
270	10:00:30.61	+02:13:01.8	5682.31	382	7.1	$8.7^{3.5}_{-2.2}$	$2.8^{1.1}_{-1.5}$	..
271	10:00:31.36	+02:13:07.2	4544.56	181	8.3	$15.1^{2.6}_{-2.9}$	$5.2^{0.6}_{-0.7}$	..
272	10:00:31.68	+02:17:57.6	5483.45	560	7.5	$17.8^{3.4}_{-3.2}$	$5.1^{0.7}_{-0.5}$	..
273	10:00:31.98	+02:15:51.0	5635.92	325	5.1	$15.8^{7.1}_{-4.9}$	$6.9^{1.4}_{-1.4}$	..
274	10:00:32.12	+02:19:11.3	4703.77	438	8.3	$17.4^{3.8}_{-2.6}$	$5.6^{0.7}_{-0.6}$	..
275	10:00:32.44	+02:15:53.0	4649.99	258	7.7	$27.1^{7.5}_{-8.0}$	$7.1^{1.2}_{-1.0}$	..
276	10:00:32.70	+02:13:59.7	4423.45	225	6.4	$9.7^{3.2}_{-3.1}$	$3.5^{0.9}_{-1.5}$	..
277	10:00:32.84	+02:13:56.6	4870.97	88	7.5	$8.5^{2.1}_{-2.0}$	$3.8^{0.7}_{-0.7}$	278,279,280,281
278	10:00:32.85	+02:13:56.8	4183.75	238	38.7	$118.1^{3.9}_{-3.5}$	$4.7^{0.2}_{-0.1}$	277,279,280,281
279	10:00:32.87	+02:13:56.4	5619.24	76	66.3	$152.4^{3.5}_{-3.9}$	$4.9^{0.1}_{-0.1}$	277,278,280,281
280	10:00:32.87	+02:13:56.4	5455.84	78	18.3	$36.8^{2.5}_{-3.3}$	$4.7^{0.3}_{-0.3}$	277,278,279,281
281	10:00:32.89	+02:13:56.1	4341.91	99	7.1	$12.1^{3.0}_{-3.0}$	$5.0^{0.8}_{-0.8}$	277,278,279,280
282	10:00:33.00	+02:15:32.1	4924.90	271	10.0	$33.8^{3.6}_{-5.2}$	$4.7^{0.5}_{-0.4}$	..
283	10:00:33.27	+02:18:24.6	5226.85	575	9.0	$22.1^{3.3}_{-3.1}$	$5.8^{0.5}_{-0.4}$	..
284	10:00:33.45	+02:13:08.5	4850.76	320	10.3	$22.1^{3.6}_{-3.4}$	$5.6^{0.6}_{-0.4}$	..
285	10:00:33.51	+02:16:14.2	5368.89	377	16.8	$42.0^{3.8}_{-2.9}$	$4.9^{0.3}_{-0.3}$	..
286	10:00:33.91	+02:13:17.9	3925.73	688	7.3	$28.4^{8.1}_{-4.3}$	$5.9^{0.7}_{-0.8}$	..
287	10:00:34.81	+02:17:42.4	5248.10	357	5.5	$6.0^{2.3}_{-3.0}$	$4.1^{1.5}_{-1.0}$	..
288	10:00:35.09	+02:17:49.4	4911.08	471	8.1	$11.9^{2.6}_{-3.3}$	$4.1^{0.9}_{-0.7}$	..
289	10:00:35.24	+02:18:07.3	5235.12	428	6.4	$17.1^{4.5}_{-4.5}$	$6.5^{1.2}_{-1.3}$	..
290	10:00:35.49	+02:18:38.8	5501.79	453	11.7	$43.5^{6.6}_{-5.9}$	$7.7^{0.7}_{-0.7}$	..

Table 1.4 (cont'd)

HPS Index (1)	α (J2000) (2)	δ (J2000) (3)	$\lambda_{\rm det}$ (Å) (4)	FWHM (km s^{-1}) (5)	S/N$_{\rm det}$ (6)	Flux (10^{-17} cgs) (7)	Spatial FWHM ($''$) (8)	Matching indices (9)
291	10:00:35.66	+02:12:22.3	5066.83	526	7.6	$27.4^{6.2}_{-4.8}$	$6.5^{0.7}_{-0.6}$	..
292	10:00:35.75	+02:18:58.1	4706.49	406	12.5	$30.1^{4.4}_{-3.5}$	$5.9^{0.5}_{-0.5}$	..
293	10:00:35.80	+02:19:00.7	5043.80	228	9.4	$20.8^{3.5}_{-3.1}$	$5.3^{0.6}_{-0.5}$	..
294	10:00:36.03	+02:15:26.9	5112.56	184	9.0	$61.3^{13.0}_{-8.2}$	$5.3^{0.7}_{-0.7}$	..
295	10:00:36.34	+02:13:17.6	4452.12	339	8.8	$24.4^{4.7}_{-4.2}$	$6.1^{0.7}_{-0.8}$	..
296	10:00:36.71	+02:13:09.8	4664.60	368	5.1	$11.1^{5.5}_{-2.8}$	$4.9^{1.2}_{-1.0}$	..
297	10:00:37.05	+02:15:08.9	4706.76	284	10.0	$67.4^{11.2}_{-8.5}$	$4.4^{0.5}_{-0.5}$	..
298	10:00:37.06	+02:13:34.5	5069.25	84	7.0	$11.5^{3.9}_{-2.4}$	$5.6^{0.9}_{-1.0}$	..
299	10:00:37.37	+02:16:12.7	4502.75	266	7.8	$31.9^{4.0}_{-6.2}$	$6.2^{0.6}_{-0.8}$	..
300	10:00:37.52	+02:12:54.6	4159.03	182	15.6	$41.8^{3.4}_{-4.4}$	$4.9^{0.2}_{-0.2}$	..
301	10:00:37.58	+02:18:47.9	5370.16	273	13.5	$24.1^{2.4}_{-2.7}$	$4.8^{0.3}_{-0.4}$	..
302	10:00:38.66	+02:18:03.9	5261.46	341	6.8	$14.7^{3.7}_{-3.6}$	$6.0^{0.9}_{-0.7}$	..
303	10:00:39.33	+02:12:46.5	4266.55	143	8.3	$31.1^{5.4}_{-6.1}$	$7.0^{0.7}_{-0.8}$	304
304	10:00:39.49	+02:12:45.3	5729.67	225	7.8	$32.4^{5.7}_{-6.7}$	$7.5^{0.9}_{-0.8}$	303
305	10:00:39.58	+02:13:20.3	4937.93	280	15.6	$38.5^{4.4}_{-3.5}$	$5.5^{0.4}_{-0.3}$	..
306	10:00:39.61	+02:13:38.6	4180.67	766	6.0	$38.3^{5.8}_{-9.2}$	$7.1^{1.0}_{-0.8}$	..
307	10:00:40.03	+02:18:02.9	5369.06	320	6.8	$19.5^{4.1}_{-4.8}$	$5.6^{0.6}_{-0.8}$	..
308	10:00:40.04	+02:12:51.7	5622.45	157	7.5	$18.4^{3.5}_{-4.2}$	$5.4^{0.8}_{-0.9}$	..
309	10:00:40.69	+02:18:32.4	5177.91	231	6.7	$11.3^{4.2}_{-3.5}$	$5.5^{1.3}_{-1.1}$	311,312
310	10:00:40.70	+02:17:41.5	4948.20	532	7.7	$10.7^{2.9}_{-2.4}$	$4.0^{0.7}_{-0.6}$	..
311	10:00:40.71	+02:18:31.9	5479.52	78	8.2	$10.2^{2.6}_{-2.7}$	$3.8^{0.9}_{-0.7}$	309,312
312	10:00:40.75	+02:18:32.1	4883.34	318	6.8	$11.0^{5.0}_{-3.2}$	$4.0^{1.1}_{-0.9}$	309,311
313	10:00:40.78	+02:18:23.6	3765.58	249	5.9	$25.1^{12.4}_{-10.1}$	$5.0^{1.8}_{-1.3}$	..
314	10:00:41.09	+02:17:03.6	4414.31	352	6.8	$14.4^{5.7}_{-2.9}$	$3.7^{1.1}_{-0.7}$	..
315	10:00:41.45	+02:18:16.5	4949.89	201	6.5	$8.6^{2.9}_{-2.4}$	$3.2^{1.0}_{-0.6}$	..
316	10:00:42.78	+02:16:31.2	4628.37	500	9.1	$22.1^{6.8}_{-4.8}$	$3.7^{0.7}_{-0.6}$	..
317	10:00:42.92	+02:18:46.0	5510.02	149	9.2	$17.0^{3.3}_{-3.5}$	$4.6^{0.5}_{-0.5}$	..
318	10:00:44.13	+02:15:58.9	4201.16	349	5.6	$30.3^{8.9}_{-11.1}$	$8.0^{1.7}_{-1.6}$	..
319	10:00:44.23	+02:16:57.4	5371.69	334	15.0	$33.4^{2.6}_{-3.8}$	$4.6^{0.3}_{-0.3}$	..

Table 1.4 (cont'd)

HPS Index (1)	α (J2000) (2)	δ (J2000) (3)	$\lambda_{\rm det}$ (Å) (4)	FWHM (km s^{-1}) (5)	S/N$_{\rm det}$ (6)	Flux (10^{-17} cgs) (7)	Spatial FWHM ($''$) (8)	Matching indices (9)
320	10:00:44.27	+02:16:26.1	5447.36	277	20.4	$47.3^{3.0}_{-3.8}$	$4.8^{0.3}_{-0.2}$	..
321	10:00:44.39	+02:18:28.8	5004.99	335	11.4	$18.4^{4.2}_{-2.1}$	$4.0^{0.5}_{-0.3}$	..
322	10:00:44.57	+02:18:31.6	5057.65	486	7.5	$16.7^{4.4}_{-3.3}$	$4.7^{0.9}_{-0.8}$	..
323	10:00:45.12	+02:18:22.0	5617.75	213	15.3	$36.7^{3.9}_{-2.8}$	$5.1^{0.4}_{-0.3}$	324,325,326
324	10:00:45.15	+02:18:22.6	5454.38	78	7.2	$19.4^{4.3}_{-4.4}$	$6.1^{0.7}_{-0.9}$	323,325,326
325	10:00:45.16	+02:18:22.7	5565.71	377	5.6	$13.0^{6.2}_{-4.1}$	$4.6^{1.3}_{-1.4}$	323,324,326
326	10:00:45.22	+02:18:23.4	4182.35	250	19.6	$75.8^{5.4}_{-4.3}$	$5.1^{0.2}_{-0.3}$	323,324,325
327	10:00:45.70	+02:16:58.7	3954.25	549	5.1	$15.5^{6.5}_{-6.0}$	$2.9^{1.0}_{-1.7}$	..
328	10:00:46.56	+02:19:12.4	5482.61	334	9.2	$20.2^{4.9}_{-3.3}$	$5.3^{0.6}_{-0.7}$	..
329	10:00:47.16	+02:17:60.0	5628.54	398	12.6	$41.9^{6.0}_{-5.2}$	$6.0^{0.5}_{-0.5}$	..
330	10:00:47.38	+02:17:08.7	4415.69	1160	6.0	$22.6^{7.6}_{-6.6}$	$2.8^{1.5}_{-0.8}$	..
331	10:00:47.43	+02:17:18.4	5370.58	349	5.6	$10.3^{5.6}_{-3.3}$	$3.9^{1.5}_{-1.2}$	..
332	12:36:14.19	+62:11:48.5	4792.43	399	17.2	$43.5^{5.9}_{-4.0}$	$5.7^{0.3}_{-0.4}$	..
333	12:36:14.22	+62:14:13.6	4498.89	182	5.4	$17.2^{15.9}_{-11.8}$	$6.0^{3.4}_{-2.2}$	..
334	12:36:15.03	+62:10:25.2	4680.15	440	10.9	$29.2^{6.3}_{-5.2}$	$4.5^{0.6}_{-0.5}$	..
335	12:36:15.85	+62:12:37.6	4790.74	288	35.2	$92.3^{3.6}_{-3.5}$	$4.6^{0.1}_{-0.1}$	..
336	12:36:15.98	+62:10:08.8	4983.93	320	19.9	$51.9^{4.6}_{-3.7}$	$4.6^{0.2}_{-0.2}$	..
337	12:36:16.55	+62:13:11.2	5355.81	205	7.6	$12.3^{4.5}_{-3.2}$	$4.9^{1.0}_{-0.7}$	..
338	12:36:17.32	+62:10:24.3	4378.80	1091	6.3	$33.3^{9.4}_{-8.2}$	$5.0^{1.0}_{-0.9}$	..
339	12:36:17.33	+62:14:17.7	5788.86	74	8.9	$28.7^{11.4}_{-8.2}$	$4.5^{1.2}_{-0.9}$	340
340	12:36:17.39	+62:14:17.4	4309.79	204	12.7	$49.5^{9.9}_{-9.4}$	$5.0^{0.7}_{-0.6}$	339
341	12:36:17.52	+62:13:10.0	4778.04	298	9.3	$12.8^{4.1}_{-2.8}$	$3.8^{0.8}_{-0.6}$	..
342	12:36:17.94	+62:14:58.1	4981.42	295	6.3	$21.4^{10.8}_{-13.8}$	$5.6^{2.3}_{-1.5}$	..
343	12:36:19.44	+62:12:52.8	5489.55	355	8.5	$15.3^{4.0}_{-3.7}$	$5.0^{0.8}_{-0.8}$	..
344	12:36:19.78	+62:12:29.8	5208.24	265	9.3	$16.1^{3.2}_{-2.1}$	$4.0^{0.5}_{-0.5}$	..
345	12:36:20.00	+62:10:22.3	5421.39	79	6.3	$7.5^{2.6}_{-2.4}$	$3.3^{1.3}_{-0.8}$	..
346	12:36:20.35	+62:10:33.6	5013.95	248	16.6	$34.4^{3.3}_{-3.5}$	$4.9^{0.2}_{-0.3}$	..
347	12:36:20.79	+62:12:04.0	5430.04	359	11.0	$21.8^{3.6}_{-4.0}$	$4.2^{0.6}_{-0.5}$	..
348	12:36:21.51	+62:12:27.0	5212.45	337	12.7	$19.8^{3.5}_{-2.7}$	$4.0^{0.5}_{-0.3}$	..

Table 1.4 (cont'd)

HPS Index (1)	α (J2000) (2)	δ (J2000) (3)	$\lambda_{\rm det}$ (Å) (4)	FWHM (km s^{-1}) (5)	S/N$_{\rm det}$ (6)	Flux (10^{-17} cgs) (7)	Spatial FWHM ($''$) (8)	Matching indices (9)
349	12:36:22.19	+62:11:06.6	4753.43	242	10.2	$19.3^{3.6}_{-4.0}$	$5.2^{0.4}_{-0.6}$	..
350	12:36:22.29	+62:12:42.3	5433.23	151	6.8	$10.0^{2.7}_{-2.7}$	$4.2^{1.0}_{-0.6}$	..
351	12:36:23.05	+62:13:45.0	5530.63	352	6.0	$33.7^{13.8}_{-12.1}$	$7.1^{1.5}_{-1.4}$	..
352	12:36:23.22	+62:11:26.1	5821.14	74	5.4	$6.5^{3.3}_{-2.4}$	$3.1^{1.1}_{-1.5}$	..
353	12:36:24.36	+62:11:38.5	4585.74	261	8.8	$13.4^{2.7}_{-3.2}$	$3.2^{0.7}_{-0.5}$	..
354	12:36:26.61	+62:12:52.2	5802.59	289	9.5	$16.3^{5.3}_{-2.9}$	$4.1^{0.9}_{-0.5}$	..
355	12:36:27.46	+62:10:18.4	4670.42	224	18.7	$54.7^{4.7}_{-4.6}$	$5.5^{0.3}_{-0.2}$	..
356	12:36:29.24	+62:11:53.4	5698.97	315	9.0	$25.6^{7.2}_{-6.1}$	$7.1^{1.0}_{-0.7}$	..
357	12:36:30.34	+62:12:09.0	5429.19	294	11.9	$16.8^{3.2}_{-2.4}$	$3.8^{0.4}_{-0.4}$	..
358	12:36:30.69	+62:14:34.4	5360.73	274	5.7	$9.7^{3.5}_{-4.3}$	$4.8^{1.2}_{-1.3}$	..
359	12:36:30.96	+62:12:36.6	5429.68	301	25.8	$35.7^{2.4}_{-2.9}$	$3.8^{0.2}_{-0.2}$	..
360	12:36:31.63	+62:11:38.7	4765.23	523	6.7	$18.7^{4.8}_{-4.9}$	$4.5^{0.7}_{-0.7}$	..
361	12:36:31.72	+62:12:40.9	5694.90	273	11.2	$24.4^{2.9}_{-2.7}$	$5.5^{0.4}_{-0.5}$	..
362	12:36:32.41	+62:10:37.7	5687.39	193	6.9	$25.6^{4.9}_{-5.7}$	$6.3^{0.8}_{-0.8}$	363
363	12:36:32.48	+62:10:36.9	4234.58	259	14.9	$61.8^{5.4}_{-6.6}$	$5.6^{0.5}_{-0.3}$	362
364	12:36:33.01	+62:11:34.7	5243.26	82	7.5	$19.3^{5.0}_{-3.9}$	$5.7^{0.7}_{-0.5}$	365,366,367
365	12:36:33.05	+62:11:34.5	5400.18	79	16.7	$37.2^{4.0}_{-4.3}$	$5.6^{0.3}_{-0.3}$	364,366,367
366	12:36:33.08	+62:11:33.3	4020.31	310	14.7	$87.6^{9.5}_{-7.6}$	$5.8^{0.3}_{-0.3}$	364,365,367
367	12:36:33.12	+62:11:34.7	5348.16	80	6.1	$19.2^{4.3}_{-4.5}$	$6.5^{0.9}_{-0.7}$	364,365,366
368	12:36:33.64	+62:11:56.7	5436.43	337	12.8	$20.9^{4.7}_{-4.4}$	$5.3^{0.7}_{-0.5}$	..
369	12:36:34.35	+62:12:13.3	5430.82	565	34.9	$106.7^{4.5}_{-4.2}$	$5.6^{0.2}_{-0.2}$	..
370	12:36:34.49	+62:12:53.7	5079.20	504	6.3	$11.8^{3.6}_{-3.3}$	$4.5^{0.7}_{-0.9}$	..
371	12:36:35.34	+62:14:23.4	4660.93	957	6.0	$13.9^{4.1}_{-5.5}$	$3.7^{1.1}_{-1.4}$	..
372	12:36:35.75	+62:12:05.7	4569.17	240	5.8	$10.8^{3.3}_{-2.1}$	$4.5^{1.0}_{-0.6}$	..
373	12:36:35.93	+62:11:38.3	4755.83	159	5.9	$19.2^{4.7}_{-4.1}$	$5.9^{1.0}_{-0.7}$	..
374	12:36:36.62	+62:11:35.6	5398.94	79	59.2	$192.7^{4.5}_{-4.8}$	$5.9^{0.1}_{-0.1}$	375,376,377,378,379
375	12:36:36.71	+62:11:35.3	4019.81	188	52.1	$407.7^{7.3}_{-9.4}$	$6.4^{0.1}_{-0.1}$	374,376,377,378,379
376	12:36:36.72	+62:11:35.2	5241.86	82	37.7	$141.3^{5.2}_{-3.1}$	$5.7^{0.1}_{-0.1}$	374,375,377,378,379
377	12:36:36.75	+62:11:34.8	5347.53	153	30.9	$100.0^{5.3}_{-4.1}$	$5.6^{0.2}_{-0.2}$	374,375,376,378,379

Table 1.4 (cont'd)

HPS Index (1)	α (J2000) (2)	δ (J2000) (3)	$\lambda_{\rm det}$ (Å) (4)	FWHM (km s^{-1}) (5)	S/N$_{\rm det}$ (6)	Flux (10^{-17} cgs) (7)	Spatial FWHM ($''$) (8)	Matching indices (9)
378	12:36:36.88	+62:11:33.9	4681.21	91	10.7	$17.3^{2.5}_{-3.6}$	$3.7^{0.6}_{-0.4}$	374,375,376,377,379
379	12:36:36.90	+62:11:33.7	4167.90	1266	9.8	$95.3^{14.5}_{-12.8}$	$4.6^{0.4}_{-0.4}$	374,375,376,377,378
380	12:36:37.43	+62:12:41.0	5436.16	330	26.7	$46.4^{2.8}_{-2.6}$	$4.4^{0.3}_{-0.2}$	..
381	12:36:37.57	+62:12:41.0	5528.52	77	6.4	$8.1^{2.3}_{-2.2}$	$4.0^{1.0}_{-0.8}$	..
382	12:36:38.36	+62:15:10.7	5449.15	162	6.1	$7.0^{4.2}_{-2.7}$	$4.4^{1.6}_{-1.2}$	..
383	12:36:41.60	+62:11:31.4	4726.80	91	7.0	$10.6^{4.1}_{-2.8}$	$4.7^{1.2}_{-1.1}$	384,385,386,387
384	12:36:41.62	+62:11:32.2	5399.84	79	22.2	$38.7^{3.0}_{-2.2}$	$4.3^{0.2}_{-0.2}$	383,385,386,387
385	12:36:41.62	+62:11:32.1	5293.63	81	18.9	$40.3^{3.5}_{-3.1}$	$4.3^{0.3}_{-0.2}$	383,384,386,387
386	12:36:41.69	+62:11:31.7	4059.19	231	30.9	$153.4^{7.6}_{-8.6}$	$4.7^{0.1}_{-0.2}$	383,384,385,387
387	12:36:41.72	+62:11:33.5	5451.96	97	25.6	$73.0^{2.7}_{-4.6}$	$5.4^{0.2}_{-0.2}$	383,384,385,386
388	12:36:41.76	+62:12:05.4	5342.22	306	7.4	$15.6^{4.2}_{-3.1}$	$4.6^{1.0}_{-0.7}$	..
389	12:36:41.77	+62:12:39.1	4362.38	658	7.9	$21.5^{4.3}_{-3.6}$	$4.0^{0.8}_{-0.5}$	..
390	12:36:42.33	+62:15:18.1	5712.72	448	8.5	$14.8^{7.3}_{-2.9}$	$4.6^{1.2}_{-0.8}$	..
391	12:36:42.51	+62:14:48.7	4812.62	631	6.3	$28.0^{6.5}_{-6.8}$	$6.0^{1.1}_{-0.8}$	..
392	12:36:42.74	+62:12:16.7	5418.34	309	17.8	$28.8^{1.7}_{-2.3}$	$4.5^{0.3}_{-0.2}$	..
393	12:36:43.04	+62:10:29.4	5777.46	388	6.7	$14.5^{5.2}_{-3.7}$	$5.0^{1.3}_{-0.9}$	..
394	12:36:43.75	+62:13:57.1	4476.90	257	14.0	$27.6^{3.6}_{-4.5}$	$5.6^{0.4}_{-0.5}$	..
395	12:36:43.86	+62:14:010.	3979.36	635	6.0	$20.4^{10.0}_{-7.5}$	$6.8^{1.8}_{-1.7}$	..
396	12:36:44.06	+62:12:49.7	5799.52	323	31.8	$71.7^{2.8}_{-4.0}$	$6.0^{0.1}_{-0.2}$	..
397	12:36:45.20	+62:13:27.7	5365.06	164	6.9	$10.5^{1.9}_{-1.7}$	$5.2^{0.8}_{-0.5}$	..
398	12:36:45.21	+62:12:01.1	5423.82	162	6.1	$4.5^{2.4}_{-1.3}$	$4.2^{1.8}_{-1.2}$	..
399	12:36:45.84	+62:13:27.3	4922.49	213	9.3	$14.0^{2.1}_{-2.0}$	$4.8^{0.6}_{-0.3}$	..
400	12:36:46.37	+62:14:08.4	5651.77	76	7.2	$5.9^{1.7}_{-2.0}$	$2.5^{1.0}_{-1.4}$	..
401	12:36:46.43	+62:14:45.8	3649.39	1118	7.9	$103.2^{20.9}_{-13.1}$	$6.8^{0.7}_{-0.7}$	..
402	12:36:46.86	+62:12:27.4	4821.05	630	8.3	$16.8^{1.7}_{-3.2}$	$3.9^{0.5}_{-0.5}$	..
403	12:36:47.06	+62:15:13.4	5079.54	161	6.3	$10.2^{1.9}_{-2.5}$	$5.2^{0.8}_{-0.7}$	..
404	12:36:47.11	+62:12:36.6	4922.80	332	22.5	$39.5^{2.8}_{-1.6}$	$5.6^{0.3}_{-0.2}$	..
405	12:36:47.13	+62:12:32.6	5304.54	353	7.0	$13.0^{2.3}_{-2.6}$	$6.4^{0.9}_{-0.9}$	..
406	12:36:47.53	+62:15:14.3	5715.47	209	7.4	$10.6^{1.2}_{-2.3}$	$4.1^{0.8}_{-0.7}$	..

Table 1.4 (cont'd)

HPS Index (1)	α (J2000) (2)	δ (J2000) (3)	$\lambda_{\rm det}$ (Å) (4)	FWHM (km s^{-1}) (5)	S/N$_{\rm det}$ (6)	Flux (10^{-17} cgs) (7)	Spatial FWHM ($''$) (8)	Matching indices (9)
407	12:36:47.95	+62:14:26.8	5535.68	77	25.4	$43.6^{1.9}_{-1.9}$	$4.7^{0.2}_{-0.1}$	408,409,411,412,413
408	12:36:48.03	+62:14:26.6	5646.82	122	12.9	$22.6^{1.9}_{-2.1}$	$5.0^{0.4}_{-0.3}$	407,409,411,412,413
409	12:36:48.07	+62:14:27.2	5701.44	133	36.2	$67.3^{2.7}_{-2.7}$	$4.8^{0.1}_{-0.1}$	407,408,411,412,413
410	12:36:48.10	+62:13:10.6	5496.03	534	16.1	$49.3^{4.6}_{-4.5}$	$6.9^{0.3}_{-0.4}$	..
411	12:36:48.11	+62:14:26.3	4941.81	87	6.9	$8.3^{2.7}_{-1.9}$	$4.7^{0.9}_{-0.7}$	407,408,409,412,413
412	12:36:48.22	+62:14:26.1	4404.75	991	8.8	$32.9^{5.5}_{-5.5}$	$5.4^{0.5}_{-0.6}$	407,408,409,411,413
413	12:36:48.23	+62:14:26.7	4244.78	293	67.4	$197.7^{4.2}_{-3.2}$	$5.6^{0.1}_{-0.0}$	407,408,409,411,412
414	12:36:49.08	+62:15:12.6	5433.79	229	5.7	$6.6^{2.5}_{-2.0}$	$4.4^{0.7}_{-0.9}$	..
415	12:36:49.38	+62:14:21.8	5308.51	476	7.2	$12.0^{3.2}_{-2.6}$	$4.8^{0.8}_{-0.7}$	..
416	12:36:49.47	+62:13:13.9	5499.10	368	15.6	$39.9^{4.8}_{-2.7}$	$7.3^{0.4}_{-0.4}$	..
417	12:36:49.59	+62:11:13.2	5498.60	354	16.5	$22.7^{2.1}_{-2.7}$	$3.4^{0.3}_{-0.3}$	..
418	12:36:49.78	+62:13:0.98	5495.93	305	5.0	$4.8^{2.1}_{-2.6}$	$2.4^{1.6}_{-1.2}$	..
419	12:36:50.04	+62:14:00.7	3932.55	476	7.7	$24.4^{3.3}_{-5.1}$	$5.3^{0.6}_{-0.6}$	..
420	12:36:50.28	+62:10:55.8	4776.35	572	8.7	$18.6^{3.5}_{-4.3}$	$4.8^{0.6}_{-0.8}$	..
421	12:36:50.37	+62:12:40.2	5494.78	312	13.8	$23.0^{3.1}_{-1.9}$	$4.5^{0.4}_{-0.3}$	..
422	12:36:50.59	+62:10:58.5	5495.25	283	14.6	$21.7^{2.5}_{-3.4}$	$4.0^{0.5}_{-0.4}$	..
423	12:36:50.88	+62:12:56.2	4924.96	332	19.2	$21.9^{2.1}_{-1.9}$	$4.2^{0.3}_{-0.3}$	..
424	12:36:51.08	+62:10:31.5	5254.58	263	9.1	$15.9^{3.0}_{-3.0}$	$4.6^{0.5}_{-0.5}$	..
425	12:36:51.18	+62:13:21.6	4475.10	246	43.5	$103.2^{4.0}_{-3.1}$	$5.9^{0.1}_{-0.1}$	..
426	12:36:51.60	+62:15:11.1	5354.45	290	6.2	$7.6^{2.3}_{-1.4}$	$3.7^{0.8}_{-0.6}$	..
427	12:36:51.62	+62:10:52.2	5657.71	76	5.8	$10.2^{3.3}_{-2.6}$	$5.1^{1.0}_{-0.7}$	..
428	12:36:51.67	+62:15:16.3	5270.01	287	9.7	$14.3^{2.8}_{-2.3}$	$5.0^{0.7}_{-0.6}$	..
429	12:36:51.78	+62:12:22.7	4845.76	247	7.9	$12.4^{2.0}_{-2.4}$	$5.5^{0.7}_{-0.6}$	..
430	12:36:52.03	+62:11:25.9	5452.19	79	5.9	$6.6^{2.3}_{-1.9}$	$4.3^{1.1}_{-1.2}$	..
431	12:36:52.15	+62:14:57.3	5059.60	207	13.7	$16.7^{1.3}_{-2.2}$	$4.4^{0.4}_{-0.5}$	..
432	12:36:52.64	+62:10:36.0	4920.32	349	16.0	$22.9^{3.0}_{-2.1}$	$4.2^{0.4}_{-0.3}$	..
433	12:36:52.66	+62:12:21.5	5219.72	556	5.6	$8.4^{2.3}_{-2.4}$	$4.1^{0.8}_{-0.9}$	..
434	12:36:54.27	+62:13:36.0	3970.24	289	6.4	$11.9^{3.8}_{-3.4}$	$6.0^{1.0}_{-1.0}$	..
435	12:36:54.72	+62:11:28.4	4672.32	359	8.1	$15.1^{2.6}_{-2.8}$	$5.1^{0.5}_{-0.5}$	..

Table 1.4 (cont'd)

HPS Index (1)	α (J2000) (2)	δ (J2000) (3)	$\lambda_{\rm det}$ (Å) (4)	FWHM (km s^{-1}) (5)	S/N$_{\rm det}$ (6)	Flux (10^{-17} cgs) (7)	Spatial FWHM ($''$) (8)	Matching indices (9)
436	12:36:54.94	+62:13:42.5	4156.58	322	5.0	$7.5^{2.8}_{-2.5}$	$5.0^{1.5}_{-1.1}$	..
437	12:36:56.40	+62:14:20.7	5532.37	189	11.8	$14.1^{1.7}_{-2.3}$	$4.0^{0.4}_{-0.3}$	438
438	12:36:56.50	+62:14:19.5	4119.36	199	12.5	$30.4^{4.2}_{-4.1}$	$5.5^{0.3}_{-0.4}$	437
439	12:36:56.87	+62:11:52.0	5760.95	232	6.5	$8.4^{3.0}_{-2.6}$	$4.2^{1.2}_{-0.9}$	..
440	12:36:57.13	+62:12:27.1	5821.76	260	8.8	$6.5^{2.4}_{-2.4}$	$3.6^{1.0}_{-0.8}$	..
441	12:36:57.49	+62:13:00.4	5494.75	327	22.8	$38.9^{2.7}_{-2.1}$	$4.6^{0.2}_{-0.2}$	..
442	12:36:58.07	+62:13:01.8	4921.47	272	15.0	$23.1^{2.6}_{-2.6}$	$5.7^{0.5}_{-0.4}$	..
443	12:36:58.64	+62:12:53.1	4920.97	253	11.6	$24.2^{3.6}_{-4.0}$	$7.3^{0.7}_{-0.5}$	..
444	12:36:58.78	+62:14:38.7	5632.70	473	5.4	$7.9^{3.4}_{-3.5}$	$4.4^{1.5}_{-1.3}$	..
445	12:36:59.27	+62:14:06.4	5449.82	112	21.9	$48.9^{2.7}_{-2.4}$	$6.2^{0.2}_{-0.2}$	446,448,449
446	12:36:59.29	+62:14:05.2	5291.05	81	8.0	$17.2^{3.1}_{-3.2}$	$6.3^{0.8}_{-0.8}$	445,448,449
447	12:36:59.37	+62:13:42.6	5016.05	318	5.8	$7.2^{2.1}_{-1.2}$	$4.4^{0.9}_{-0.9}$	..
448	12:36:59.40	+62:14:05.5	5397.40	184	7.4	$14.8^{3.6}_{-2.2}$	$6.3^{0.9}_{-0.6}$	445,446,449
449	12:36:59.50	+62:14:04.9	4057.59	217	15.9	$65.9^{9.5}_{-6.2}$	$6.2^{0.5}_{-0.4}$	445,446,448
450	12:36:59.85	+62:14:05.9	5645.65	275	8.5	$8.9^{2.0}_{-2.1}$	$2.8^{0.9}_{-1.4}$	..
451	12:37:00.31	+62:14:06.5	5303.80	409	6.6	$11.3^{3.7}_{-2.9}$	$5.1^{1.0}_{-0.9}$	..
452	12:37:01.73	+62:13:22.8	5256.55	131	7.0	$11.6^{3.0}_{-2.5}$	$4.7^{0.7}_{-0.9}$	..
453	12:37:01.94	+62:11:23.6	4386.82	1074	6.8	$11.3^{4.3}_{-3.9}$	$2.0^{1.5}_{-0.8}$	455,456,457,458
454	12:37:01.96	+62:13:49.4	5633.22	176	9.6	$16.4^{3.4}_{-2.9}$	$5.0^{0.7}_{-0.5}$	..
455	12:37:02.05	+62:11:24.0	5631.72	76	9.3	$15.1^{2.1}_{-2.4}$	$5.6^{0.5}_{-0.5}$	453,456,457,458
456	12:37:02.08	+62:11:24.1	5686.34	144	19.9	$30.5^{2.8}_{-2.3}$	$5.0^{0.2}_{-0.2}$	453,455,457,458
457	12:37:02.09	+62:11:24.5	5521.00	78	16.6	$26.7^{2.8}_{-3.7}$	$5.4^{0.3}_{-0.4}$	453,455,456,458
458	12:37:02.14	+62:11:23.7	4233.33	235	44.5	$114.3^{2.7}_{-4.2}$	$5.4^{0.1}_{-0.1}$	453,455,456,457
459	12:37:03.92	+62:10:11.1	4925.27	280	13.9	$30.4^{3.3}_{-3.1}$	$3.7^{0.4}_{-0.2}$	..
460	12:37:04.02	+62:14:42.5	5496.46	347	12.8	$19.8^{2.6}_{-2.6}$	$4.5^{0.4}_{-0.4}$	..
461	12:37:04.17	+62:14:46.7	4977.89	479	9.2	$13.5^{4.4}_{-3.0}$	$4.2^{0.8}_{-0.7}$	462
462	12:37:04.49	+62:14:46.6	3905.67	546	12.4	$78.9^{8.8}_{-7.9}$	$6.4^{0.5}_{-0.4}$	461
463	12:37:04.55	+62:10:29.9	5256.63	334	14.7	$29.2^{2.3}_{-3.4}$	$4.1^{0.2}_{-0.2}$	..
464	12:37:04.59	+62:14:29.5	5814.80	253	5.7	$9.4^{2.9}_{-2.6}$	$4.9^{1.4}_{-1.0}$	..

Table 1.4 (cont'd)

HPS Index (1)	α (J2000) (2)	δ (J2000) (3)	λ_{det} (Å) (4)	FWHM (km s^{-1}) (5)	S/N$_{\mathrm{det}}$ (6)	Flux (10^{-17} cgs) (7)	Spatial FWHM ($''$) (8)	Matching indices (9)
465	12:37:05.21	+62:12:11.7	5169.47	259	8.1	$15.6^{2.8}_{-3.5}$	$6.0^{0.8}_{-0.7}$	..
466	12:37:05.85	+62:15:03.1	5152.53	371	14.6	$20.5^{2.6}_{-2.1}$	$4.2^{0.4}_{-0.4}$	..
467	12:37:07.53	+62:11:38.3	4622.35	93	6.0	$9.4^{3.9}_{-2.7}$	$4.8^{1.1}_{-0.9}$	..
468	12:37:07.74	+62:11:39.4	5804.44	296	12.9	$16.5^{2.7}_{-2.9}$	$4.0^{0.6}_{-0.5}$	..
469	12:37:08.19	+62:10:57.1	5302.28	389	34.5	$70.3^{3.6}_{-3.3}$	$5.2^{0.2}_{-0.2}$	..
470	12:37:08.24	+62:14:55.0	5823.58	274	12.6	$20.1^{2.9}_{-3.0}$	$5.1^{0.5}_{-0.6}$	..
471	12:37:08.76	+62:10:52.1	5258.97	287	14.6	$24.7^{3.7}_{-2.1}$	$5.0^{0.6}_{-0.3}$	..
472	12:37:10.81	+62:10:50.2	5527.22	217	5.6	$3.9^{2.6}_{-1.9}$	$3.1^{1.8}_{-1.9}$	..
473	12:37:10.93	+62:11:30.5	5497.45	478	5.9	$7.5^{3.5}_{-2.5}$	$3.5^{1.1}_{-1.2}$	..
474	12:37:11.00	+62:11:40.9	3980.21	564	5.6	$13.6^{8.8}_{-6.4}$	$4.2^{1.8}_{-1.8}$	..
475	12:37:11.50	+62:11:29.4	5256.73	427	5.6	$11.2^{3.3}_{-2.9}$	$4.0^{0.6}_{-0.7}$	..
476	12:37:11.60	+62:10:21.1	5264.56	440	12.7	$19.1^{3.9}_{-2.2}$	$4.0^{0.4}_{-0.3}$	..
477	12:37:11.68	+62:15:14.5	4840.35	303	38.1	$70.8^{2.7}_{-2.7}$	$5.1^{0.1}_{-0.2}$	478
478	12:37:11.69	+62:15:14.4	5023.20	334	6.2	$7.2^{3.8}_{-2.1}$	$4.1^{1.0}_{-0.8}$	477
479	12:37:13.52	+62:15:11.6	5677.75	295	8.3	$15.5^{4.3}_{-4.5}$	$5.2^{0.7}_{-1.0}$	..

Table 1.5. HETDEX Pilot Survey Emission Line Classifications

HPS Index (1)	Counter-part (2)	Counter-part $m_R{}^*$ (3)	Counter-part P (4)	$EW_{R,rest}{}^*$ (Å) (5)	$EW_{interp,rest}$ (Å) (6)	Trans-ition (7)	z_{est} (8)	Lyα P (9)	X-ray counterpart (10)
001	J0221112-043126	23.05	0.93	$51.9^{14.7}_{-14.6}$	$62.9^{17.0}_{-17.4}$	[OII]	0.4004	0.07	..
002	J0221122-043225	23.17	0.96	$42.0^{14.9}_{-16.3}$	$59.8^{20.5}_{-23.0}$	[OII]	0.4620	0.04	..
003	J0221143-043138	24.31	0.98	$58.8^{22.2}_{-15.1}$	$109.0^{36.8}_{-26.5}$	Lyα	3.0915	1.00	..
004	J0221150-043156	21.05	0.98	$10.4^{3.4}_{-3.5}$	$7.1^{2.3}_{-2.4}$	CIII]1909	1.7561	0.02	J0221151-043156
005	J0221150-043156	21.05	1.00	$54.9^{10.9}_{-9.7}$	$55.1^{9.9}_{-9.2}$	CIV1549	1.7570	0.00	J0221151-043156
006	J0221164-042933	23.82	0.89	$56.7^{12.6}_{-11.5}$	$74.1^{15.8}_{-14.8}$	Lyα	2.7770	1.00	..
007	J0221163-043116	21.38	0.98	$31.2^{6.2}_{-6.0}$	$48.3^{8.8}_{-8.9}$	[OII]	0.3850	0.02	..
008	J0221171-042757	22.82	0.67	$51.2^{16.8}_{-12.1}$	$57.4^{18.3}_{-13.3}$	[OII]	0.5616	0.01	..
009	J0221174-043001	23.21	0.98	$51.0^{11.2}_{-12.4}$	$49.0^{9.9}_{-11.6}$	[OII]	0.4661	0.02	..
010	J0221174-042729	21.43	0.99	$24.0^{5.1}_{-4.6}$	$39.1^{8.2}_{-7.5}$	[OII]	0.2901	0.01	..
011	J0221185-042734	23.93	0.56	$40.8^{12.2}_{-11.1}$	$39.3^{11.3}_{-10.6}$	Lyα	2.7764	1.00	..
012	J0221194-043029	20.27	1.00	$5.1^{1.3}_{-1.1}$	$14.3^{3.4}_{-3.1}$	[OII]	0.1802	0.00	..
013	J0221193-043039	24.91	0.70	$62.9^{26.5}_{-17.5}$	$92.3^{31.4}_{-23.3}$	Lyα	3.3194	1.00	..
014	J0221194-042822	21.69	1.00	$39.3^{7.8}_{-7.3}$	$55.5^{10.9}_{-10.3}$	[OII]	0.3050	0.00	..
015	J0221196-042934	20.62	1.00	$10.7^{2.2}_{-2.0}$	$18.8^{3.8}_{-3.5}$	[OII]	0.3199	0.00	..
016	J0221198-042801	22.17	0.84	$17.0^{7.3}_{-4.8}$	$25.8^{11.1}_{-7.2}$	[OII]	0.3150	0.00	..
017	J0221199-042743	24.33	0.96	$36.4^{13.7}_{-11.3}$	$34.2^{12.0}_{-10.4}$	Lyα	2.7742	1.00	..
018	J0221208-043057	20.49	0.74	$14.4^{3.9}_{-3.4}$	$20.4^{5.3}_{-4.7}$	[NeIII]3869	0.4617	0.00	..
019	J0221208-043057	20.48	0.75	$24.3^{4.8}_{-4.3}$	$41.1^{7.5}_{-7.0}$	[OII]	0.4629	0.00	..
020	J0221211-042744	21.80	0.99	$22.7^{6.0}_{-5.6}$	$27.0^{6.9}_{-6.6}$	[OII]	0.5532	0.01	..
021	J0221223-043034	23.13	0.60	$29.5^{10.1}_{-7.9}$	$40.2^{13.2}_{-10.6}$	[OII]	0.4619	0.03	..
022	J0221230-042925	25.14	0.81	$103.4^{122.1}_{-42.9}$	$682.6^{1000.0}_{-328.6}$	Lyα	2.7727	1.00	..
023	J0221229-042944	22.44	1.00	$27.1^{7.1}_{-7.5}$	$44.1^{11.1}_{-12.1}$	[OII]	0.2182	0.00	..
024	J0221233-042923	22.03	1.00	$14.6^{4.8}_{-3.5}$	$21.2^{6.8}_{-5.0}$	[OII]	0.2322	0.00	..
025	J0221235-042901	24.27	0.98	$158.9^{45.7}_{-36.9}$	$256.4^{65.9}_{-56.5}$	Lyα	2.5532	1.00	..
026	J0221238-043000	20.75	0.68	$28.8^{5.7}_{-5.1}$	$42.7^{7.6}_{-7.2}$	[OII]	0.4318	0.32	..
027	J0221245-043000	21.25	0.99	$29.4^{6.5}_{-5.7}$	$31.4^{6.5}_{-5.9}$	[OIII]5007	0.1594	0.01	..
028	J0221245-043000	21.23	0.99	$12.3^{3.8}_{-3.0}$	$13.6^{4.0}_{-3.2}$	Hβ	0.1595	0.01	..
029	J0221245-043000	21.22	0.99	$21.9^{4.6}_{-4.0}$	$42.1^{8.1}_{-7.4}$	[OII]	0.1597	0.01	..

Table 1.5 (cont'd)

HPS Index (1)	Counter-part (2)	Counter-part m_R* (3)	Counter-part P (4)	$EW_{R,rest}$* (Å) (5)	$EW_{interp,rest}$ (Å) (6)	Trans-ition (7)	z_{est} (8)	Lyα P (9)	X-ray counterpart (10)
030	J0221245-043000	21.23	0.98	$8.6^{3.5}_{-3.1}$	$9.3^{3.7}_{-3.4}$	[OIII]4959	0.1594	0.02	..
031	J0221256-043025	21.43	0.93	$17.3^{4.0}_{-3.6}$	$24.2^{5.3}_{-4.8}$	[OII]	0.4584	0.07	..
032	J0221259-042949	19.91	1.00	$2.0^{0.8}_{-0.6}$	$3.5^{1.5}_{-1.1}$	[OII]	0.4618	0.00	..
033	J0221269-043006	22.59	0.54	$51.6^{12.4}_{-12.7}$	$69.2^{15.5}_{-16.6}$	[OII]	0.4650	0.01	..
034	J0221272-042939	24.45	0.92	$63.5^{21.7}_{-19.0}$	$71.4^{22.7}_{-20.9}$	Lyα	2.7585	1.00	..
035	J0221277-043017	18.04	1.00	$17.1^{3.3}_{-2.9}$	$44.7^{7.8}_{-7.2}$	[OII]	0.0841	0.00	..
036	J0221277-043017	18.04	1.00	$1.7^{0.3}_{-0.3}$	$2.3^{0.5}_{-0.4}$	Hγ	0.0839	0.00	..
037	J0221277-043017	18.04	1.00	$11.3^{2.2}_{-1.9}$	$13.2^{2.3}_{-2.2}$	Hβ	0.0841	0.00	..
038	J0221277-043017	18.04	1.00	$16.1^{3.1}_{-2.8}$	$18.4^{3.2}_{-3.0}$	[OIII]5007	0.0839	0.00	..
039	J0221277-043017	18.04	1.00	$7.4^{1.4}_{-1.3}$	$8.4^{1.5}_{-1.4}$	[OIII]4959	0.0840	0.00	..
040	J0221277-042951	22.77	0.99	$36.9^{12.8}_{-9.6}$	$50.6^{16.9}_{-12.9}$	[OII]	0.4644	0.01	..
041	J0221302-043046	22.01	0.99	$14.1^{4.4}_{-5.9}$	$25.5^{7.8}_{-10.6}$	[OII]	0.2242	0.01	..
042	J0306301+000351	20.43	0.99	$12.7^{3.4}_{-3.0}$	$52.7^{13.9}_{-12.6}$	[OII]	0.2362	0.00	..
043	J0306308+000129	20.73	0.95	$12.4^{3.3}_{-3.3}$	$18.2^{4.6}_{-4.7}$	[OIII]5007	0.1187	0.05	..
044	J0306308+000129	20.73	0.99	$12.3^{3.2}_{-3.2}$	$36.9^{9.7}_{-9.6}$	[OII]	0.1191	0.01	..
045	J0306321+000145	21.85	0.99	$20.3^{6.2}_{-4.9}$	$38.7^{11.4}_{-9.2}$	[OII]	0.3719	0.01	..
046	J0306327+000150	20.90	1.00	$23.2^{4.9}_{-4.3}$	$50.3^{9.7}_{-8.8}$	[OII]	0.3717	0.00	..
047	J0306334-000132	21.17	0.91	$18.5^{5.2}_{-4.4}$	$30.1^{8.0}_{-7.0}$	[OII]	0.5337	0.02	..
048	J0306336-000130	21.25	0.67	$48.5^{10.3}_{-8.9}$	$81.2^{15.7}_{-14.1}$	[OII]	0.5226	0.25	..
049	J0306343-000048	21.69	1.00	$27.4^{7.7}_{-6.5}$	$57.9^{15.4}_{-13.5}$	[OII]	0.3686	0.00	..
050	J0306343+000021	20.05	1.00	$2.4^{0.9}_{-0.8}$	$6.9^{2.4}_{-2.1}$	[OII]	0.3668	0.00	..
051	J0306348-000051	23.67	0.47	$14.8^{9.3}_{-7.0}$	$26.3^{15.5}_{-12.3}$	Lyα	3.0971	0.52	..
052	J0306351+000003	17.81	1.00	$2.7^{0.6}_{-0.5}$	$8.5^{1.7}_{-1.5}$	[OII]	0.4248	0.00	J0306351+000004
053	..	..	0.61	$313.1^{121.1}_{-101.6}$	$123.9^{47.9}_{-40.2}$	Lyα	3.5726	1.00	..
054	J0306357-000055	23.09	0.93	$33.9^{12.2}_{-12.5}$	$69.5^{23.8}_{-25.3}$	[OII]	0.4267	0.07	..
055	J0306359+000106	23.17	0.95	$32.5^{14.9}_{-10.3}$	$55.9^{25.0}_{-17.6}$	[OII]	0.4121	0.02	..
056	J0306360-000038	21.22	0.87	$18.8^{4.4}_{-4.2}$	$36.2^{8.0}_{-7.8}$	[OII]	0.4246	0.00	..
057	J0306362-000040	19.51	0.99	$8.7^{1.8}_{-1.6}$	$22.5^{4.7}_{-4.1}$	[OII]	0.2718	0.00	..
058	J0306372-000259	19.32	0.99	$5.4^{1.3}_{-1.2}$	$15.2^{3.4}_{-3.1}$	[OII]	0.3719	0.01	..

Table 1.5 (cont'd)

HPS Index (1)	Counter-part (2)	Counter-part m_R* (3)	Counter-part P (4)	$EW_{R,rest}$* (Å) (5)	$EW_{interp,rest}$ (Å) (6)	Trans-ition (7)	z_{est} (8)	Lyα P (9)	X-ray counterpart (10)
059	J0306373+000346	20.33	1.00	$4.3^{1.9}_{-1.5}$	$11.1^{4.7}_{-3.7}$	[OII]	0.3706	0.00	..
060	J0306374+000205	19.54	1.00	$3.4^{1.1}_{-0.9}$	$9.0^{2.9}_{-2.3}$	[OII]	0.4772	0.00	..
061	J0306378-000029	20.84	0.92	$6.3^{1.9}_{-1.9}$	$17.5^{4.9}_{-5.2}$	[OII]	0.3340	0.08	..
062	J0306382+000039	24.11	0.95	$125.3^{52.1}_{-44.5}$	$205.9^{84.9}_{-73.0}$	Lyα	2.0780	1.00	..
063	J0306385-000130	21.39	1.00	$15.8^{5.8}_{-5.0}$	$34.5^{12.3}_{-10.8}$	[OII]	0.4271	0.00	..
064	J0306387+000023	20.83	1.00	$10.0^{2.5}_{-2.1}$	$23.3^{5.7}_{-4.9}$	[OII]	0.2727	0.00	..
065	J0306388-000017	17.20	1.00	$2.6^{0.5}_{-0.5}$	$16.3^{3.3}_{-3.0}$	[OII]	0.1121	0.00	..
066	J0306388-000017	17.20	1.00	$0.5^{0.1}_{-0.1}$	$1.0^{0.3}_{-0.2}$	Hβ	0.1118	0.00	..
067	J0306389-000240	19.12	1.00	$2.9^{1.1}_{-0.9}$	$16.6^{6.4}_{-5.5}$	[OII]	0.1123	0.00	..
068	J0306388-000017	20.47	0.63	$26.3^{6.9}_{-7.0}$	$43.5^{10.7}_{-11.3}$	[OIII]5007	0.1113	0.00	..
069	J0306391+000124	20.87	1.00	$12.4^{3.2}_{-3.0}$	$22.7^{5.5}_{-5.4}$	[OII]	0.5231	0.00	..
070	J0306395+000335	20.25	0.33	$17.0^{6.6}_{-4.1}$	$34.2^{12.7}_{-8.1}$	[OII]	0.4269	0.00	..
071	J0306396+000344	16.09	1.00	$0.5^{0.1}_{-0.1}$	$0.9^{0.3}_{-0.2}$	Hδ	0.1060	0.00	J0306395+000343
072	J0306396+000344	16.09	1.00	$0.7^{0.2}_{-0.2}$	$1.4^{0.4}_{-0.3}$	[NeV]3426	0.1067	0.00	J0306395+000343
073	J0306396+000344	16.09	1.00	$1.7^{0.3}_{-0.3}$	$3.3^{0.6}_{-0.6}$	[OII]	0.1073	0.00	J0306395+000343
074	J0306396+000344	16.09	1.00	$1.9^{0.4}_{-0.3}$	$3.5^{0.7}_{-0.6}$	[NeIII]3869	0.1068	0.00	J0306395+000343
075	J0306396+000344	16.09	1.00	$4.0^{0.8}_{-0.7}$	$6.2^{1.1}_{-1.0}$	[OIII]4959	0.1071	0.00	J0306395+000343
076	J0306396+000344	16.09	1.00	$8.3^{1.6}_{-1.4}$	$13.3^{2.3}_{-2.2}$	Hβ	0.1072	0.00	J0306395+000343
077	J0306396+000344	16.09	1.00	$13.2^{2.5}_{-2.3}$	$20.2^{3.5}_{-3.3}$	[OIII]5007	0.1071	0.00	J0306395+000343
078	J0306396+000344	16.09	1.00	$2.5^{0.5}_{-0.4}$	$4.9^{1.0}_{-0.9}$	Hγ	0.1074	0.00	J0306395+000343
079	J0306401-000004	21.12	1.00	$10.2^{3.2}_{-2.5}$	$27.3^{8.1}_{-6.4}$	[OII]	0.3912	0.00	..
080	J0306400-000249	21.93	0.92	$34.7^{11.8}_{-10.1}$	$61.8^{20.6}_{-17.9}$	[OII]	0.3222	0.08	..
081	J0306407+000151	21.07	0.93	$5.6^{2.8}_{-1.8}$	$18.3^{9.0}_{-6.0}$	[OII]	0.3337	0.00	..
082	J0306407-000131	24.42	0.90	$232.5^{122.4}_{-83.3}$	$2845.6^{1000.0}_{-1422.8}$	Lyα	2.2498	1.00	..
083	J0306410+000023	21.00	1.00	$9.3^{2.3}_{-2.1}$	$22.0^{5.0}_{-4.7}$	[OII]	0.3716	0.00	..
084	J0306411-000250	24.06	0.55	$77.3^{35.5}_{-21.4}$	$160.4^{65.8}_{-41.6}$	Lyα	3.2445	1.00	..
085	J0306417+000108	19.53	0.99	$17.8^{6.6}_{-4.7}$	$37.1^{13.9}_{-9.9}$	MgII2798	0.3220	0.01	J0306417+000109
086	J0306417+000108	19.53	0.99	$9.4^{2.6}_{-2.3}$	$16.1^{4.5}_{-3.9}$	[NeV]3426	0.3339	0.01	J0306417+000109
087	J0306426+000019	21.90	1.00	$21.5^{5.2}_{-4.9}$	$45.3^{10.5}_{-10.1}$	[OII]	0.3568	0.00	..

Table 1.5 (cont'd)

HPS Index (1)	Counter-part (2)	Counter-part m_R* (3)	Counter-part P (4)	$EW_{R,rest}$* (Å) (5)	$EW_{interp,rest}$ (Å) (6)	Trans-ition (7)	z_{est} (8)	Lyα P (9)	X-ray counterpart (10)
088	J0306434+000032	19.49	0.92	$4.6^{1.1}_{-1.1}$	$19.7^{4.6}_{-4.7}$	[OII]	0.2830	0.00	..
089	J0306440-000129	24.28	0.02	$75.1^{23.6}_{-22.3}$	$124.5^{43.1}_{-38.0}$	Lyα	2.5368	0.02	..
090	J0306442+000349	21.29	0.95	$20.9^{5.6}_{-5.4}$	$50.4^{13.5}_{-13.0}$	[OII]	0.2790	0.03	..
091	J0306443+000046	23.41	0.98	$20.9^{8.9}_{-7.4}$	$42.0^{16.8}_{-14.7}$	Lyα	2.9964	1.00	..
092	J0306444+000146	23.33	0.98	$18.0^{7.2}_{-6.6}$	$29.7^{11.1}_{-10.8}$	Lyα	3.6741	1.00	..
093	..	..	0.98	$2196.6^{572.4}_{-662.6}$	$869.1^{226.5}_{-262.2}$	Lyα	2.2627	1.00	..
094	J0306463+000219	21.03	0.99	$68.9^{14.1}_{-13.1}$	$105.9^{19.7}_{-19.3}$	[OII]	0.5474	0.01	..
095	J0306465+000306	25.70	0.93	$307.5^{235.3}_{-134.3}$	$788.1^{1000.0}_{-393.6}$	Lyα	2.4521	1.00	..
096	J0306468+000024	20.02	1.00	$4.1^{1.1}_{-0.9}$	$10.8^{2.7}_{-2.3}$	[OII]	0.3915	0.00	..
097	J0306466+000221	21.05	0.99	$40.8^{12.7}_{-9.5}$	$75.0^{22.3}_{-17.1}$	[OII]	0.5481	0.01	..
098	J0306483-000260	19.52	1.00	$2.5^{0.9}_{-0.7}$	$8.4^{2.9}_{-2.3}$	[OII]	0.2909	0.00	..
099	J0306484+000017	24.75	0.55	$142.8^{63.9}_{-39.7}$	$401.3^{190.1}_{-114.5}$	Lyα	3.0047	1.00	..
100	J0306489-000059	19.95	0.96	$4.2^{1.2}_{-1.0}$	$10.4^{2.8}_{-2.5}$	[OII]	0.3642	0.00	..
101	J0306490-000101	21.14	0.68	$12.2^{3.4}_{-2.8}$	$26.9^{7.3}_{-6.2}$	[OII]	0.2826	0.00	..
102	J0306492-000015	22.42	0.65	$41.9^{11.9}_{-10.5}$	$95.2^{25.6}_{-23.2}$	[OII]	0.4246	0.00	..
103	J0306495+000123	21.67	1.00	$12.8^{4.2}_{-3.7}$	$27.4^{8.7}_{-7.8}$	[OII]	0.3567	0.00	..
104	J0306497-000315	21.30	1.00	$49.7^{10.4}_{-10.2}$	$65.0^{12.5}_{-12.9}$	[OIII]5007	0.1093	0.00	..
105	J0306497-000315	21.30	1.00	$26.5^{5.8}_{-6.2}$	$56.3^{12.3}_{-13.2}$	[OII]	0.1094	0.00	..
106	J0306497-000315	21.30	1.00	$24.1^{6.7}_{-6.7}$	$31.8^{8.4}_{-8.8}$	[OIII]4959	0.1092	0.00	..
107	J0306497-000315	21.30	1.00	$18.8^{6.1}_{-4.7}$	$25.3^{7.9}_{-6.2}$	Hβ	0.1093	0.00	..
108	J0306501+000204	19.44	1.00	$4.2^{1.1}_{-0.9}$	$11.3^{2.8}_{-2.3}$	[OII]	0.3714	0.00	..
109	J0306502-000215	22.84	0.96	$24.0^{9.2}_{-6.3}$	$48.1^{17.9}_{-12.4}$	Lyα	3.2045	1.00	..
110	J0306505-000119	21.42	0.99	$18.8^{5.3}_{-3.7}$	$36.0^{9.7}_{-6.7}$	[OII]	0.4120	0.01	..
111	J0306504+000140	23.85	0.60	$29.9^{11.1}_{-11.8}$	$39.3^{14.1}_{-15.5}$	Lyα	3.1793	1.00	..
112	J0306510+000133	19.92	0.69	$4.6^{1.5}_{-1.0}$	$17.4^{5.4}_{-3.7}$	[OII]	0.3709	0.00	..
113	J0306514+000103	21.95	0.99	$25.5^{7.8}_{-7.6}$	$55.6^{16.2}_{-16.4}$	[OII]	0.4122	0.01	..
114	J0306516-000128	19.40	1.00	$1.6^{1.8}_{-1.5}$	$3.0^{3.4}_{-2.7}$	Hβ	0.0949	0.00	..
115	J0306520-000236	20.19	0.99	$3.3^{1.2}_{-1.1}$	$5.5^{1.9}_{-1.9}$	[OIII]5007	0.1073	0.00	..
116	J0306520+000122	19.00	1.00	$1.9^{0.6}_{-0.5}$	$2.8^{0.9}_{-0.7}$	Hβ	0.1120	0.00	..

Table 1.5 (cont'd)

HPS Index (1)	Counter-part (2)	Counter-part m_R * (3)	Counter-part P (4)	$EW_{R,rest}$ * (Å) (5)	$EW_{interp,rest}$ (Å) (6)	Trans-ition (7)	z_{est} (8)	Lyα P (9)	X-ray counterpart (10)
117	J0306520+000122	19.00	1.00	$2.4^{0.7}_{-0.7}$	$3.5^{1.0}_{-1.0}$	[OIII]4959	0.1120	0.00	..
118	J0306520-000236	20.19	1.00	$6.8^{1.7}_{-1.4}$	$27.3^{6.9}_{-5.8}$	[OII]	0.1072	0.00	..
119	J0306520+000122	19.00	1.00	$11.7^{2.3}_{-2.1}$	$31.6^{6.3}_{-5.6}$	[OII]	0.1121	0.00	..
120	J0306526+000048	20.13	1.00	$7.4^{1.8}_{-1.8}$	$17.7^{3.9}_{-4.3}$	[OII]	0.3920	0.00	..
121	J0306528+000209	21.74	0.98	$8.7^{4.0}_{-2.9}$	$19.1^{8.5}_{-6.3}$	[OII]	0.3729	0.01	..
122	J0306533+000313	22.19	0.98	$34.8^{11.0}_{-10.5}$	$90.2^{28.5}_{-27.2}$	[OII]	0.2062	0.02	J0306535+000311
123	J0306536-000201	20.73	0.99	$29.4^{5.8}_{-5.1}$	$49.8^{8.8}_{-8.2}$	[OII]	0.4549	0.01	..
124	J0306538-000234	24.63	0.59	$58.2^{47.8}_{-27.9}$	$87.8^{57.7}_{-40.5}$	Lyα	3.7438	1.00	..
125	J0306553-000051	17.64	1.00	$3.6^{0.9}_{-0.9}$	$14.2^{3.5}_{-3.4}$	[OII]	0.1118	0.00	..
126	J0306554+000033	24.31	0.77	$461.7^{156.3}_{-109.9}$	$5461.0^{1000.0}_{-2730.5}$	Lyα	2.8276	1.00	..
127	J0306554+000333	24.09	0.95	$45.7^{25.4}_{-16.1}$	$87.2^{49.6}_{-30.9}$	Lyα	2.5358	1.00	..
128	J0306558+000103	20.00	1.00	$5.5^{1.6}_{-1.4}$	$15.7^{4.3}_{-3.9}$	[OII]	0.3485	0.00	..
129	J0306559+000212	21.12	0.99	$20.6^{4.6}_{-4.5}$	$46.0^{10.3}_{-10.1}$	[OII]	0.1377	0.01	..
130	J0306559+000052	20.20	0.98	$10.9^{2.7}_{-2.2}$	$27.2^{6.6}_{-5.4}$	[OII]	0.2826	0.02	..
131	J0306559+000212	21.12	1.00	$22.6^{6.3}_{-5.7}$	$29.4^{7.7}_{-7.2}$	[OIII]4959	0.1373	0.00	..
132	J0306558-000026	21.68	0.50	$42.9^{15.6}_{-15.3}$	$77.7^{27.3}_{-27.5}$	[OII]	0.4285	0.01	..
133	J0306558+000157	19.57	1.00	$2.2^{0.6}_{-0.7}$	$18.9^{5.2}_{-6.1}$	[OII]	0.2366	0.00	..
134	J0306559+000212	21.12	1.00	$38.6^{8.5}_{-7.5}$	$49.8^{10.1}_{-9.3}$	[OIII]5007	0.1373	0.00	..
135	J0306564+000304	22.15	0.99	$20.3^{8.2}_{-6.2}$	$43.6^{17.5}_{-13.3}$	[OII]	0.2920	0.01	..
136	J0306573-000303	21.57	0.97	$20.7^{5.0}_{-4.2}$	$39.7^{9.6}_{-8.0}$	[OII]	0.2688	0.03	..
137	J0306574-000001	21.00	0.98	$13.8^{6.7}_{-7.4}$	$33.1^{15.7}_{-17.7}$	[OII]	0.2503	0.02	..
138	J0306577-000139	19.60	1.00	$9.2^{1.8}_{-1.6}$	$26.4^{5.3}_{-4.7}$	[OII]	0.1027	0.00	..
139	J0306577-000139	19.60	1.00	$9.0^{1.9}_{-1.6}$	$13.5^{2.5}_{-2.3}$	[OIII]5007	0.1025	0.00	..
140	J0306577-000139	19.60	0.99	$5.6^{1.2}_{-1.1}$	$8.7^{1.7}_{-1.7}$	Hβ	0.1026	0.01	..
141	J0306577-000139	19.60	1.00	$2.7^{0.7}_{-0.7}$	$4.0^{1.0}_{-1.0}$	[OIII]4959	0.1026	0.00	..
142	J0306590-000235	23.34	0.62	$21.7^{8.4}_{-4.9}$	$49.6^{19.2}_{-11.3}$	Lyα	2.5800	0.70	..
143	J1000056+021608	21.05	0.99	$28.1^{3.4}_{-2.8}$	$46.1^{5.3}_{-4.3}$	[OII]	0.2365	0.01	..
144	J1000058+021949	26.50	0.52	$109.7^{93.2}_{-55.2}$	$446.7^{1000.0}_{-223.3}$	Lyα	2.7298	0.85	..
145	J1000062+021307	24.08	0.51	$154.6^{35.3}_{-21.6}$	$2380.9^{1000.0}_{-1190.5}$	Lyα	2.1751	1.00	..

Table 1.5 (cont'd)

HPS Index (1)	Counter-part (2)	Counter-part m_R* (3)	Counter-part P (4)	$EW_{R,rest}$* (Å) (5)	$EW_{interp,rest}$ (Å) (6)	Trans-ition (7)	z_{est} (8)	Lyα P (9)	X-ray counterpart (10)
146	J1000064+021803	21.87	0.67	$16.5^{4.2}_{-3.2}$	$30.0^{7.2}_{-5.5}$	[OII]	0.3084	0.12	..
147	J1000070+021327	20.24	1.00	$11.5^{1.5}_{-1.2}$	$24.3^{3.2}_{-2.5}$	[OII]	0.2168	0.00	..
148	J1000071+021926	24.77	0.43	$41.9^{14.7}_{-14.0}$	$180.5^{74.1}_{-62.4}$	Lyα	3.4176	1.00	J100007.1+021925
149	J1000071+021707	22.85	0.88	$57.1^{15.6}_{-11.7}$	$106.7^{27.6}_{-21.0}$	[OII]	0.3404	0.12	..
150	J1000073+021455	23.79	0.72	$50.6^{13.7}_{-12.2}$	$91.8^{23.9}_{-21.8}$	Lyα	2.9011	1.00	..
151	J1000074+021847	21.41	0.98	$17.3^{3.9}_{-2.7}$	$27.7^{6.0}_{-4.3}$	[OII]	0.4379	0.02	..
152	J1000074+021721	19.83	0.99	$5.6^{0.8}_{-0.7}$	$14.6^{1.8}_{-1.7}$	[OII]	0.2674	0.01	..
153	J1000074+021245	24.88	0.89	$143.9^{35.5}_{-32.1}$	$687.2^{756.1}_{-260.2}$	Lyα	2.7081	1.00	..
154	J1000076+021518	25.98	0.20	$138.0^{74.6}_{-46.7}$	$280.8^{422.5}_{-120.9}$	Lyα	2.8726	0.93	..
155	J1000078+021737	22.05	0.97	$9.0^{5.6}_{-3.4}$	$19.3^{11.9}_{-7.2}$	[OII]	0.3259	0.03	..
156	J1000082+021542	20.67	0.90	$8.8^{1.4}_{-1.3}$	$22.0^{2.9}_{-2.9}$	[OII]	0.2821	0.10	..
157	J1000085+021522	19.93	0.71	$8.9^{1.2}_{-0.9}$	$26.1^{2.9}_{-2.2}$	[OII]	0.2501	0.29	..
158	J1000086+021542	20.43	0.99	$9.4^{1.5}_{-1.1}$	$29.2^{4.2}_{-3.0}$	[OII]	0.0929	0.01	..
159	J1000086+021542	20.43	0.99	$7.1^{1.6}_{-0.9}$	$8.8^{1.9}_{-1.1}$	[OIII]5007	0.0927	0.00	..
160	J1000086+021739	27.35	0.61	$698.3^{1000.0}_{-333.5}$	$1034.3^{1000.0}_{-559.0}$	Lyα	2.4346	1.00	..
161	J1000087+021250	23.40	0.81	$52.0^{8.1}_{-7.0}$	$101.4^{14.3}_{-12.8}$	Lyα	3.2515	1.00	..
162	J1000088+021529	24.45	0.20	$214.4^{52.8}_{-39.0}$	$564.3^{165.4}_{-114.8}$	Lyα	2.4284	1.00	J100008.8+021528
163	J1000089+021420	20.78	0.95	$13.8^{2.2}_{-1.4}$	$23.7^{3.4}_{-2.2}$	[OII]	0.3731	0.05	..
164	J1000089+021721	24.32	0.31	$63.3^{35.6}_{-32.3}$	$126.4^{70.5}_{-64.5}$	Lyα	2.4518	1.00	..
165	J1000094+021627	22.25	0.93	$17.5^{4.7}_{-5.2}$	$40.4^{10.9}_{-12.1}$	[OII]	0.2186	0.07	..
166	J1000093+021535	21.49	1.00	$17.4^{2.5}_{-2.1}$	$29.6^{3.6}_{-3.2}$	[OII]	0.3728	0.00	..
167	J1000095+021225	21.37	0.99	$13.0^{2.2}_{-2.1}$	$27.2^{4.0}_{-4.1}$	[OII]	0.3439	0.01	..
168	J1000098+021454	24.98	0.78	$207.7^{35.6}_{-29.1}$	$462.3^{126.8}_{-86.7}$	Lyα	3.4496	1.00	..
169	J1000098+021241	20.75	1.00	$13.6^{1.8}_{-1.5}$	$27.1^{3.1}_{-2.6}$	[OII]	0.2624	0.00	..
170	J1000101+021549	21.42	0.98	$7.5^{2.3}_{-1.4}$	$23.2^{6.9}_{-4.0}$	[OII]	0.2818	0.02	..
171	J1000101+021659	22.59	0.91	$41.6^{7.4}_{-6.3}$	$88.2^{14.0}_{-12.5}$	[OII]	0.2829	0.08	..
172	J1000101+021659	22.59	0.90	$9.6^{4.7}_{-4.5}$	$16.9^{8.1}_{-7.8}$	[NeIII]3869	0.2826	0.09	..
173	J1000104+021323	20.88	0.88	$8.3^{1.3}_{-1.2}$	$14.8^{2.0}_{-2.1}$	[OII]	0.3796	0.01	..
174	J1000110+021227	26.34	0.45	$67.2^{77.3}_{-49.3}$	$146.4^{156.9}_{-107.2}$	Lyα	3.4465	0.73	..

Table 1.5 (cont'd)

HPS Index (1)	Counter-part (2)	Counter-part m_R* (3)	Counter-part P (4)	$EW_{R,rest}$* (Å) (5)	$EW_{interp,rest}$ (Å) (6)	Trans-ition (7)	z_{est} (8)	Lyα P (9)	X-ray counterpart (10)
175	J1000113+021432	21.01	0.99	$17.3^{2.3}_{-2.2}$	$37.7^{4.1}_{-4.3}$	[OII]	0.2824	0.01	..
176	J1000115+021741	22.34	0.91	$48.1^{10.6}_{-7.6}$	$64.4^{13.7}_{-9.9}$	[OII]	0.4911	0.09	..
177	J1000114+021348	21.99	0.85	$20.2^{3.9}_{-3.9}$	$32.8^{5.8}_{-6.1}$	[OII]	0.3808	0.00	..
178	J1000115+021513	23.27	0.64	$38.5^{14.4}_{-10.4}$	$59.7^{22.3}_{-16.1}$	[OII]	0.4717	0.36	..
179	J1000119+021340	22.67	0.86	$14.7^{6.2}_{-4.0}$	$26.6^{11.0}_{-7.0}$	[OII]	0.3442	0.08	..
180	J1000121+022004	24.63	0.70	$46.5^{31.9}_{-26.2}$	$54.7^{36.2}_{-30.6}$	[OII]	0.3789	0.21	..
181	J1000123+021430	20.92	0.88	$16.4^{2.5}_{-2.0}$	$33.5^{4.3}_{-3.6}$	[OII]	0.2751	0.12	..
182	J1000124+021416	25.04	0.60	$124.1^{35.2}_{-28.3}$	$180.8^{49.4}_{-40.5}$	Lyα	2.4337	1.00	..
183	J1000125+021753	25.26	0.27	$152.4^{134.5}_{-63.6}$	$459.5^{672.7}_{-220.6}$	Lyα	2.1624	1.00	..
184	J1000125+021754	25.80	0.44	$73.2^{82.5}_{-40.2}$	$108.4^{99.0}_{-57.8}$	Lyα	3.2058	0.95	..
185	J1000126+021307	21.58	0.99	$10.9^{3.0}_{-2.3}$	$25.1^{6.7}_{-5.3}$	[OII]	0.1864	0.01	..
186	J1000127+021229	20.52	0.99	$22.4^{2.8}_{-2.6}$	$54.8^{6.2}_{-6.1}$	[OII]	0.1864	0.01	..
187	J1000127+021229	20.53	1.00	$5.7^{2.1}_{-1.2}$	$6.5^{2.3}_{-1.3}$	Hβ	0.1861	0.00	..
188	J1000131+022023	19.89	0.98	$3.6^{1.1}_{-0.7}$	$8.5^{2.4}_{-1.6}$	[OII]	0.3776	0.00	..
189	J1000132+021855	24.99	0.64	$60.2^{42.5}_{-31.6}$	$85.3^{59.2}_{-44.6}$	Lyα	2.4515	0.90	..
190	..	..	0.50	$643.6^{156.0}_{-194.0}$	$643.6^{156.0}_{-194.0}$	Lyα	2.2742	1.00	..
191	J1000134+021958	21.61	0.99	$30.8^{4.6}_{-3.4}$	$42.9^{6.2}_{-4.5}$	[OII]	0.4771	0.01	..
192	J1000135+021317	22.02	0.99	$25.3^{5.2}_{-5.6}$	$44.1^{8.2}_{-9.4}$	[OII]	0.3130	0.01	..
193	J1000138+021416	21.67	0.99	$15.7^{3.4}_{-2.7}$	$25.5^{5.4}_{-4.3}$	[OII]	0.4789	0.01	..
194	J1000142+021426	23.98	0.73	$106.0^{14.8}_{-12.0}$	$213.8^{37.5}_{-28.7}$	Lyα	2.2882	1.00	..
195	J1000146+021700	20.51	1.00	$8.8^{1.6}_{-1.0}$	$20.1^{3.6}_{-2.3}$	[OII]	0.2172	0.00	..
196	J1000146+021628	24.44	0.39	$70.9^{14.1}_{-15.6}$	$139.2^{34.6}_{-32.8}$	Lyα	2.6534	1.00	..
197	J1000148+021746	25.80	0.33	$174.0^{219.0}_{-77.6}$	$258.9^{317.6}_{-114.9}$	Lyα	2.4419	1.00	..
198	J1000149+021223	21.64	0.95	$18.2^{3.7}_{-3.1}$	$39.5^{7.3}_{-6.3}$	[OII]	0.2653	0.05	..
199	J1000155+021412	21.03	0.98	$14.3^{2.1}_{-2.0}$	$30.8^{4.4}_{-4.3}$	[OII]	0.2081	0.02	..
200	J1000156+021617	20.51	0.96	$3.4^{1.3}_{-1.0}$	$4.3^{1.5}_{-1.3}$	[OII]	0.5618	0.01	..
201	J1000161+021918	22.00	1.00	$42.6^{7.3}_{-7.0}$	$44.4^{7.1}_{-7.0}$	[OII]	0.5045	0.00	..
202	J1000163+021839	21.96	0.92	$33.9^{5.4}_{-5.8}$	$52.3^{7.9}_{-8.8}$	[OII]	0.4275	0.08	..
203	J1000162+021360	19.17	1.00	$1.7^{0.3}_{-0.3}$	$7.6^{1.2}_{-1.2}$	[OII]	0.1862	0.00	..

Table 1.5 (cont'd)

HPS Index (1)	Counter-part (2)	Counter-part m_R * (3)	Counter-part P (4)	$EW_{R,rest}$ * (Å) (5)	$EW_{interp,rest}$ (Å) (6)	Trans-ition (7)	z_{est} (8)	Lyα P (9)	X-ray counterpart (10)
204	J1000162+021435	19.36	1.00	$3.6^{0.5}_{-0.4}$	$8.0^{0.8}_{-0.8}$	[OII]	0.3449	0.00	..
205	J1000165+022031	26.04	0.69	$312.1^{170.6}_{-106.6}$	$1057.5^{1000.0}_{-528.8}$	Lyα	2.9081	1.00	..
206	J1000167+021619	19.85	0.91	$0.8^{0.4}_{-0.5}$	$1.9^{1.0}_{-1.1}$	[OII]	0.2168	0.00	..
207	J1000168+021821	26.18	0.57	$147.0^{106.1}_{-58.3}$	$173.5^{221.9}_{-77.2}$	Lyα	2.7091	1.00	..
208	J1000167+021219	19.98	1.00	$4.2^{0.8}_{-0.8}$	$12.4^{2.2}_{-2.2}$	[OII]	0.1856	0.00	..
209	J1000170+021239	20.52	1.00	$16.3^{2.5}_{-1.8}$	$32.1^{4.5}_{-3.3}$	[OII]	0.1867	0.00	..
210	J1000171+021614	24.90	0.24	$58.3^{25.2}_{-19.8}$	$70.5^{25.4}_{-22.8}$	Lyα	3.4874	0.36	..
211	J1000173+021737	22.60	0.99	$23.7^{9.2}_{-8.2}$	$38.9^{14.9}_{-13.4}$	[OII]	0.4379	0.01	..
212	J1000174+022042	22.59	0.99	$16.9^{5.6}_{-6.2}$	$26.1^{8.5}_{-9.5}$	[OII]	0.4793	0.01	..
213	J1000174+021657	24.55	0.20	$50.0^{15.9}_{-12.8}$	$80.6^{23.6}_{-19.9}$	Lyα	3.2996	0.91	..
214	J1000175+021905	27.09	0.45	$327.9^{308.1}_{-145.9}$	$454.3^{434.1}_{-202.8}$	Lyα	3.2955	0.99	..
215	J1000177+021932	18.79	0.97	$1.1^{0.3}_{-0.3}$	$5.8^{1.5}_{-1.4}$	[OII]	0.2216	0.03	..
216	J1000179+021760	20.94	0.94	$17.7^{2.3}_{-2.2}$	$35.1^{3.7}_{-3.9}$	[OII]	0.2795	0.02	..
217	J1000178+022018	20.25	1.00	$15.7^{2.3}_{-1.8}$	$25.5^{3.5}_{-2.9}$	[OII]	0.4379	0.00	..
218	J1000179+021631	20.92	0.99	$12.9^{1.9}_{-1.8}$	$24.1^{3.0}_{-3.1}$	[OII]	0.3601	0.01	..
219	J1000182+021817	19.02	0.99	$10.8^{1.3}_{-1.1}$	$33.8^{3.1}_{-2.7}$	[OII]	0.1231	0.01	..
220	J1000182+021817	19.02	1.00	$4.0^{0.7}_{-0.8}$	$5.4^{0.9}_{-1.1}$	Hβ	0.1230	0.00	..
221	J1000182+021817	19.02	1.00	$7.5^{1.0}_{-0.9}$	$9.4^{1.1}_{-1.0}$	[OIII]5007	0.1231	0.00	..
222	J1000182+021551	23.55	0.98	$123.0^{15.3}_{-13.6}$	$278.1^{41.0}_{-34.5}$	Lyα	2.9430	1.00	J100018.2+021551
223	J1000187+021460	25.46	0.31	$268.2^{157.1}_{-86.7}$	$1919.9^{1000.0}_{-959.9}$	Lyα	2.3057	1.00	..
224	J1000189+021810	20.84	0.97	$6.7^{1.8}_{-1.4}$	$10.3^{2.6}_{-2.2}$	[OII]	0.5023	0.03	..
225	J1000189+021425	20.06	1.00	$8.3^{1.0}_{-0.9}$	$18.9^{1.7}_{-1.6}$	[OII]	0.1243	0.00	..
226	J1000189+021425	20.06	1.00	$8.7^{1.1}_{-1.0}$	$9.7^{1.0}_{-1.0}$	[OIII]5007	0.1241	0.00	..
227	J1000189+021425	20.06	1.00	$3.0^{0.8}_{-0.6}$	$3.5^{0.9}_{-0.6}$	Hβ	0.1243	0.00	..
228	J1000195+022024	20.95	0.95	$9.4^{2.8}_{-2.1}$	$17.0^{5.0}_{-3.7}$	[OII]	0.4758	0.05	..
229	J1000194+021312	23.37	0.87	$50.7^{7.8}_{-7.5}$	$71.3^{9.2}_{-9.6}$	Lyα	3.0393	1.00	..
230	J1000205+021243	22.04	0.99	$36.9^{7.8}_{-6.4}$	$55.0^{11.2}_{-9.3}$	[OII]	0.4267	0.01	..
231	J1000208+021918	26.02	0.74	$400.3^{168.7}_{-118.3}$	$1633.7^{1000.0}_{-816.9}$	Lyα	2.7215	1.00	..
232	J1000211+021930	20.46	0.97	$22.8^{2.9}_{-2.3}$	$37.7^{4.0}_{-3.3}$	[OII]	0.3812	0.03	..

Table 1.5 (cont'd)

HPS Index (1)	Counter-part (2)	Counter-part m_R* (3)	Counter-part P (4)	$EW_{R,rest}$* (Å) (5)	$EW_{interp,rest}$ (Å) (6)	Trans-ition (7)	z_{est} (8)	Lyα P (9)	X-ray counterpart (10)
233	J1000214+021451	19.66	0.99	$8.6^{1.0}_{-0.9}$	$17.1^{1.4}_{-1.4}$	[OII]	0.3116	0.01	..
234	J1000215+021350	23.37	0.63	$136.8^{26.0}_{-20.6}$	$133.8^{25.4}_{-20.1}$	[OIII]5007	0.0917	0.37	..
235	J1000218+021220	19.69	0.97	$3.9^{0.8}_{-0.6}$	$45.6^{8.7}_{-7.1}$	[OII]	0.1317	0.03	..
236	J1000219+021237	21.22	0.95	$8.7^{4.5}_{-3.8}$	$9.3^{4.7}_{-4.0}$	[OIII]5007	0.1222	0.00	..
237	J1000219+021237	21.21	0.94	$8.5^{2.8}_{-2.0}$	$16.7^{5.4}_{-3.8}$	[OII]	0.1230	0.06	..
238	J1000231+021755	19.70	0.81	$5.2^{1.1}_{-0.8}$	$15.9^{3.2}_{-2.3}$	[OII]	0.3610	0.10	..
239	J1000230+021313	18.17	0.95	$8.0^{0.9}_{-0.7}$	$11.4^{1.1}_{-0.9}$	[OII]	0.1859	0.05	J100022.9+021313
240	J1000230+021313	18.17	0.98	$1.1^{0.2}_{-0.2}$	$1.3^{0.2}_{-0.2}$	Hγ	0.1855	0.00	J100022.9+021313
241	J1000230+021313	18.17	0.97	$2.9^{0.4}_{-0.4}$	$3.9^{0.5}_{-0.5}$	[NeIII]3869	0.1849	0.00	J100022.9+021313
242	J1000230+021313	18.17	0.99	$6.7^{0.8}_{-0.6}$	$6.8^{0.6}_{-0.5}$	Hβ	0.1858	0.00	J100022.9+021313
243	J1000230+021513	21.98	0.96	$17.6^{3.3}_{-2.7}$	$32.0^{5.3}_{-4.4}$	[OII]	0.3205	0.04	..
244	J1000238+021310	26.02	0.25	$111.3^{73.5}_{-47.7}$	$114.1^{89.3}_{-50.6}$	Lyα	2.0996	1.00	..
245	J1000239+021443	22.36	0.97	$19.4^{5.2}_{-3.7}$	$26.2^{6.7}_{-4.7}$	[OII]	0.5326	0.03	..
246	J1000239+021351	22.22	0.98	$11.9^{6.4}_{-3.6}$	$22.5^{11.9}_{-6.7}$	[OII]	0.3014	0.02	..
247	J1000244+021358	20.91	0.99	$6.8^{2.2}_{-0.9}$	$15.5^{4.9}_{-2.0}$	[OII]	0.1855	0.01	..
248	J1000264+021325	21.04	0.49	$21.7^{2.8}_{-2.4}$	$54.7^{6.0}_{-5.6}$	[OII]	0.3720	0.32	..
249	J1000267+021741	26.24	0.39	$134.9^{90.1}_{-55.2}$	$329.8^{236.0}_{-136.9}$	Lyα	3.2731	0.96	..
250	J1000268+021302	23.05	0.88	$23.0^{8.3}_{-9.1}$	$33.9^{11.9}_{-13.4}$	[OII]	0.3726	0.12	..
251	J1000272+021731	24.81	0.58	$169.0^{58.0}_{-46.0}$	$498.5^{300.0}_{-167.5}$	Lyα	2.2851	1.00	..
252	J1000275+021705	19.39	1.00	$10.6^{1.4}_{-1.2}$	$20.5^{2.5}_{-2.2}$	[OII]	0.4400	0.00	..
253	J1000275+021551	24.33	0.75	$62.3^{13.4}_{-14.3}$	$91.6^{18.3}_{-20.6}$	Lyα	3.1829	1.00	..
254	J1000279+021258	21.85	1.00	$17.3^{3.1}_{-2.1}$	$24.9^{4.3}_{-3.0}$	[OII]	0.4287	0.00	..
255	J1000283+021906	21.71	0.99	$14.2^{3.4}_{-2.8}$	$36.7^{8.5}_{-7.1}$	[OII]	0.2357	0.01	..
256	J1000283+021758	25.26	0.84	$188.3^{66.2}_{-43.8}$	$271.4^{96.9}_{-63.8}$	Lyα	2.4907	1.00	..
257	J1000284+021736	21.84	0.97	$5.4^{2.1}_{-2.5}$	$11.1^{4.3}_{-5.2}$	[OII]	0.2829	0.02	..
258	J1000285+021756	23.86	0.75	$56.6^{8.2}_{-10.0}$	$137.5^{25.9}_{-26.6}$	Lyα	2.8101	1.00	..
259	J1000286+021443	22.16	0.43	$10.1^{7.4}_{-5.3}$	$14.2^{10.2}_{-7.5}$	[OII]	0.5293	0.01	..
260	J1000287+021857	21.45	0.94	$12.2^{3.1}_{-3.0}$	$27.9^{6.6}_{-6.8}$	[OII]	0.1063	0.06	..
261	J1000286+021749	23.76	0.87	$193.4^{38.9}_{-21.9}$	$536.7^{157.8}_{-92.4}$	Lyα	2.0960	1.00	J100028.6+021745

Table 1.5 (cont'd)

HPS Index (1)	Counter-part (2)	Counter-part m_R* (3)	Counter-part P (4)	$EW_{R,rest}$* (Å) (5)	$EW_{interp,rest}$ (Å) (6)	Trans-ition (7)	z_{est} (8)	Lyα P (9)	X-ray counterpart (10)
262	J1000287+021857	21.46	0.98	$6.8^{2.5}_{-2.1}$	$7.6^{2.7}_{-2.4}$	[OIII]5007	0.1061	0.02	..
263	J1000291+021408	24.17	0.89	$52.4^{18.9}_{-17.1}$	$66.3^{22.9}_{-21.4}$	Lyα	2.4323	1.00	..
264	J1000292+021858	20.09	1.00	$4.8^{1.0}_{-0.7}$	$10.5^{1.9}_{-1.4}$	[OII]	0.3583	0.00	..
265	J1000293+021501	19.40	1.00	$6.7^{1.1}_{-0.8}$	$15.9^{2.4}_{-1.8}$	[OII]	0.2493	0.00	..
266	..	..	0.01	$1441.3^{200.4}_{-196.2}$	$1441.3^{200.4}_{-196.2}$	Lyα	2.1971	1.00	..
267	J1000303+021844	19.28	1.00	$1.0^{0.3}_{-0.3}$	$5.6^{1.9}_{-1.4}$	[OII]	0.2184	0.00	J100030.1+021845
268	J1000306+021735	20.15	1.00	$7.6^{1.0}_{-0.8}$	$18.5^{2.0}_{-1.6}$	[OII]	0.2796	0.00	..
269	J1000306+021743	25.37	0.90	$94.6^{39.1}_{-23.6}$	$133.4^{56.6}_{-33.9}$	Lyα	2.5657	1.00	..
270	J1000306+021303	22.74	0.99	$21.2^{9.1}_{-5.7}$	$28.1^{11.7}_{-7.4}$	[OII]	0.5246	0.01	..
271	J1000314+021306	20.39	0.99	$3.4^{0.7}_{-0.7}$	$11.7^{2.5}_{-2.4}$	[OII]	0.2194	0.01	..
272	J1000317+021758	22.57	0.91	$35.7^{8.1}_{-7.0}$	$51.9^{11.7}_{-10.2}$	[OII]	0.4713	0.09	..
273	..	..	0.15	$374.5^{167.3}_{-115.7}$	$374.5^{167.3}_{-115.7}$	Lyα	3.6361	1.00	..
274	J1000321+021911	24.38	0.98	$51.3^{13.0}_{-8.8}$	$95.5^{24.9}_{-16.7}$	Lyα	2.8693	1.00	..
275	J1000326+021552	22.14	0.89	$30.8^{9.4}_{-9.3}$	$74.0^{21.9}_{-22.2}$	[OII]	0.2476	0.11	..
276	J1000327+021360	21.41	0.88	$5.4^{1.9}_{-1.8}$	$11.4^{4.0}_{-3.7}$	[OII]	0.1869	0.01	..
277	J1000329+021356	19.84	0.99	$1.4^{0.4}_{-0.4}$	$2.0^{0.5}_{-0.5}$	Hγ	0.1221	0.00	..
278	J1000329+021356	19.84	0.99	$14.6^{1.7}_{-1.4}$	$29.9^{2.5}_{-2.2}$	[OII]	0.1226	0.01	..
279	J1000329+021356	19.87	0.99	$34.8^{4.0}_{-3.3}$	$38.1^{3.6}_{-3.1}$	[OIII]5007	0.1223	0.01	..
280	J1000329+021356	19.84	0.99	$7.8^{1.0}_{-1.0}$	$8.6^{1.1}_{-1.1}$	Hβ	0.1224	0.00	..
281	J1000329+021356	19.84	0.99	$1.7^{0.5}_{-0.4}$	$3.1^{0.8}_{-0.8}$	Hδ	0.0585	0.00	..
282	J1000331+021531	21.48	0.99	$22.3^{3.5}_{-3.9}$	$42.4^{5.7}_{-7.0}$	[OII]	0.3214	0.01	..
283	J1000333+021825	24.20	0.94	$61.8^{11.7}_{-10.0}$	$108.1^{19.3}_{-16.9}$	Lyα	3.2996	1.00	..
284	J1000335+021308	19.84	1.00	$3.2^{0.6}_{-0.6}$	$7.3^{1.4}_{-1.2}$	[OII]	0.3015	0.00	..
285	J1000335+021615	20.63	1.00	$13.8^{2.0}_{-1.5}$	$23.5^{3.3}_{-2.5}$	[OII]	0.4405	0.00	..
286	J1000340+021316	24.48	0.54	$77.5^{1000.0}_{-39.0}$	$81.4^{1000.0}_{-40.7}$	Lyα	2.2293	0.61	..
287	J1000349+021744	26.61	0.33	$155.2^{128.3}_{-83.6}$	$248.3^{165.6}_{-131.3}$	Lyα	3.3170	1.00	..
288	J1000351+021749	24.39	0.89	$37.3^{9.3}_{-10.7}$	$50.3^{11.9}_{-14.2}$	Lyα	3.0398	1.00	..
289	J1000351+021806	23.37	0.63	$68.4^{20.2}_{-18.7}$	$146.0^{41.9}_{-39.6}$	[OII]	0.4046	0.37	..
290	J1000355+021839	19.91	1.00	$7.6^{1.5}_{-1.2}$	$17.0^{3.2}_{-2.7}$	[OII]	0.4762	0.00	..

Table 1.5 (cont'd)

HPS Index (1)	Counter-part (2)	Counter-part $\mathrm{m_R}^*$ (3)	Counter-part P (4)	$\mathrm{EW_{R,rest}}^*$ (Å) (5)	$\mathrm{EW_{interp,rest}}$ (Å) (6)	Trans-ition (7)	z_{est} (8)	Lyα P (9)	X-ray counterpart (10)
291	J1000356+021222	22.12	0.94	$33.3^{8.7}_{-6.4}$	$71.3^{17.6}_{-13.2}$	[OII]	0.3595	0.06	..
292	J1000357+021858	24.83	0.41	$135.7^{29.4}_{-21.7}$	$285.9^{108.1}_{-64.9}$	Lyα	2.8715	1.00	..
293	J1000358+021900	22.83	0.88	$48.7^{10.1}_{-8.2}$	$82.8^{15.8}_{-13.2}$	[OII]	0.3533	0.12	..
294	J1000360+021526	21.58	0.98	$46.0^{11.3}_{-7.3}$	$72.2^{16.7}_{-10.8}$	[OII]	0.3718	0.02	..
295	J1000363+021318	19.86	1.00	$3.3^{0.7}_{-0.6}$	$9.8^{2.2}_{-1.8}$	[OII]	0.1946	0.00	..
296	J1000368+021310	24.99	0.23	$57.1^{31.6}_{-15.7}$	$80.8^{47.0}_{-23.1}$	Lyα	2.8371	0.47	..
297	J1000371+021508	20.59	0.97	$18.7^{3.9}_{-2.8}$	$40.8^{7.8}_{-5.8}$	[OII]	0.2629	0.03	..
298	J1000370+021334	19.48	1.00	$1.2^{0.5}_{-0.3}$	$3.2^{1.1}_{-0.7}$	[OII]	0.3601	0.00	..
299	J1000374+021612	21.79	0.99	$25.5^{4.4}_{-5.4}$	$58.7^{9.8}_{-12.3}$	[OII]	0.2081	0.01	..
300	J1000375+021253	19.79	1.00	$4.9^{0.7}_{-0.7}$	$12.4^{1.4}_{-1.5}$	[OII]	0.1159	0.00	..
301	J1000376+021848	21.35	1.00	$15.3^{2.3}_{-2.2}$	$23.6^{3.4}_{-3.3}$	[OII]	0.4409	0.00	..
302	J1000387+021805	22.28	0.96	$21.6^{6.1}_{-5.6}$	$35.8^{9.9}_{-9.1}$	[OII]	0.4117	0.04	..
303	J1000393+021246	20.92	0.99	$10.6^{2.2}_{-2.2}$	$27.8^{5.5}_{-5.7}$	[OII]	0.1448	0.01	..
304	J1000393+021246	20.94	0.63	$20.2^{4.3}_{-4.5}$	$23.7^{4.7}_{-5.1}$	[OIII]5007	0.1443	0.37	..
305	J1000395+021321	21.06	0.99	$17.3^{2.8}_{-2.2}$	$31.9^{4.5}_{-3.5}$	[OII]	0.3249	0.01	..
306	J1000396+021339	24.07	0.72	$75.6^{14.6}_{-19.0}$	$90.4^{15.6}_{-22.2}$	Lyα	2.4390	1.00	..
307	J1000400+021804	20.86	1.00	$7.9^{1.9}_{-2.0}$	$15.5^{3.7}_{-4.0}$	[OII]	0.4406	0.00	..
308	J1000401+021251	22.11	1.00	$24.8^{5.6}_{-6.0}$	$26.6^{5.7}_{-6.4}$	[OII]	0.5086	0.00	..
309	J1000408+021832	22.44	0.98	$20.9^{8.2}_{-6.6}$	$37.9^{14.5}_{-11.8}$	Hδ	0.2623	0.02	..
310	J1000407+021741	24.92	0.72	$54.7^{18.7}_{-13.7}$	$79.5^{24.0}_{-18.6}$	Lyα	3.0703	0.98	..
311	J1000408+021832	22.44	0.99	$21.2^{6.1}_{-5.7}$	$37.0^{10.6}_{-10.0}$	Hγ	0.2623	0.01	..
312	J1000408+021832	22.44	0.97	$18.0^{8.6}_{-5.4}$	$34.3^{16.1}_{-10.2}$	[NeIII]3869	0.2622	0.03	..
313	J1000408+021823	22.75	0.98	$13.4^{6.9}_{-5.4}$	$23.9^{12.3}_{-9.7}$	Lyα	2.0975	1.00	..
314	..	..	0.97	$435.4^{173.4}_{-87.7}$	$435.4^{173.4}_{-87.7}$	Lyα	2.6312	1.00	..
315	J1000415+021817	24.35	0.68	$26.3^{9.5}_{-7.6}$	$32.3^{11.2}_{-9.1}$	Lyα	3.0717	1.00	..
316	J1000429+021631	24.12	0.42	$50.5^{16.9}_{-11.6}$	$74.3^{25.2}_{-17.2}$	Lyα	2.8073	0.47	..
317	J1000430+021845	23.08	0.98	$54.8^{12.7}_{-12.0}$	$62.7^{14.3}_{-13.6}$	[OII]	0.4784	0.02	..
318	J1000443+021558	23.69	0.32	$42.7^{13.7}_{-15.9}$	$74.5^{22.9}_{-27.6}$	Lyα	2.4558	0.67	..
319	J1000443+021656	21.12	1.00	$17.3^{2.4}_{-2.5}$	$27.4^{3.6}_{-3.8}$	[OII]	0.4413	0.00	..

Table 1.5 (cont'd)

HPS Index (1)	Counter-part (2)	Counter-part m_R* (3)	Counter-part P (4)	$EW_{R,rest}$* (Å) (5)	$EW_{interp,rest}$ (Å) (6)	Trans-ition (7)	z_{est} (8)	Lyα P (9)	X-ray counterpart (10)
320	J1000443+021626	20.23	0.98	$10.9^{1.4}_{-1.3}$	$15.9^{2.0}_{-1.9}$	[OII]	0.4616	0.00	..
321	J1000445+021829	21.90	0.74	$18.2^{4.7}_{-2.6}$	$35.7^{8.7}_{-4.7}$	[OII]	0.3429	0.07	..
322	J1000446+021830	21.14	0.84	$8.2^{2.4}_{-1.8}$	$27.9^{8.0}_{-5.8}$	[OII]	0.3570	0.08	..
323	J1000453+021822	19.88	0.89	$8.5^{1.3}_{-1.0}$	$9.9^{1.4}_{-1.0}$	[OIII]5007	0.1220	0.11	..
324	J1000453+021822	19.87	0.90	$4.2^{1.1}_{-1.0}$	$5.1^{1.3}_{-1.2}$	Hβ	0.1221	0.10	..
325	J1000453+021822	19.87	0.91	$2.9^{1.5}_{-0.9}$	$3.5^{1.7}_{-1.1}$	[OIII]4959	0.1223	0.09	..
326	J1000453+021822	19.87	0.97	$9.6^{1.3}_{-1.0}$	$24.9^{2.7}_{-2.2}$	[OII]	0.1222	0.03	..
327	..	..	0.04	$523.2^{219.5}_{-201.6}$	$523.2^{219.5}_{-201.6}$	Lyα	2.2527	0.10	..
328	J1000465+021913	22.11	0.93	$26.5^{7.3}_{-4.9}$	$40.3^{11.0}_{-7.4}$	[OII]	0.4711	0.07	..
329	J1000472+021760	20.22	1.00	$9.9^{1.9}_{-1.5}$	$16.8^{2.8}_{-2.4}$	[OII]	0.5102	0.00	..
330	J1000473+021711	22.55	0.95	$36.0^{13.1}_{-10.9}$	$68.7^{24.3}_{-20.5}$	[OII]	0.1848	0.05	..
331	J1000473+021716	21.28	0.98	$6.2^{3.5}_{-2.0}$	$14.0^{7.9}_{-4.6}$	[OII]	0.4410	0.02	..
332	J1236141+621147	20.46	0.99	$11.0^{2.0}_{-1.4}$	$25.4^{4.0}_{-2.8}$	[OII]	0.2859	0.01	..
333	J1236140+621415	20.16	1.00	$3.1^{2.9}_{-2.1}$	$9.5^{8.9}_{-6.5}$	[OII]	0.2071	0.00	..
334	..	..	0.00	$832.4^{180.6}_{-149.5}$	$912.6^{198.0}_{-163.9}$	Lyα	2.8499	1.00	J1236150+621027
335	J1236159+621237	19.58	1.00	$10.3^{1.2}_{-1.0}$	$23.4^{2.1}_{-1.8}$	[OII]	0.2854	0.00	..
336	J1236160+621008	20.70	1.00	$16.8^{2.4}_{-1.9}$	$35.2^{4.2}_{-3.4}$	[OII]	0.3372	0.00	..
337	J1236167+621310	23.53	0.89	$58.2^{22.6}_{-15.7}$	$93.4^{35.8}_{-25.0}$	[OII]	0.4370	0.11	..
338	J1236173+621025	26.00	0.56	$410.3^{312.8}_{-146.8}$	$986.1^{1000.0}_{-493.1}$	Lyα	2.6020	1.00	..
339	J1236175+621416	20.45	1.00	$11.6^{4.9}_{-3.4}$	$13.1^{5.4}_{-3.8}$	[OIII]5007	0.1562	0.00	..
340	J1236175+621416	20.44	1.00	$11.0^{2.6}_{-2.3}$	$22.4^{5.0}_{-4.5}$	[OII]	0.1564	0.00	..
341	J1236175+621301	24.81	0.97	$57.1^{23.4}_{-14.6}$	$87.1^{37.3}_{-22.8}$	Lyα	2.9304	1.00	..
342	J1236180+621457	21.06	1.00	$9.7^{5.1}_{-6.3}$	$21.0^{10.9}_{-13.5}$	[OII]	0.3366	0.00	..
343	J1236195+621253	20.20	0.94	$3.5^{1.0}_{-0.9}$	$8.6^{2.5}_{-2.2}$	[OII]	0.4729	0.00	J1236194+621252
344	J1236199+621230	22.86	0.98	$40.2^{9.4}_{-6.2}$	$68.3^{15.1}_{-10.0}$	[OII]	0.3974	0.02	..
345	J1236200+621020	21.72	0.94	$6.8^{2.6}_{-2.2}$	$12.3^{4.6}_{-4.1}$	[OII]	0.4546	0.01	..
346	J1236203+621034	21.58	1.00	$25.2^{3.8}_{-3.4}$	$44.0^{5.5}_{-5.2}$	[OII]	0.3453	0.00	..
347	J1236210+621204	20.89	0.96	$9.2^{1.9}_{-1.8}$	$20.4^{4.1}_{-4.1}$	[OII]	0.4569	0.04	..
348	J1236216+621227	20.47	1.00	$5.4^{1.2}_{-0.9}$	$11.8^{2.4}_{-1.8}$	[OII]	0.3986	0.00	..

Table 1.5 (cont'd)

HPS Index (1)	Counter-part (2)	Counter-part m_R* (3)	Counter-part P (4)	$EW_{R,rest}$* (Å) (5)	$EW_{interp,rest}$ (Å) (6)	Trans-ition (7)	z_{est} (8)	Lyα P (9)	X-ray counterpart (10)
349	J1236223+621107	21.18	1.00	$9.3^{2.1}_{-2.1}$	$22.8^{4.8}_{-4.9}$	[OII]	0.2754	0.00	..
350	J1236224+621241	20.91	0.99	$4.3^{1.3}_{-1.2}$	$9.7^{2.9}_{-2.7}$	[OII]	0.4578	0.00	J1236225+621240
351	J1236231+621346	21.10	1.00	$17.5^{7.6}_{-6.4}$	$33.2^{14.2}_{-12.0}$	[OII]	0.4839	0.00	J1236230+621347
352	J1236233+621125	23.92	0.96	$48.2^{25.8}_{-18.1}$	$62.5^{32.3}_{-23.2}$	[OII]	0.5619	0.04	..
353	J1236245+621140	21.38	0.99	$7.5^{1.8}_{-1.9}$	$15.9^{3.8}_{-3.9}$	[OII]	0.2304	0.01	..
354	J1236266+621252	21.04	1.00	$8.5^{3.0}_{-1.6}$	$12.5^{4.2}_{-2.3}$	[OII]	0.5569	0.00	..
355	J1236275+621018	20.77	1.00	$17.7^{2.5}_{-2.2}$	$36.5^{4.7}_{-4.1}$	[OII]	0.2531	0.00	..
356	J1236292+621153	22.84	0.98	$68.2^{21.1}_{-16.9}$	$106.6^{31.4}_{-25.9}$	[OII]	0.5291	0.02	..
357	J1236304+621209	21.00	1.00	$7.9^{1.8}_{-1.3}$	$15.1^{3.4}_{-2.4}$	[OII]	0.4567	0.00	..
358	J1236309+621433	21.59	0.99	$7.7^{3.0}_{-3.5}$	$15.7^{6.0}_{-7.1}$	[OII]	0.4383	0.01	..
359	J1236312+621236	21.85	0.99	$36.6^{4.8}_{-4.4}$	$60.5^{7.7}_{-7.1}$	[OII]	0.4568	0.01	J1236312+621237
360	J1236316+621140	24.67	0.47	$73.7^{30.7}_{-22.8}$	$234.1^{169.6}_{-85.1}$	Lyα	2.9198	1.00	..
361	J1236319+621241	21.86	0.93	$26.4^{4.4}_{-3.7}$	$41.3^{5.9}_{-5.3}$	[OII]	0.5280	0.06	..
362	J1236325+621038	20.38	0.98	$9.5^{2.1}_{-2.2}$	$11.8^{2.5}_{-2.7}$	[OIII]5007	0.1359	0.00	..
363	J1236325+621038	20.37	0.99	$12.6^{1.8}_{-1.7}$	$31.5^{3.9}_{-4.0}$	[OII]	0.1362	0.01	..
364	J1236332+621134	20.55	1.00	$7.5^{2.2}_{-1.6}$	$9.5^{2.7}_{-2.0}$	Hβ	0.0786	0.00	J1236331+621134
365	J1236332+621134	20.55	1.00	$15.3^{2.4}_{-2.2}$	$19.1^{2.9}_{-2.7}$	[OIII]5007	0.0785	0.00	J1236331+621134
366	J1236332+621134	20.55	1.00	$20.0^{3.2}_{-2.5}$	$39.1^{5.3}_{-4.2}$	[OII]	0.0787	0.00	J1236331+621134
367	J1236332+621134	20.55	1.00	$7.8^{2.0}_{-1.9}$	$9.7^{2.4}_{-2.4}$	[OIII]4959	0.0785	0.00	J1236331+621134
368	J1236338+621157	22.12	0.99	$27.4^{7.0}_{-6.2}$	$54.4^{13.8}_{-12.2}$	[OII]	0.4587	0.01	..
369	J1236345+621213	19.26	1.00	$10.0^{1.2}_{-1.0}$	$25.2^{3.0}_{-2.4}$	[OII]	0.4572	0.00	J1236345+621213
370	J1236349+621253	25.45	0.70	$100.9^{52.2}_{-33.9}$	$162.7^{67.3}_{-50.8}$	Lyα	3.1781	0.97	..
371	J1236356+621424	23.45	0.36	$22.2^{7.1}_{-9.0}$	$30.5^{9.7}_{-12.3}$	CIV1549	2.0090	0.27	J1236356+621424
372	J1236360+621206	26.26	0.11	$176.5^{341.4}_{-74.8}$	$247.5^{1000.0}_{-123.7}$	Lyα	2.7586	1.00	..
373	..	..	0.01	$539.5^{132.5}_{-114.0}$	$591.5^{145.3}_{-125.0}$	Lyα	2.9121	0.01	..
374	J1236369+621135	18.02	1.00	$7.7^{0.9}_{-0.7}$	$10.5^{1.1}_{-0.9}$	[OIII]5007	0.0783	0.00	J1236372+621135
375	J1236369+621135	18.02	1.00	$9.1^{1.0}_{-0.8}$	$21.3^{1.7}_{-1.5}$	[OII]	0.0786	0.00	J1236372+621135
376	J1236369+621135	18.02	1.00	$5.3^{0.6}_{-0.5}$	$7.5^{0.7}_{-0.6}$	Hβ	0.0784	0.00	J1236372+621135
377	J1236369+621135	18.02	1.00	$3.9^{0.5}_{-0.4}$	$5.4^{0.6}_{-0.5}$	[OIII]4959	0.0783	0.00	J1236372+621135

Table 1.5 (cont'd)

HPS Index (1)	Counter-part (2)	Counter-part m_R * (3)	Counter-part P (4)	$EW_{R,rest}$ * (Å) (5)	$EW_{interp,rest}$ (Å) (6)	Trans-ition (7)	z_{est} (8)	Lyα P (9)	X-ray counterpart (10)
378	J1236369+621135	18.02	1.00	$0.5^{0.1}_{-0.1}$	$0.8^{0.1}_{-0.2}$	Hγ	0.0784	0.00	J1236372+621135
379	J1236369+621135	18.02	1.00	$2.3^{0.4}_{-0.4}$	$4.8^{0.8}_{-0.7}$	[NeIII]3869	0.0773	0.00	J1236372+621135
380	J1236376+621241	20.86	0.99	$19.1^{2.5}_{-2.0}$	$31.5^{3.9}_{-3.3}$	[OII]	0.4586	0.01	..
381	J1236376+621241	20.86	1.00	$3.4^{1.1}_{-1.0}$	$5.1^{1.6}_{-1.4}$	[OII]	0.4834	0.00	..
382	J1236386+621510	23.72	0.75	$39.9^{25.2}_{-15.9}$	$72.5^{45.4}_{-28.7}$	[OII]	0.4621	0.25	..
383	J1236417+621132	19.70	1.00	$1.5^{0.6}_{-0.4}$	$2.3^{0.9}_{-0.6}$	Hγ	0.0889	0.00	J1236418+621132
384	J1236417+621132	19.70	1.00	$7.2^{1.0}_{-0.8}$	$9.0^{1.2}_{-0.9}$	[OIII]4959	0.0889	0.00	J1236418+621132
385	J1236417+621132	19.70	1.00	$7.2^{1.0}_{-0.8}$	$9.2^{1.2}_{-1.0}$	Hβ	0.0890	0.00	J1236418+621132
386	J1236417+621132	19.70	1.00	$16.2^{2.0}_{-1.7}$	$34.5^{3.2}_{-3.0}$	[OII]	0.0891	0.00	J1236418+621132
387	J1236417+621132	19.70	1.00	$13.9^{1.6}_{-1.5}$	$17.2^{2.0}_{-1.9}$	[OIII]5007	0.0889	0.00	J1236418+621132
388	J1236420+621205	21.07	0.99	$7.6^{2.3}_{-1.6}$	$15.5^{4.5}_{-3.2}$	[OII]	0.4334	0.01	..
389	J1236417+621239	24.46	0.92	$63.5^{18.3}_{-13.3}$	$120.0^{39.5}_{-27.0}$	Lyα	2.5885	1.00	..
390	J1236426+621518	22.21	0.99	$22.2^{11.4}_{-4.7}$	$35.3^{17.8}_{-7.3}$	[OII]	0.5328	0.01	..
391	J1236424+621449	24.58	0.93	$102.3^{35.1}_{-28.5}$	$324.1^{190.8}_{-107.8}$	Lyα	2.9588	1.00	..
392	J1236430+621216	20.89	1.00	$12.2^{1.6}_{-1.5}$	$23.2^{2.9}_{-2.7}$	[OII]	0.4538	0.00	..
393	J1236431+621030	22.19	1.00	$21.5^{8.2}_{-5.7}$	$31.6^{11.7}_{-8.2}$	[OII]	0.5502	0.00	..
394	J1236438+621357	20.90	1.00	$9.7^{1.7}_{-1.8}$	$23.4^{4.0}_{-4.2}$	[OII]	0.2012	0.00	..
395	J1236441+621410	24.09	0.74	$39.2^{20.8}_{-14.6}$	$58.5^{30.3}_{-21.7}$	Lyα	2.2734	1.00	..
396	J1236440+621250	21.14	0.88	$40.8^{4.8}_{-4.3}$	$65.0^{5.8}_{-5.7}$	[OII]	0.5561	0.00	J1236440+621250
397	J1236455+621326	22.65	0.56	$22.1^{4.8}_{-4.0}$	$36.4^{7.7}_{-6.5}$	[OII]	0.4395	0.08	..
398	J1236449+621200	23.06	0.85	$14.1^{7.8}_{-4.1}$	$26.3^{14.5}_{-7.7}$	[OII]	0.4553	0.14	..
399	J1236459+621326	21.03	0.95	$6.1^{1.2}_{-1.0}$	$13.9^{2.4}_{-2.1}$	[OII]	0.3208	0.05	..
400	J1236465+621408	23.75	0.59	$48.1^{15.3}_{-16.9}$	$50.2^{15.4}_{-17.6}$	[OIII]	0.1290	0.01	J1236463+621405
401	..	..	0.01	$3774.9^{766.3}_{-479.4}$	$4138.8^{840.2}_{-525.6}$	Lyα	2.0020	1.00	J1236467+621446
402	J1236470+621226	25.27	0.43	$115.5^{35.8}_{-29.2}$	$220.0^{108.5}_{-65.2}$	Lyα	2.9658	1.00	..
403	J1236474+621513	24.65	0.29	$41.9^{13.2}_{-11.9}$	$66.9^{16.2}_{-17.7}$	Lyα	3.1784	0.39	..
404	J1236471+621237	21.06	0.97	$17.7^{2.4}_{-1.8}$	$34.4^{3.7}_{-2.7}$	[OII]	0.3208	0.03	J1236470+621238
405	J1236473+621231	22.67	0.47	$27.6^{5.9}_{-6.0}$	$46.0^{9.4}_{-9.9}$	[OII]	0.4233	0.04	..
406	J1236478+621513	21.69	0.90	$9.9^{1.6}_{-2.3}$	$15.9^{2.2}_{-3.6}$	[OII]	0.5335	0.10	..

Table 1.5 (cont'd)

HPS Index (1)	Counter-part (2)	Counter-part m_R * (3)	Counter-part P (4)	$EW_{R,rest}$ * (Å) (5)	$EW_{interp,rest}$ (Å) (6)	Trans-ition (7)	z_{est} (8)	Lyα P (9)	X-ray counterpart (10)
407	J1236483+621426	19.05	1.00	$4.5^{0.5}_{-0.5}$	$5.5^{0.6}_{-0.5}$	Hβ	0.1388	0.00	J1236484+621426
408	J1236483+621426	19.05	1.00	$2.4^{0.3}_{-0.3}$	$2.9^{0.3}_{-0.3}$	[OIII]4959	0.1387	0.00	J1236484+621426
409	J1236483+621426	19.06	1.00	$7.4^{0.9}_{-0.7}$	$8.6^{0.8}_{-0.7}$	[OIII]5007	0.1387	0.00	J1236484+621426
410	J1236481+621309	20.85	0.99	$20.3^{3.0}_{-2.6}$	$59.7^{8.4}_{-7.3}$	[OII]	0.4747	0.01	J1236481+621309
411	J1236483+621426	19.05	1.00	$0.7^{0.2}_{-0.2}$	$1.0^{0.3}_{-0.2}$	Hγ	0.1384	0.00	J1236484+621426
412	J1236483+621426	19.05	1.00	$2.1^{0.4}_{-0.4}$	$3.9^{0.8}_{-0.7}$	[NeIII]3869	0.1385	0.00	J1236484+621426
413	J1236483+621426	19.05	1.00	$12.0^{1.4}_{-1.1}$	$23.8^{2.1}_{-1.8}$	[OII]	0.1389	0.00	J1236484+621426
414	J1236491+621512	22.82	0.99	$16.6^{6.7}_{-5.1}$	$29.3^{11.8}_{-9.0}$	[OII]	0.4580	0.01	..
415	J1236495+621421	25.25	0.61	$89.6^{39.1}_{-24.7}$	$165.9^{65.8}_{-43.8}$	Lyα	3.3667	0.97	..
416	J1236498+621313	21.82	0.64	$40.2^{6.7}_{-4.5}$	$96.6^{15.6}_{-10.4}$	[OII]	0.4755	0.36	J1236497+621313
417	J1236497+621113	21.75	1.00	$21.4^{3.1}_{-3.1}$	$34.8^{4.9}_{-5.0}$	[OII]	0.4753	0.00	..
418	J1236497+621258	22.36	0.95	$7.8^{3.7}_{-4.4}$	$15.0^{7.1}_{-8.3}$	[OII]	0.4746	0.05	..
419	J1236501+621401	24.57	0.79	$72.3^{18.5}_{-17.8}$	$184.1^{59.0}_{-48.5}$	Lyα	2.2349	1.00	..
420	J1236504+621055	25.02	0.41	$100.8^{40.7}_{-29.6}$	$297.2^{273.4}_{-111.2}$	Lyα	2.9290	0.68	..
421	J1236503+621240	20.84	0.99	$9.4^{1.7}_{-1.1}$	$16.8^{3.0}_{-2.0}$	[OII]	0.4743	0.01	..
422	J1236508+621059	21.49	0.96	$16.0^{2.6}_{-2.8}$	$27.9^{4.5}_{-4.8}$	[OII]	0.4744	0.04	..
423	J1236509+621256	22.51	0.98	$37.1^{5.6}_{-4.5}$	$66.1^{8.3}_{-7.0}$	[OII]	0.3214	0.02	..
424	J1236512+621031	20.63	1.00	$5.1^{1.2}_{-1.0}$	$12.4^{2.7}_{-2.5}$	[OII]	0.4099	0.00	J1236511+621030
425	J1236511+621321	19.70	1.00	$11.9^{1.4}_{-1.1}$	$27.0^{3.0}_{-2.4}$	[OII]	0.2007	0.00	..
426	J1236517+621510	25.24	0.30	$56.7^{25.8}_{-14.5}$	$92.1^{34.8}_{-20.9}$	Lyα	3.4045	0.98	..
427	J1236517+621052	23.15	0.91	$36.1^{12.6}_{-9.5}$	$54.0^{18.2}_{-13.9}$	[OII]	0.5180	0.03	J1236513+621051
428	J1236519+621515	23.89	0.95	$30.3^{7.5}_{-5.7}$	$42.2^{9.3}_{-7.3}$	Lyα	3.3351	1.00	..
429	J1236517+621220	21.63	0.96	$9.2^{1.9}_{-1.9}$	$25.9^{4.7}_{-5.1}$	[OII]	0.3002	0.04	J1236517+621221
430	J1236519+621125	21.88	1.00	$9.3^{3.4}_{-2.7}$	$11.5^{4.2}_{-3.3}$	[OIII]5007	0.0889	0.00	..
431	J1236522+621457	21.89	0.99	$16.6^{2.3}_{-2.6}$	$30.6^{3.5}_{-4.5}$	[OII]	0.3576	0.00	J1236521+621457
432	J1236525+621036	21.81	0.98	$20.5^{3.6}_{-2.6}$	$37.2^{5.8}_{-4.2}$	[OII]	0.3202	0.02	..
433	J1236527+621220	23.44	0.83	$35.8^{10.8}_{-10.4}$	$68.3^{19.9}_{-19.7}$	[OII]	0.4005	0.06	..
434	J1236542+621336	26.89	0.53	$298.9^{442.1}_{-130.2}$	$559.1^{1000.0}_{-289.3}$	Lyα	2.2659	1.00	..
435	J1236547+621127	20.91	1.00	$5.5^{1.2}_{-1.1}$	$19.0^{3.8}_{-3.7}$	[OII]	0.2536	0.00	..

Table 1.5 (cont'd)

HPS Index (1)	Counter-part (2)	Counter-part m_R * (3)	Counter-part P (4)	$EW_{R,rest}$ * (Å) (5)	$EW_{interp,rest}$ (Å) (6)	Trans-ition (7)	z_{est} (8)	Lyα P (9)	X-ray counterpart (10)
436	J1236546+621341	25.41	0.66	$51.1^{26.9}_{-18.8}$	$56.6^{26.3}_{-20.2}$	Lyα	2.4192	0.90	..
437	J1236565+621420	21.07	1.00	$9.6^{1.6}_{-1.8}$	$11.8^{1.9}_{-2.1}$	[OIII]5007	0.1049	0.00	..
438	J1236565+621420	21.07	1.00	$11.5^{2.1}_{-1.8}$	$23.5^{3.8}_{-3.5}$	[OII]	0.1053	0.00	..
439	J1236573+621153	24.17	0.54	$77.0^{33.4}_{-25.3}$	$92.5^{34.8}_{-29.0}$	[OII]	0.5457	0.46	..
440	J1236573+621226	22.62	0.95	$14.4^{5.7}_{-5.4}$	$19.4^{7.5}_{-7.2}$	[OII]	0.5620	0.05	..
441	J1236573+621260	21.23	0.96	$22.7^{3.0}_{-2.4}$	$38.8^{5.0}_{-4.0}$	[OII]	0.4743	0.02	J1236569+621302
442	J1236581+621300	22.21	0.85	$29.8^{4.9}_{-4.2}$	$48.3^{6.8}_{-6.2}$	[OII]	0.3205	0.02	..
443	J1236588+621252	21.20	0.98	$12.3^{2.4}_{-2.3}$	$26.6^{4.6}_{-4.7}$	[OII]	0.3204	0.02	..
444	J1236588+621438	22.73	0.80	$18.9^{8.6}_{-8.5}$	$30.1^{13.4}_{-13.6}$	[OII]	0.5113	0.01	J1236589+621435
445	J1236594+621405	19.92	1.00	$11.4^{1.4}_{-1.2}$	$14.8^{1.8}_{-1.5}$	[OIII]5007	0.0884	0.00	J1236597+621404
446	J1236594+621405	19.92	1.00	$3.8^{0.8}_{-0.8}$	$5.1^{1.1}_{-1.0}$	Hβ	0.0885	0.00	J1236597+621404
447	J1236595+621341	24.22	0.93	$19.7^{7.5}_{-4.3}$	$31.3^{10.1}_{-5.9}$	Lyα	3.1262	1.00	..
448	J1236594+621405	19.92	1.00	$3.4^{0.9}_{-0.6}$	$4.4^{1.2}_{-0.7}$	[OIII]4959	0.0884	0.00	J1236597+621404
449	J1236594+621405	19.92	0.99	$8.5^{1.6}_{-1.1}$	$20.9^{3.5}_{-2.4}$	[OII]	0.0887	0.01	J1236597+621404
450	J1236599+621406	22.78	0.36	$22.2^{5.9}_{-5.6}$	$29.6^{7.4}_{-7.4}$	[OII]	0.5148	0.00	J1236597+621404
451	J1237005+621406	20.76	0.80	$4.1^{1.5}_{-1.1}$	$10.2^{3.6}_{-2.7}$	[OII]	0.4231	0.01	J1236597+621404
452	J1237021+621323	21.00	0.98	$5.2^{1.5}_{-1.2}$	$10.9^{3.1}_{-2.5}$	[OII]	0.4104	0.02	..
453	J1237021+621123	19.06	1.00	$0.7^{0.3}_{-0.3}$	$1.7^{0.7}_{-0.6}$	[NeIII]3869	0.1338	0.00	J1237020+621122
454	J1237021+621349	22.56	0.99	$33.3^{8.0}_{-6.5}$	$50.9^{11.6}_{-9.6}$	[OII]	0.5115	0.01	..
455	J1237021+621123	19.06	1.00	$1.6^{0.3}_{-0.3}$	$2.1^{0.3}_{-0.4}$	[OIII]4959	0.1357	0.00	J1237020+621122
456	J1237021+621123	19.06	1.00	$3.4^{0.5}_{-0.4}$	$4.2^{0.5}_{-0.4}$	[OIII]5007	0.1357	0.00	J1237020+621122
457	J1237021+621123	19.06	1.00	$2.8^{0.4}_{-0.4}$	$3.7^{0.5}_{-0.6}$	Hβ	0.1358	0.00	J1237020+621122
458	J1237021+621123	19.06	1.00	$7.0^{0.8}_{-0.7}$	$17.9^{1.6}_{-1.4}$	[OII]	0.1359	0.00	J1237020+621122
459	J1237039+621009	22.09	0.92	$35.2^{5.6}_{-4.7}$	$52.4^{7.1}_{-6.2}$	[OII]	0.3215	0.07	..
460	J1237040+621441	21.76	0.99	$18.9^{3.3}_{-3.0}$	$35.5^{6.1}_{-5.5}$	[OII]	0.4748	0.01	..
461	J1237044+621446	24.39	0.82	$54.2^{20.0}_{-13.4}$	$56.1^{19.3}_{-13.2}$	CIV1549	2.2136	0.08	..
462	J1237044+621446	24.39	0.96	$195.4^{37.2}_{-29.2}$	$335.2^{116.6}_{-72.5}$	Lyα	2.2128	1.00	..
463	J1237047+621029	21.96	0.72	$32.0^{4.4}_{-4.6}$	$62.4^{7.7}_{-8.6}$	[OII]	0.4104	0.28	..
464	J1237047+621429	21.39	1.00	$6.7^{2.3}_{-1.9}$	$10.6^{3.5}_{-3.0}$	[OII]	0.5602	0.00	J1237046+621429

Spectral classification

As mentioned in §1.3.1, the presence of multiple, strong emission-lines can be used to identify some low-z objects, but the absence of such lines is not sufficient evidence to classify a source as an LAE. We begin all source classifications by cross-correlating the primary emission line at various assumed redshifts to other bright, expected emission lines. We automatically search all the detection spectra for MgII2798, [OII]3727, Hγ4341, Hβ4861, [OIII]4959, and [OIII]5007 assuming the detected line to be, variously, [OII]3727, Hβ4861, [OIII]4959, and [OIII]5007. At high redshift we test Lyα for the presence of CIV1549. We have manually tried using the other, commonly weaker lines as confirmation of the primary detection, but have found only two cases of interest. For emission line index 4 of Tables 1.4 and 1.5, the CIII]1909 line is detected with the also-significantly detected [OII]3727 line of index 5. For emission line index 85 of the same tables, the broad MgII2798 line is brighter than the also-significantly detected [OII]3727 line. We have also mis-identified index 400 as an [OII] emitter in the first pass of analysis; it is known to be an [OIII]5007 emitter from the literature (Barger et al. 2008), but we find no other detections at other wavelengths.

A demonstration of this cross-correlation process for a multiple-emission-line source is shown in Figure 1.25. We find only two cases where the correlation against data below the catalog signal-to-noise cut aids classification as shown in Figure 1.26. The first is emission line index 234, which is formally a single emission line detection. However, we find that an identification of the primary line with [OIII]5007 leads to a S/N=3.2 detection at the wavelength of [OII], a S/N=5.1 detection at Hβ. and a S/N=3.6 detection at [OIII]4959. The second case is emission line index 430 which is also a single emission line detection. We again find that an identification of the primary line with [OIII]5007 leads to a S/N=3.7 detection at the wavelength of [OII] and a S/N=2.9 detection at Hβ. In practice, the primary utility in the emisison

Table 1.5 (cont'd)

HPS Index (1)	Counter-part (2)	Counter-part m_R* (3)	Counter-part P (4)	$EW_{R,rest}$* (Å) (5)	$EW_{interp,rest}$ (Å) (6)	Trans-ition (7)	z_{est} (8)	Lyα P (9)	X-ray counterpart (10)
465	J1237052+621211	22.59	0.97	$30.0^{6.4}_{-7.2}$	$55.3^{11.1}_{-13.0}$	[OII]	0.3870	0.03	..
466	J1237061+621501	23.55	0.94	$31.0^{5.8}_{-4.4}$	$58.9^{9.3}_{-7.3}$	Lyα	3.2384	1.00	..
467	..	..	0.02	$270.7^{113.0}_{-77.4}$	$296.8^{123.9}_{-84.9}$	Lyα	2.8023	1.00	..
468	J1237078+621138	22.70	0.98	$39.6^{7.9}_{-7.7}$	$52.3^{9.5}_{-9.7}$	[OII]	0.5574	0.02	..
469	J1237084+621056	20.32	0.95	$17.1^{2.1}_{-1.7}$	$30.1^{3.3}_{-2.8}$	[OII]	0.4227	0.05	J1237083+621056
470	J1237084+621454	22.19	0.98	$30.2^{5.6}_{-5.2}$	$42.3^{7.0}_{-6.9}$	[OII]	0.5625	0.01	..
471	J1237087+621051	21.01	0.94	$11.3^{2.2}_{-1.4}$	$21.1^{3.8}_{-2.4}$	[OII]	0.4110	0.00	..
472	J1237111+621048	23.29	0.47	$15.4^{10.5}_{-7.7}$	$23.9^{16.3}_{-11.9}$	[OII]	0.4830	0.03	..
473	J1237109+621129	23.16	0.96	$25.8^{12.6}_{-9.0}$	$46.7^{22.7}_{-16.2}$	[OII]	0.4750	0.02	..
474	J1237110+621140	25.14	0.23	$68.6^{48.2}_{-32.9}$	$102.0^{70.6}_{-48.7}$	Lyα	2.2741	0.28	..
475	J1237116+621126	21.94	0.83	$12.1^{3.9}_{-3.2}$	$23.0^{7.2}_{-6.0}$	[OII]	0.4104	0.08	..
476	J1237119+621020	22.02	0.97	$22.1^{5.3}_{-3.2}$	$38.0^{8.7}_{-5.3}$	[OII]	0.4125	0.03	..
477	J1237118+621515	20.09	1.00	$12.8^{1.5}_{-1.3}$	$25.4^{2.2}_{-1.9}$	[OII]	0.2987	0.00	..
478	J1237118+621515	20.09	1.00	$1.4^{0.8}_{-0.4}$	$2.4^{1.3}_{-0.7}$	[NeIII]3869	0.2983	0.00	..
479	J1237137+621511	21.67	0.97	$14.0^{4.3}_{-4.2}$	$24.6^{7.2}_{-7.3}$	[OII]	0.5234	0.03	..

*The Johnson or SDSS R band filters used are listed in Table 1.3. The MUNICS fields, at α=3 hours, instead use an SDSS *i* filter.

line cross-correlation is to discriminate between various low-z possibilities with high S/N detections.

EW-based classification

In any LAE survey at sufficient redshift, the most likely contaminants are [OIII]5007 and [OII]3727. Many of the former objects can be identified by the presence of [OIII]4959 or Hβ. The latter may be identified by either splitting the [OII] doublet, or by using line equivalent width as a discriminant (Cowie & Hu 1998). Since we lack the resolution to split [OII]3727, we follow Gronwall et al. (2007) and require LAEs to have $\mathrm{EW}_{\mathrm{rest}} > 20$Å. A number of different EW estimators are possible with measurements in many filters. We look at two ways to estimate the EW using broadband data, and conclude that the cleanest selection of LAEs is obtained when the *R*-band data is used alone.

The observed wavelengths and EWs are shown in Figure 1.27. Emission lines without counterparts are shown as limits. We calculate the EW first by using the nearest-available filter that lies redward of the entire sample. For XMM-LSS, GOODS-N, and COSMOS, this is the *R*-band. MUNICS lacks an *R*-band image, so we used i'. The redward choice is important to avoid attentuation by the intergalactic medium (IGM) for these data and the Lyman break. Although there may be some diversity in LAE dust content (Finkelstein et al. 2009), it appears most LAEs at our redshifts of interest have only small amounts of dust and exhibit flat continua (Gawiser et al. 2007; Guaita et al. 2010; Blanc et al. 2010). Of course, low redshift, star-forming galaxies may also exhibit flat continua or, more likely, some level of a Balmer/4000Å break, but by extrapolating the continua from the *R*-band, the low redshift EWs will be somewhat underestimated while the LAE EWs should remain unaffected. Still, while such a property is beneficial to the classification process, an unbiased EW is also desireable for physical studies. So, we next calculate the

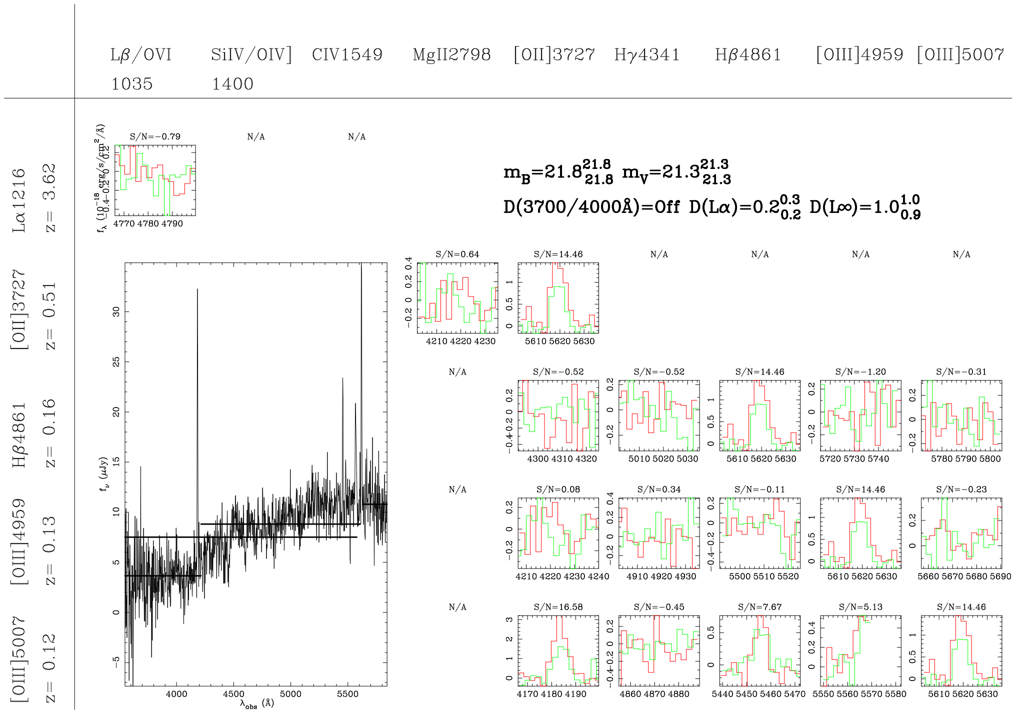

Figure 1.25 The attempts to find matching lines to an [OIII]5007 detection in index 323 of Table 1.4. The detection is formed from two fibers represented independently with the red and green lines. The leftmost column shows the prospective identifications of our originally detected line at 5619Å. For each prospective identification, we attempt fits to the emission-line possibilities in the top row. In this case, matches to [OII] and Hβ both give a clear identification. The [OIII]4959 is detected but overlapping with the mask around 5577Å. This technique only rarely gives positive evidence for Lyα classification by ruling out low$-z$ emission line combinations because our wavelength bandpass is not much larger than common bright optical emission-line spacings. However, matching emission-lines often aid in classifying transitions between different low redshift options as in this case. The full spectrum is shown in the large window to the left. Various continuum regions are evaluated by assuming the primary emission line to be Lyα and [OII] shown by the horizontal lines. The continuum fits are used to look for various breaks as calculated in the upper right. This galaxy is also identified by significant detections of Hβ, [OIII]4959, and [OII] in entries 325, 326, and 327 of Table 1.4.

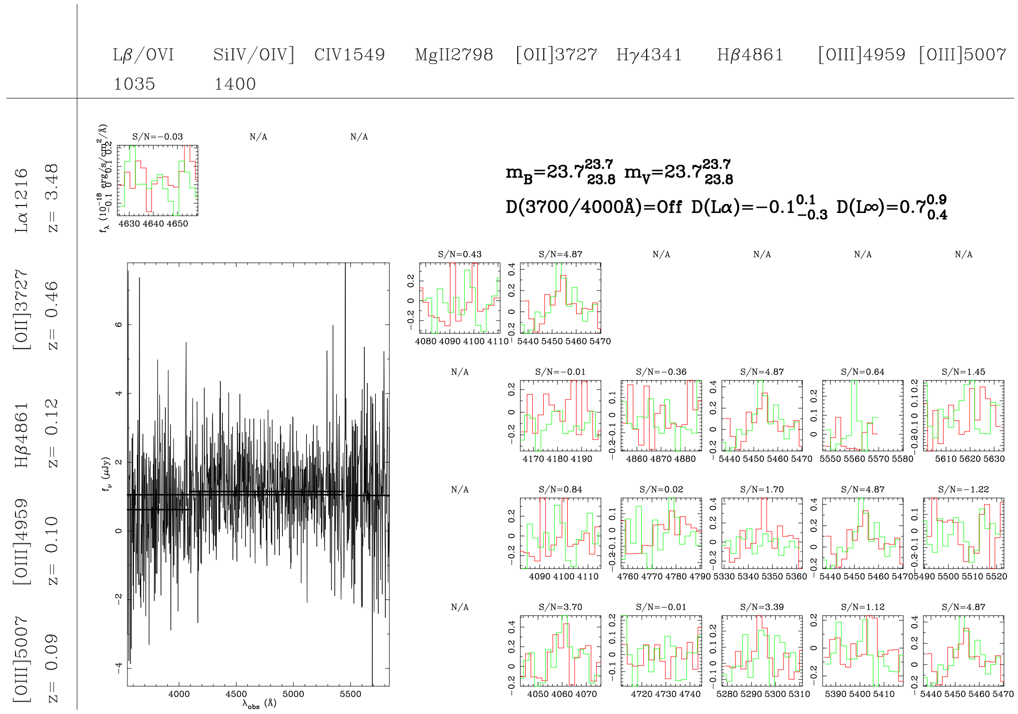

Figure 1.26 The automated search for multiple emission line in index 430. The format is the same as in Figure 1.25. This is one of the few cases where the consideration of marginally significant counterpart lines aids the classification. The primary detection is revealed to be [OIII]5007, with marginal detections in [OII] and Hβ that did not make the primary emission line catalog.

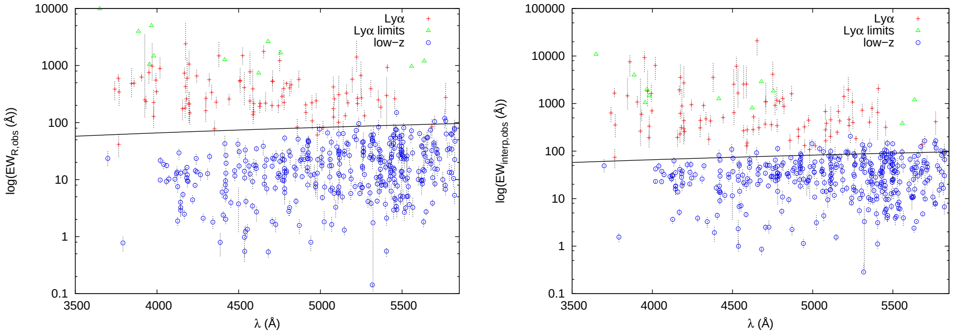

Figure 1.27 The distribution of observed wavelength and observed EW. The line marks the usual EW cut used in narrowband imaging and adopted here. Exceptions to the EW selection are discussed in §1.3.4. *Left* Continuum estimated only from the R-band photometry (or the i'-band in MUNICS). *Right* Continuum estimated from interpolation with the two nearest filters bounding each emission line's wavelength.

EWs in the right panel of Figure 1.27 by interpolating each emission-line with the two nearest, bounding broadband filters. Clearly, the high and low EW populations have more overlap in the interpolated EW measurements. For this reason, we adopt the R-band EW in our classification scheme. Figure 1.28 shows the emission line flux against continuum magnitude for each emission line. We have also checked the GALEX (Martin et al. 2005) GR4/GR5 database for all objects. None of the LAE classified objects are GALEX sources, while most of the low-z classified objects do have counterpart GALEX detections.

There are nine objects for which we make exceptions: four low EW objects we identify as LAEs and five high EW sources we believe are low redshift interlopers.

1) The lowest wavelength exception is observed at λ=3765.6Å with EW$_{\rm obs}$ = 41^{+21}_{-17}Å as index 313. If this were [OII], the galaxy would be extremely nearby (45 Mpc) away and have M$_R$ =-10.5. The photometric redshift of Ilbert et al. (2009) suggests the line to be Lyα and excludes all the low-z options with 95% confidence.

2) The next low EW object is in the MUNICS field as index 51 and has m$_{i'}$=23.7. The detected wavelength is 4981.6Å with EW$_{\rm obs}$ = 61^{+38}_{-29}Å. The case

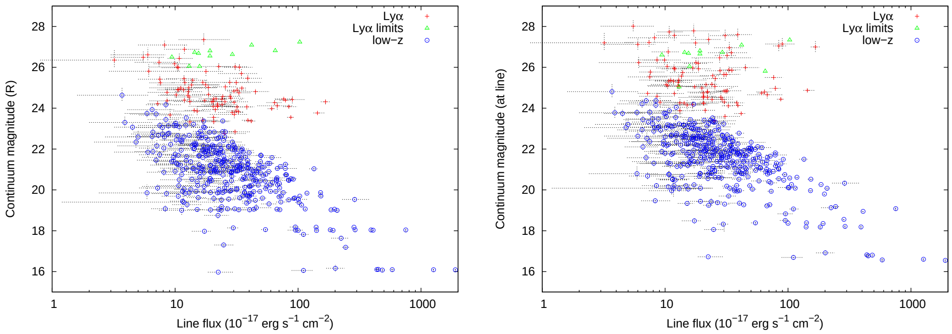

Figure 1.28 The distribution of emission line flux and broadband magnitude. *Left* Continuum estimated only from the R-band photometry (or the i'-band in MUNICS). *Right* Continuum estimated from interpolation with the two nearest filters bounding each emission line's wavelength.

for this object is not terribly strong, but the dim continuum and lack of a GALEX detection suggest this to be an LAE.

3) The third low EW object is in the GOODS-N field as index 447 at wavelength 5017.2Å with $\mathrm{EW_{obs}} = 81^{+31}_{-18}$Å. It was originally listed as an Lyman Break Galaxy (LBG) in Steidel et al. (2003), but no redshift measurement exists in the literature. The counterpart has m_R=24.2.

4) The final low EW object is in the MUNICS field as index 92 at wavelength 5683.3Å with $\mathrm{EW_{obs}} = 84^{+34}_{-31}$Å. The counterpart has $\mathrm{m}_{i'}$=23.3, but no GALEX detection. Again, this is a borderline classification.

Next, we consider the five high EW objects reclassified as being at low redshifts.

5) The first high EW low$-z$ object is in COSMOS as index 289 at wavelength 5235.9Å with $\mathrm{EW_{obs}} = 96^{+28}_{-26}$Å. It does not have a GALEX detection, but the counterpart has m_R=23.4. The photometric redshift of (Ilbert et al. 2009) suggests the line to be [OII] and excludes all other reasonable options with 95% confidence.

6) This COSMOS object is index 234 with m_R=23.4, wavelength 5466.7Å

and $\mathrm{EW}_{\mathrm{obs}} = 149^{+28}_{-23}$Å. As discussed in §1.3.4, the source shows low significance emission lines such that the primary detection is likely [OIII]5007. Such an identification is possible since unlike [OII], [OIII]5007 can have extremely high EWs (Hu et al. 2009). The source also has a GALEX detection.

7) This GOODS-N object is index 356 at m_R=22.8, wavelength 5700.5Å and $\mathrm{EW}_{\mathrm{obs}} = 104^{+32}_{-26}$Å. It has a GALEX detection and has a measured redshift in Barger et al. (2008) as being from [OII] emission.

8) This is index 439 from the GOODS-N field with m_R=24.2, wavelength 5762.4Å and $\mathrm{EW}_{\mathrm{obs}} = 119^{+52}_{-39}$Å. The object is detected with GALEX.

9) This is index 94 from the MUNICS field with $\mathrm{m}_{i'}$=21.0, wavelength 5768.4Å and $\mathrm{EW}_{\mathrm{obs}} = 107^{+22}_{-20}$Å. The object is detected with GALEX.

We next review the likely levels of contamination in the LAE sample from low redshift objects based on previous studies. The frequency of EW in bright, rest-frame-optical lines at low redshift has been studied in Hammer et al. (1997), Hogg et al. (1998), Treyer et al. (1998), Sullivan et al. (2000), Gallego et al. (2002), and Teplitz et al. (2003). By combining the observation that ∼2% of [OII] emitters have $\mathrm{EW}_{\mathrm{rest}} > 60$Å (Hogg et al. 1998) with the $0 < z < 0.4$ [OII] luminosity function of Sullivan et al. (2000) and assuming no redshift evolution of either the [OII] or LAE EW distributions (Gronwall et al. 2007), we estimate our that sample may contain 1.6 high EW [OII] interlopers. Similarly, if we use the local luminosity function of Gallego et al. (2002), we predict zero high EW interloping [OII] emitters. As a second comparison, Kakazu et al. (2007) presents narrowband imaging and limited spectroscopic follow-up in their search for low metallicity galaxies. They find [OIII]5007 at $z = 0.63$ and $z = 0.83$, and [OII] at $z = 1.19$ and $z = 1.45$ at high enough EW values to contaminate our sample. By comparing their high EW [OII] number density to the Schechter (Schechter 1976) function fits of Ly et al. (2007) at $z = 1.18$ and $z = 1.47$ without extinction corrections, we find the high EW [OII] fraction should only be 3%. In contrast, the same analysis suggests the high EW [OIII]5007 fraction is much higher (33%). However, there is no evidence for such a large fraction of high EW [OIII]5007 over our redshifts of interest, and the VIRUS-P bandpass will always enclose [OII] and [OIII]4959 when [OIII]5007 is observed. Thus, neither high EW [OII] nor [OIII]5007 emitters should form important catalog contaminants. The wavelength spacing between AGN lines is smaller than for [OII] and the other optical lines, so AGN lines should be identifiable with multiple detections. For example, index 4 is our only CIII]1909 detection, identified with a co-detection in index 5 as CIV1549. The best available contamination estimate is that this LAE sample contains 0-2 contaminants from mis-identified redshifts if only EW information is used. A complementary question is how our rest-frame EW affects the selection of high-redshift galaxies. Assuming the LAE distribution in Gronwall et al. (2007), the answer is that ∼21-26% of potential detections are lost by the EW cut.

We briefly state how we propogate errors to the EW estimation. In cases where the flux density measurement is very noisy, the usual first-order error propagation breaks down. Importantly, the error on equivalent width becomes asymmetric in the case of a low S/N continuum even if the original errors on flux and flux density are symmetric. One simple solution is to treat the maximum liklihood distributions in flux and flux density as Gaussian functions, transform the flux into EW and flux density, and define the EW errors using the extrema of the 68% confidence interval. Similarly, in the case of asymmetric errors for the line fluxes, we use the same equation evaluated with each one-sided error to arrive at final EW limits. When we find no upper limit, we list the upper uncertainty as 1000Å.

Counterpart association

The coarse spatial resolution of our VIRUS-P survey often prevents us from associating with certainty a given emission line to a unique broadband counterpart. However, stringent redshift probabilities can often be made by marginalizing over all possible counterparts and their implied rest-frame emission-line equivalent widths. We quantify this association probability by using the astrometric error, discussed in §1.3.1, and the differential number counts for the R-band images. Since MUNICS lacks R-band data, we use the i'-band there. The exact band choice for this step is not critical, so long as the filter samples a fairly flat spectral region for both low-z and high-z objects. We describe the method for R-band continuum association as it applies to equivalent-width-based redshift discrimination. We use the same formalism for AGN association through X-ray data in §1.3.4.

The problem of assigning counterpart probabilities to detections in multiple bandpasses has been explored by Bayesian methods in Sutherland & Saunders (1992) and is commonly implemented in X-ray surveys (e.g. Luo et al. 2010). We choose not to use the Bayesian technique here since it requires assuming a prior on the continuum counterparts to the emission-line detections. We instead make a simpler, frequentist estimate that still uses the information from multiple candidates. The only assumed inputs are the astrometric error and the number counts of background and foreground objects.

The probability of an emission line being associated with any one image-based counterpart can be constructed as the joint probability of all the remaining imaging detections being unassociated and drawn from established number counts and the preferred counterpart having the observed offset evaluated against the astrometric error budget. For simplicity, we treat all the individual probabilities as independent; this simplication is justified since the range of distances in our redshift range is much larger than cross-correlation scales between galaxies. We begin by identifying all the significant imaging detections within some large area of the detected emission line. We then define: i as the set of all imaging detections in the survey field, Δr_i as the angular offset between the position of the emission line and the centroid of counterpart i, S_i as the flux density of counterpart i (or X-ray flux in a defined bandpass), σ_i as the astrometric error for the emission line under consideration and counterpart i, and $n(S)$ as the differential number count of galaxies in the observed bandpass. We begin by assembling the set of imaging detections with cardinality j as $C_j = (j \in i : \Delta r_j < 10'')$. The exact value of the angular limit is not important so long as it is several times the astrometric error. The chance of a superposition by one or more imaging detections without them being actual counterparts is then $P_{nc,j} = 1 - f(0, \lambda)$ where $f(n, \lambda) = \frac{\lambda^n e^{-\lambda}}{n!}$ is the Poisson probability distribution and λ is the expectation value for the number of galaxies brighter than S_j within Δr_j, so $\lambda = \pi \Delta r_j^2 \int_{S_j}^{\infty} n(S) dS$. Alternatively, the detection j may be the true counterpart. If we model the astrometric error as a two-dimensional Gaussian distribution in the astrometry error and take its cumulative evaluation from infinity, the chance of measuring the true counterpart at Δr_j or further is $P_{c,j} = \exp(\frac{-\Delta r_j^2}{2\sigma^2})$. It may also be that we have not measured the true imaging counterpart, either due to imaging depth or the emission-line detection being spurious, in which case all imaging detections must be explained as superpositions.

We give in Equation 1.6 the full joint probabilities assembled from the individual probabilities just described, under the assumption that either one or none of the imaging detections is the true counterpart to the emission-line detection. A similar calculation is done to evaluate the significance of X-ray counterparts in

§1.3.4.

$$P = \begin{cases} \dfrac{\prod\limits_{1\leq k\leq j} P_{nc,k}}{\prod\limits_{1\leq k\leq j} P_{nc,k} + \sum\limits_{1\leq\ k\leq j} \left(P_{c,k} \times \prod\limits_{1\leq m\leq j, m\neq k} P_{nc,m} \right)} & : \text{no counterpart} \\ \dfrac{P_{c,k} \times \prod\limits_{1\leq m\leq j, m\neq k} P_{nc,m}}{\prod\limits_{1\leq k\leq j} P_{nc,k} + \sum\limits_{1\leq\ k\leq j} \left(P_{c,k} \times \prod\limits_{1\leq m\leq j, m\neq k} P_{nc,m} \right)} & : \text{counterpart } k \end{cases} \tag{1.6}$$

In the case of imaging, the astrometric error is dominated by the positional uncertainty of the emission-lines, but in the case of X-ray data the positional uncertainty of both the emission-line and X-ray detections are comparable and important. The normalization is simply chosen to make the probabilities sum to unity.

In order to match R-band objects, we performed a least squares minimization fit to the R-band differential number counts of Furusawa et al. (2008) with a double power law function to estimate $n(S)$ as given in Equation 1.7.

$$n(f_\nu)[\text{per } \square^\circ] = \begin{cases} 5142 \times (f_\nu/10^{-28})^{-1.996} & : f_\nu > 7.81 \times 10^{-30} \text{erg/s/cm}^2\text{/Hz} \\ 10882.6 \times (f_\nu/10^{-28})^{-1.702} & : f_\nu \leq 7.81 \times 10^{-30} \text{erg/s/cm}^2\text{/Hz} \end{cases} \tag{1.7}$$

In practice, we consider a threshold distance of 1″ when calculating the expected number counts of sources based on common seeing conditions to avoid the claim of total counterpart certainty at Δr_j =0 regardless of other counterpart options, although the exact threshold makes little difference. Finally, in defining Δr_j, we take the radial offset from the emission-line centroid to the nearest position contained in the imaging's Kron aperture instead of the Kron aperture center. This is motivated by the fact that [OII] emission in nearby galaxies may be from HII regions located at large galactocentric radii.

Object classification starts by identifying all imaging catalog counterparts within $10''$ from the emission-line centroid. The association probability for each possible counterpart is calculated using Equation 1.6. The emission line is classified under the EW rule of §1.3.4 to be at either low (most likely as [OII]) or high (most likely as Lyα) redshift. In 74% of the cases, the best counterpart probability exceeds 90%; we refer to these objects as the isolated sample. In another 3% of the cases, our analysis is most consistent with there being no broadband counterpart; we classify these sources as LAEs since all the image depths imply $\mathrm{EW}_{\mathrm{Ly}\alpha,\mathrm{rest}} > 20$Å. For the remaining cases, our classification is less certain due to there being multiple likely counterparts; nevertheless the most probable association is always presented. We illustrate step-by-step two representative classification cases in §1.3.4 and 1.3.4, and a case with less certainty in §1.3.4.

We confirm the proper classification of many low redshift objects by observing multiple emission lines. In total, there are 118 emission-line sources with one or more associated emission lines in combinations of [OII], Hδ, Hγ, Hβ, [OIII]4959, and [OIII]5007. Of these, all are classified automatically by our EW cut as being at low redshift.

AGN contamination

We attempt to identify the Lyα sources that are AGN through existing X-ray data. All our survey fields have either Chandra or XMM/Newton coverage, although to quite non-uniform depths. We use the point-source catalogs of Elvis et al. (2009); Cappelluti et al. (2009) in COSMOS, Alexander et al. (2003) in GOODS-N, Pierre et al. (2004) in XMM-LSS, and Watson et al. (2009) in MUNICS. The data covering MUNICS is described in Severgnini et al. (2005) but not cataloged. The same methodology for determining broadband imaging counterparts is applied to the X-ray data. The cataloged X-ray spatial uncertainty is added in quadrature to the emission-line spatial uncertainty, and the fit of Cappelluti et al. (2007) from 2-10 keV is used for the differential number count. Unlike with the imaging counterparts, the association of an X-ray source with a VIRUS-P emission line is nearly binary in nature: there is either a single likely counterpart or no likely counterpart. Table 1.6 summarizes our results by listing the fraction of X-ray sources in the low and high-z objects. We find 6-8% contamination of LAEs by AGN over all the fields with the range depending on what fraction of the line detections we attribute to noise. AGN contamination is likely a strong function of flux limit, but we compare briefly to other, deeper surveys. The sample of Gawiser et al. (2007); Gronwall et al. (2007) at $z = 3.1$ contains 1% AGN contamination, the sample of Nilsson et al. (2009, 2010) at $z = 2.3$ contains 6-15% AGN contamination, and the sample of Guaita et al. (2010) at $z = 2.1$ contains 5% AGN contamination. These numbers, all utilizing X-ray detections of AGN, are consistent with the value we find. However, other work with mid-IR and far-IR AGN identification has potentially shown a much higher AGN fraction of 75% at $z = 2.2$ (Bongiovanni et al. 2010). We do not perform any mid-IR or far-IR AGN analysis here. There is no significant variation between AGN fractions of GOODS-N with the deeper X-ray data and the COSMOS field. The small number statistics and shallower X-ray data in MUNICS and XMM-LSS explain the lack of AGN detections in those fields.

There are two other potential indicators of AGN activity: broad Lyα emission-line widths (which may also be seen in Lyman-α "blobs" where AGN activity is not evident (Francis et al. 2001; Bower et al. 2004; Matsuda et al. 2006; Smith & Jarvis 2007; Saito et al. 2008)), and the presence of CIV1549 over a fraction of the redshift range. The distributions of line widths, without any deblending of the [OII] doublet, is given in Figure 1.29. From the distributions, it is clear that line width information does not aid object classification. We find two cases where broad line objects (FWHM line widths > 500 km s^{-1}) have been classifed as Lyα without any

Table 1.6. Emission line/X-ray counterpart statistics

Field	Low-z counterparts *	High-z counterparts *	Depth †
COSMOS	2/112	4/55	0.73
GOODS-N	27/94	2/25	0.14
XMM-LSS	1/24	0/8	∼27
MUNICS	4/62	0/17	∼20

*(Counterparts/total emission lines)

†Assuming a point source, 10^{-15} erg s^{-1} cm^{-2} in 2-10 keV, if available, or 2-8 keV. The depth for XMM-LSS varies over the observed regions, and the sensitivity map for the X-ray coverage in MUNICS is not published.

X-ray detections, but none at > 1000 km s^{-1}. However, only one Lyα and CIV1549 source (indices 461 and 462) was not detected in X-ray.

Example sources

The rules to classify the emission-line objects have been described, but the display of the steps on actual VIRUS-P data is useful to establish confidence and the range of objects encountered. We will walk through the evidence for one emission source of each type and then give a summary display of representative subsamples.

LAEs The detection image of Figure 1.30 shows source index 229 in Tables 1.4 and 1.5 as a broadened, bright emission line detected in four fiber positions. The high flux ($41.6^{+4.2}_{-5.0} \times 10^{-17}$erg s^{-1} cm^{-2}) and the lack of a spectral continuum detection are already sufficient to meet the classification cut as an LAE. However, classification from the spectrum alone is only possible for the brightest emission-

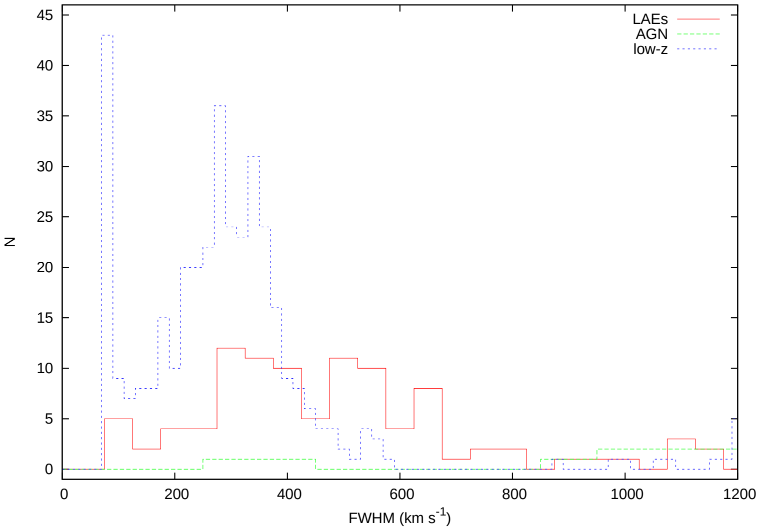

Figure 1.29 The line width distributions for all survey objects. We have subtracted an instrumental resolution of 300 km s^{-1} in quadrature. There is significant overlap between all populations making width-based classification impossible. No attempts have been made here to deconvolve the blended [OII] doublet. The low-z objects are generally contained to low widths, but the LAE distribution overlaps heavily with both the AGN and low-z distributions.

line sources in this sample. There are no counterpart emission lines at any of the tested transitions (§1.3.4), nor is there any associated X-ray detection. We next move to the deep, COSMOS R image in Figure 1.31. There, we find three plausible broadband counterparts with the brightest counterpart dominating the likelihood. There is no literature redshift for this object, but our Lyα line identification leads to EW$_0$=51^{+8}_{-8}Å, so the object is classified as an LAE. We give compact detection images for five additional LAEs in Figure 1.32.

Low-z objects The detection image in Figure 1.33 shows source index 308 as a high S/N, only slightly and not significantly broadened, emission-line source detected jointly in four fiber positions. The line flux is $18.4^{+3.5}_{-4.2} \times 10^{-17}$erg s^{-1} cm^{-2}, and the lack of a spectral continuum is insufficient for our EW-based classification scheme. There are no other emission lines detected in the object nor does the source have a X-ray counterpart. The COSMOS image (Figure 1.34) shows one bright continuum source barely offset from the emission-line centroid. A second, fainter object at larger separation is also analyzed at a much decreased likelihood, but would carry an LAE classification. Based on the most probable counterpart, we find a rest frame EW, assuming the line to be Lyα, of EW$_0$ = 8^{+2}_{-2}Å. This fails the EW cut, so we classify this as a low redshift object, presumably an [OII] emitter. The actual rest frame EW is then EW$_0$ = 25^{+6}_{-6}Å. We note that association with the other possible counterpart would lead to the opposite conclusion. However, the likelihood of that association is quite low, P= 0.1%, so we confidently classify the source as an [OII] emitter. We give compact detection images for five additional low redshift objects in Figure 1.35.

Objects with uncertain redshifts The detection image in Figure 1.36 shows source index 322 as a high S/N, broadened line along with a continuum detection in three fiber positions. The emission line flux is $16.7^{+4.4}_{-3.3} \times 10^{-17}$erg s^{-1} cm^{-2}. The

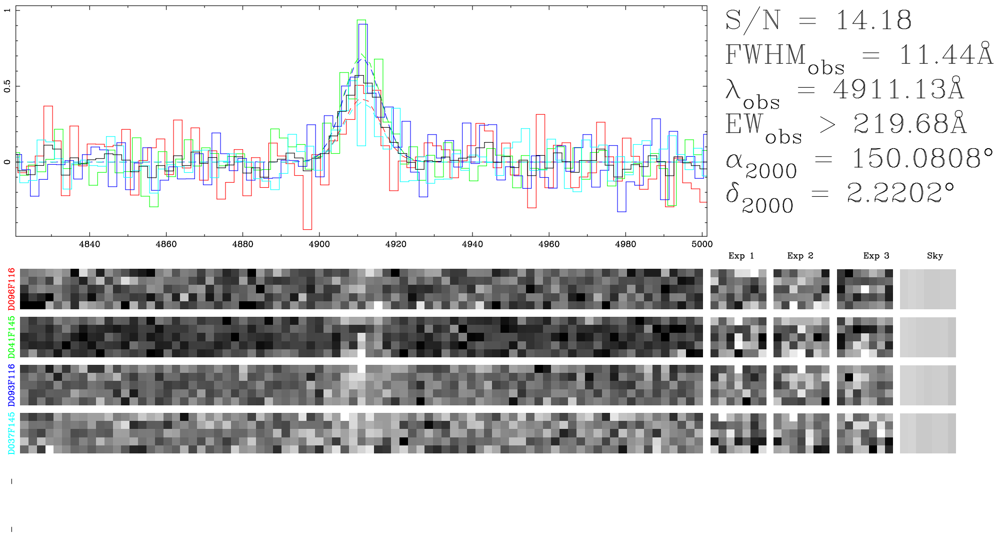

Figure 1.30 The VIRUS-P emission-line detection image for index 229 which lies in the COSMOS field. This object is undoubtably a real detection with one of the largest S/N ratios we find for any high-z object. In this case, the aperture is grown to include four fibers. The four rows in the Figure's bottom half show the spectra from the four detection fibers. The right side, square cut-outs show the spectra from individual 20-minute exposures and the sky model. The three exposures in each fiber are then biweight combined into the two-dimensional, bottom-left spectra and the one-dimensional spectra in the upper-left line plot. The collapsed, one-dimensional spectra are color-coded by fiber number. The Gaussian fits to each fiber are given by dotted curves. For visual clarity, the spectra are resampled and stacked into the black histogram. Continuum is not detected within a 200Å boxcar around the line, and the high level of flux permits the Lyα classification from the spectrum alone in this rare case. The tabulated EW instead is based on the flux density of the imaging counterpart. The quoted central wavelength in this figure has not yet had the heliocentric and vacuum corrections applied as is done with the tabulated values.

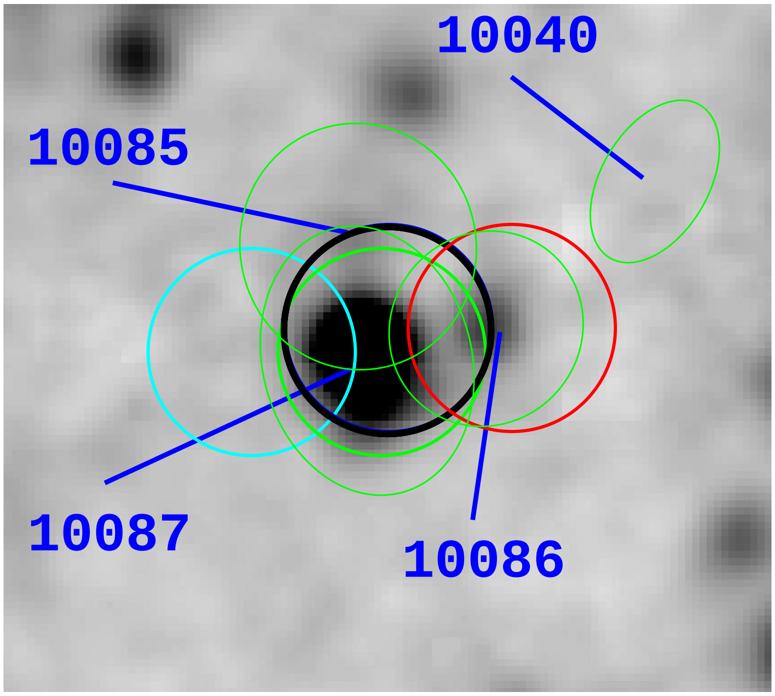

Figure 1.31 The ground-based, V_j imaging cutout for the Table 1.4 index 229. The four color circles represent fiber positions and are color coded in accordance with the spectra of Figure 1.30. The black circle indicates the emission line centroid. The Kron apertures from the imaging catalog are drawn as green, numbered ellipses. The best centered and brightest source is #10087 with an association likelihood of 87% and r^+=23.4. The next two most likely counterparts are #10085 at 6% and r^+=25.1 and #10087 at 5% and r^+=24.9. Either of these would also make the LAE EW cut, and it is possible that one or more LAEs at similar redshifts are jointly contributing to the emission-line flux, but this is unlikely.

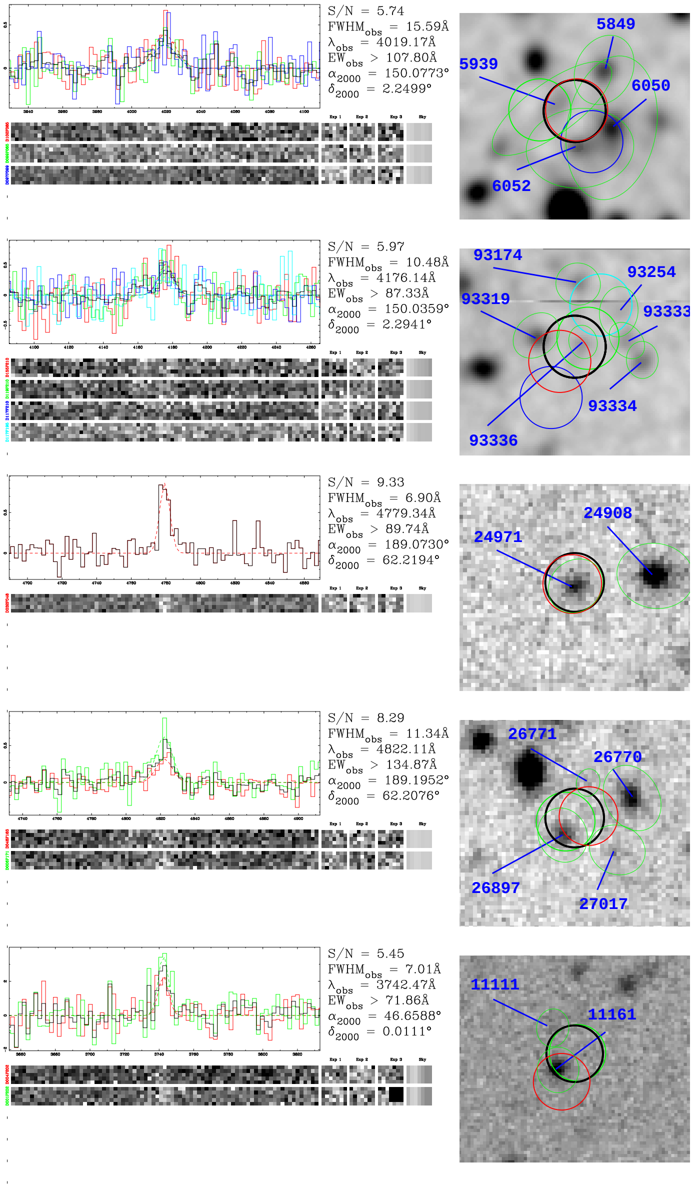

Figure 1.32 Five example detections of LAEs with the same formats as Figures 1.30 and 1.31. The first two lie in the COSMOS field, the next two lie in the GOODS-N field with the first redshift previously measured and the second new, and the final one lies in the MUNICS field. The entries from Table 1.4 for these five are indicies 223, 160, 341, 402, and 62. The best continuum counterpart matches are to #'s 5939, 93336, 24971, 26897, and 11161.

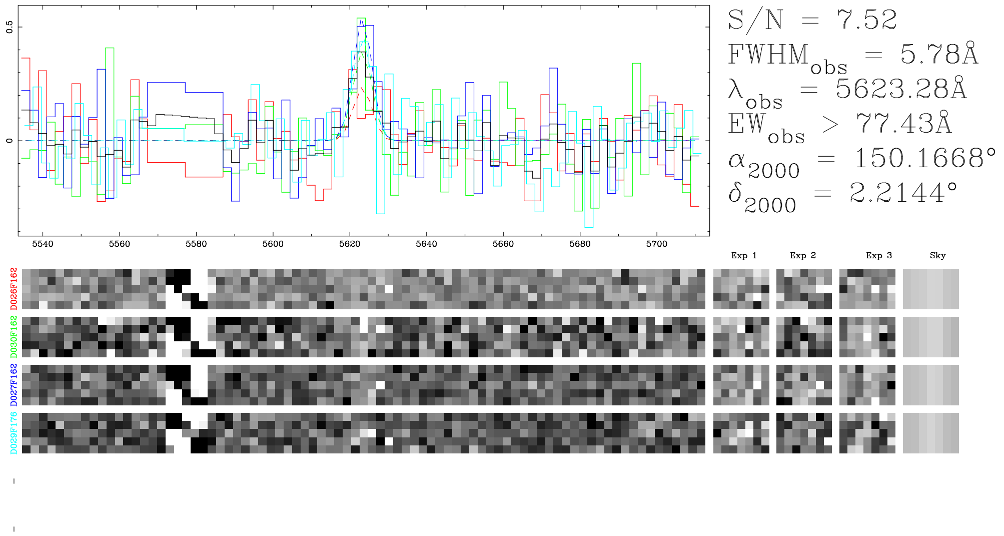

Figure 1.33 The emission-line source detection for index 308 which lies in the COSMOS field. The format is the same as in Figure 1.30. The spectrum-based EW does not go deep enough to discriminate between the classifications. This source neither shows alternate emission lines nor has an X-ray counterpart.

COSMOS image (Figure 1.37) reveals three plausible counterparts. The most likely (84%) counterpart implies an easy classification as an [OII] emitter with $\mathrm{EW}_{obs} = 37^{+8}_{-9}$Å. However, there is a non-trivial likelihood (8%) that the counterpart not the bright galaxy, but instead the fainter object. In this case, the source would be classified as an LAE. Despite this uncertainty, we place this object in Tables 1.5 with a [OII] classification.

1.3.5 Emission line source catalog

GOODS-N comparisons

Most of the detections and redshift classifications in this catalog are new to the literature. For instance in the COSMOS field, the magnitude limit of the spectroscopic cut (I_{AB} <22.5) to zCOSMOS (Lilly et al. 2009) gives little overlap with this sample. Fortunately, the large number of deep spectroscopic observations in

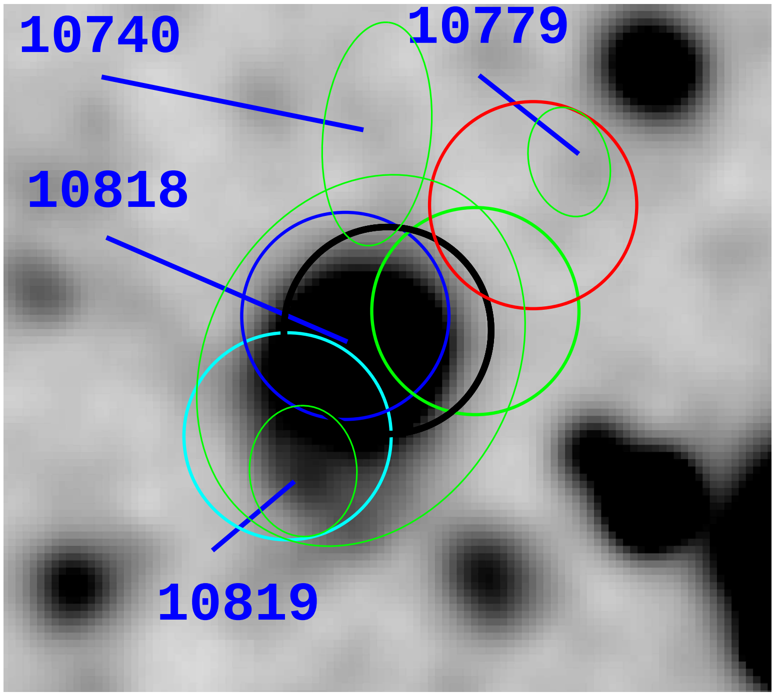

Figure 1.34 The ground-based, V_j imaging cutout for the Table 1.4 index 308. The detection spectra are given in Figure 1.33. The format is the same as in Figure 1.31. The counterpart #10818 at r^+=22.1 has a 99.5% likelihood of being associated. The observed EW of $30.9^{+14.9}_{-9.5}$Å leads to a firm low-z classification, presumably for [OII].

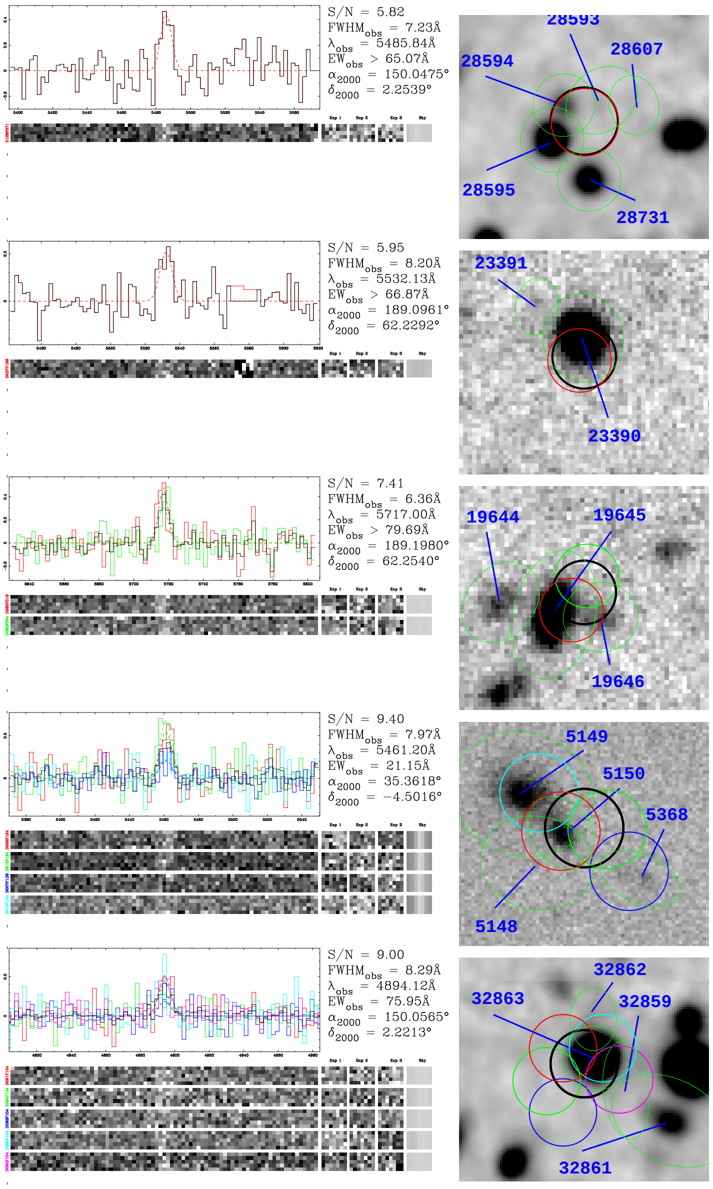

Figure 1.35 Five example detections of low-z objects with the format of Figure 1.33. The first and fifth lie in the COSMOS field, the second and third lie in the GOODS-N field both with previously measured redshifts, and the fourth lies in the XMM-LSS field. The entries from Table 1.4 for these five are indicies 178, 351, 406, 33, and 192. The best continuum counterpart matches are to #'s 28595, 23390, 19645, 5150, and 32863.

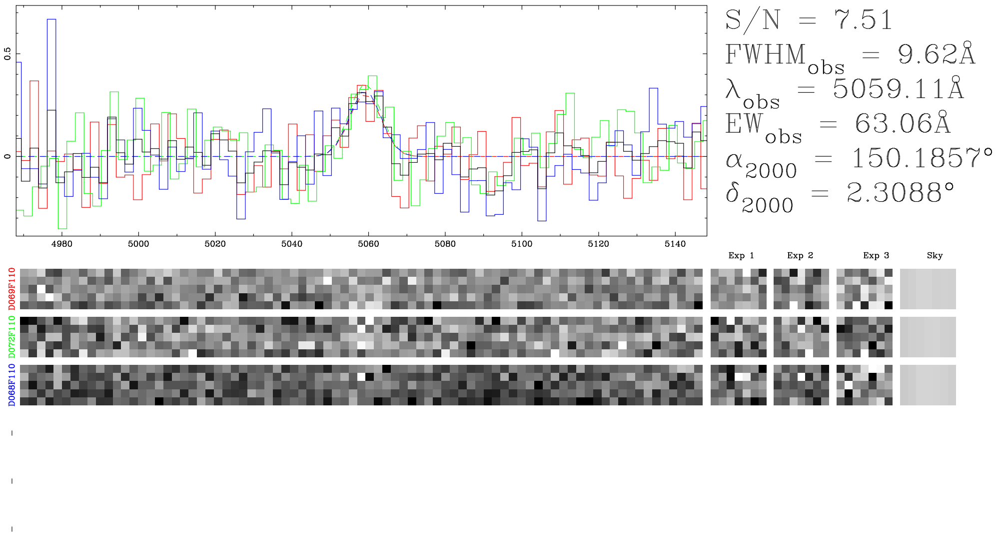

Figure 1.36 The emission-line source detection for index 322 which lies in the COSMOS field. The spectrum-based EW suggests a low-z classification. The format is the same as in Figure 1.30. Note that the emission line is broadened compared to the instrumental resolution.

the GOODS-N field comprise a better test sample. We have made a detailed comparison of our measurements to those of Barger et al. (2008), which includes most previous GOODS-N measured redshifts. We further include one Lyα match from Lowenthal et al. (1997) and one [OIII]5007 source from Wirth et al. (2004). We note that the observations from the literature often have larger spectral coverage and higher resolution than our data, allowing alternate classification methods.

We find 119 unique emission-line sources in GOODS-N. Three of these do not have measured optical broadband counterparts from the ground-based imaging, appear to be blended with foreground objects when examined with the Hubble Space Telescope (HST) images of Giavalisco et al. (2004), and are without published redshifts. We classify these as LAEs. In addition, there are nine other LAEs where we do measure a robust continuum counterpart but that are without published redshifts. We give the twelve new LAEs in GOODS-N in Figures 1.38 and 1.39. In addition, we find 92 low-z objects in common to the literature and 13 high-z objects

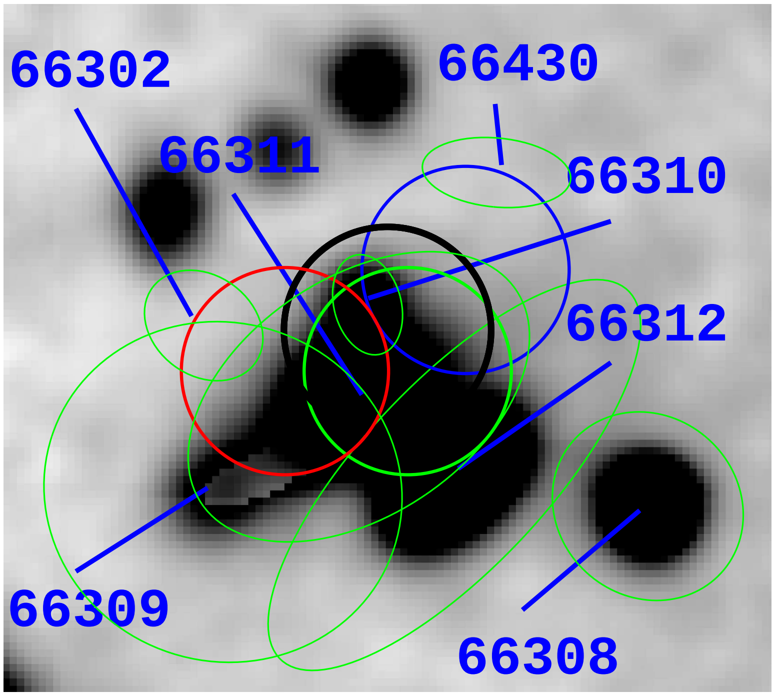

Figure 1.37 The ground-based, V_j imaging cutout for the Table 1.4 index 322. The detection spectra are given in Figure 1.36. The format is the same as in Figure 1.31. The counterpart #66311 at r^+=21.1 has a 84% likelihood in association. The counterpart #66312 is already assigned to the VIRUS-P detection of Table 1.4 index 310 at $\lambda_{\rm obs}$ = 4948.2Å. The counterpart #66310 at r^+=24.9 would be a LAE based on EW and looks like a reasonable candidate system resolved from #66311 in the HST image, but it only holds a 6% chance of association. This source is associated to #66311 as an [OII] emitter in the catalog.

(12 Lyα and 1 [CIV]). Finally, we find only two ojects in our catalog were misclassified. Source index 371 was originally called an LAE, but the literature reveals it to be a [CIV]1549 emitter. Source index 400 was originally called an [OII] emitter, but the literature reveals it to be an [OIII]5007 emitter. We have rectified Table 1.5 to reflect these two cases, and we then find an rms in $\frac{\Delta z}{1+z}$ of 0.001 and no offset compared to the literature, which is completely consistent with our 0.5Å line center uncertainty. A weakness in the literature samples is the lack of emission-line flux calibration, so we cannot use the previous samples to quantitatively test this survey's completeness. We have qualitatively confirmed the completeness by searching for literature objects in our spectra and finding many dozen at $3 < S/N < 5$.

Catalog summary

Table 1.4 contains a segment of the detected emission-line catalog with the full version available electronically. The entry ".." is given where there is not an applicable value. Each emission-line is prefixed with the identifier "HPS" to stand for HETDEX Pilot Survey. The column descriptions are: (1) the catalog number, (2) the emission-line right ascension in hrs:min:sec (J2000), (3) the emission-line declination $^\circ$:$'$:$''$ (J2000), (4) the observed emission wavelength in a vacuum, heliocentric frame (Å) with an estimated 0.5 Åuncertainty based on simulations. (5) the intrinsic FWHM of the emission line (km s^{-1}) after removal of a 5Å FWHM instrumental resolution and (with an estimated 300 km s^{-1} uncertainty), (6) the S/N of the emission-line flux detected within the aperture set of fibers, (7) the emission-line flux and error in 10^{-17} erg s^{-1} cm^{-2} as measured with the curve of growth method (§1.3.3), (8) the spatial FWHM of the emission line ($''$) as measured with the curve of growth method (§1.3.3), and (9) any additional entries in the table that share a position and redshift with the emission line (i.e. as with detections of other emission lines from the same source).

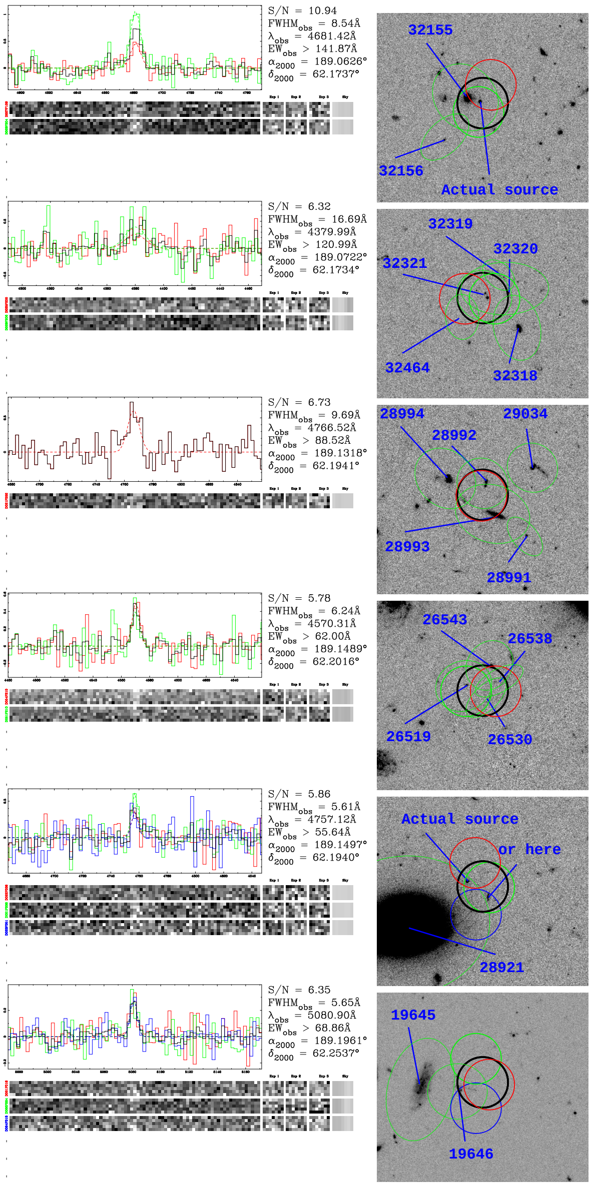

Figure 1.38 The spectral detection and HST ACS F606W (Giavalisco et al. 2004) cutouts for six of the twelve new, high-z redshift measurements in GOODS-N. From top to bottom, the objects are indicies 334, 338, 360, 372, 373, and 403 in Table 1.5. The first and fifth objects do not have identified counterparts in the ground-based images due to blending, although likely counterparts are identified in the HST data. The best counterparts for the second, third, fourth, and sixth objects are #'s 32321, 28992, 26519, and 19646.

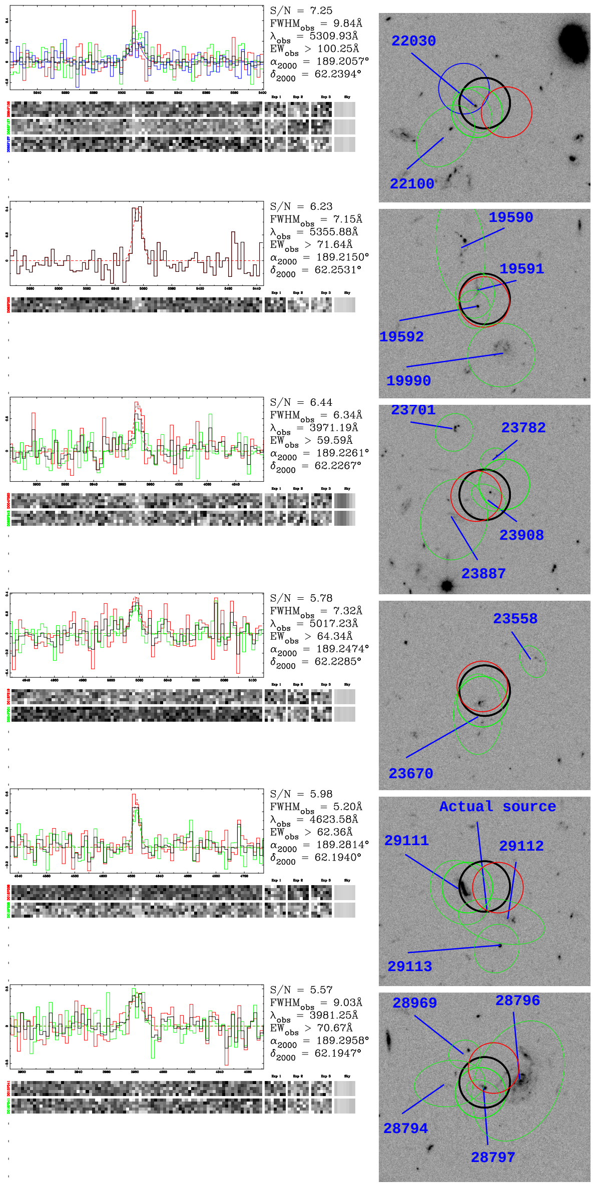

Figure 1.39 The spectral detection and HST ACS F606W (Giavalisco et al. 2004) cutouts for the final six of twelve new, high-z redshift measurements in GOODS-N. From top to bottom, the objects are indicies 415, 426, 434, 447, 467, and 474 in Table 1.5. The object with index 467 does not have an identified counterpart in the ground-based images due to blending, although a likely counterpart is identified in the HST data. The best counterparts for the remaining five, in order of listing, are 22030, 19592, 23908, 23670, and 28797.

Table 1.5 shows a segment of the counterpart and classification information for each emission-line detection with the full version available electronically. The entry ".." is given where there is not an applicable value. The column descriptions are: (1) the catalog number, (2) the best continuum-selected counterpart in the standard J2000 naming convention, (3) the R-band magnitude for this best counterpart (or the i' magnitude for MUNICS), (4) the probability of counterpart association (from Equation 1.6), (5) the rest-frame EW and uncertainties for this counterpart and the selected transition based on the R-band photometry, or the i'-band in MUNICS where no R-band is available (Å), (6) the rest-frame EW and uncertainties for this counterpart and the selected transition based on an interpolation between the two nearest filters (Å), (7) the transition of the emission line based on the EW cut and/or the presence of multiple emission lines, (8) the estimated redshift, (9) the probability of the emission line being Lyα as calculated by marginalizing over all potential counterparts, and (10) the X-ray counterpart in the standard J2000 naming convention.

Catalog properties

Figure 1.40 compares the distribution of rest frame EW for LAEs and [OII] emitters to the emission-line luminosity. Histograms of the rest frame EW distributions of both low and high redshift sources are shown in Figure 1.41. A maximum likelihood fit was made by taking $\mathrm{EW}_{\mathrm{rest}} > 20$Å where the samples should be complete. An exponential scale length of 128±20Å fits the LAE distribution and 22±1.6Å fits the [OII] distribution. The redshift distribution of all sources is given in Figure 1.42. No previously identified groups or clusters lie in our fields (e.g. Koester et al. 2007). In Figure 1.43, we give the color-color diagram for the sample's LAEs. We do not try to transform the filter systems into filter sets which are usually applied to LBG and BX galaxy samples, but we do plot the location of the LAE spectral template

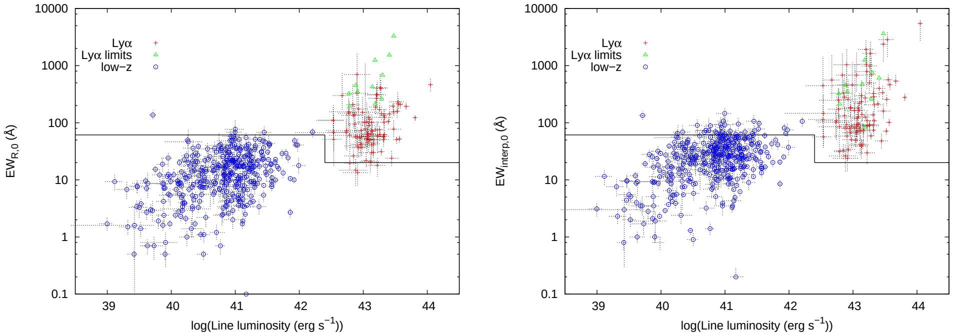

Figure 1.40 The distribution of rest-frame equivalent width and line luminosity for both the LAE and low-z samples. The primary classification line based on EW is drawn. The jog in the EW cut line is simply due to the cut being defined as $\mathrm{EW}_{\mathrm{rest}} > 20$Å assuming the line to be Lyα so the equivalent threshold in the [OII] restframe is 61Å. The drawn EW cut doesn't strictly apply to the low-z objects with emission at transitions other than [OII]. A trend between higher EW and line luminosity in the LAEs is somewhat visible but noisy over this survey's dynamic range. The same trend is seen in surveys with lower flux limits and discussed in Cassata et al. (2010). *Left* Continuum estimated only from the R-band photometry (or the i'-band in MUNICS). *Right* Continuum estimated from interpolation with the two nearest filters bounding each emission line's wavelength.

from Gawiser et al. (2007), made from Maraston (2005) stellar population synthesis modeling, over the relevant redshifts. We also show the locus of stars from Pickles (1998). Many of the LAEs appear consistent with color space expectations based on continuum-selected samples.

Spatially extended high-z sources Based on the detection threshold of §1.3.3, we find five objects whose Lyα emission appears significantly extended. Figure 1.44 gives the detection and broadband images for the objects, and Figure 1.45 shows the curve-of-growth analysis which determines their sizes. These five objects are indices 99 and 126 in the MUNICS field and indices 162, 164, and 261 in the COSMOS field. Index 99 is also a high EW object. Indices 162 and 261 are high EW if one use the R-band continua for the EW estimation, and they are both X-ray sources.

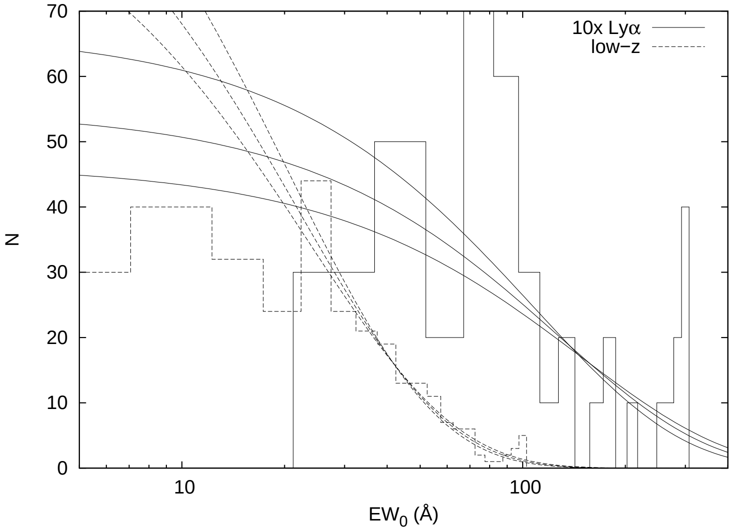

Figure 1.41 The distribution of rest frame equivalent width for values with S/N>3 for both the LAE and low-z sample by interpolating from the bounding broadband data. The LAE histogram has been scaled by 10× for visual clarity. A maximum likelihood fit was made by taking $\mathrm{EW}_{\mathrm{rest}} > 20$Å where the samples should be complete. An exponential scale length of 128±20Å fits the LAE distribution and 22±1.6Å fits the [OII] distribution. The exponential fits and error ranges are also plotted. The largest plotted bins contain all values that lie higher than the histogram range.

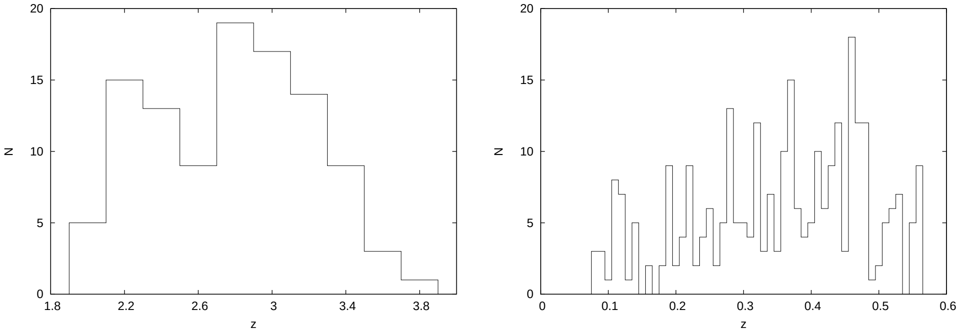

Figure 1.42 The distribution in redshift for all the survey objects. *Left* The LAE sample. *Right* The low-z sample. Each significantly overdense low-z bin is primarily contained in one survey field. The overdensities may be early indicators of groups or clusters, but the low number statistics preclude firm classification. There are no clusters from the Koester et al. (2007) catalog in any of this pilot survey's area.

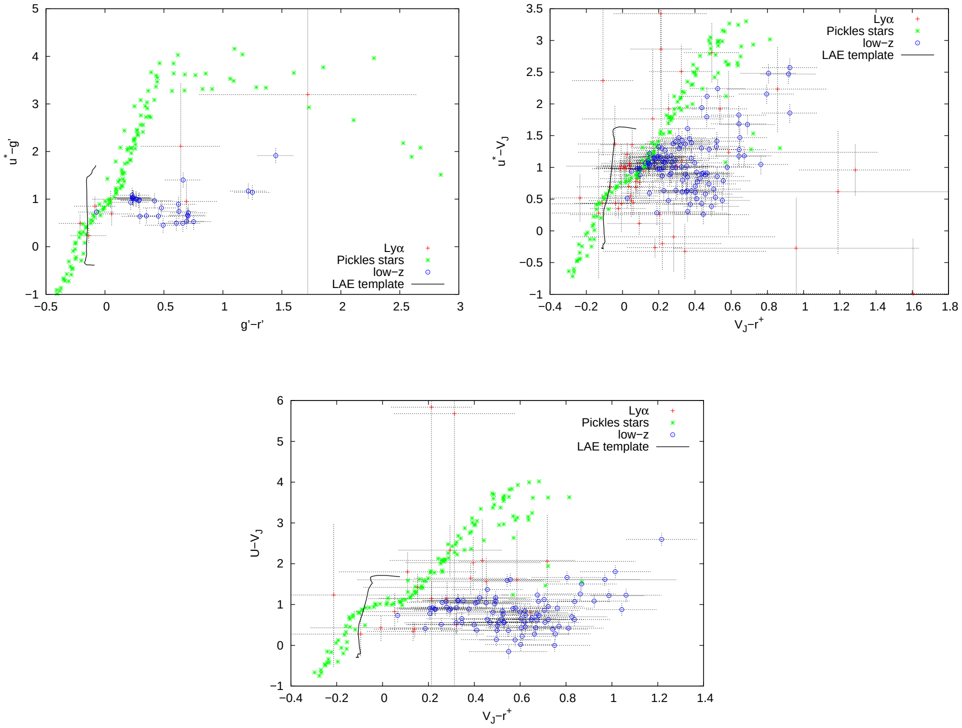

Figure 1.43 Color-color plots in the photometry bands that commonly define the Lyman Break Galaxy selection. Detections are not shown for the MUNICS field where we lack U-band data. The LBG selection rules are sensitive to the exact filter and telescope choice, so we do not transform these filter data into systems with published LBG rules. Instead, we synthesize colors of the Gawiser et al. (2007) LAE template as the solid, black curve for $1.3 < z < 4.5$ and stars (Pickles 1998). Albeit with some exceptions and frequently large color errors, the LAE sample is segregated from the low-z objects and lies where expected. *Top left* XMM-LSS objects, *Top right* COSMOS objects, and *Bottom* GOODS-N objects.

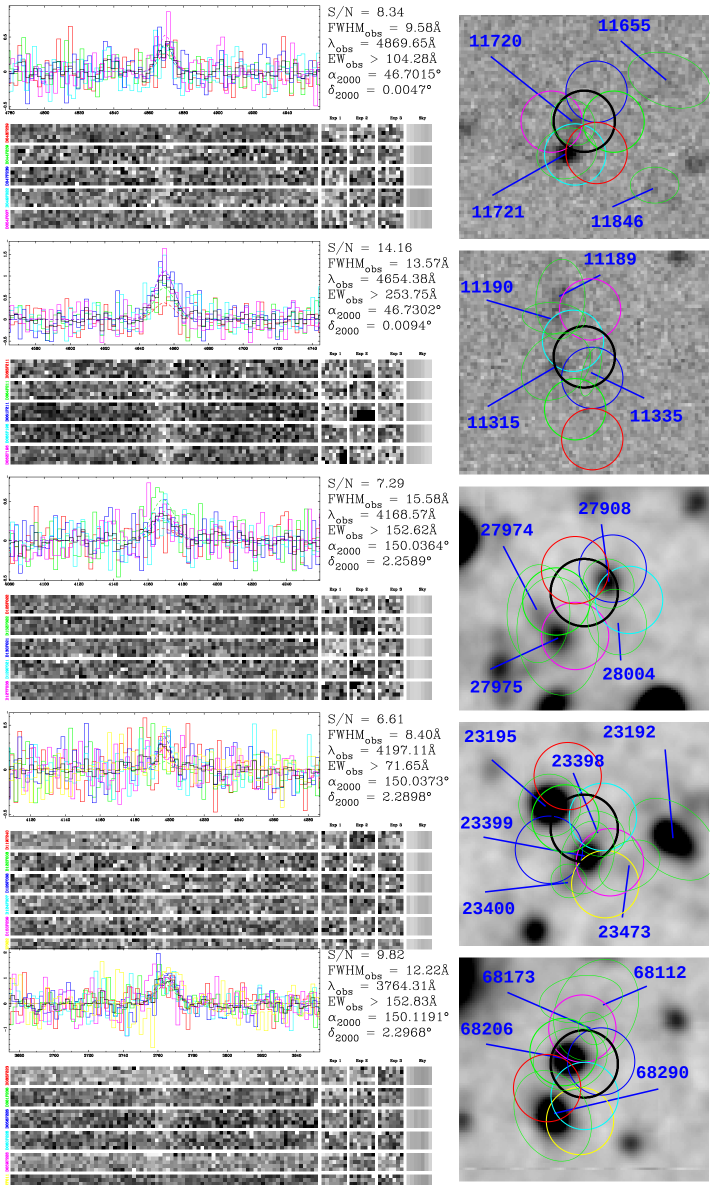

Figure 1.44 The five objects significantly extended in Lyα. *Left* The spectral detections. *Right* The R-band images (i' for the first two MUNICS objects). *First* Index 99 in MUNICS. The best counterpart is #11720. *Second* Index 126 in MUNICS. The best counterpart is #11315. This source is also a high EW LAE. *Third* Index 162 in COSMOS. The best counterpart is #27975. This source has an X-ray detection. *Fourth* Index 164 in COSMOS. The best counterpart is #23399. *Fifth* Index 261 in COSMOS. The best counterpart is #68206. This source has an X-ray detection.

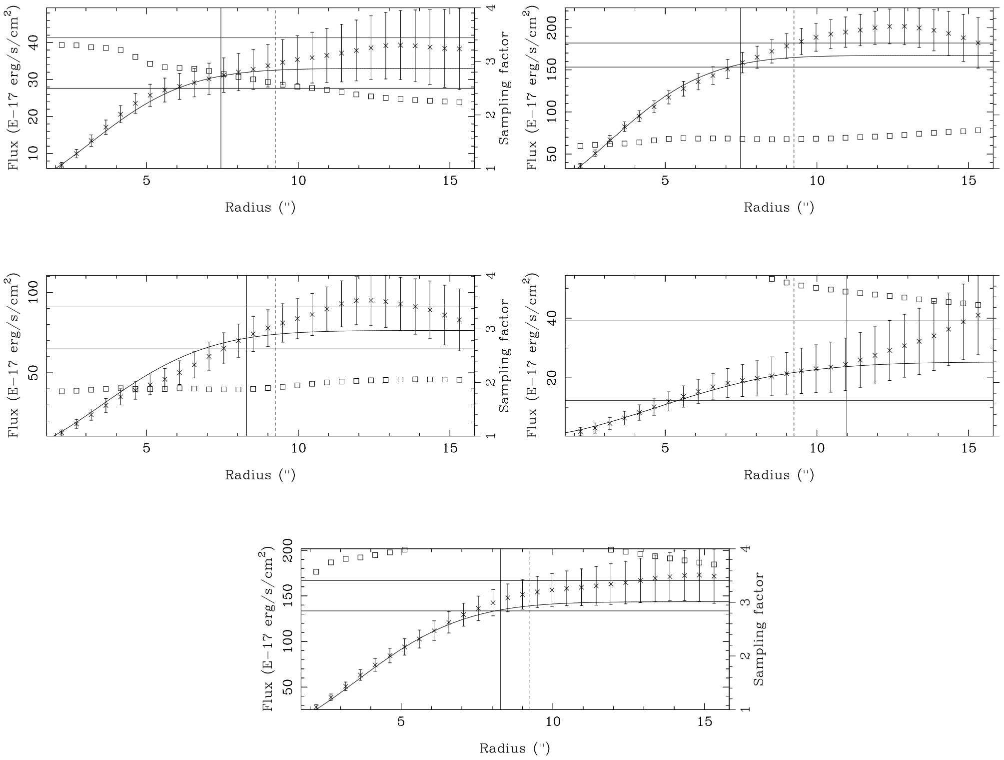

Figure 1.45 The curve-of-growth plots for the five significant objects extended in Lyα. The format is the same as in Figure 1.23 and described therein. *Top Left* Index 99 in MUNICS. The best counterpart is #11720. *Top Right* Index 126 in MUNICS. The best counterpart is #11315. This source is also a high EW LAE. *Middle Left* Index 162 in COSMOS. The best counterpart is #27975. This source has an X-ray detection. *Middle Right* Index 164 in COSMOS. The best counterpart is #23399. *Bottom* Index 261 in COSMOS. The best counterpart is #68206. This source has an X-ray detection.

High EW LAEs LAEs with $\mathrm{EW_{rest}} > 240\text{Å}$ are potential sites of exotic energy sources or unusual metallicity since stellar population modeling has shown that a normal initial mass function (IMF) cannot produce such high EWs (Charlot & Fall 1993). If we consider our whole catalog and use the EW measurements derived from interpolating with the two nearest filters, we find 11 LAEs without broadband counterparts and a further 21 LAEs with counterparts that have $\mathrm{EW_{rest}} > 240\text{Å}$ at $> 1\sigma$ significance. However, in order to make a conservative estimate, we instead use EW estimates based on the R-band photometry only and restrict the discussion to sources with emission-line detection S/N>6.5 to avoid false detections. This instead leaves only 1 LAE without a counterpart and 2 LAEs with counterparts meeting the high EW criterion. We note that a number of the emission lines without broadband counterparts may have their origins obscured by ground-based seeing. For instance, three of the objects with new redshifts in GOODS-N have their best counterparts blended behind foreground object and are shown as part of Figures 1.38 and 1.39. For homogeneity between all fields, we only measure continua from the ground-based images in this work. Some of the entries in Table 1.5 as being without counterparts may be caused by blending and not image depth. In fact, the only emission-line detection with high confidence as being without a counterpart is index 314.

Figure 1.46 shows the detection and image data for the three significant high EW LAEs. The top figures show the data for index 314, an LAE with $z = 2.6312$ but with no counterpart in the COSMOS image and $\mathrm{EW_{rest}} > 348\text{Å}$ (1σ). The middle figures show the data for index 126 in MUNICS. Although the counterpart is fairly bright at $m_{i'} = 24.3$, the very bright emission line implies $\mathrm{EW_{rest}} > 352\text{Å}$ (1σ). We note that this z= 2.8276 object is also significantly extended in Lyα with FWHM=$7\farcs5$. Finally, the bottom figures show the data for index 231 in COSMOS with $\mathrm{EW_{rest}} > 282\text{Å}(1\sigma)$ and $z = 2.7215$. This object is marginally extended in Lyα (FWHM=$6\farcs3$), but also compatible with a point source and poor seeing. We find a 3% high-EW fraction in the LAE sample by our best estimates. However, the fraction could be as high as 31% by our most inclusive criteria.

LAE number density expectation The spectral and spatial sensitivity limits along with the completeness simulation of §1.3.3 completely define the survey's selection characteristics and are necessary inputs to the luminosity function calculations that will follow in future papers (Blanc et al. 2010). By considering all these effects, namely, the completeness distribution we are able to achieve with the detection routine (§1.3.3) and simulated data (§1.3.3), and finally the LAE luminosity function of Gronwall et al. (2007), we predict this sample should contain 121 LAEs. The dominant uncertainty in this prediction is cosmic variance, which can be approximated by linear theory for a given redshift, volume, and number density from Somerville et al. (2004) Figure 3. The effective Lyα survey volume in Gronwall et al. (2007) is 1.1×10^5 h_{70}^{-3} Mpc^3 which implies a relative cosmic variance of σ_v ∼35% and σ_v ∼15% for the volume of this survey. Within these factors, the LAE number statistics from this survey are low but not in serious conflict with earlier determinations.

1.3.6 Summary of science sample

We present untargeted integral field spectroscopic observations over 169 $\square'$ with the goal of characterizing emission-line galaxies at low ($z < 0.56$) and high ($z >\approx 2$) redshifts. In this first of a series of papers, we describe the design, observations, calibrations, reductions, detections, measurements, and classification methods for the survey. The primary classification method we employ uses equivalent width cuts computed by matching the emission-line objects to continuum counterparts in existing, deep images. We find that effective object classification can be made using $\mathrm{EW}_{\mathrm{rest}} > 20$Å where the continuum is defined using a single band of deep photometry, preferably in the R-band. We find 397 unique emission-line galaxies:

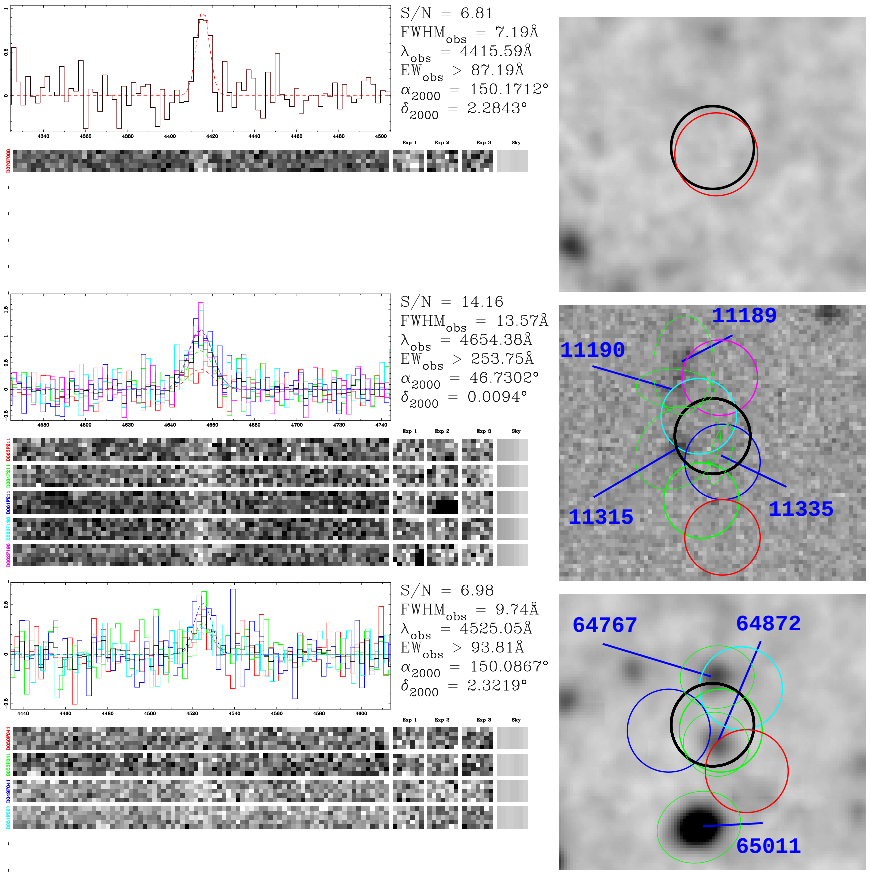

Figure 1.46 The three high-significance LAEs with EW$_0$ >240Å. *Left* The spectral detection figures. *Right* The *R*-band images. *Top* Index 314 in the COSMOS field. No continuum counterpart is found. *Middle* Index 126 in the MUNICS field. The best counterpart is listed as #11815. The emission line is also significantly spatially extended. *Bottom* Index 231 in the COSMOS field. The best counterpart is listed as #64872.

168 over a 71.56 $\square'$ area in the COSMOS field, 118 over a 35.52 $\square'$ area in the GOODS-N field, 79 over a 49.85 $\square'$ area in the MUNICS field, and 32 over a 12.30 $\square'$ area in the XMM-LSS field. The two transitions most frequently observed are [OII] (285 galaxies) and Lyα (105 galaxies). Based on a non-evolving Gronwall et al. (2007) luminosity function, we should have detected 121 LAEs in this survey; the difference is within the range of cosmic variance. The field with the deepest X-ray data (GOODS-N) shows an AGN fraction in the LAE sample consistent with that of the shallower fields (6%). We compare our data to the extensive GOODS-N targeted spectroscopy to verify our object classification and confirm 92 low-z and 13 high-z galaxies. Moreover, we derive new redshifts for a further 2 low-z and 12 high-z galaxies in the GOODS-N field. Over all fields, eleven high-z objects do not possess optical counterparts despite the imaging depth; these are either very high EW objects, contamination from noise, or objects whose counterparts have been blended by ground-based seeing. However, within the remaining LAEs we find a distribution of EW_0 that can be described by an exponential scale length of 128 ± 20Å and with only three objects at $\mathrm{EW}_0 > 240$Å at $>1\sigma$ significance. Many of the newly discovered LAEs lie in the color ranges consistent with previous work.

The main contaminant in our LAE sample is simply noise, which should be 10% of the LAE sample based on simulations. A totally pure subsample of 68 LAEs can be defined using this catalog at $S/N > 6$. We find five sources of Lyα emission that have a high significance as being spatially resolved, at least two of which are AGN. The pilot survey has validated that IFS searches for LAEs perform as expected. The forthcoming larger FOV of the full HETDEX survey will vastly improve the survey efficiency of this method.

Acknowledgements: This work was done in collaboration with Guillermo A. Blanc, Gary J. Hill, Karl Gebhardt, Niv Drory, Lei Hao, Ralf Bender, Joyce Byun, Robin Ciardullo, Mark E. Cornell, Steven L. Finkelstein, Alex Fry, Eric Gawiser,

Caryl Gronwall, Ulrich Hopp, Donghui Jeong, Andreas Kelz, Ralf Kelzenberg, Eiichiro Komatsu, Phillip J. MacQueen, Jeremy Murphy, P. Samuel Odoms, Martin Roth, Donald P. Schneider, Joseph R. Tufts, and Christopher P. Wilkinson.

Chapter 2

Lyman-α halos in radio galaxies

2.1 Introduction

Progress in understanding high redshift radio galaxies (HzRGs, where we arbitrarily consider high to mean z>≈2) will advance our picture of both massive galaxy formation and evolution. HzRG are thought to be the progenitors of massive local cluster giant elliptical galaxies. Their radio signal allows detection over a huge range of cosmic time. We will only discuss a few revelant trends of HzRGs as extensive summaries are given by McCarthy (1993) and Miley & De Breuck (2008). Radio galaxies are found to be associated with some of the largest stellar mass galaxies at all redshifts (Lilly & Longair 1984; Pentericci et al. 2001). The environments of massive radio galaxies have also been progressively traced to higher redshifts with radio galaxies typically residing in cluster environments at all redshifts (Longair & Seldner 1979; Prestage & Peacock 1988; Hill & Lilly 1991; Carilli et al. 1997; Best 2000). HzRGs often show extended Lyman-α emission up to and beyond their radio emission radii. The Lyman-α emission probes warm, ionized gas. Against this emission is often seen line profile structure which serves as a probe of the neutral gas through scattering and absorption. The properties of Lyman-α

blobs (LABs) (Keel et al. 1999; Steidel et al. 2000; Palunas et al. 2004) and the gas halos of quasars (Heckman et al. 1991; Barkana & Loeb 2003) are morphologically similar to those in HzRGs.

Cooling radiation may be an important source of extended Lyman-α radiation, and an indication of ongoing galaxy formation as infalling gas continues to build the galaxy's mass (Haiman et al. 2000; Fardal et al. 2001). The most direct signature of a high redshift cooling flow is extended Lyman-α emission powered by the decrease in gravitational potential energy from infalling material. This is a challenging observation and interpretation as other sources of Lyman-α generation are usually stronger than the cooling radiation, but Nilsson et al. (2006) and Smith & Jarvis (2007) show promising cases. Low redshift cooling flows have a long history of investigation primarily through X-ray observations (e.g. Fabian 1994), but space based observations (Kaastra et al. 2001; Peterson et al. 2001; Tamura et al. 2001) have given evidence against most cases of low redshift, strong cooling flows and diminished the importance of this mechanism for galaxy growth. Most massive galaxy growth is now thought to occur through major mergers. Li et al. (2007) show by a semi-analytic model, for example, the likely growth history of a galaxy like the SDSS quasar J1148+5251 at z=6.42 (Fan et al. 2003) where gas rich major mergers dominate as the source of the mass growth and a starburst phase predates a quasar phase. Observationally checking and challenging theories for the relative contributions of mergers and steady gas accretion for different galaxy types and epochs is an important goal.

In terms of evolution, AGN feedback has been proposed (Valageas & Silk 1999) as the mechanism to produce the tight black hole/stellar mass correlation (Magorrian et al. 1998; Gebhardt et al. 2000a; Ferrarese & Merritt 2000) and the difference between the theoretical (Kaiser 1986) and the observed (Markevitch 1998; Arnaud & Evrard 1999) relation between cluster temperature and X-ray luminosity.

Radio galaxies in particular and their powerful jets have been invoked as candidates for causing feedback (Inoue & Sasaki 2001; Rawlings & Jarvis 2004; Croton et al. 2006) by depositing mechanical and thermal energy to their surroundings. A signature of outflowing gas at a velocity exceeding the halo escape speed would be an important observation of high redshift feedback.

2.2 Observations

On 2007 UT March 14 and 15 we observed B2 0902+34 with the visible integral-field replicable unit spectrograph prototype (VIRUS-P) (Hill et al. 2008b) on the 2.7m Harlan J. Smith Telescope at McDonald Observatory. VIRUS-P is a spectrograph with an integral field unit (IFU) of 247 fibers in a hexagonal pattern close pack with a one third fill factor. Fed at f/3.65, the fibers have a diameter of 4.1″ and a 107x107 □″ field of view. Seeing was ≈2″, significantly smaller than the fiber diameter. The first night was nominally photometric, while the second was not. The instrument configuration gave us 236 working fibers spread over the field. Astrometry of the fiber positions has been calibrated to 1.0″ rms from a fixed, offset guide field. Observations of three offset positions (called dithers) fill in the area. We took three exposures of 1200s at each of six subdither positions. A subdither as defined here is a second dithering pattern centered on the fiber intersections of the first dither set. We use this mode to decrease the astrometric uncertainty of spatially unresolved sources, mitigate local CCD cosmetics, and subsample extended emission. The wavelength range was 3400-5680Å with a spectral resolution of 5.0Å. Wavelength calibration was done with eleven arc lamp lines of Hg and Ne yielding a $\sigma_\lambda = 0.4$Å. Twilight flats were used to remove pixel-to-pixel variation, fiber-to-fiber variation, and the fiber illumination profile. We have used our own custom written software for all reductions. Notably, this reduction does not perform any resampling or linearization of the data. The estimates of the sky spectrum were made from neighboring objectless fibers and fit with bsplines (Dierckx 1993) in a similar manner to optimal longslit sky subtraction methods (Kelson 2003). We estimate a spectrally unresolved 5σ line flux limit of 7×10^{-17} erg s^{-1} cm^{-2} and a surface brightness limit of 24.0 AB mag arcsec^{-2} for wavelengths longer than 4000Å when under photometric conditions.

We detected Lyman-α emission from the low surface brightness halo of B2 0902+34 in fifteen different fiber positions. We only include fibers that show emission above a signal-to-noise ratio of 3, calculated from the noise and counts within the full width half maximum of a single Gaussian fit. We perform Monte Carlo line fitting where 100 realizations of our data sampled from normal distributions with our estimated errors produce distributions in our fit parameters from which are extracted central values and dispersions. All uncertainty quotes are 1 sigma estimates by this method and similar to the uncertainties from the covariance matrices. All quotes of line width remove the instrument resolution in quadrature. Table 2.1 shows single Gaussian fits to each fiber's spectrum. Figure 2.1 shows the positions of the detections against a narrowband image we have taken and the radio data of Carilli (1995). We confirm the general line profile properties reported in Reuland et al. (2007) for the region covering their slit, but our observations span the entire 2D structure. The entire halo contains an emission peak at 5339.0 ± 2.0Å with a FWHM of 600±90 km s^{-1} which is well fit by a single Gaussian. This primary emission is mostly spatially symmetric and smoothly varying in brightness near the radio core emission although slightly extended toward the NE. At $\approx$ 15% of the strength of the primary emission, a secondary emission peak can be fit as a Gaussian at 5324.5±1.7Å with a FWHM of 630±270 km s^{-1}. This secondary emission exists in three fibers on the SW side of the halo. Throughout this work, we will refer to any flux with a line center above 5330Å as primary emission and any flux with a line center below 5330Å as secondary emission. For the three fibers with S/N high enough for a more complex fit, we give fits in Table 2.2 where the fitting function consists of two independent positive Gaussians. Depending on interpretation, this feature may be due to discrete emission sites or scattering and absorption by neutral hydrogen. To aid comparison, we give fits in Table 2.3 with a single positive Gaussian and an absorbing Voigt function. Figure 2.3 shows the data and fits to select, representative spectra, and Figure 2.4 shows the brightness maps of the two spectrally decomposed signatures as positive Gaussians. Our data show that the longslit spectroscopy of Lilly (1988), Martin-Mirones et al. (1995), and Reuland et al. (2007) are consistent though only the latter found this secondary, bluer emission because of the different slit position angles under their observations and the different flux limits. The two dimensional spatial constraints on the secondary emission afforded by our data will be crucial to a proper interpretation. We have searched for nearby LAEs in the surrounding fibers but have found none within the field. We do not make a statistically significant detection of continuum in B2 0902+34 which places a lower limit on the rest frame equivalent width from the six brightest fibers at > 67 Å($5\ \sigma$ continuum limit) as shown in Figure 2.5. We have not attempted a flux calibration due to the non-photometric conditions, so the aperture to aperture variation in surface brightness is overestimated by our data, and the flux limit between apertures is not constant.

2.3 Interpretation

A bimodal Lyman-α line profile may be generated by several effects. First, Cooke et al. (2008) give imaging and spectroscopy of a Lyman Break Galaxy where the line profile is similar to that of B2 0902+34, which they interpret as being due to multiple merging galaxies even though the line widths are surprisingly narrow and the morphology undisturbed. This possibility in B2 0902+34 cannot be easily discarded. The secondary Lyman-α peak and a peak of continuum emission in Fig-

Table 2.1. Individual fiber Lyman-α detections in B2 0902+34

Unique position number	RA (J2000)	Dec (J2000)	Central λ (Å)	Dispersion (Å)	Normalized Flux	S/N	χ^2	Degrees of Freedom
1	9:5:30.35	34:8:01.9	5339.24±7.1	11.5±9.7	$0.27^{+0.31}_{-0.27}$	3.0	10.8	11
2	9:5:29.71	34:8:01.8	5338.96±0.9	1.1±1.5	0.19±0.07	5.2	6.4	3
3	9:5:30.05	34:7:55.1	5337.24±1.0	9.8±1.1	1.00±0.11	18.2	25.0	17
4	9:5:30.03	34:7:59.7	5338.60±0.6	3.5±0.6	0.39±0.05	9.4	1.1	5
5	9:5:30.36	34:7:53.0	5338.84±2.2	4.4±3.6	0.40±0.20	3.3	2.5	4
6	9:5:29.73	34:7:53.0	5332.51±2.8	8.8±3.2	0.33±0.11	5.3	13.1	11
7	9:5:30.35	34:7:57.6	5338.45±1.0	7.9±2.0	0.68±0.13	10.9	11.3	11
8	9:5:29.71	34:7:57.5	5339.27±1.5	4.3±2.0	0.26±0.07	3.9	7.7	5
10	9:5:29.81	34:7:59.7	5337.92±1.0	2.5±1.0	0.20±0.05	5.1	4.4	4
11	9:5:30.15	34:7:53.0	5337.66±1.3	2.3±2.2	0.25±0.09	6.5	5.7	3
12	9:5:30.13	34:8:01.9	5336.14±5.6	6.4±5.1	0.22±0.13	4.6	16.0	7
13	9:5:30.46	34:7:55.2	5339.12±2.2	4.0±1.6	0.19±0.07	4.3	3.8	3
14	9:5:29.83	34:7:55.1	5338.03±2.9	14.1±1.9	0.68±0.16	8.6	39.8	21
15	9:5:30.13	34:7:57.6	5338.96±1.0	4.4±1.9	0.33±0.09	7.9	1.7	4

Table 2.2. Select regions in B2 0902+34 fit with two Gaussians

Unique position number	Central λ_1 (Å)	Dispersion$_1$ (Å)	Normalized Flux$_1$	Central λ_2 (Å)	Dispersion$_2$ (Å)	Normalized Flux$_2$
2	5339.22±1.5	6.5±2.5	0.78±0.27	5323.34±7.7	$3.3^{+5.0}_{-3.3}$	$0.19^{+0.28}_{-0.19}$
5	5338.98±4.0	4.3±3.3	0.15±0.10	5326.97±3.2	2.8±2.7	0.14±0.09
12	5344.37±1.5	4.7±3.0	0.31±0.13	5325.49±1.0	2.9±1.0	0.22±0.06

Table 2.3. Select regions in B2 0902+34 fit with Gaussian and Voigt profile

Unique position number	Central λ_e (Å)	Dispersion (Å)	Normalized Flux	Central λ_a (Å)	b (km/s)	Column density (1/cm^2)
2	5335.79±2.0	8.9±1.6	1.11±0.39	5329.86±1.7	110^{+275}_{-110}	$8.3\times10^{13}{}^{+1.4\times10^{14}}_{-8.3\times10^{13}}$
12	5335.77±2.7	8.1±3.4	1.25±1.00	5335.40±1.4	255^{+262}_{-255}	$2.4\times10^{14}{}^{+3.8\times10^{14}}_{-2.4\times10^{14}}$

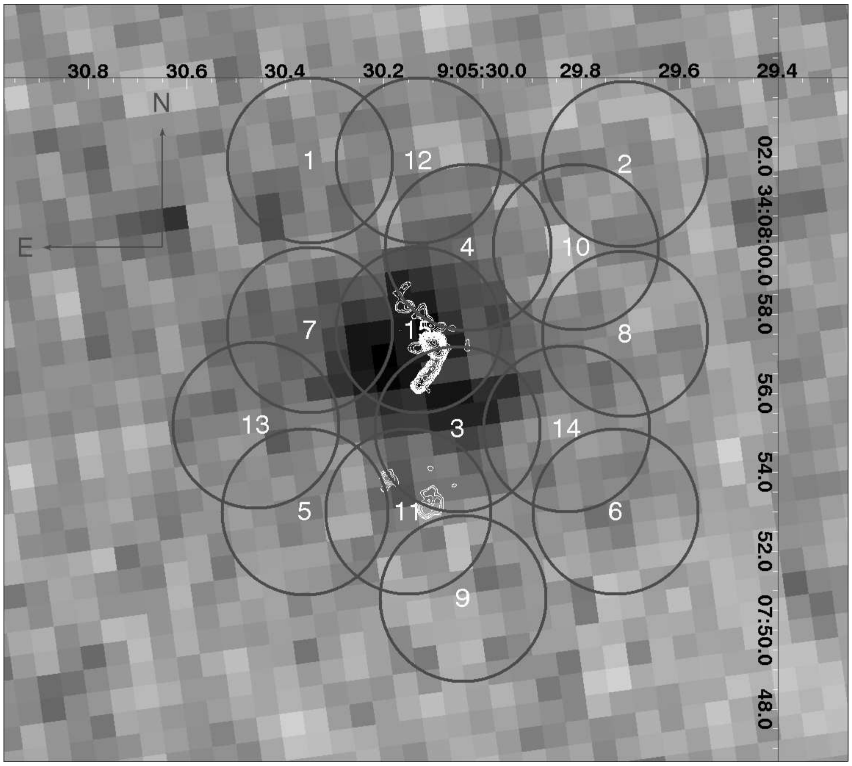

Figure 2.1 The fibers with detected Lyman-α emission are plotted over a narrowband Lyman-α image of the radio galaxy center. For reference, log scale contours are drawn of the 1.65 GHz image at $0.15''$ resolution from Carilli (1995) with range 0.36-92.16 mJy/beam. Each fiber has a diameter of $4.2''$.

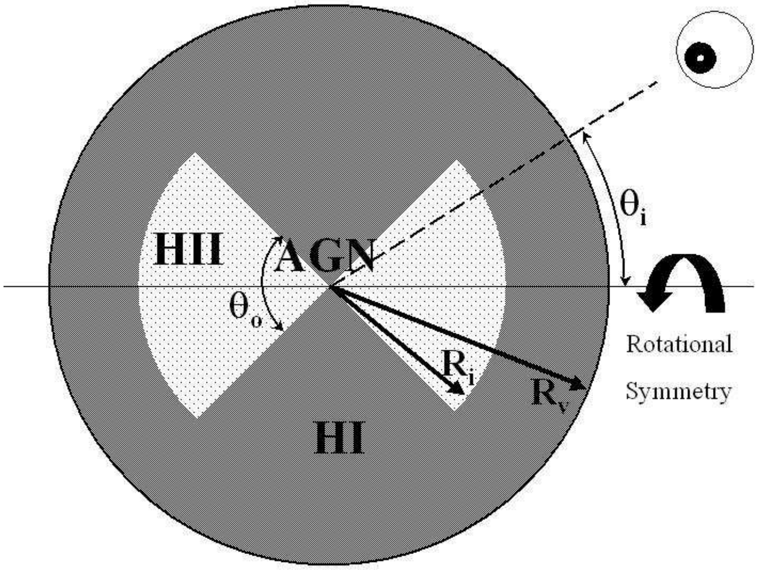

Figure 2.2 The geometry of our simulation. θ_i is the inclination as constrained by Carilli (1995). R_v is the system's virial radius. R_i is the ionization radius of the cones. θ_o is the opening angle of the ionization cones assumed here to be 90°. R_i, R_v, θ_o, and two variables controlling the velocity field are the model's five tunable parameters.

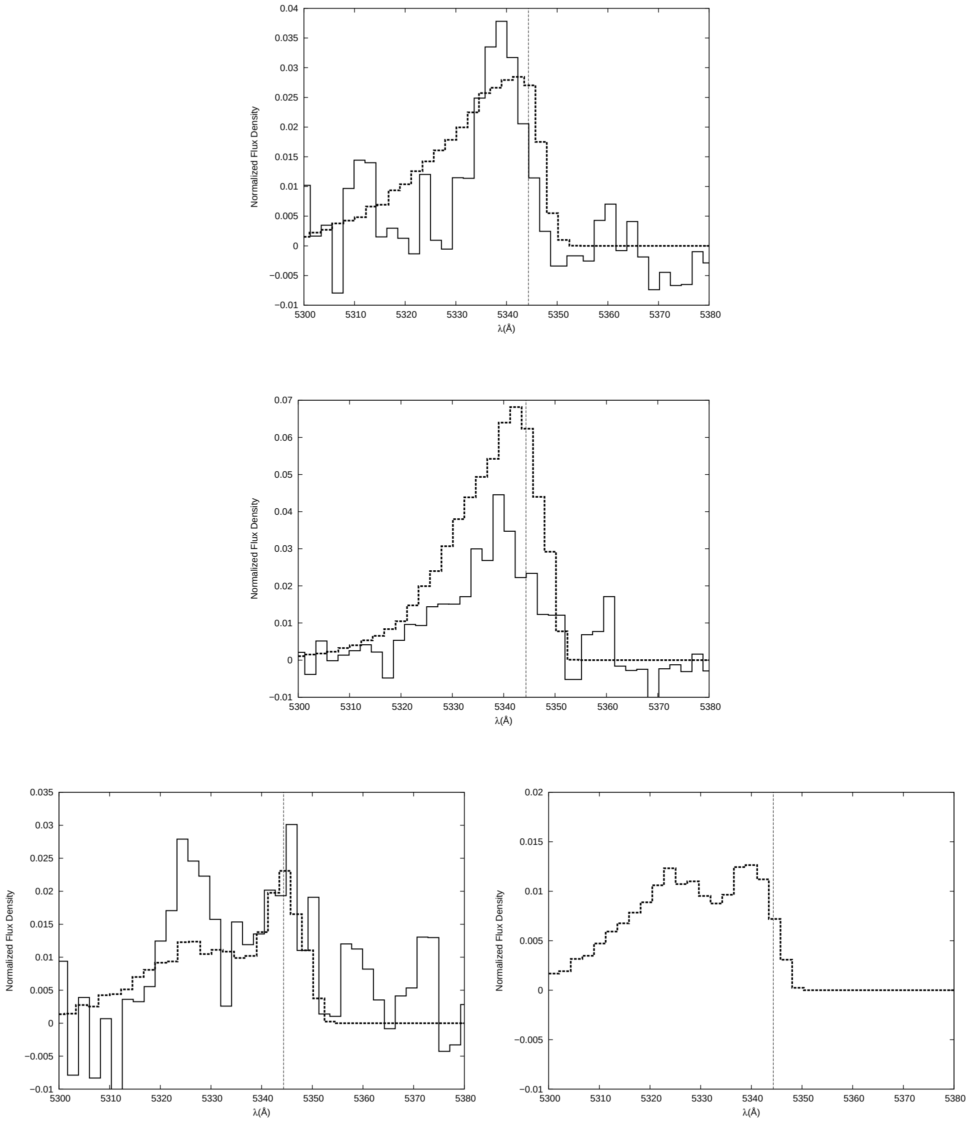

Figure 2.3 The spectra of both our IFS data and resonant scattering simulation from select fibers. The thin dotted line indicates the redshift measured for 21 cm absorption. *Solid* Observed. *Thick dotted* Simulated. *Top* Fiber 4, representative of most of the halo area where neither cone directly projects. *Middle* Fiber 7, representative of regions spanned by the near photoionized cone. *Bottom left* Fiber 14, representative of regions spanned by the rear photoionized cone. Only these regions show a bimodal line profile. *Bottom right* A region in the simulation near fiber 14. While we did not have a fiber on this exact position, the bimodal spectrum here is a good match to its neighbor in fiber 14.

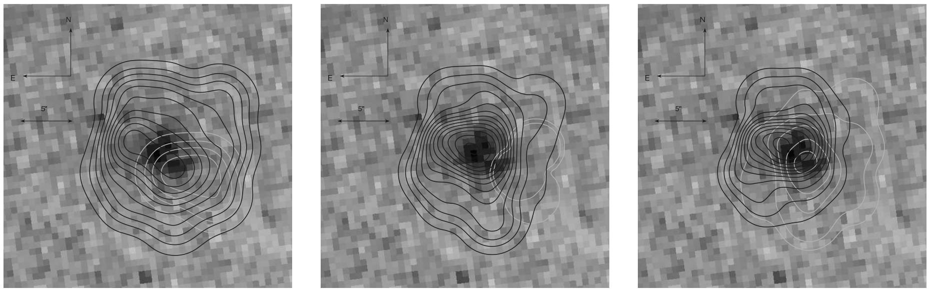

(a) Observed

(b) Simulated, Spectral Decomposition

(c) Simulated, Origin Cone Decomposition

Figure 2.4 Log contours of surface brightness. *Left* Fits to the data. The primary and secondary peaks are respectively dark and light. *Middle* The simulations described in §2.3, where the same type of spectral decomposition as for the data between primary and secondary is performed. *Right* The same simulations, but now with a decomposition regardless of the spectral signature but where the dark contour follows emission from the near photoionized cone and the light contour from the rear photoionized cone. This optimistically represents a clean detangling of spectral signal that a model with more optimized parameters may accomplish.

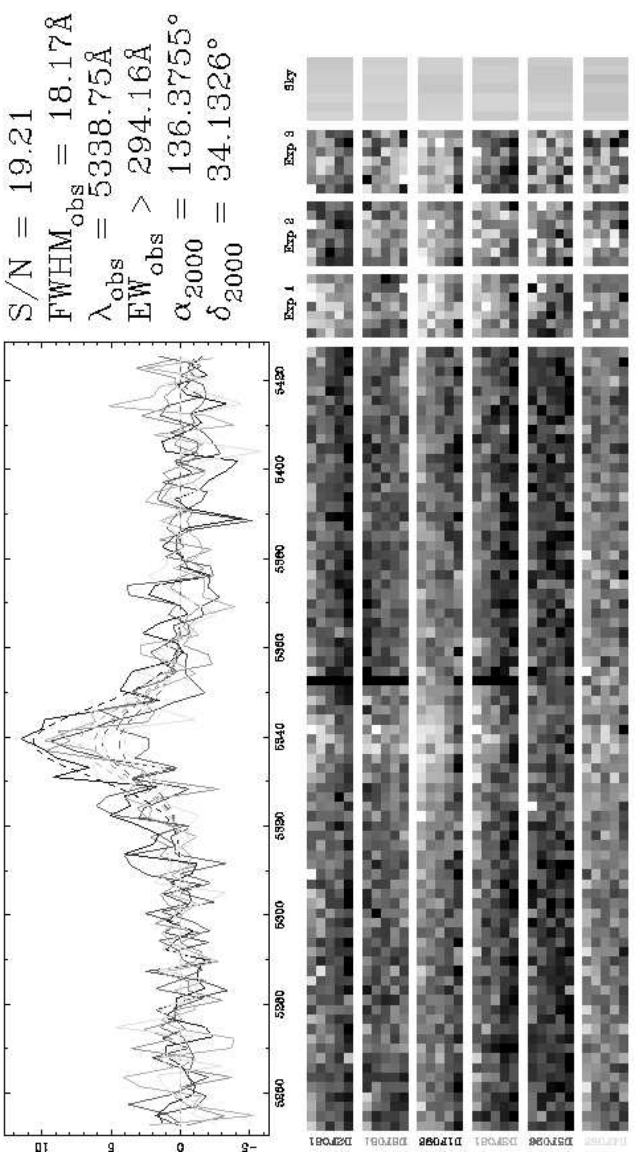

Figure 2.5 The joint detection of Lyman-α emission in a subset of the central fibers. The equivalent width limit is shown. Each row in the figure's bottom half corresponds to the spectrum from a fiber with a unique position on sky. In the labeling of Figure 2.1, these fibers are numbers 4, 15, 3, 7, 14, and 11 from top to bottom.

ure 8 of Reuland et al. (2003) appear somewhat coincident. However, our detection of the secondary emission peak spans three fibers, which covers a much larger area than the continuum signal. We speculate that this continuum may be stimulated or entrained material in the larger radio jet as invoked as a leading candidate to explain the alignment effect (Begelman & Cioffi 1989; Chambers & Miley 1990; McCarthy 1993) for radio galaxies. In the case of our supposition, the Lyman-α emission in this region originates around the rear radio jet and has a kinematic signature unaffected by peculiar motion of the continuum component. The large HI halo and scattering process we postulate would also cause a frequency redistribution which would wipe out any signature of the original kinematics, be they from a merging component or a rear photoionized cone. Also, the primary Lyman-α peak does not have a counterpart continuum peak, making it at least unlikely to be affiliated with a merger event. The second possibility is scattering from discrete regions of neutral hydrogen such as an outbound shell due to a starburst superwind, and has been modeled and observed for LABs (Ohyama et al. 2003; Wilman et al. 2005) and Lyman Break Galaxies (Shapley et al. 2003). Third, a robust feature of optically thick resonant scattering in static hydrogen clouds is a bimodal line profile straddling the rest wavelength (Urbaniak & Wolfe 1981). The addition of bulk, distributed velocity fields can then process the escaping spectra and be used to match a wide range of observed, high redshift galaxies (Ahn & Lee 2002; Verhamme et al. 2007, 2008). In these models, the source of Lyman-α emission is either a central point or a spherical distribution surrounded by a scattering medium. None of these pictures can seemingly explain the differing line profile seen between B2 0902+34's Lyman-α and 21cm line profiles. We submit a fourth mechanism, related to the third mechanism, to generate Lyman-α bimodality which is particularly suited to radio galaxies: two spatially segregated emission cones within a resonantly scattering halo. Resonant scattering effects have been shown through Lyman-α and Hα imaging to be important in low redshift objects (Hayes et al. 2007) and specifically with bulk velocity structure as the primary factor determining Lyman-α escape (Kunth et al. 1998).

2.3.1 Physical Assumptions and Constraints

The basic geometry we investigate is shown in Figure 2.2. This scenario is based on a proposal in van Ojik et al. (1997), although that work does not investigate the key effects of resonant scattering. The Lyman-α emission in HzRGs is often strongest along the radio axis in a biconal geometry. This geometry has been advocated on AGN ionizing photon counting grounds (McCarthy & van Breugel 1989) and for AGN unification models (Barthel 1989; Antonucci 1993). Surrounding the cones is a large halo of neutral hydrogen gas. Our model postulates an opening angle of 90° for each cone. Matching the spatial location of the bimodal emission in our data and that of Reuland et al. (2007), we model the projection of the emission cones axis on the sky at 60° east of north. It is not clear from the radio data exactly where the radio axis projects, but given the large deprojection uncertainty in such a low inclination system and the complex bending of the radio image, this geometry is reasonable. The ionization cone radius could be constrained by the Lyman-α luminosity, but since the filling factor is highly uncertain we keep this radius as an open parameter. We model the density profile as baryons at 17% of the total mass following Navarro-Frenk-White (NFW) profiles (Navarro et al. 1997) with a thermal core and concentration parameters of c = 5 following Dijkstra et al. (2006a), hereafter DHS. The input velocity field is parameterized as a simple power law with $v_{bulk} = v_{amp} \times v_{vir} \times (r/r_{vir})^{\alpha}$ where α is the index, r is radius, r_{vir} is the virial radius, v_{vir} is the virial velocity, and v_{amp} is a scaling factor of order one. The input parameters and acceptable ranges we explore in common to DHS are total halo mass, v_{amp}, and α. The halo is isothermal at 10^4K, and the neutral fraction in the ionization cones is 10^{-4}, both appropriate to the common ranges of density in photoionized regions. We model a completely smooth distribution of gas as a simplifying assumption. In a very similar type of problem, low redshift cooling flows, Fabian et al. (1984) have shown how smooth flow assumptions adequately model infalling gas. The linear relation between the average number of photon scatterings before escape and the line center optical depth as shown in Appendix A ensures that gas clumping is irrelevant to our results.

2.3.2 Resonant Scattering Model

Given our new data of spatially resolved two dimensional Lyman-α emission, we have sufficient information to create a simple model for this system based on propagation of Lyman-α photons through an optically thick halo of HI with geometry as in Figure 2.2. Lyman-α radiative transfer is a mature field (Harrington 1973; Urbaniak & Wolfe 1981; Neufeld 1991; Loeb & Rybicki 1999; Ahn et al. 2000, 2001, 2002; Zheng & Miralda-Escudé 2002; Richling 2003; Hansen & Oh 2006; Dijkstra et al. 2006a,b; Verhamme et al. 2006; Tasitsiomi 2006; Laursen et al. 2009) with both analytic and computational results for simple geometries. Broadly, the model will work by emitting Lyman-α photons in two photoionized cones roughly aligned with the radio axes. A red and blue emission line relative to systemic will emerge for each cone absent a velocity field in the scattering gas giving four peaks in the line profile. The far cone's emission will be weaker and further from the HzRGs systemic redshift. Global dynamics of infall will enhance the two blue emission peaks and suppress the two red emission peaks. Outflow will produce a mirror image spectrum about the systemic redshift and suppress the two blue emission peaks and enhance the two red emission peaks. The relative wavelengths between the stronger, narrower emission from the near cone and the weaker, broader emission from the rear cone can then discriminate between infall and outflow even if the systemic redshift is unknown. This method provides constraints on the HI mass and velocity field by measuring the bimodal line properties and the systemic redshift if available.

The study of Lyman-α resonant scattering can be profitably attacked through Monte Carlo methods. We base our computations primarily on DHS, where DHS used Monte Carlo methods to attempt discrimination between energy sources and conditions in the data on LABs. Our version of the Monte Carlo resonant scattering code differs in three ways from their description. First, we do not include deuterium in our simulations. Although they show convincingly that deuterium is important for certain wavelengths and conditions, our very high optical depth and temperature environments make its contribution negligible and a needless drain on computing performance. Second, all of DHS's geometries are restricted to spherical symmetry. As we will invoke the two cones of the AGN as coaxial with the cones of Lyman-α emission, our models are without spherical symmetry. Our simulations therefore are a function of inclination angle and require the same number of simulation photons in each inclination angle bin as in an entire DHS simulation to reach an equal S/N. Third, DHS have a geometry that yields an analytic expression between optical depth and traversed physical distance for thin shells of constant density and velocity gas. The general density and velocity field conditions in our model mean that we must integrate this distance numerically. We use a root finding algorithm with a relative accuracy of 10^{-8} on a fifth order Runge-Kutta code to calculate optical depths and sites of scatter. It is this generalization that enables us to pursue arbitrary density, temperature, and velocity fields. It will be possible to leverage this generalization by coupling our code to the more realistic conditions output by hydrodynamic codes in future work, but for now we use relatively ad hoc parameterizations. We used, in common with DHS, an acceleration scheme with $\mathrm{x}_{crit} = 3$ as described in their §3.1.1. Our simulation work is an extension and application of the powerful method of DHS to a different class of object, HzRGs. We have run our code for the four test cases shown in DHS's Figure 1 and found agreement as demonstrated in Appendix A.

Our main differences in operation from the DHS models are the changes in HI density in the presence of ionization cones and AGN photoionization as the dominant Lyman-α energy source determining the emissivity profile. Lyman-α emission powered by a cooling flow and its associated uncertainties are unnecessary in B2 0902+34 with the strong evidence for AGN photoionization. Within the ionization cones, Lyman-α is generated randomly in position following the recombination rate.

Our simulation ends when a photon leaves the virial radius. Further radiative transfer effects in the IGM are beyond this work's scope, although they can be important (Dijkstra et al. 2006b; Barkana 2004). We briefly discuss the qualitative impact that IGM processing by infalling neutral hydrogen outside the virial radius could have to our model. Figure 2 of Dijkstra et al. (2006b) gives transmission curves at $z = 3$ for a variety of impact parameters and for cases with and without a nearby bright, ionizing quasar. Multiplying this transmission into a single peaked emission profile can produce a bimodal line profile, but this is not a likely explanation by itself for B2 0902+34. Only emission lines that are well centered around the systemic redshift can be modified by the IGM into a bimodal profile as the transmission minimum occurs slightly redward of systemic. All our models produce Lyman-α emission that is blueshifted enough that the IGM processing could not create a bimodal spectrum. The higher 21 cm redshifts also imply that the Lyman-α emission is not near the systemic redshift. We also do not observe the spatial dependence with impact parameter that IGM processing would create. For these reasons and scope, we neglect IGM processing.

We must review a few of the broad findings in DHS to understand our models. Radiative escape from a static gas cloud will produce a bimodal spectrum. A photon has a much longer mean free path when it is at an off-resonance wavelength, which the thermal kicks in a scatter can cause. This situation will produce peaks redward and blueward of systemic with higher optical depths pushing the peaks out to more separated wavelengths. If the same situation has global infall (outflow) in the scattering gas, the photon moving outward and being scattered will have on average a blue-(red-)shift in the frame of the atom. A photon formerly in the red (blue) wing will move into resonance and have its travelling distance supressed, while a photon formerly in the blue (red) wing will be pushed further into the scattering wing and travel further before its next scatter. In practice, the suppressed emission peak is likely to be far below detection limits for the range of optical depths we investigate. Therefore we return to a solitary emission line with no information remaining on the system's systemic redshift for cases of spherical symmetry. As DHS acknowledge, there is a degeneracy in observation between systems in infall and outflow. We turn to a stark physical difference between the DHS modeled LABs and our HzRGs to solve this problem. HzRGs frequently have two discrete regions of emission as ionization cones powered by the AGN. In a low inclination angle system such as B2 0902+34, the optical depth difference between these two regions to an observer can be substantial. Such a system should exhibit a weaker, spatially restricted emission profile caused by the rear ionization cone superimposed on a stronger, nearly circularly distributed emission profile caused by the near ionization cone. The relative order in wavelength between the weak and strong emission peaks will point in the direction of the unobserved, systemic redshift. So, HzRGs may be unique as high redshift halos where observation can distinguish without ambiguity between infall and outflow, solely from Lyman-α emission profiles. B2 0902+34 provides a further test of this idea since it is the only HzRG with a detection of 21 cm HI absorption.

2.3.3 Evaluation of Model

In Figure 2.3 we give the observed and simulated spectra in identical apertures for a particular model. There are five tunable parameters to our model: the virial radius, the ionization radius, the velocity strength, the power law index to the velocity field, and the photoionized cones' opening angle. We have coarsely run models over the likely halo parameter space, but we only present one model which captures many of the necessary observed traits. This model realization uses 700,000 photons generated in a $6 \times 10^{12} \mathrm{M}_\odot$ halo which corresponds to a virial radius of 134 kpc and a virial velocity of 437 km s^{-1}. The ionization radius extends to 101 kpc for this realization. We use an infall model where the velocity varies as the radius to the power α where here $\alpha = 0.5$ and with a maximum radially inward velocity at the virial radius of 656 km s^{-1}. The cone opening angle is 90°. We have one further parameter which we hold constant as it is well constrained by a previously discussed observation: the system's inclination angle. We believe $\theta_i = 45^\circ$ as most likely given the absence of an observed broad line region, so in practice we bin the spatial projections and wavelengths for all photons that exit within 35° to 55° of an ionization cone axis. For our model, we have assumed a systemic redshift of $z_{systemic} = 3.3990$. We have done this after judging the velocity offset that the 21 cm absorption measurement should have in §2.3.4. The various redshifts are reviewed in Table 2.4.

This model reproduces many features of the observation. Most importantly, the size of the split in wavelength between the primary and secondary peak is recovered in the bottom panel of Figure 2.3. The relative intensities between the primary (near cone) and secondary (rear cone) emission are also fairly well matched. The regions of the halo not in projection of the receding radio cone also show the proper behavior as demonstrated in the top plot of Figure 2.3. The emission there is not bimodal, and the peak is nearly constant at the same wavelength as the redder peak in the bimodal region. Several features in the model clearly do not meet the data, and our model is not to be considered the optimum match in parameter space but instead an early attempt. The model data all display a blueward skew, especially in Fiber 4 (top panel, Figure 2.3) and regions away from either photoionized cone. Our data's S/N does not allow a useful measure of skew, but we predict that a much deeper and perhaps higher spectral resolution observation would show skew. This lack of skew is currently the most outstanding mismatch between our model and data.

We consider our results as surface brightness distributions in Figure 2.4. The left panel shows the observed decomposition between the primary and secondary peaks. The middle panel shows a similar decomposition for our model, where emission is decomposed spectrally. The right panel shows the model with the emission decomposed by the photoionized cone of origin. When we fairly decompose the model as in the middle panel, the region of secondary emission is pushed out slightly from the HzRG center and the relative intensity from secondary emission is underpredicted. Other models we have run have matched the spatial contours more closely, but have other failings such as underpredicting the bimodal wavelength separation, giving much broader lines, or showing even more skew. The modest S/N's so far observed for this dim object will inevitably cause confusion between skew, line width, and a bimodal line profile, so our unoptimized model parameter choices are appropriate to the state of certainty in the current data. The spatial distributions and relative intensities are fairly well matched at the level of the coarse spatial sampling allowed by our observation's fiber size. The offset spatial peak from the near ionized cone is also a robust match and explains why the Lyman-α peak and the radio core do not coincide.

Other parameter choices have some important trends. We cannot use a much smaller total halo mass, because the rest frame wavelength separation in the bimodal regions drops from 4Å to 1Å for a total halo mass of $3 \times 10^{12} \mathrm{M}_{\odot}$. Larger halo masses

Table 2.4. Redshift estimates in B2 0902+34

Primary Lyman-α	Secondary Lyman-α	21 cm absorption	Systemic from model
3.3918	3.3795	3.3962	3.3990

are allowed and give more freedom in the other model parameters to reach the crucial rest frame wavelength separation of 4Å, so we consider our gas mass to be a lower limit. Larger α values produce narrower emission lines with more skew, while a value of -0.5 creates lines of huge (40Å) dispersion and spectral shifts (thousands of km s^{-1} from systemic) that are incompatible with the data. Smaller R_i to R_v ratios seem to also lower the rest frame 4Å line profile separation unacceptably. A smaller value of $\theta_o = 60^\circ$ gives the appealing feature of more cleanly separating the near and rear photoionized cones spectrally much as the right panel of Figure 2.4 shows, but the emission not in projection of the near cone begins to show line centers improperly centered around the wavelength of secondary emission contrary to observation. The most robust result of these models is that a rest frame line separation of 4Å can be accomplished with resonant scattering from HzRG cones with a very large HI mass ($10^{12}M_\odot$), but a separation of much more (say, 8Å) can not without masses an order of magnitude larger.

2.3.4 21 cm Predictions

Any correct physical model of B2 0902+34 must take account of the 21 cm absorption data. Table 2.3 shows that fits of absorption to the Lyman-α line profile do not match the absorbing population of HI evident in the 21 cm data. Cody & Braun (2003) detect an absorption feature of FWHM 120 km s^{-1} at z = 3.3962 with a column density of 3×10^{21} cm^{-2} under an assumed spin temperature of $T_s=10^3$K. The relative velocities between the Lyman-α emission and the 21 cm absorbing HI and the absence of a signature from the 21 cm absorping gas in the Lyman-α profile both give strong constrains on possible geometries and conditions.

Our model naturally reproduces the 21 cm absorption measurements without the need for a counterpart dip in the Lyman-α profile. By embedding the emission sites of Lyman-α in a larger neutral halo, the effects of scattering will not leave an absorption-like imprint on the Lyman-α profile, but they will do so on the 21 cm profile against the radio continuum emission. All existing 21 cm data on B2 0902+34 are spatially unresolved. Figure 2.6 predicts the 21 cm maps that could be made using radio interferometry. The exact source distribution at 21 cm (323 MHz observed frame) is unknown, but we estimate it to be the same as the 1.65 GHz distribution of Carilli (1995). We assume the radio source plane to be the sky plane rotated onto the radio axis at an inclination of 45°. We use the same model parameters as introduced in §2.3.3. We find a column density of 1.0×10^{21} to $1.0\times10^{22}\text{cm}^{-2}$, a dispersion of 135 to 210 km s^{-1}, and a velocity shift from systemic of -190 to -275 km s^{-1}. These column densities would make this object a Damped Lyman-α system with a radius $>$ 50 kpc. The highest intensity radio emission resides is in a region of large gradients for the absorption properties, so slight changes in source distribution or rotation in the plane of the sky cause large changes in the integrated values. We give the ranges that misalignments of $\pm1''$ can create. The predicted line width is a factor of 2 above the measurement, but the rather unconstrained α parameter in the velocity field could likely remedy the mismatch as it takes a value closer to zero. Otherwise, the observations are bounded by these ranges, and the velocity shift tells us that our model self-consistently has both Lyman-α emission peaks blueward of both the 21 cm redshift and the systemic redshift. It is the velocity shift of 190 km s^{-1} for our fiducial astrometry that led us to the earlier assertion of $z_{systemic} = 3.3990$. When building our resonant scattering model, we only let the 21 cm measurements guide our choice of systemic redshift. It is encouraging that our model designed to match the bimodal Lyman-α line profiles recovers so well the spatially unresolved 21 cm absorption signatures.

Our most robust prediction comes from the southern radio lobe. Approximately 10% of the radio signal originates from this region in a $\sim 1''$ diameter aperture judging from the 1.65GHz data. Assuming the absorption strength is uniform over the halo, this aperture should have an absorption strength of 1.6mJy. Spatially resolved observations would need an unattainably long 1100 hours of exposure with 4 dishes from the Very Long Baseline Array (VLBA) and the phased Very Large Array (VLA) to reach the same S/N of 6 as in the spatially unresolved absorption measurement (Cody & Braun 2003) at a spectral resolution of 62.5kHz (restframe 58km s^{-1}) around the 323.053MHz observed frequency according to the European VLBI Network calculator[1]. Adding more VLBA dishes or other facilities, such as Greenbank or Arecibo, does not lower the exposure time as the increased baselines overresolve the southern lobe. However, the brighter northern jet could be measured at a S/N of 5 in 40 hours under the same configuration, and we are pursuing that observation. A spatially resolved 21cm measurement will give important confirming or falsifying evidence for a vast and massive infalling gas halo.

2.4 Implications: Infall Versus Outflow

We are left with two serious, competing pictures: outflow from a 100 kpc HII region or infall of a 100 kpc HI region with embedded cones of HII. Deciding between these mechanisms has impact beyond B2 0902+34. The bimodal line profile we see in B2 0902+34 is fairly common in HzRG halos. an OjikVAN OJIK et al. (1997) found 11 of 18 such systems to carry the feature in longslit spectroscopy, although they all have not been studied for the confirming 2D spatial profiles as can be done with IFS.

---

[1] http://www.evlbi.org/cgi-bin/EVNcalc

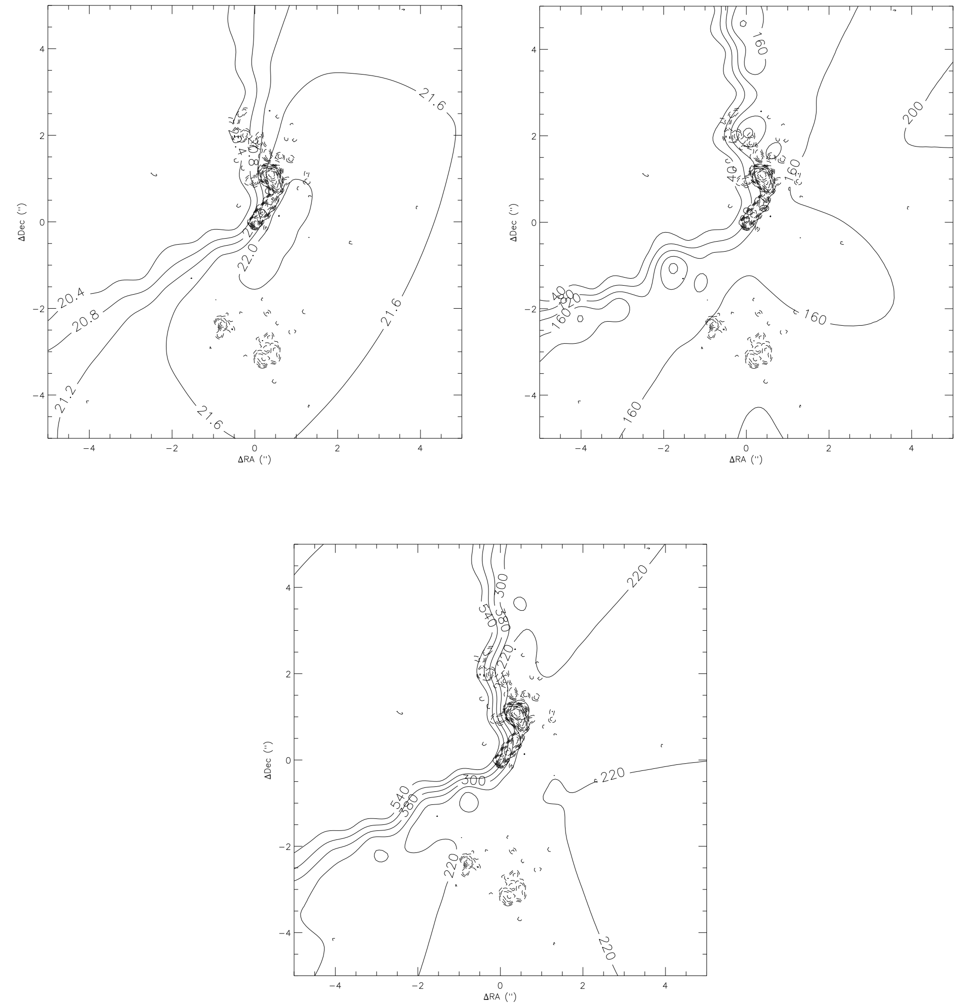

Figure 2.6 The predicted 21 cm maps for B2 0902+34. The 1.65 GHz data of Carilli (1995) is plotted as the dashed contour as a likely source distribution. *Top Left* Column density where the log of N(HI) in cm^{-2} is given. *Top Right* Velocity dispersion in km s^{-1}. *Bottom* Velocity shift in km s^{-1}.

The outflow picture requires shells or clumps of HI at a large radius from the emission halo. This gas scatters a fraction of the line emission, and the blueshift in the absorption trough argues for outflow. The energy mechanism might be a starburst-driven superwind as discussed above. Wilman et al. (2005) has applied such an explanation to LAB2 as has Reuland et al. (2007) for several HzRGs including B2 0902+34. If correct, these systems may be showing feedback in action with gas being heated and driven out. We see three reasons that this model is likely inappropriate to B2 0902+34. First, the 21 cm absorbing HI has no natural home in this picture. The radio emission, which extends to ≈40 kpc must lie behind this bit of HI, but the Lyman-α photons must be generated in front or must at least have many scatterings after the absorption as no spectra shows Lyman-α absorption at the 21 cm redshift and column density. Reuland et al. (2007) recognize this and predict a small, dense cloud of HI around the AGN. This too is unlikely, as the amount of spectrally flat radio core emission available for absorption in the data of Carilli (1995) and the amount required by the 21cm measurement of Cody & Braun (2003) are modestly incompatible. Second, the surface brightness profile has the wrong slope for unscattered, extended emission. As shown in Figure 2.7, the observed surface brightness profile follows a power law. Taking an NFW profile for density and integrating the square of the density through the halo, assuming an optically thin case and highly extended photoionization, we find surface brightness profiles that are too steep for all reasonable halo masses. Our simulation of resonant scattering gives a nearly power law profile with an appropriate slope. Third, the geometry of an absorbing cloud would have to be finely tuned to produce the observation. Based on our spectroscopy and that of Reuland et al. (2007), the primary peak's center stays very constant at 5339.0 ± 2.0Å in all positions. In the NE, there is no secondary emission peak so the absorption must be total and go quite blue. In the SW, the absorption would have to be weaker, narrower, and redder than in the NE

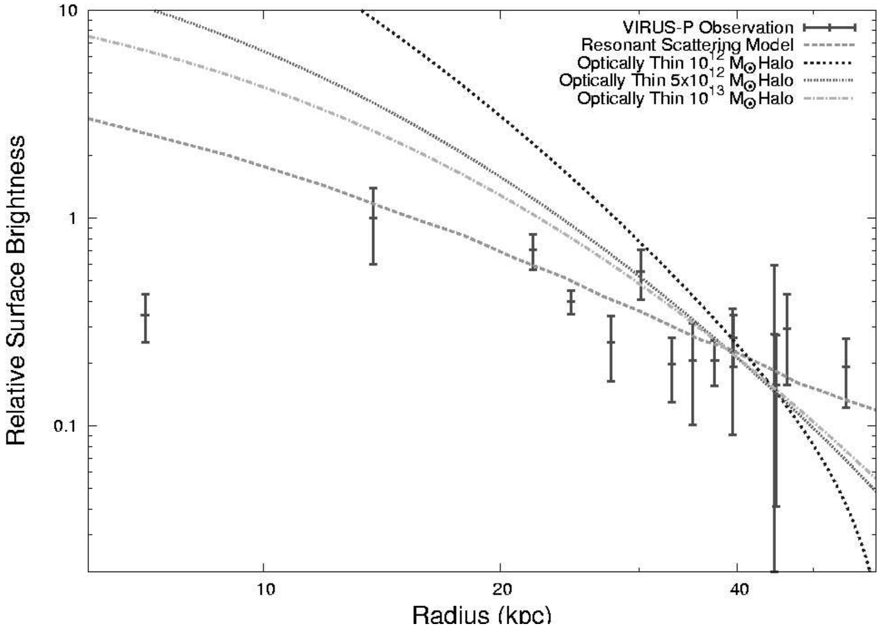

Figure 2.7 Observed and simulated surface brightness profiles. All models have been scaled in intensity by least squares to the data. The optically thin integrals through NFW halos fail, though the resonant scattering model reproduces the observed, shallower profile.

to produce Figure 4 of Reuland et al. (2007). The outflow picture does not produce a natural explanation for the spatial variation in the line profile.

Our result is surprising compared to the study of Nesvadba et al. (2008) with data from three other HzRGs. The authors find extended emission in rest-frame optical lines and kinematics indicative of outflow. A possibly crucial difference between the datasets is that for B2 0902+34 the emission line regions extend far beyond the radio lobes, while the other three HzRGs are bounded by radio emission and significantly elongated along the radio axis. If we speculate that both our and their conclusions are true, the next questions becomes whether the same HzRGs show different dynamical signatures through different lines or whether different HzRGs show different dynamical signatures across all their lines.

The infall picture has been suggested before for HzRGs (e.g. Humphrey et al.

2007). Villar-Martín et al. (2007) produced a model of optically thin biconal emission in Lyman-α to recover their observations of a peak emission position and peak velocity offset position. Their models, however, required postulation of a dense core that blocks emission from a rear cone that would have upset their trends, so their model is inappropriate to a bimodal line profile. They also could not produce lines at the width of their observations. We agree with the infall picture but use an optically thick regime of ionization cones embedded in one large, continuous neutral halo to explain all the available data on B2 0902+34 as we discussed above. If correct, this method has the capability to measure distributed hydrogen mass which we predict to be of the order $10^{12}M_{\odot}$. This is 5 orders of magnitude higher than the warm and cool hydrogen populations estimates by De Breuck et al. (2003) for the HzRG J2330+3927 from optically thin assumptions and Lyman-α line profile absorption specifically, and similarly high for the typical mass budget of HzRGs (Miley & De Breuck 2008). The neutral gas mass is dominant by a factor of $\geq$17 compared to the estimate of stellar mass in B2 0902+34 of $6 \times 10^{10}M_{\odot}$ (Seymour et al. 2007). We note that in the work of Seymour et al. (2007), B2 0902+34 has an usually low stellar mass compared to other radio galaxies at a similar epoch. Combined with our work here, this low stellar mass may indicate HzRGs exist in a fairly heterogeneous range of galaxy evolution, with B2 0902+34 at an earlier stage of evolution than the average HzRG. The unusually early evolutionary state and large HI halo for B2 0902+34 may also be why only B2 0902+34 so far has shown 21 cm absorption. Our model also puts the system in a radically different evolutionary state from that predicted by outflow. Instead, we have infalling gas that is still building up what will become the galaxy's luminous mass. Star and dust formation have not yet built up to a dominant level to affect the Lyman-α line. The central AGN has not yet blown out or heated a significant fraction of its environment in an act of feedback. The model mass would place B2 0902+34 as one of the larger halos that should collapse at the observed redshift. This picture does not deny HzRGs the role of feedback agents, but does show that radio emission can be output in a protogalactic phase as well and that AGN buildup may predate significant star formation. Further study on B2 0902+34 may be important in deciding the origin of supermassive black holes (Djorgovski et al. 2008), and their coevolution with stellar bulges. Two likely paths of early black hole formation are as end biproducts of the earliest stars (Madau & Rees 2001; Ricotti & Ostriker 2004) or as gas that avoided molecular cooling and fragmentation and collapsed into a black hole without associated star formation (Silk & Rees 1998; Loeb & Rasio 1994; Eisenstein & Loeb 1995; Bromm & Loeb 2003; Koushiappas et al. 2004). In the latter case, a phase of galaxy evolution may exist where the stellar bulge and black hole masses are not tightly related. Although we do not have an estimate of B2 0902+34's black hole mass, the large radio continuum luminosity suggests an already large black hole. B2 0902+34, although we do not observe any associated cluster LAEs, may yet grow into a rich cluster as the normal cluster members begin their own star formation, possibly triggered by B2 0902+34 itself as described in Rawlings & Jarvis (2004).

While we advocate a resonantly scattering, infalling model to explain the extent of emission and the otherwise conflicting Lyman-α and 21cm absorption data, our model does require a minimum of $10^{12} M_{\odot}$ in HI subject to the modeled constraint of a maximum infall velocity of $v_{bulk} = v_{amp} \times v_{vir} \times (r/r_{vir})^{\alpha}$ with here $v_{amp} \leq 1.5$. Having this much HI inside a galaxy's virial radius conflicts with the classic galaxy formation scenario (Binney 1977; Rees & Ostriker 1977; Silk 1977). In that picture, a shock near the virial radius should ionize incoming gas and heat it to $\approx 10^{6} K$ where it stays in quasi-hydrostatic equilibrium. Especially in the most massive halos, the low density gas is expected to have a cooling time longer than the galaxy age. This scenario has been adjusted in recent years with rapidly cooling accretion flows showing up in semi-analytic simulations (Croton et al. 2006) and cold accretion in smoothed particle hydrodynamics (SPH) simulations where a virial shock is mass conditionally unstable (Birnboim & Dekel 2003) and filaments provide many paths where cold gas ($< 10^5 K$) can flow to the forming galaxy's center (Fardal et al. 2001; Kereš et al. 2005; Dekel & Birnboim 2006; Dekel et al. 2009; Kereš et al. 2009; Ocvirk et al. 2008). The ability of cooling and cold flows to exist have a redshift and halo mass dependence. Croton et al. (2006) give $M_{halo} < 2 - 3 \times 10^{11} M_{\odot}$ for z=0-6 and Kereš et al. (2005) give $M_{halo} < 10^{11.4} M_{\odot}$ at z=0 with some redshift evolution. In either case, our advocacy for a $M_{halo} > 5 \times 10^{12} M_{\odot}$ at z=3.4 appears to be in conflict with theory. Instead, the growth mechanism of such a massive halo is expected to be mergers. Future radiative transfer simulations of Lyman-α in more realistic, filament conditions may alleviate this mismatch in mass scale, although since the velocity fields in Kereš et al. (2005) are of the same order as those we modeled, an easy solution is not obvious. The potential conflict with theory at such a large mass makes B2 0902+34 a compelling target for further observations and simulations.

2.5 Conclusions

We have made new spatially resolved IFS observations of Lyman-α in B2 0902+34. We find a spatially resolved region of weaker and bluer emission superimposed on a symmetric halo of primary emission. We have shown that all properties of B2 0902+34 can best be fit with a resonant scattering infall model with a large, mostly neutral, hydrogen mass. The sign of the velocity field is relatively robust and model independent. Signal seen through higher optical depths becomes increasingly bluer indicative of infall and resonant scattering. We match our data with a model dependent HI mass of $\geq 10^{12} M_{\odot}$ which is $\geq$17× larger than the stellar mass. For three reasons an outflowing HI scenario cannot fit our observations: 1) the strength of the observed 21cm absorption and the Lyman-α profile are incompatible with a single

HI population if optically thin and the velocity offsets between the 21cm signal and the higher optical depth Lyman-α signal carry the wrong sign for outflow if optically thick, 2) the surface brightness profile, with the assumption that the gas follows the dark matter, would be steeper than observed if optically thin, and 3) the bimodal Lyman-α line profile exists only in a small, non-central region of the galaxy which is incompatible with an outflowing shell geometry. The 21 cm HI absorption has been a powerful confirmation of the kinematics through its redshift offset from the Lyman-α halo emission, and we believe observational progress in understanding this class of object will benefit from further deep 21 cm measurements on other HzRGs. This new scenario of a massive, infalling HI halo with resonant scattering places B2 0902+34 in a much earlier evolutionary state than the previously formulated starburst superwind picture, and we classify B2 0902+34 as a protogiant elliptical galaxy in an early collapse phase before significant feedback has disrupted star formation and AGN fueling. Observations of other HzRGs with IFS will be important in correctly classifying systems between formation and feedback modes and allow detailed observational tests of these two processes. We are observing a large sample of HzRGs with VIRUS-P in order to undertake a similar analysis on other systems.

Further types of data on this system will allow confirmation of our infalling, resonant scattering model. Polarization measurements of Lyman-α could confirm the scattering process (Lee & Ahn 1998). The bright regions of HzRGs have been found to have modest levels of polarization (≈10%, Vernet et al. (2001)) while scattering simulations in similar situations to our model (Dijkstra & Loeb 2008) predict higher (≈40%) values. A measurement between HzRGs with and without emission line halos may demonstrate this split. The key, potentially falsifying observation for this resonant scattering, infalling model of B2 0902+34 will be radio interferometry spectral imaging to spatially resolve the distribution of HI gas through its 21 cm absorption. Carilli (1995) discussed the utility of such a measurement, and we have now given an observationally motivated model that predicts spatially extended HI.

Acknowledgements: This work was done in collaboration with Gary J. Hill and Phillip J. MacQueen.

Chapter 3

Dark matter profiles in late-type dwarf galaxies

3.1 Introduction

The observations of kinematics in low surface brightness (LSB) and dwarf-late type galaxies have stubbornly resisted giving clear evidence for the cuspy Navarro-Frenk-White (NFW) dark matter (DM) halo profiles that N-body simulations with ΛCDM inputs predict (Navarro et al. 1996b). Instead, most LSBs and late type dwarfs suggest cored DM halos (e.g. Oh et al. 2008; de Blok et al. 2008; Kuzio de Naray et al. 2008; Spano et al. 2008; Oh et al. 2010) or the observations are not constraining enough to rule out cusps (Swaters et al. 2003; Simon et al. 2005). Some simulations have produced cored DM halos by rapidly removing the baryonic disk which causes the DM halo to expand to a cored equilibrium (Navarro et al. 1996a), initializing numerical simulations with a primordial bar that forms a resonance with and disrupts the cusp (Weinberg & Katz 2002), or by implementing a supernova feedback recipe in high-resolution hydrodynamical simulations (Governato et al. 2010). As further motivation, other questions critically rely on knowing the DM density structure in galaxies, For instance, the prospects of DM annihilation searches depends sensitively on the true density profile in galaxies (e.g. Diemand et al. 2008). Determining DM profiles observationally is important, but most of the extant attempts rely on gas as the dynamical tracer. A small number of works have studied nearby disk galaxy kinematics with longslit stellar kinematics for the DM halo shapes (Corsini et al. 1999; Corbelli & Walterbos 2007) or the mass-to-light ratios (van der Kruit & Freeman 1984; Bahcall & Casertano 1984; van der Kruit & Freeman 1986; Bottema et al. 1987; Bottema 1989b,a, 1990; Bottema et al. 1991; Bottema 1992; Swaters 1999), but better structure constraints come from 2D spectroscopy (e.g. Copin et al. 2004; Krajnović et al. 2005; Cappellari et al. 2006; van den Bosch et al. 2008; Weijmans et al. 2009; Murphy et al. 2011).

So far, NGC 2976 has made one of the cleanest cases for a cored DM halo via its gaseous kinematics (Simon et al. 2003, hereafter SBLB03). We chose to observe NGC 2976 in our first attempt to derive DM mass profiles from stellar kinematics due to several of its properties. NGC 2976 is an SAc dwarf galaxy in the M81 group. There are some dynamical indications (Spekkens & Sellwood 2007) and photometric indications (Menéndez-Delmestre et al. 2007) that a weak bar may be present, but NGC 2976 is usually given an unbarred designation (de Vaucouleurs et al. 1991). NGC 2976 has some dark patches that are likely due to dust, but its dust content is modest for its Hubble class. A full treatment regarding the potential impact of dust on the measured kinematics is beyond the scope of this work, but several literature estimates of the dust content exist. Williams et al. (2010) fit star-formation history models from the broadband colors of resolved stars in the Advanced Camera for Surveys Nearby Galaxy Survey Treasury (ANGST) (Dalcanton et al. 2009) by modelling 0.8 magnitudes of differential extinction in the V-band for ages above 100 Myr, 0.5 magnitudes for younger ages, and a foreground screen of 0.46 magnitudes. Our data lie within the “INNER-1” region of that work. Prescott et al. (2007) use

Spitzer 24μm data to estimate $A_B \sim 1.5$. SBLB03 estimates $A_B \sim 0.23$ based on an inclination proscription (Sakai et al. 2000). NGC 2976 appears to be highly dark matter dominated at all radii according to SBLB03 (although de Blok et al. (2008) disagree), so the impact of stellar population synthesis (SPS) mass-to-light (Υ_*) uncertainties is minimized in this target. The stellar surface brightness profiles in many bands are very smooth and indicate a bulgeless disk with a small nuclear star cluster and a break to an outer disk at ~1.2 kpc. The distance to NGC 2976 from the tip of the red giant branch method is 3.56±0.38 Mpc (Karachentsev et al. 2002); we adopt a distance of 3.45 Mpc and a scale conversion of 16.7 pc arcsec^{-1} in this work for consistency with SBLB03. The total mass of NGC 2976 is estimated to be 3.5×10^9 $M_\odot$ based on the inclination-corrected line width of 165 km s^{-1} (SBLB03). The inclination is variously estimated as $61\overset{\circ}{.}5$ (de Vaucouleurs et al. 1991), $61\overset{\circ}{.}4$ (SBLB03), and $64\overset{\circ}{.}5$ (de Blok et al. 2008). The HI heliocentric velocity is 4.0±2.0 km s^{-1} (Stil & Israel 2002b). The stellar dispersion in NGC 2976 has never been measured. Attempts were made in Ho et al. (2009), but the results were unresolved in the presence of the best $\sigma_{inst} = 42$ km s^{-1} instrumental resolution. They estimate $\sigma = 36.0\pm16.8$ km s^{-1} from the [NII]6583Å line.

We present observations of NGC 2976 with the large field-of-view fiber fed Visible Integral field Replicable Unit Spectrograph Prototype (VIRUS-P) (Hill et al. 2008b) to concurrently measure the gaseous and stellar kinematics, fit mass models, and study the dark matter halo profile shape in the context of the “core-cusp” controversy with a collisionless tracer. The structure of the paper follows. Our data reduction and kinematic measurements are described in §3.2. We fit the stellar kinematic data with anisotropic Jeans models in §3.3. We perform fits to our [OII] rotation curve and the SBLB03 Hα rotation curve in §3.4. In §3.5, we investigate the constraints on Υ_* through matching SPS models to our spectral data and its effect on the mass models. Finally, we review our conclusions in §3.6.

3.2 Observations and data reduction

Over April 27 through May 1 of 2009, we took 18 hours of science pointings on NGC 2976 with the VIRUS-P instrument and the 2400 lines mm^{-1} VP2 grating on the McDonald Observatory's 2.7m Harlan J. Smith telescope under non-photometric conditions. Photometric conditions were continuously monitored by stars in the guider camera's data, which was read out and saved every five seconds and used to make relative flux calibrations. The seeing ranged from $1\farcs4$-$3\farcs0$ full-width-half-maximum (FWHM). The VIRUS-P field-of-view covers $1\farcm61 \times 1\farcm65$ with fibers projected to on-sky diameters of $4\farcs235$. VIRUS-P has a one-third filling factor, so we spread three dithers across the galaxy to maintain continuous spatial coverage in the middle and to maximize the data's spatial extent. We set the instrument to measure 3680-4400Å with R=2400, nominally. The spectral data were taken under 1×1 binning, yielding four pixels sampling the instrumental FWHM. Individual exposures were of 30 minute duration. We took 20 minute sky nods offset from the galaxy by $10'$ between the science data frames. Our best stellar kinematics come from around the G-band at 4300Å and its many surrounding, mostly Fe, features. We also measured the [OII]$\lambda\lambda$3726, 3729 lines and all Balmer lines higher than and including Hγ. The data were reduced with the `vaccine` pipeline described in Adams et al. (2011). We have corrected all observations to the heliocentric velocity frame. The instrumental wavelength zeropoint is observed to drift by $\sim$10 km s^{-1} over normal swings in nightly operating conditions. We have track this and correct the zeropoint by fitting the 4358.3Å Hg I skyline in every nodded sky exposure. Quoted wavelengths are not corrected to vacuum conditions.

3.2.1 Binning

We have, in total, 738 spectra with signal-to-noise (S/N) ranging from 0-60 per pixel. In order to extract reliable stellar dispersions under high S/N conditions,

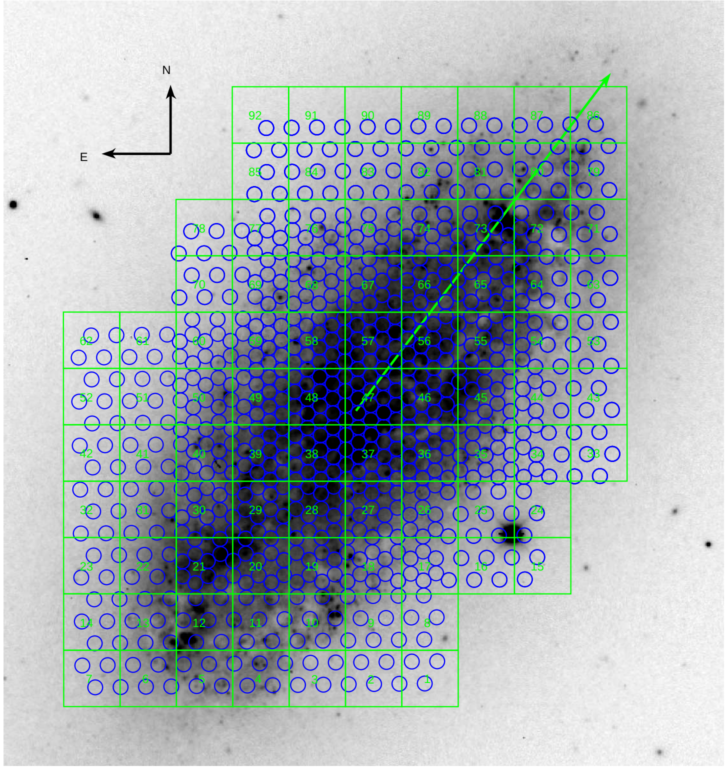

Figure 3.1 The SINGS R-band image of NGC 2976 overlayed with the VIRUS-P fiber positions. The numbered squares show the spatial bins used in the extraction of the stellar kinematics. The arrow indicates the major axis with a scale of 120″ (2 kpc at our assumed distance).

we bin our data as shown in Figure 3.1. Constant sized bins were chosen for the simplicity of matching to the mass modelling code of §3.3 rather than binning to a constant S/N (e.g. Cappellari & Copin 2003). Such binning is desireable when the velocity extraction is systematically affected by the S/N. However, we test for such systematics in §3.2.4 and find none. The stacks are made with one interpolation to a common, linear wavelength scale considering the different wavelength solutions in each fiber and the individual heliocentric corrections.

3.2.2 Spectral resolution

Our observations were taken with an instrumental dispersion of between 30-50 km/s across different fibers and wavelengths. We measure this resolution to 0.5 km s^{-1} uncertainty in every fiber and wavelength with our twilight flats and high resolution solar spectrum data (Kurucz et al. 1984). Finally, the binning process combines fibers with different instrumental resolutions, per our dithering scheme. We average the instrumental resolution for each bin. A fit to one fiber is shown in Figure 3.2. The fits to all fibers and bins are summarized in Figure 3.3. The solutions agree with arc lamp data, although the sparse number of available arc lamp lines leads to a less constrained solution. We also took spectra of a number of template stars (Prugniel & Soubiran 2001) to test our instrumental resolution and found agreement. We experimented with degrading all the data in a bin to the maximum instrumental resolution prior to stacking, but we found differences in the final kinematics only at levels far smaller than the formal errors since the instrumental resolution does not strongly vary over 4110Å$< \lambda <$4340Å nor over neighboring fibers.

3.2.3 Gaseous kinematics

We measure the gaseous kinematics through the [OII]$\lambda\lambda$3726.032, 3728.815 doublet. Without binning and in each fiber, we simultaneously fit two Gaussian functions over an 18Å window. Five parameters are fit through a least-squares minization: the intensities of each emission line, a constant continuum, the radial velocity, and the line width. The best fit models are perturbed with the observed errors in 101 Monte Carlo realizations to generate velocity errors. Line widths are measured to not be significantly larger than the instrumental resolution (§3.2.2). Of the 738 spectra, 483 were found to have a $>5\sigma$ significance in the velocity measurement away from the systemic velocity. We make models of the circular velocity profile

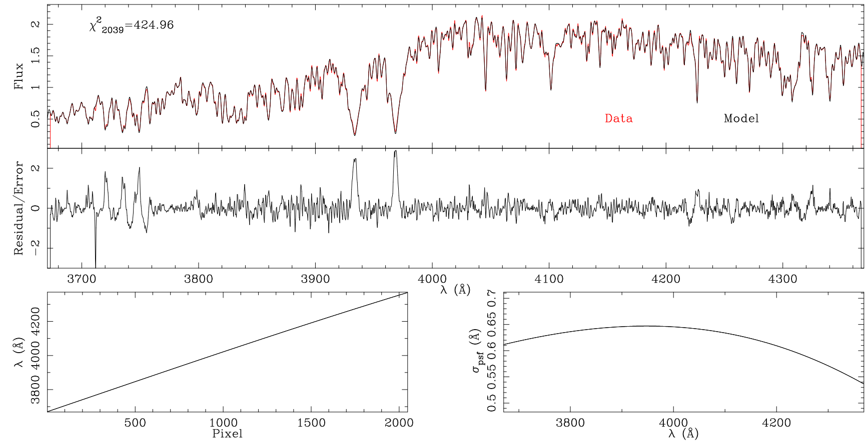

Figure 3.2 The simultaneous wavelength and instrumental resolution fit for a particular VIRUS-P fiber. The solutions are parameterized by a fourth order polynomial in wavelength and a third order polynomial in spectral resolution. The fits are made by matching a higher resolution solar spectrum to twilight flat frames.

from these measurements in §3.4.

3.2.4 Stellar kinematics extraction

We fit the stellar kinematics in each bin with a maximum penalized likelihood estimate of the Gaussian line-of-sight velocity distribution (LOSVD) in pixel space via code described in Gebhardt et al. (2000b). The Jeans models fit to the projected, second velocity moment of the data. For a Gaussian kernel, the second-moment is simply $V_{rms} = \sqrt{V_{los}^2 + \sigma^2}$. We use the empirical, R = 10k stellar templates of Prugniel & Soubiran (2001) (ELODIEv3.1) convolved to the instrumental resolution of each bin. The spectral window fit was 4110Å$< \lambda <$4340Å which includes the G-band, a strong Ca absorption line at 4227Å (Worthey et al. 1994), and a large number of weak Fe features. Fits to the spectral window 3980Å$< \lambda <$4100Å give similar measurements, although noisier due to the smaller bandpass and less prominent features. We show the consistency between spectral regions in Figure 3.4. Errors are determined by making Monte Carlo realizations of the best-fitting model

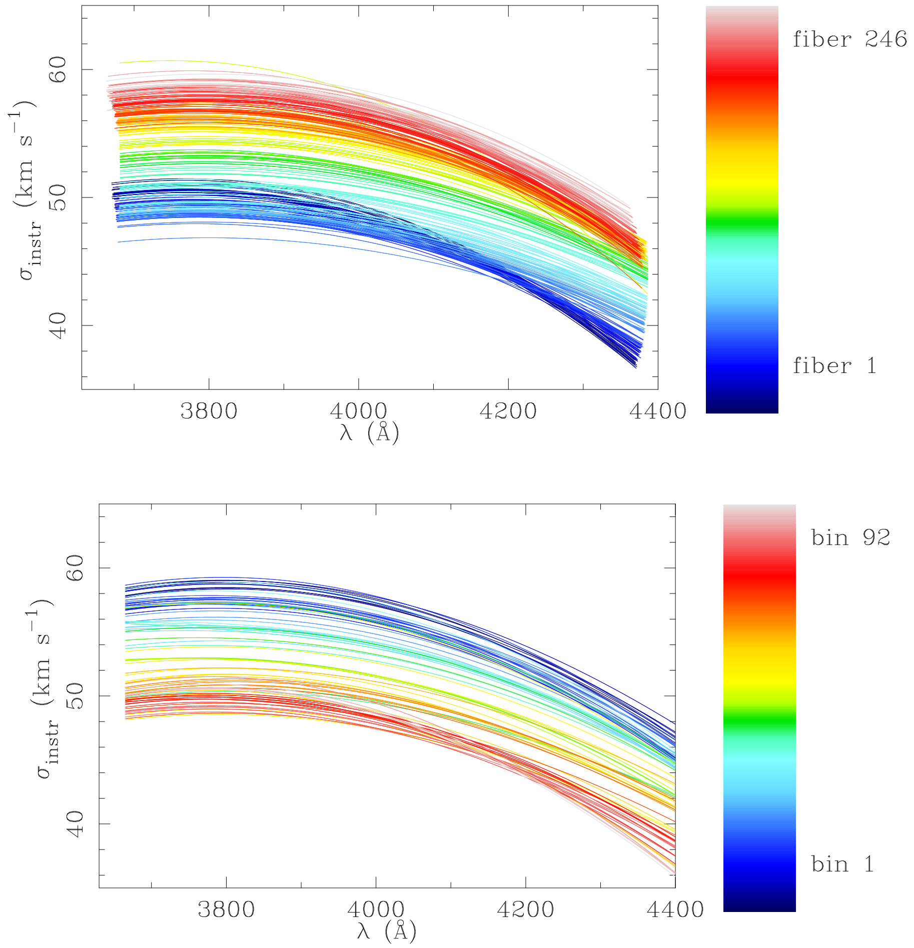

Figure 3.3 *Top*: The instrumental resolution in each native fiber as derived from the twilight flats. *Bottom*: The instrumental resolution in each kinematic extraction bin.

Table 3.1. Kinematic template stars

HYPERLEDA #	HD #	Type	[Fe/H]	Average weight	Intrinsic σ (km s^{-1})
00672	HD181214	F8III	-0.01	0.086	30.8
01269	HD058923	F0III	0.21	0.185	0
01286	HD062509	K0IIIb	0.02	0.006	11.1
01298	HD068017	G4V	-0.41	0.067	10.6
01322	HD073667	K1V	-0.55	0.032	10.9
01359	HD088609	G5IIIwe	-2.67	0.197	12.3
01366	HD089744	F7V	0.11	0.008	15.3
01733	HD169985	G0III+	0.34	0.138	12.3
01828	HD193793	WC+	0.77	0.280	0

with errors determined from the residuals. All data and templates are normalized prior to convolution by a running two boxcars over each spectra. The first boxcar has a 40Å width. All pixels deviating from the smoothed continuum estimate by $> 1.5\sigma$ are masked in the second boxcar, which has a 14Å width. The specifics of this normalization have little impact, as judged by varying the normalization parameters, on the convolution since both the flux-calibrated VIRUS-P and ELODIE spectra hava very shallow slopes over the extracted wavelengths.

The choice of templates is made from amongst the 1959 available, although only a small number are required to describe the data. The membership is determined by manually iterating the list to determine a local miminum in root-mean-square (rms). Several such minima can be found, but the exact choice is unimportant so long as similar stellar types are included. We list our chosen, final set in Table 3.1. Although we track formal errors, we also tally an empirically determined error as the rms from the best-fit model. We compare the two in Figure 3.5. The two generally agree, expect at high S/N where template mismatch becomes evident. All further errors are based on the empirical errors, although these may overestimate the actual uncertainty.

Tests were run to determine the limits of reliable kinematic extraction under a range of S/N and intrinsic dispersion. First, a subset of the template spectra were

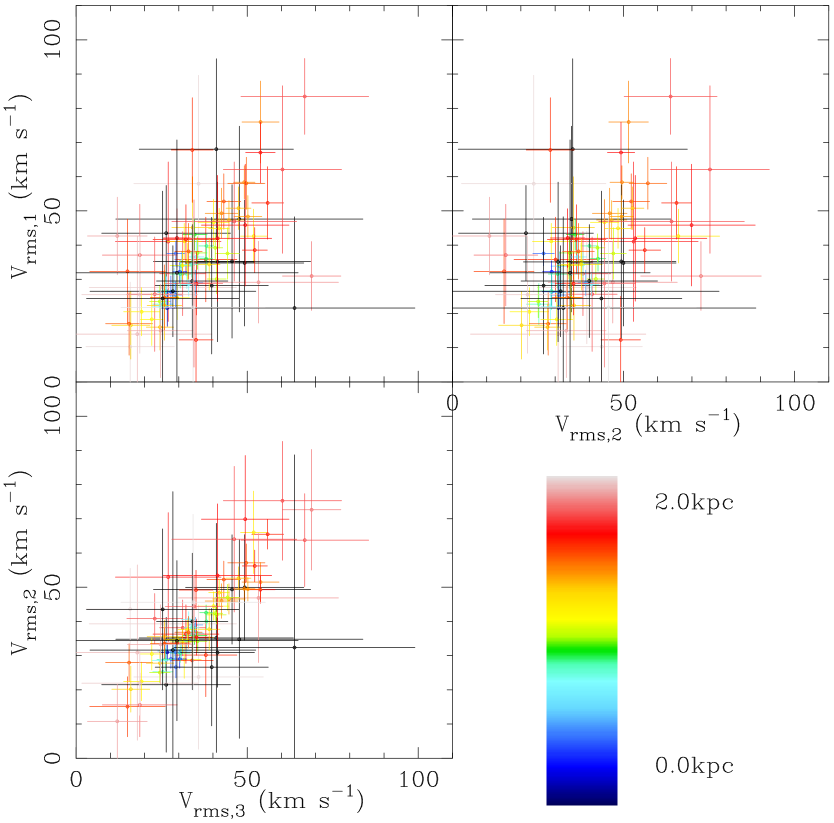

Figure 3.4 The rms velocity as measured in various spectral windows. The values are color coded by their distance along the major axis. The first, second, and third labels refer to the 3900Å$< \lambda <$4100Å, 4100Å$< \lambda <$4340Å, and joint windows respectively. The estimates generally agree, especially for the high S/N datapoints which drive the modeling. We use the 4100Å$< \lambda <$4340Åkinematics as the preferred value due to the lower errors and the more homogenous instrumental resolution compared to the joint range.

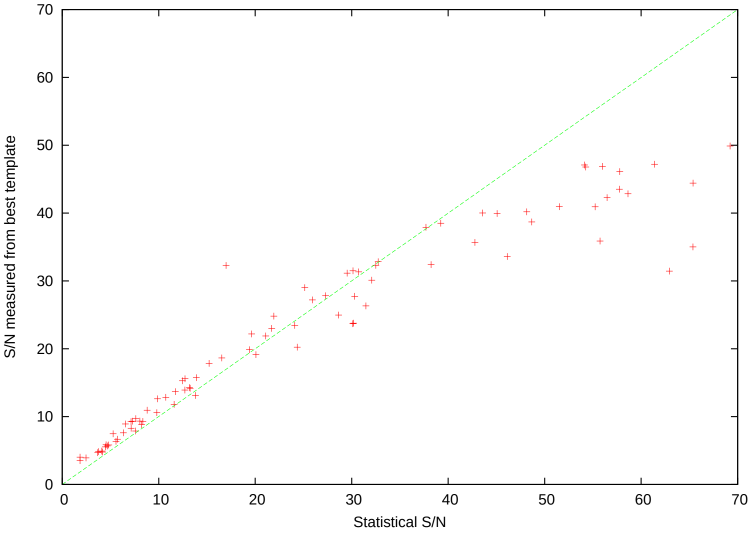

Figure 3.5 The S/N per pixel in each kinematic bin measured both with the statistical noise and the final rms from the best fitting set of templates and kinematics. At S/N∼30, the template mismatch starts significantly contributing to the fit quality, which may or may not also degrade the kinematic determinations. We produce velocity errors for the kinematic modelling from the more conservative, rms error estimation.

combined, then convolved by a simulation dispersion and the instrumental resolution, and noise was added. The extraction of the dispersion are shown in Figure 3.6. The errors are accurately estimated, and no systematic effects are seen down to S/N>5 and $\sigma > 10$ km s^{-1}. These tests also make evident how an instrument with a resolution better matched to dwarf galaxy dispersions can make accurate measurements at lower S/N. VIRUS-W (Fabricius et al. 2008) is such an instrument that is now coming available. Next, a similar test was made to capture the possibility of template mismatch. We combined the ELODIE templates for HD000432, HD068380, and HD081809 in a 21:53:27% ratio. The stars are not part of our fitting template, but they have similar spectral types. The extractions of dispersion are shown again in Figure 3.6. The errors are marginally larger, but again they are accurately estimated and without systematic trends.

Representative spectra and their best-fit models are given in Figure 3.7. Several additional corrections are made. The instrumental resolution error, estimated as 0.5 km s^{-1}, is propogated as a random error to V$_{rms}$ along with the statistical errors. The ELODIE headers quote broadening of the stellar features for some stars beyond their R = 10k resolution; this is likely because the templates are actually binaries. The average value for our templates is $\sigma = 5.2$ km s^{-1}. We subtract off the ELODIE instrumental resolution and the average broadening in quadrature from our VIRUS-P instrumental resolution prior to template convolution. However, The effect is small compared to the final errors. Additionally, the systemic velocity is estimated directly from our data. The inverse-variance weighted average of our stellar bins is 7.71 km s^{-1}. This is subtracted from the line-of-sight velocities before forming V$_{rms}$.

The rotational velocity and dispersion for each bin, with errors, are given in Table 3.2. Figure 3.8 shows the maps of line-of-sight velocity, dispersion, V$_{rms}$, and V$_{rms}$ error that we measured from the data. The final dispersions are not

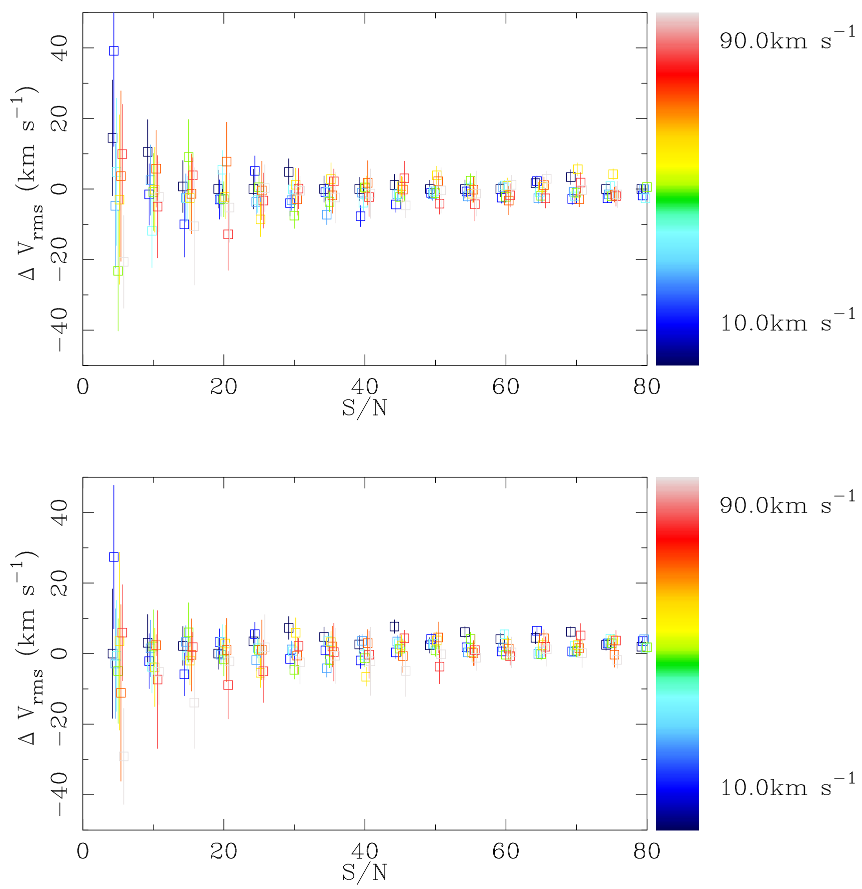

Figure 3.6 *Top*: The extracted dispersions in simulated data. The simulated data came from a subset of the LOSVD template set. No systematics are seen down to very low S/N and dispersions. *Bottom*: The extracted dispersions in simulated data. The simulated data come from stars in the ELODIE dataset which are not contained in our LOSVD template set. This tests for template mismatch. No systematics are seen down to very low S/N and dispersions.

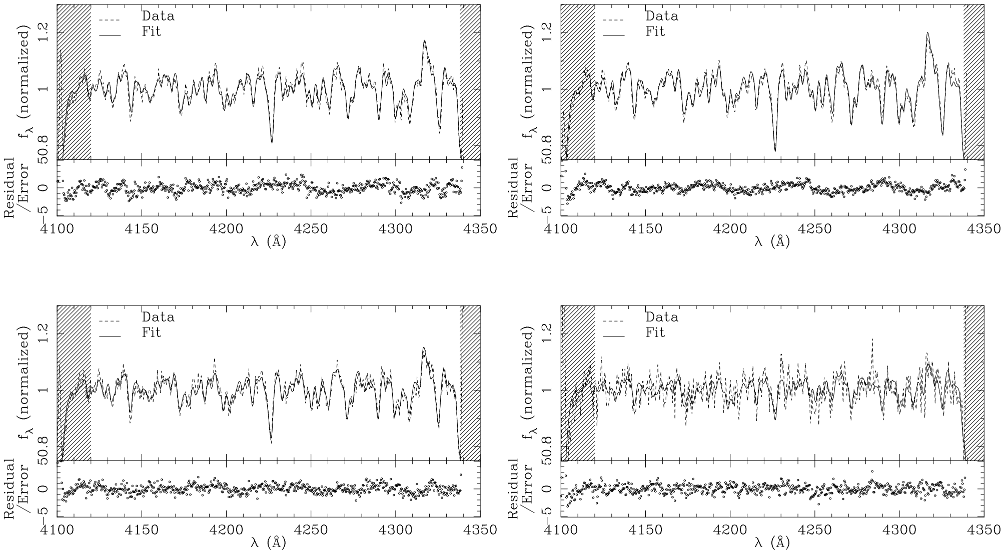

Figure 3.7 Spectra and fits in several bins. The chosen bins (56, 38, 19, and 5), represent a range of S/N (63, 66, 48, and 24) starting from the top left going clockwise. The error normalized residuals are shown in the bottom panel.

allowed to fall below 8 km s^{-1} in order for their error estimates to impact the error on V_{rms}. This is consistent with the lowest dispersions that we can reliably extract in simulated data. The weighted-average rotational velocity in all bins is 1.3±3.7 km s^{-1}, consistent with an earlier optical determination of 3±5 km s^{-1} de Vaucouleurs et al. (1991). We have set the systemic velocity to zero for this analysis.

Table 3.2. Stellar kinematic measurements in NGC 2976*

Bin #[†]	Major axis distance (″)	Minor axis distance (″)	$v_{los,*}$ (km s^{-1})	$v_{los,*}$, 1 σ uncertainty (km s^{-1})	σ_* (km s^{-1})	σ_*, 1 σ uncertainty (km s^{-1})
1	-48.1	-62.5	-26.10	28.62	8.33	34.70
2	-57.7	-49.7	-14.55	19.56	8.33	29.80
3	-67.3	-37.0	-26.69	16.76	40.24	20.25
4	-76.9	-24.2	-40.25	3.54	20.72	10.75
5	-86.5	-11.4	-48.81	5.34	8.33	10.53
6	-96.2	1.3	-57.23	4.07	8.33	12.53
7	-105.8	14.1	-64.43	17.48	8.33	26.69
8	-35.3	-52.9	30.44	29.25	20.91	20.52
9	-44.9	-40.1	-6.27	15.06	26.76	11.25
10	-54.5	-27.3	-10.00	4.33	30.58	6.64
11	-64.2	-14.6	-27.68	2.96	26.96	5.66
12	-73.8	-1.8	-39.09	3.05	46.60	16.80
13	-83.4	11.0	-36.65	4.53	26.13	8.42
14	-93.0	23.8	-41.30	10.30	57.12	21.14
15	-3.3	-68.8	-25.47	33.91	11.67	29.87
16	-12.9	-56.0	-1.57	20.64	38.16	14.00
17	-22.5	-43.2	3.76	3.96	14.54	8.88
18	-32.1	-30.5	-5.42	2.62	25.73	5.95
19	-41.8	-17.7	-13.80	1.48	28.68	2.97
20	-51.4	-4.9	-21.95	1.45	26.90	3.27
21	-61.0	7.9	-24.31	1.45	27.04	3.53
22	-70.6	20.6	-20.62	3.29	36.94	4.95
23	-80.3	33.4	-36.13	8.49	46.28	16.90
24	9.5	-59.1	-6.06	27.24	16.49	11.88
25	-0.1	-46.4	-6.72	14.93	33.30	6.70
26	-9.7	-33.6	7.67	2.71	22.47	5.55
27	-19.4	-20.8	-3.60	1.36	32.31	3.30
28	-29.0	-8.0	-7.60	1.16	27.37	2.72
29	-38.6	4.7	-9.61	1.33	32.23	2.83
30	-48.3	17.5	-7.56	1.35	30.60	3.13

Table 3.2 (cont'd)

Bin #†	Major axis distance ($''$)	Minor axis distance ($''$)	$v_{los,*}$ (km s^{-1})	$v_{los,*}$, 1 σ uncertainty (km s^{-1})	σ_* (km s^{-1})	σ_*, 1 σ uncertainty (km s^{-1})
31	-57.9	30.3	-4.96	3.53	44.19	5.13
32	-67.5	43.1	-2.88	10.41	45.64	19.24
33	31.9	-62.3	-12.40	17.09	45.75	15.03
34	22.3	-49.5	1.92	3.61	37.69	8.20
35	12.7	-36.7	7.56	2.49	20.21	6.62
36	3.0	-24.0	5.89	1.78	25.19	3.54
37	-6.6	-11.2	-1.54	1.65	24.97	3.15
38	-16.2	1.6	-2.68	1.43	27.07	2.65
39	-25.9	14.4	0.32	1.15	30.87	2.96
40	-35.5	27.2	-3.23	1.86	32.20	3.42
41	-45.1	39.9	-5.83	3.01	25.20	7.76
42	-54.7	52.7	-21.71	10.10	39.61	18.45
43	44.7	-52.7	13.74	5.88	43.18	11.98
44	35.1	-39.9	12.73	3.33	27.51	5.49
45	25.4	-27.1	9.11	1.74	25.02	2.74
46	15.8	-14.3	10.42	1.76	31.23	2.90
47	6.2	-1.5	10.84	1.35	30.78	2.38
48	-3.5	11.2	9.87	1.32	28.97	2.68
49	-13.1	24.0	11.78	1.58	28.62	3.04
50	-22.7	36.8	9.93	1.69	27.73	3.72
51	-32.4	49.6	2.52	4.34	14.73	9.64
52	-42.0	62.4	-1.44	18.55	25.00	16.94
53	57.5	-43.0	15.37	3.38	40.11	7.39
54	47.8	-30.2	20.74	2.63	33.05	5.08
55	38.2	-17.5	18.60	1.38	28.77	2.76
56	28.6	-4.7	21.23	1.38	36.53	2.24
57	18.9	8.1	25.20	1.34	25.57	2.67
58	9.3	20.9	19.64	1.41	25.99	2.71
59	-0.3	33.7	12.64	2.45	30.07	4.63
60	-10.0	46.4	2.84	3.80	35.05	5.30

Table 3.2 (cont'd)

Bin #[†]	Major axis distance ($''$)	Minor axis distance ($''$)	$\mathrm{v}_{los,*}$ (km s^{-1})	$\mathrm{v}_{los,*}$, 1 σ uncertainty (km s^{-1})	σ_* (km s^{-1})	σ_*, 1 σ uncertainty (km s^{-1})
61	-19.6	59.2	38.22	47.71	8.33	19.71
62	-29.2	72.0	38.99	57.99	8.33	22.59
63	70.2	-33.4	29.88	2.85	25.32	6.14
64	60.6	-20.6	29.65	2.53	43.13	4.02
65	51.0	-7.8	27.11	1.55	37.88	2.33
66	41.3	5.0	23.78	1.20	37.27	2.32
67	31.7	17.7	23.10	1.38	34.91	2.36
68	22.1	30.5	16.30	1.66	33.57	2.67
69	12.4	43.3	9.12	2.95	33.52	4.34
70	2.8	56.1	-0.65	7.49	20.30	9.57
71	83.0	-23.8	48.51	3.41	38.68	5.67
72	73.4	-11.0	43.36	3.93	12.33	14.48
73	63.7	1.8	37.28	2.69	36.57	4.34
74	54.1	14.6	38.09	1.57	29.58	2.54
75	44.5	27.4	25.64	1.97	33.06	2.87
76	34.8	40.2	13.52	2.65	36.37	4.63
77	25.2	53.0	9.43	4.86	10.68	10.70
78	15.6	65.7	-0.72	6.73	29.71	10.32
79	95.8	-14.1	50.84	2.96	23.86	6.15
80	86.2	-1.3	49.35	2.75	26.83	4.72
81	76.5	11.4	41.93	3.10	40.01	3.44
82	66.9	24.2	34.95	2.61	41.23	3.70
83	57.3	37.0	35.55	4.30	40.54	6.32
84	47.6	49.8	23.53	6.62	29.27	12.69
85	38.0	62.6	-1.38	12.02	38.94	20.30
86	108.6	-4.5	44.81	7.00	24.42	12.60
87	98.9	8.3	48.30	6.71	56.91	22.32
88	89.3	21.1	27.30	15.62	49.72	21.64
89	79.7	33.9	55.00	20.21	43.17	22.51
90	70.0	46.7	6.45	20.33	45.59	25.72

Table 3.2 (cont'd)

Bin #[†]	Major axis distance ($''$)	Minor axis distance ($''$)	$v_{los,*}$ (km s^{-1})	$v_{los,*}$, 1 σ uncertainty (km s^{-1})	σ_* (km s^{-1})	σ_*, 1 σ uncertainty (km s^{-1})
91	60.4	59.4	-11.91	27.74	38.84	22.32
92	50.7	72.2	-2.50	40.00	32.83	21.10

[*] Column 4 contains the systemic velocity which we measure as a weighted average to be 7.71 km s^{-1}. The quantity fit in the Jeans models is the velocity second-moment (V_{rms}), or the sum in quadrature of columns 4 and 6 with the systematic velocity removed. The V_{rms} error is formed by the propagation of the listed terms as well as an estimated 0.5 km s^{-1} uncertainty on the average 50 km s^{-1} instrumental resolution.

[†] The central position of each bin is given. The bins are $16'' \times 16''$in size and rotated by -53° east of north.

3.3 Jeans models

The necessary components to the NGC 2976 mass model are a stellar disk with a uniform population, atomic hydrogen, and a dark matter halo under a power-law parameterization. We use extant photometry to infer the distribution of the first two, and we use kinematic measurements and Jeans model solutions to infer the later.

3.3.1 HI deprojection

We use the robust weighting, zeroth moment map of 21cm atomic hydrogen in NGC 2976 from The HI Nearby Galaxy Survey (THINGS, Walter et al. 2008) to characterize the HI mass model. The HI distribution is highly clumped around the two off-center star forming complexes and unlikely to be axisymmetric. Nevertheless, we perform Multi-Gaussian Expansion (MGE Cappellari 2002) fits to the data, subject to the axisymmetric limitations of this work's modelling and fit a resultant circular velocity profile. SBLB03 have shown that HI is a dynamically somewhat important component at r > $80''$, but that H_2 (from CO measurements) is a minor contributor to the potential everywhere. Therefore, we neglect the molecular

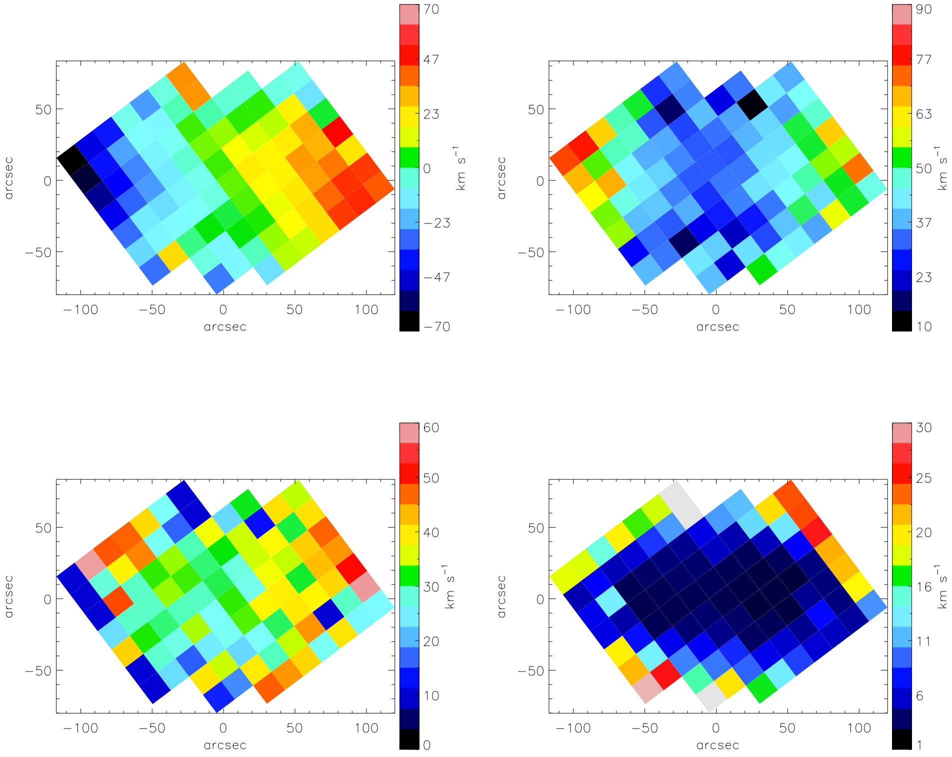

Figure 3.8 The velocity maps for NGC 2976. *Top left*: The stellar line-of-sight velocity map. *Bottom left*: The stellar dispersion map. The data are consistent with a flat or only modestly sloped dispersion profile. *Top right*: The second-moment map. *Bottom right*: The second-moment error map.

Table 3.3. Rotation curve data

Radius (arcsec)	$\mathrm{v}_{c,TR,[OII]}$ (km s^{-1})	$\mathrm{v}_{c,HD,[OII]}$ (km s^{-1})	$\mathrm{v}_{rad,[OII]}$ (km s^{-1})	$\mathrm{v}_{c,*}{}^{*}$ (km s^{-1})	$\mathrm{v}_{c,HI}$ (km s^{-1})
14.1	14.5 ± 3.2	11.1 ± 0.2	5.1 ± 0.2	9.5	2.9
19.1	31.7 ± 3.2	24.9 ± 0.3	6.7 ± 0.2	11.2	3.1
24.1	38.8 ± 3.2	30.7 ± 0.1	7.8 ± 0.1	13.0	3.3
29.1	45.4 ± 3.0	32.7 ± 0.1	6.3 ± 0.3	15.0	3.5
34.1	40.0 ± 3.0	29.4 ± 1.5	3.8 ± 0.4	16.9	3.5
39.1	43.8 ± 3.1	37.2 ± 0.8	4.3 ± 0.2	18.8	3.2
44.1	51.2 ± 3.3	44.3 ± 0.7	0.1 ± 1.0	20.5	2.5
49.1	56.5 ± 2.8	45.7 ± 1.6	3.1 ± 0.4	22.1	0.4
54.1	58.8 ± 3.2	50.3 ± 0.2	-1.0 ± 2.0	23.5	2.9
59.1	56.0 ± 2.5	51.0 ± 0.2	-2.3 ± 2.5	24.8	4.4
64.1	57.1 ± 2.4	55.3 ± 0.7	-1.2 ± 1.2	25.9	5.6
69.1	63.0 ± 1.8	58.0 ± 0.6	-7.1 ± 1.7	26.8	6.8
74.1	66.9 ± 1.5	60.1 ± 0.5	-4.0 ± 2.4	27.6	7.8
79.1	69.7 ± 1.4	67.7 ± 0.1	-4.9 ± 1.8	28.2	8.7
84.1	75.6 ± 1.5	67.2 ± 0.1	-9.5 ± 4.1	28.7	9.6
89.1	73.7 ± 1.0	67.3 ± 2.0	-13.2 ± 6.7	29.0	10.3
94.1	71.3 ± 0.2	68.7 ± 5.2	-8.9 ± 4.9	29.2	10.9
99.1	79.1 ± 2.0	67.7 ± 5.5	-12.1 ± 6.9	29.4	11.5
104.1	79.6 ± 3.7	93.7 ± 10.5	-0.5 ± 4.7	29.4	11.9
109.1	77.2 ± 2.3	77.6 ± 18.6	-11.7 ± 2.0	29.3	12.3

[*] Assuming $\Upsilon_{*,R}=\Upsilon_{\odot,R}$. This column scales as $\propto (\Upsilon_{*,R})^{1/2}$

component. SBLB03 fit the HI from an older dataset (Stil & Israel 2002a) and by assuming an infinitely thin disk; they present a circular velocity profile that is in general a factor of two times larger than our derived values. We apply this mass model to the fits of §3.3.3 and §3.4, although the presence of the HI component does not strongly influence our final results. The contribution from HI to the circular velocity is given in Table 3.3, and the MGE fit is shown in Figure 3.9. The MGE model requires negative components and infers a rather thick distribution with vertical-to-radial scale lengths of 1:2 to 1:4 at a nominal $i = 63^{\circ}$ for different components.

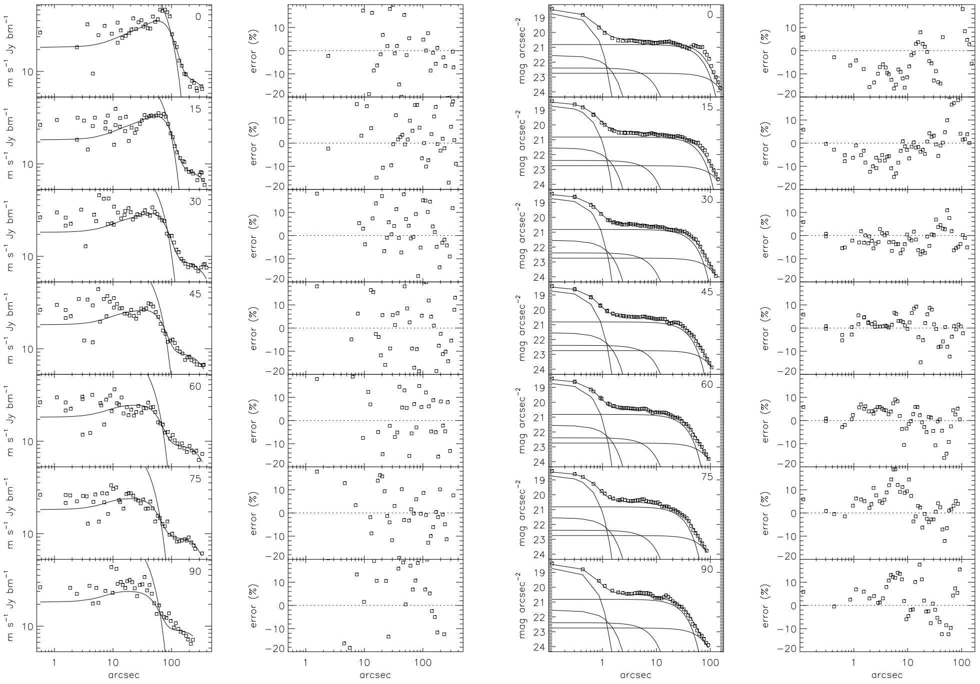

Figure 3.9 The sector photometry of NGC 2976, folded into one quadrant, with the Multi-Gaussian Expansion (MGE) fit also shown. *Left*: The HI distribution is strongly asymmetric and requires some negative mass components in the model's central regions. However, the total HI mass is significantly smaller than the stellar and DM mass, and its inclusion or exclusion does not strongly alter the DM halo fits. *Right*: The R-band data and fit. The nuclear stellar cluster and the break between inner and outer disk near r∼70″ on the major axis and r∼25″ on the minor axis are captured in the fit. The two star forming regions near r∼70″ on the major axis remain as residuals since they are asymmetric.

3.3.2 Stellar deprojection

We use the R-band image taken at the Kitt Peak National Observatory's 2.1m telescope from the Spitzer Infrared Nearby Galaxies Survey (SINGS, Kennicutt et al. 2003) to model the stellar mass distribution. The MGE fit is shown in Figure 3.9. The MGE model fits both the nuclear star cluster and the inner and outer disks well. The inferred vertical-to-radial scale length is 1:8 at a nominal $i = 63^\circ$ over most of the radial range, although it is near-circular for the nuclear star cluster. Strong color gradients are not seen in NGC 2976 (SBLB03), so we limit our analysis to a single value of $\Upsilon_{*,R}$ for all components. There is some debate as to the best filter to use for accurate recovery of stellar mass. Thermally pulsing asymptotic giant branch stars and polycyclic aromatic hydrocarbons disfavor the NIR. Dust extinction, star formation history, and nebular emission disfavor the optical. The studies on NGC 2976 of SBLB03 and de Blok et al. (2008) used K_s and Spitzer 3.6 μm data, respectively. Portinari et al. (2004) advocates i-band photometry and Zibetti et al. (2009) calibrates for combinations of i and H band photometry. We chose to use the available R-band image primarily for its depth and resolution in this work. However, our spectral energy fits that are consistent across multiple bandpasses (§3.5) mean this choice is probably unimportant.

3.3.3 Best-fitting dark matter halo

We use the Jeans Anisotropic MGE modelling package (JAM Cappellari 2008) to fit the binned stellar kinematic field in NGC 2976 in lieu of more computationally intensive Schwarzschild modelling (Schwarzschild 1979). The fits are made to the projected, second-moment velocity ($V_{rms} = \sqrt{V_{los}^2 + \sigma^2}$). We make models assuming a single anisotropy parameter ($\beta_z = 1 - (\sigma_z/\sigma_R)^2$) and a spatially constant Υ_*. The DM halo shape is approximated as a power law ($\rho = \rho_0 \times r^{-\alpha}$ with r in units of pc). This is justified since the core radius of NGC 2976 is likely to lie at $r_s \sim 2.5$

kpc (SBLB03, Appendix B), and our stellar data do not extend into the asymptotic region of the rotation curve. We place the JAM code within a non-linear least-squares minimzation package (`MPFITv.1.64`[1]) to reach our optimal solutions.

The best-fit, five-parameter model has a shallow minimum at $\Upsilon_{*,R}$=3.09 $\Upsilon_{\odot,R}$, i =63.2°, β_z =0.466, ρ_0 =0.339 $M_\odot$ pc$^{-3+\alpha}$, and α =0.268 at $\chi^2_{\nu=87}$ =91.9. The second-moment model and residuals are shown in Figure 3.10. The enclosed mass distribution for this model is shown in Figure 3.11. The anisotropy is larger than the $\beta_z \sim 0.3$ commonly fit by the same method in E's and SO's(Cappellari 2008). We test an isotropic solution as well, and find a similar solution in the remaining parameters. The kinematically determined inclination is also significantly above the value in de Vaucouleurs et al. (1991) based on photometric ellipticity (i = 61.5°). However, we find i =64.6±1.5° from our [OII] tilted ring [OII] fit §3.4, so the kinematically determined value is reasonable. Inclinations are often poorly constrained by kinematic fits (Krajnović et al. 2005) and can have a strong degeneracy with β_z. There is tension in the Υ_* value compared to that which we determine from the stellar population synthesis (SPS) fits presented in §3.5.

Anticipating the constraint we derive from SPS, we add an additional constraint of $\Delta\Upsilon_{*,R}$=0.8 with a central value of $\Upsilon_{*,R}$=1.08 $\Upsilon_{\odot,R}$. The parameters then reach a minimum at $\Upsilon_{*,R}$=1.178 $\Upsilon_{\odot,R}$, i =64.1°, β_z =0.519, ρ_0 =28.5 $M_\odot$ pc$^{-3+\alpha}$, and α =0.84 at $\chi^2_{\nu=88}$ =92.5. The V_{rms} map and residuals are shown in Figure 3.12. The enclosed mass model is shown for the joint constraint in Figure 3.3.3. This solution is within the 1 σ confidence interval from the kinematic data only.

Finally, we fix $\Upsilon_{*,R}$=1 $\Upsilon_{\odot,R}$ and α =0.1 as an illustration of a cored DM model. The V_{rms} map and residuals are shown in Figure 3.14. After optimizing the remaining three variables, this model yields $\chi^2_{\nu=88}$ =115.5.

---

[1] `http://cow.physics.wisc.edu/~craigm/idl/idl.html`

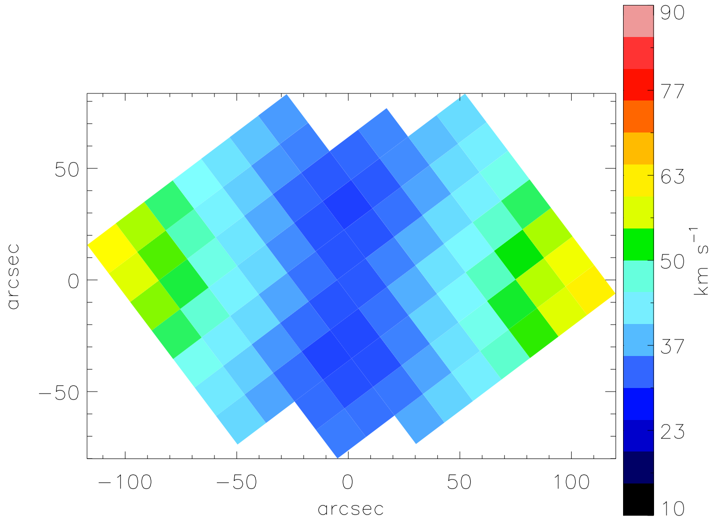

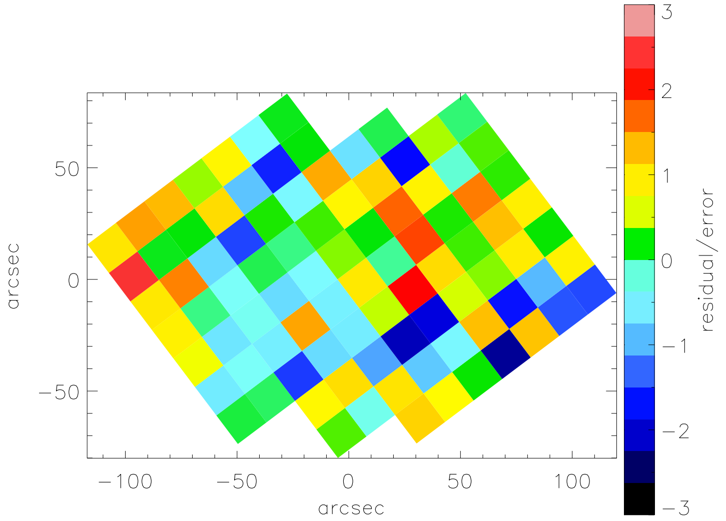

Figure 3.10 *Top*: The model second-moment velocity map for the least-squares minimum fit made to the kinematic data alone. This model disagrees with the SPS constraint on $\Upsilon_{*,R}$. *Bottom*: The residual/error for each bin for this model. The model is characterized by $\chi^2_{\nu=87} = 91.9$.

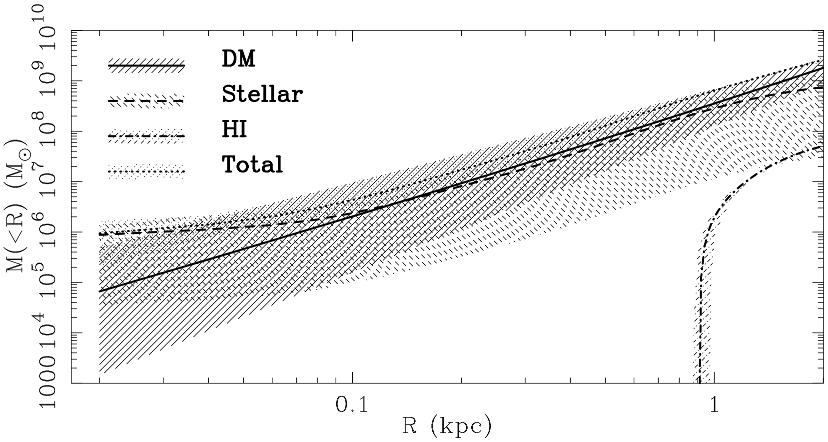

Figure 3.11 The enclosed mass profiles and confidence intervals at the least-squares minimum for a fit to the kinematic data alone. The $\Upsilon_{*,R}$ fit here exceeds that fit through stellar population synthesis analysis. With these poor constraints, NGC 2976 may be DM or baryon dominated to the largest radius measured.

3.3.4 Parameter degeneracies

We fix several combinations of parameter pairs while marginalizing over the remaining three. By our parameterization, there is an obvious degeneracy between ρ_0 and α with a weaker degeneracy on Υ_*. The most important degeneracy for our purposes is that betweeen Υ_* and α. In NGC 2976, they anti-correlate as shown in Figure 3.15. A similar exercise is done with the joint kinematic and SPS likelihoods by which the cored DM fit is excluded at 2σ significance but a pure cusp is permitted. We conclude that honoring even a loose Υ_* constraint makes a DM halo measurement entirely consistent with the NFW form.

3.4 Tilted ring fits to gaseous kinematics

The [OII] data are fit with a tilted ring (TR) (Rogstad et al. 1974, 1976) and harmonic decomposition (HD) algorithm to determine a rotation curve assuming an infinitely thin geometry for the gas. The code is the same as used and described in

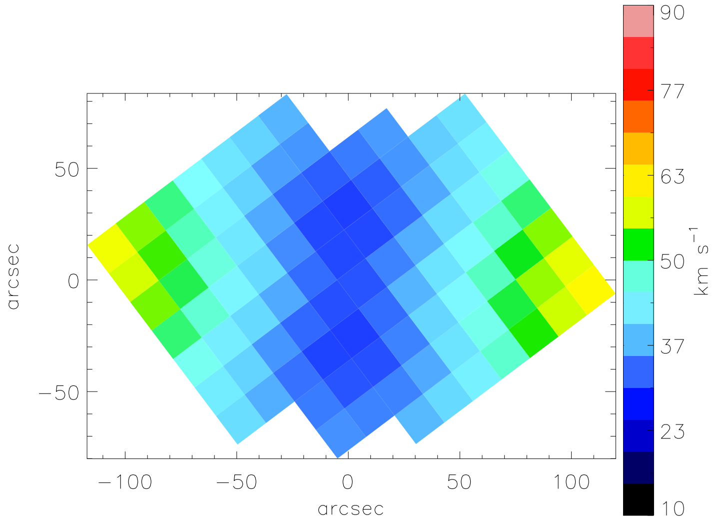

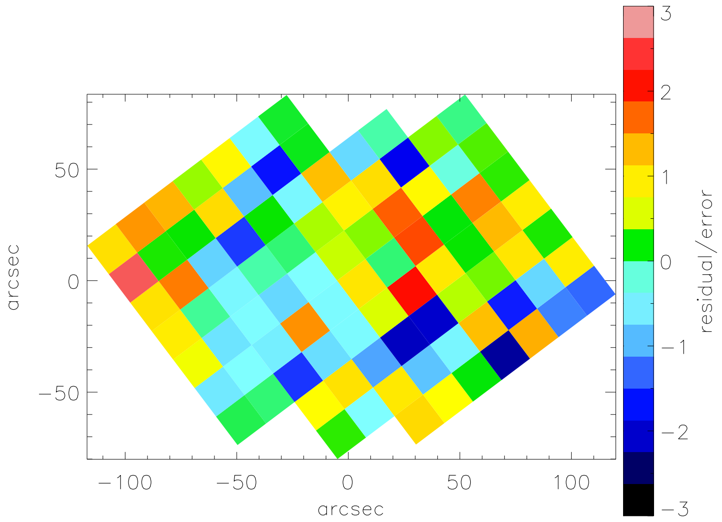

Figure 3.12 *Top*: The model second-moment velocity map for the least-squares minimum fit to the combined SPS and kinematic data. *Bottom*: The residual/error for each bin for this model. Including the SPS constraint, the fit is characterized by $\chi^2_{\nu=88} = 92.5$.

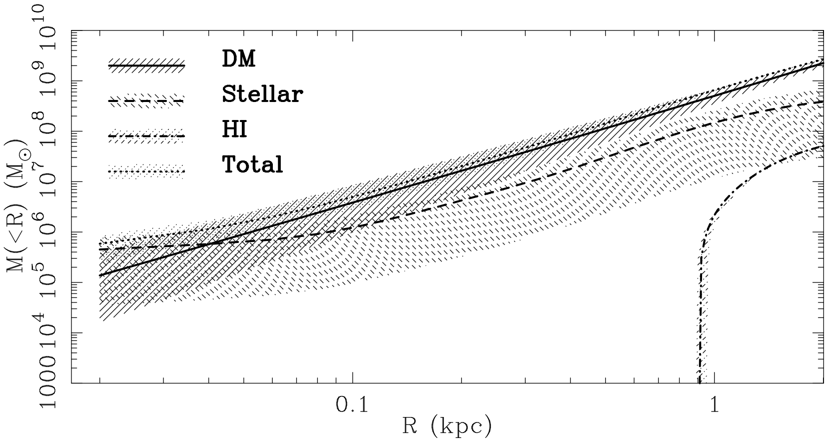

Figure 3.13 The enclosed mass profiles and confidence intervals at the least-squares minimum to the combined SPS and kinematic data. The DM halo dominates at least to r $>$ 300 pc and perhaps everywhere.

Fathi et al. (2005). The HD model and terms are shown in Figure 3.16. Driven by the same complex structures and kinematic twists as discussed by SBLB03 for the Hα in this galaxy, we have make harmonic fits through the $m = 3$ terms. SBLB03 only present circular and radial terms, however. Our TR fit is allowed a position angle that varies with radius which can also explain the kinematic twist.

The [OII] rotation curves are given in Table 3.3 and shown in Figure 3.17. The asymmetric drift correction for the ionized gas in NGC 2976 has been calculated in SBLB03 and found to be small and not used in their analysis because of substantial uncertainties in its exact value. Similarly, we do not apply an asymmetric drift correction to our gas rotation curve fits. There is remarkable consistency between our TR [OII] rotation curve and the Hα rotation curve of SBLB03. The irregular structure in the curve at r$= 30''$ and r$= 60''$ is found in both datasets, particularly in our tilted ring fit.

We next fit a velocity power law of the form $v_{circ} \propto r^{\beta}$ after subtracting off in quadrature the stellar and HI component circular velocities. The well-known relation for the density and circular velocity indices for power laws of $\alpha = 2 \times (1 - \beta)$

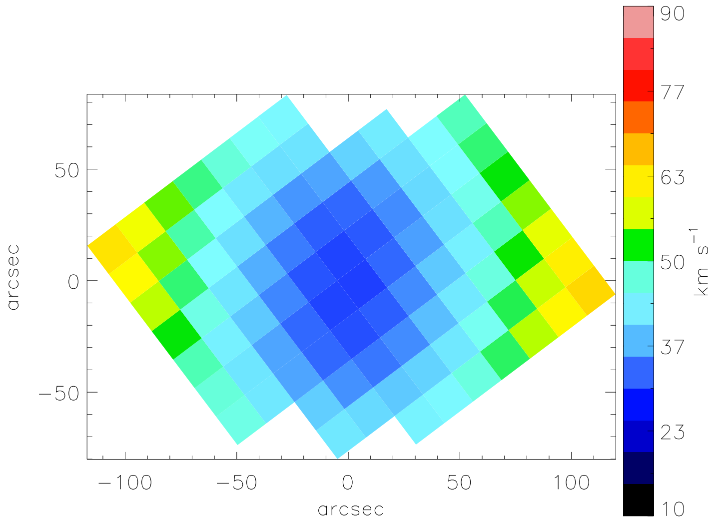

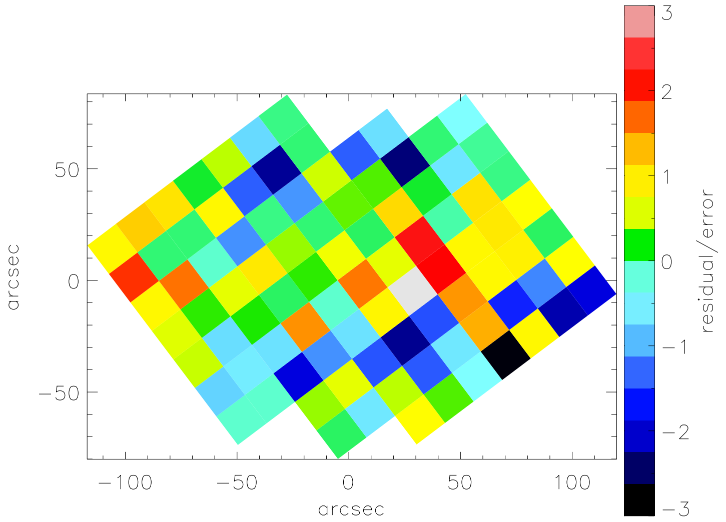

Figure 3.14 *Top*: The model second-moment velocity map for a fit fixed to $\Upsilon_{*,R} = 1.08$, $\alpha = 0.1$, and the remaining parameters varied. This model represents the class of baryon-dominated, DM-cored models that are excluded by our data. *Bottom*: The residual/error map for this model. The penalty in χ^2 comes from model velocities that rise more slowly than the data along the major axis and excess model velocities offset from the major axis. This fit is characterized by $\chi^2_{\nu=89} = 115.5$, while the global minimum is characterized by $\chi^2_{\nu=87} = 91.9$.

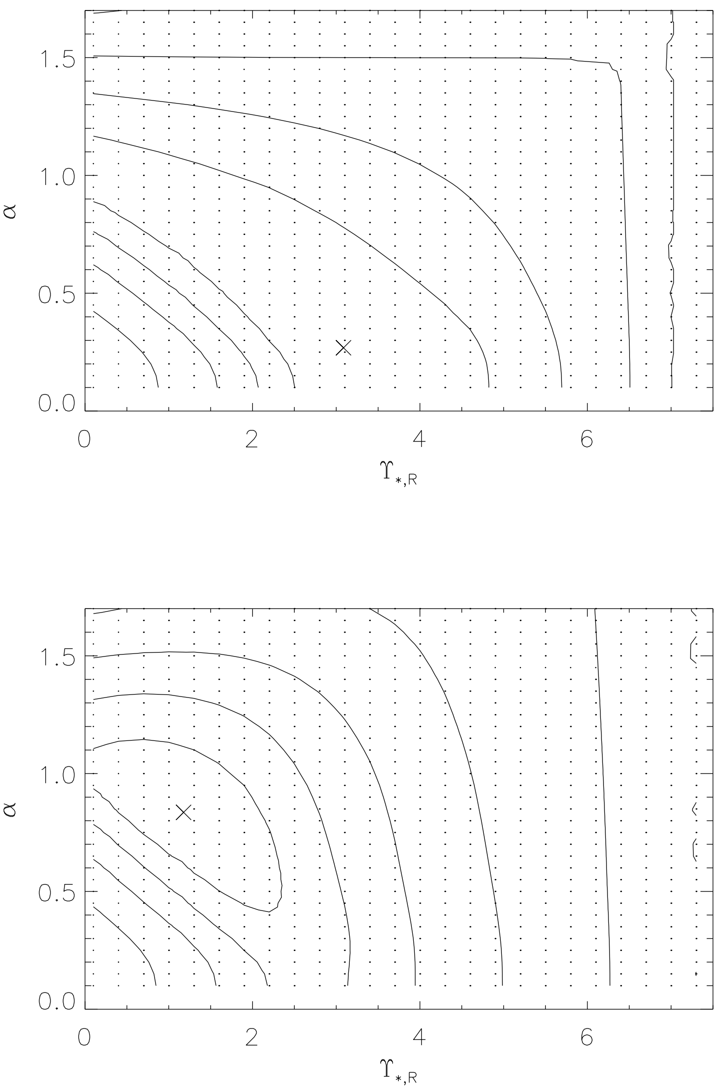

Figure 3.15 The $\Delta\chi^2$ distributions for combinations of the five parameters being minimized in the Jeans modelling. The inner three contours correspond to $\Delta\chi^2 =$ 2.3, 6.2, and 12.9 or 1, 2, and 3 σ significance. The additional contours increase each by a factor of two. A cross symbols mark the formal minima. *Top*: The confidence intervals from the kinematic data alone. *Bottom*: The confidence intervals when the kinematic and SPS constraints are combined.

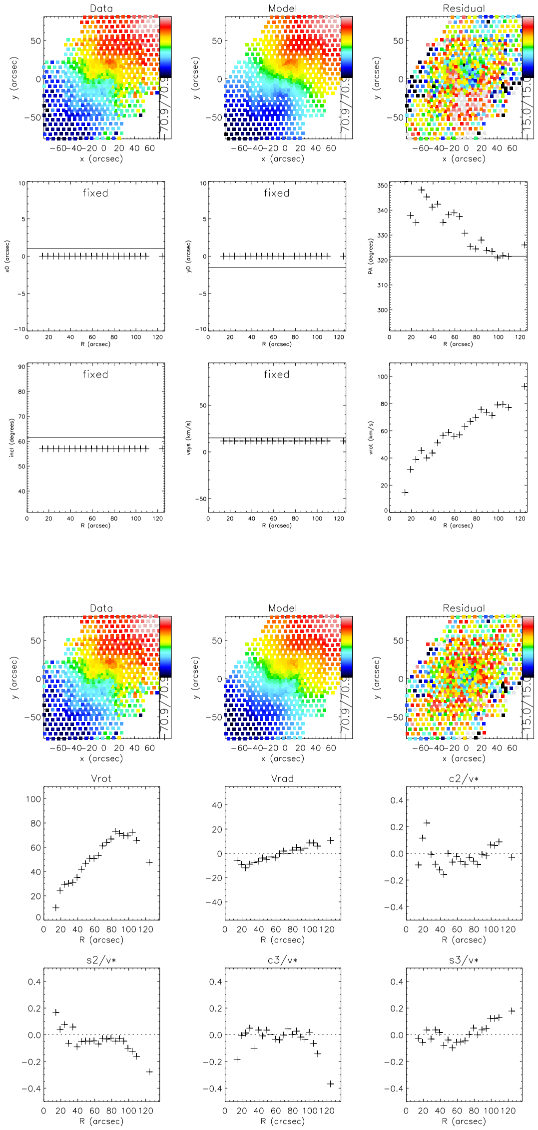

Figure 3.16 The data and fits to the [OII] velocity field representing the two ways that the kinematic twist can be recovered. *Top*: The fit with a tilted ring (TR) model and a variable position angle. *Bottom*: The fit with a harmonic decomposition (HD) model through three orders. Signficant radial velocity is observed, particularly in the galaxy's center. The sign of the radial velocity is uncertainty as we cannot identify the galaxy's near side. The higher-order terms are noisy, but similar rotational and radial velocity fits are made when the higher order terms are not fit.

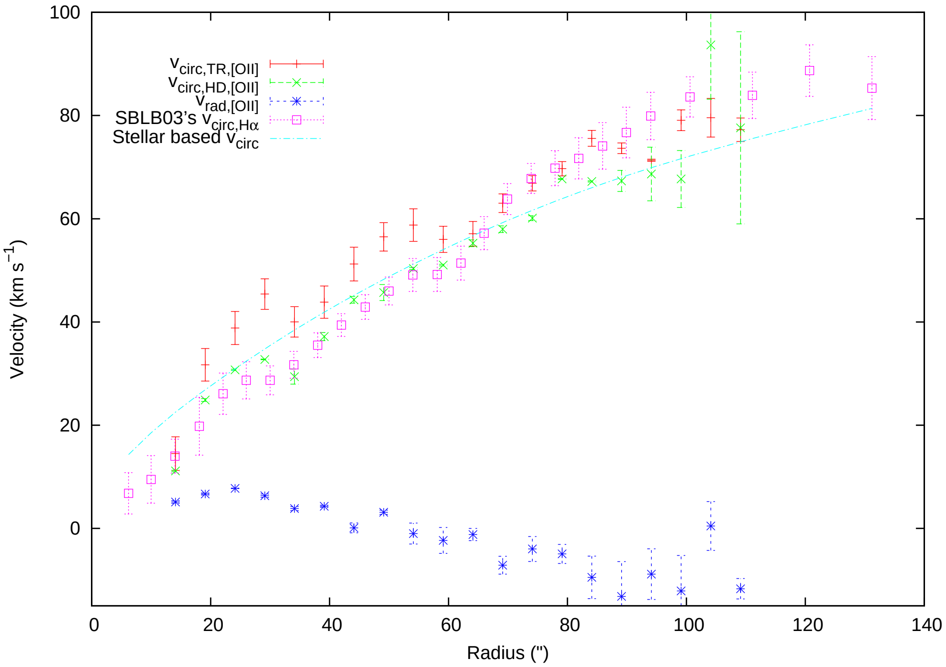

Figure 3.17 The gas rotation field under different datasets and fitting assumptions. The gas kinematics display systematic disagreement with the mass model based on the stellar kinematics and the SPS $\Upsilon_{*,R}$ constraint. The large radial velocities at small radii imply that the gas may not be in dynamical equilibrium. The harmonic decomposition fit to our [OII] data displays the least amount of disagreement with the stellar-based circular velocity curve with the only important deviation at the inner-most datapoint.

Table 3.4. Dark matter density index constraints from gaseous kinematics[†]

Assumption	This dataset's tilted ring fit	This dataset's harmonic decomposition	SBLB03 dataset
M_*/L_R =0	0.12 ± 0.05	0.54 ± 0.01	0.43 ± 0.06
M_*/L fixed[††]	-0.27 ± 0.07	0.48 ± 0.01	0.16 ± 0.10
freely fit M_*/L_R	0.11 ± 0.35	0.54 ± 0.01	0.12 ± 0.50

[†] The fits considered the statistical uncertainties in the [OII] data and an approximated 1 km s^{-1} systematic uncertainty. The harmonic decomposition error bars, in particular, are likely too low due to the small number of degrees of freedom.

[††] Assuming $\Upsilon_{*,R} = 1.08\ \Upsilon_{\odot,R}$ for our data and $\Upsilon_{*,K} = 0.19\ \Upsilon_{\odot,K}$ for the SBLB03 data.

(e.g. SBLB03 Appendix B) is used. A variety of Υ_* values are tested as detailed in Table 3.4, some fixed and some fit live. We also refit the SBLB03 data of their Table 3 in the same manner, taking their mass model rotation curves and trying their maximal disk value of $M_*/L_K = 0.19$. The residuals from the best fit were used to estimate the uncertainty in the rotation curve; these systematic uncertainties are larger than the statistical errors and included in the error determination of α in Table 3.4.

The TR fits to the [OII] data require a cored DM halo, regardless of the Υ_* assumptions. The [OII] HD fits require DM slopes that are significantly steeper than the TR fits, but still fall short of the NFW expectations. The harmonic decomposition can fit for radial infall or outflow, but some other motions may be degenerate with rotation such as the motions due to a bar-like potential (Spekkens & Sellwood 2007). A bar is expected to show power in the third order terms, and our m = 3 sine term does show some power at large radius. Finally, we fit the harmonic decomposition data of SBLB03 in the same manner. From their fits with a range in M/L chosen to represent maximal and submaximal disks, SBLS03 reach ranges of $0.01 < \alpha < 0.17$. We find agreement with their determinations. We find a larger, but still significantly cored, DM halo slope when we constrain the disk to have no mass.

We agree with the SBLB03 conclusion that the gaseous kinematics in NGC 2976 appear to be best-fit with a cored DM halo.

3.5 Stellar population synthesis constraints

A loose, external constraint on Υ_* value can be made by comparing stellar population models to Spectral Energy Distribution (SED) data, either photometrically (e.g. Bell & de Jong 2001) or spectrophotometrically. Substantial systemaic uncertainties in, for instance, the initial mass function (IMF) and the properties of thermally pulsing asymptotic giant branch (TP-AGB) stars (e.g. Maraston 2005) at NIR wavelengths limit the precision of M/L constraints from SED fits. Experiments designed to provide optimal observational constraints on stellar M/L's are underway (Herrmann & Ciardullo 2009; Bershady et al. 2010a,b), but such a goal is not the primary focus of this work. Specific to NGC 2967, SBLB03 found tension in the maximal disk value of $\mathrm{M}_*/\mathrm{L}_K < 0.09^{+0.15}_{-0.08}$ $\mathrm{M}_\odot/\mathrm{L}_{\odot,K}$ compared to the higher values implied by some SED fits (one of their models has $\mathrm{M}_*/\mathrm{L}_K$ =2).

We analyze the stellar population by fitting spectra with synthetic population synthesis (SPS) models from Bruzual & Charlot (2003) and the preliminary release of their 2007 version that incorporates new TP-AGB values (Bruzual A 2007). We use the Padova 1994 and Marigo 2007 evolutionary tracks, respectively. Both Chabrief and Salpeter IMF's are tried, which represent reasonable lower and upper bounds on Υ_*. To achieve robust star formation histories, we use the same 39 templates as Tremonti et al. (2004) which entail combinations of three metallicities ($Z = 0.2, 1, 2.5 Z_\odot$) and a variety of star formation histories (instantaneous-bursts of age 0.005, 0.025, 0.10, 0.29, 0.64, 0.90, 1.4, 2.5, 5, and 11 Gyr; a 6 Gyr old population under a constant star formation rate, and two tau models sampled at a 12 Gyr age with $\tau_{SFR} = 5, 9$ Gyr). We further add a grid of dust extinction with the form of Calzetti et al. (2000) over 21 values of E(B-V) uniformly spaced from 0 to 1. We resample our spectra to the rest frame, convolve the templates to match the 8Å FWHM SINGS instrumental resolution, and mask out windows 4Å wide around each of the Balmer lines, [OII], and [NeIII]3869. Repeated observations of spectrophotometric standards stars with VIRUS-P have shown the relative flux calibration to be accurate to better than 10% (Adams et al. 2011) and the match to the SINGS $20'' \times 20''$drift-scan spectrum is excellent as shown in Figure 3.18. The templates' normalizations are fit through least-square minimization, first individually and then in all 334,971 two-component combinations from the metallicity, star formation history, and dust grid. The relative probability of each model is calculated as $\exp(-\chi^2/2)$ (e.g. Kauffmann et al. 2003). All quoted Υ_* values include the effects of dust. The 1σ confidence intervals centered on the highest probability $\Upsilon_{*,R}$ are variously: 0.63±0.39, 1.23±0.52, 1.04±0.23, and 1.42±0.42 for the BC03/Chabrier, BC03/Salpeter, CB07/Chabrier, and CB07/Salpeter models. Given the tight ranges from the statistical errors alone, the M/L uncertainty is dominated by the limited number of population components we considered and the systematic uncertainties. We consider $\Upsilon_{*,R}$ =1.08±0.8 as the best spectrophotometric constraint; therefore we present mass models with $\Upsilon_{*,R}$ both freely fit and constrained by this conservative confidence interval in §3.3.3 and 3.4.

Finally, we investigate the Υ_* constraints enabled by broad-band photometry. We use the optical-through-2MASS datapoints of SBLB03 by assuming 10% errors and two IRAC datapoints of Dale et al. (2007) for NGC 2976 without any aperture corrections as shown in Figure 3.19. The same stellar population models are fit through the EAZY package (Brammer et al. 2008). The best-fit value of Υ_* is consistent with the earlier spectral fits.

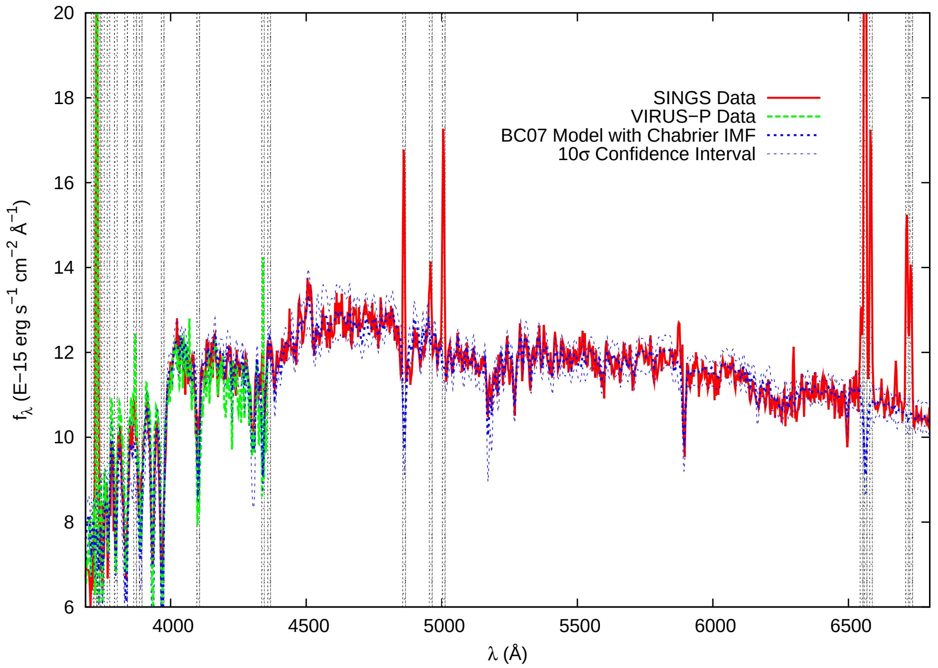

Figure 3.18 Data and fits to synthetic stellar population models. The spectra have been corrected for their radial velocity, broadened appropriately, and stacked. The SINGS spectrum has poorer resolution than the SPS models, so the SPS models are broadened to match. The average S/N per pixel over the displayed data is 60. Regions with emission lines have been masked in the fit and shaded in grey hatches. The best two-component model is shown with confidence intervals. Our VIRUS-P data agree well in absolute and relative flux calibration with the SINGS spectrum. The SPS fit is made to the SINGS spectrum, preferred by its wider bandpass and better coverage of the 4000Å break. The displayed best-fit model proscribes $\Upsilon_{*,R} = 0.90$ with luminosity weighted fractions of 0.91:0.09 for a $Z = 0.2Z_\odot$, E(B-V)=0, $\tau_{SFR} = 5$ Gyr, 12 Gyr age model and a $Z = 0.2Z_\odot$, E(B-V) = 0.60, instantaneous burst, 25 Myr age model respectively.

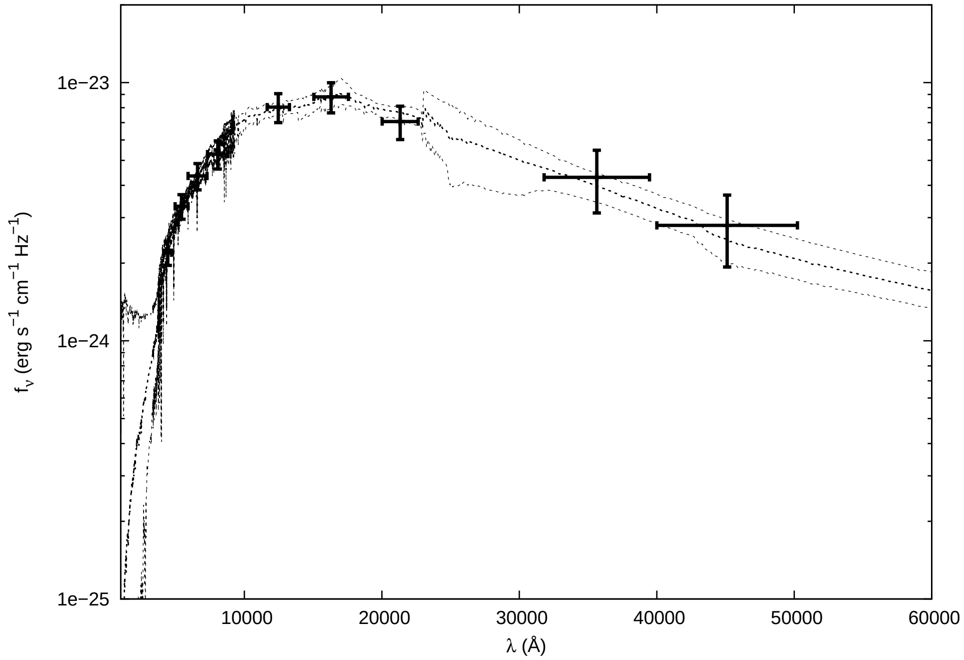

Figure 3.19 The stellar population fits to the optical and NIR data. The fits predict mass-to-light ratios that are consistent, but more loosely constrained, than the fit to the SINGS spectrum. The mass modelling of Oh et al. (2008) uses the 3.6μm photometry, but uses a stellar population fixed to a 12 Gyr age that does not match the K-[3.6 μm] color of NGC 2976. With a value of $\Upsilon_{*,3.6\mu m} = 0.66$ for a Diet-Salpeter IMF , de Blok et al. (2008) claim that NGC 2976 is baryon-dominated. Our models, specifically fit to the spectrophotometry of NGC 2976, disagree. We show a the best-fit model and confidence interval with various two-component SPS models. The best-fit model shown proscribes $\Upsilon_{*,R} = 0.64$ with luminosity weighted fractions of 0.67:0.33 for a $Z = 0.2Z_\odot$, E(B-V)=0.40, instantaneous burst, 100 Myr age model and a $Z = 0.2Z_\odot$, E(B-V)=0, instantaneous burst, 2.5 Gyr age model, respectively.

3.6 Conclusions

We present spatially resolved stellar and gaseous kinematics in the late-type dwarf galaxy NGC 2976. The gaseous kinematics, in concordance with earlier work, imply a cored dark matter halo when modeled with either a tilted-ring or harmonic decomposition method. Theory predicts a cuspy dark matter halo to exist in low mass halos when gravity alone is simulated. Baryonic feedback processes have been proposed as a mechanism to create a cored halo, which observations such as ours may constrain. The leverage of the stellar kinematics as a collisionless tracer is a major advantage to our work. We fit the stellar kinematics with an axisymmetric, semi-isotropic Jeans model to measure the DM profile and constrain Υ_*. The Jeans model permits both a cored or cuspy halo with a mild preference for a cored, high $\Upsilon_{*,R}$. We next fit a suite of stellar population histories to an optical spectrum with a broader bandpass. We find a limit of $\Upsilon_{*,R}$=1.08±0.8 driven primarily by uncertainty in the initial mass function. However, this limit in combination with the kinematic data provides a much tighter limit on the DM profile. The combined constraint suggests a DM cusp and excludes a DM core at 2σ significance. NGC 2976 is dark matter dominated everywhere outside of the nuclear star cluster and requires no history of baryonic feedback to explain the dark matter halo profile. A larger sample with stellar kinematics is motivated to compare with the vast literature on gaseous kinematics and reassess the quantity and distributions of dark matter in late-type dwarf galaxies.

Acknowledgements: This work was done in collaboration with Karl Gebhardt, Guillermo A. Blanc, Maximilian H. Fabricius, Gary J. Hill, Jeremy D. Murphy, Remco C. E. van den Bosch, and Glenn van de Ven.

Chapter 4

Ultraviolet metagalactic background

4.1 Introduction

The strength of the metagalactic ultraviolet background (UVB) has great impact on theoretical models of structure formation (e.g. Haardt & Madau 1996) and a variety of physical processes such as the inhibition of small halo collapse (e.g. Efstathiou 1992), the temperature and ionization state of the intergalactic medium (IGM) (e.g. Hui & Gnedin 1997), and IGM metallicity determinations (e.g. Rauch et al. 1997a). The likely contributors to the UVB are active galactic nuclei and star formation in galaxies (Schirber & Bullock 2003; Faucher-Giguère et al. 2008b) which appear compatible with observed populations (Gallego et al. 1995; Hopkins 2004; Hopkins et al. 2007; Bouwens et al. 2009) under reasonable corrections for dust attenuation, low luminosity extrapolations, redshift evolution, and escape fractions. The strength of the UVB, especially at low redshift (Davé & Tripp 2001), is still highly uncertain despite its importance. Most recent efforts have focused on high redshifts, $z > 2$, where the strongest UVB measurements exist. For instance, the detailed history of star formation (Madau et al. 1999; Faucher-Giguère et al. 2008a) and the potential to measure individual active galactic nuclei (AGN) host halo masses (Loeb & Eisenstein 1995; Faucher-Giguère et al. 2008c) have been explored. Measurements of the photoionization rate have used three methods: observations of Hα such as described in this paper, the line-of-sight proximity effect method (e.g. Carswell et al. 1982; Bajtlik et al. 1988), and the flux decrement method (e.g. Cen et al. 1994; Rauch et al. 1997b). The latter two require backlighting quasars and are therefore difficult or impossible at low redshift. We are motivated to constrain the current model with a different, low redshift measurement. Instead of using Lyman-α forest features, we pursue a measurement of the UVB-powered Hα emission that should occur in the outskirts of local disk galaxies. As a secondary motivation, the kinematics of Hα at distances beyond HI data are important probes to the total dark halo masses in nearby disk galaxies (Christlein & Zaritsky 2008).

Galactic disks are optically thick to Lyman limit photons and maintain their observed HI distributions through self-shielding against the UVB. As recognized for decades (Sunyaev 1969; Felten & Bergeron 1969; Bochkarev & Sunyaev 1977), the influence of the UVB may be investigated in the extreme outskirts of disks where the self-shielding begins to fail. These early works sought to measure this effect through disk truncation in HI. However, there appear to be cases with (Corbelli et al. 1989; van Gorkom 1993) and without (Walsh et al. 1997; Carignan & Purton 1998; Oosterloo et al. 2007) HI truncations above the critical column density predicted using current UVB estimates, implying that other processes may strip gas and mimic the result. Moreover, reaching the UVB implied truncation thresholds in HI would require rather long observations at 21 cm with current facilities. A more robust signature of the UVB strength would be the detection of the Hα in these outskirt regions. Hα has been found at such radii before in actively star forming and warped galaxies by Bland-Hawthorn et al. (1997) (hereafter BFQ) with Fabry-Perot staring measurements. However, the $\mu(H\alpha) = 2.3\times10^{-19}$ erg/s/cm^2/$\square''$ detection was attributed to non-UVB sources as indicated by an abnormally high [NII]λ6548 to Hα ratio. Searches have also yielded limits in quiescent systems (Vogel et al. 1995; Weymann et al. 2001; Madsen et al. 2001) with an upper limit for the UVB photoionization rate, Γ, of $\Gamma(z = 0) < 2.4 - 9.5 \times 10^{-14}\mathrm{s}^{-1}(2\sigma)$ being the deepest. The wide range on this limit is due to gas cloud geometrical uncertainty. Despite the numerous theoretical implications and the efforts of numerous groups, a UVB powered Hα detection still awaits discovery.

The tactical advantages we bring to this problem are deep surface brightness limits, a large two dimensional field of view through integral field spectroscopy compared to the previous longslit and Fabry-Perot staring data, and target selection of very high inclinations to maximize signal and minimize contamination uncertainty. Our targets are edge-on, low surface brightness Sd galaxies that are rather isolated and minimally warped in order to avoid density distribution uncertainties and exposure to internally generated ionization from smaller radii. Indeeed, our most constraining target, UGC 7321, has a gas surface density below that required for significant star formation (Kennicutt 1989) at all radii, as well as being unusually isolated with no known companions and minimal ($< 3^\circ$) warping (Uson & Matthews 2003).

In this paper we begin with a description of the simple ionization state and density model of disk galaxies that will be used to link a measured Hα surface brightness with a particular UVB photoiozation rate in §4.2.1. In §4.2.2, we argue that UGC 7321 in particular is likely to extend its HI profile beyond the current 21 cm limits without truncation. In addition, the HI observations of UGC 7321 are amongst the most sensitive such measurements published to-date. The 21 cm data allow a very precise model to be made for the gas distribution in the galaxy outskirts at the locations where we search for Hα emission. In §4.2.3, we give disk parameter constraints based on fits to existing 21 cm data. Next, in §4.3, we present deep integral field spectroscopy observations at radii corresponding to the outermost detections of 21 cm emission and beyond. We describe the choices made to stack spectra on various spatial scales. The stacked spectra are searched for Hα detections and upper limits are derived. Particular focus is given to systematic errors. Finally, in §4.4, we discuss the context, the likely cause of the unexpectedly low limit, and further observations that can confirm our conclusions. Appendix C provides the analytic details necessary to construct the full and general Hα surface brightness distribution model. We will quote most of the surface brightness limits in units of erg s^{-1} cm^{-2} arcsec^{-2}, but for easy comparison to alternative units we note the conversion at the wavelength of Hα of 1 millirayleigh (mR)$= 5.66 \times 10^{-21}$ erg s^{-1} cm^{-2} arcsec^{-2} $= 2.8 \times 10^{-3}$ cm^{-6} pc in emission measure assuming the case B recombination coefficient we adopt.

4.2 HI based models and Hα predictions

4.2.1 Model assumptions

A three dimensional gas density distribution must be inferred in order to translate Hα surface brightness into a UVB strength. BFQ made estimates assuming exponential forms both radially and vertically in the gas distribution with a plane parallel assumption. Motivated by the regular HI structure on local scales (García-Ruiz et al. 2002; Uson & Matthews 2003) of our chosen targets showing simple exponential trends and needing an extrapolated model in gas density for interpretation of UVB limits, we also assume exponential forms.

In order to interpret Hα measurements generically inside and outside of the UVB photoionization front around gaseous disks, we have generalized the model of BFQ. Some toy calculations in the model also show the importance of high inclination selection to make the deepest possible UVB constraints. This high inclination boon has been known before, but not carefully followed in earlier works' target selection. The model assumes both regular gas distributions and sharp photoionization transitions in a plane parallel approximation under arbitrary disk inclinations and sight lines. Our model assumes sharp photoionization fronts exist. We verify this assumption by estimating the Lyman limit photon mean free path at the midplane ionization front. In their Equation 3, BFQ estimate the hydrogen density at this point as $n_H \approx 0.05\text{cm}^{-3}$. The Lyman limit photon mean free path is given by $l_{mpf} \approx (n \times a_\nu)^{-1} \approx 1.1\text{pc}$ with a_ν (Osterbrock & Ferland 2006) as the hydrogen Lyman limit photoionization cross section. This is much smaller than the common disk scale lengths in either direction. The vertical scales for cold disk galaxies are of order 100 pc or greater. More sophisticated models can be made (Maloney 1993; Dove & Shull 1994) by solving for the ionization and excitation states of hydrogen and helium with full radiative transfer solutions in a grid of plane-parallel gas layers, but such an analysis is beyond the scope of this work.

The forthcoming derivation follows BFQ equations 1-6. The important differences are that this derivation is generalized for any viewing inclination, i, and for arbitrary positioning of the spectral data in the galaxy's field of observation. The BFQ derivations were specifically for $i = 0°$ and the field position along the major axis where all gas is photoionized. We denote the generic surface brightness in Hα as μ. We denote μ_0 as the special case of the peak Hα surface brightness where the photoionization front intersects the disk midplane. Our results reduce to the BFQ values of μ_0 for $i = 0°$. In Equation 4.1 we give the assumed gas distribution in cylindrical coordinates R and z with radial scale-length h$_r$, vertical scale length h$_z$, and central hydrogen density n_0.

$$n_H(R, z) = n_0 \exp(\frac{-|z|}{h_z}) \exp(\frac{-R}{h_r}) \tag{4.1}$$

The commonly assumed form of the UVB spectrum is given in Equation 4.2 where ν is the frequency, ν_0 is the Lyman limit frequency, J_0 is the UVB strength at the Lyman limit in units of erg cm^{-2} s^{-1} Hz^{-1} sr^{-1}, and β is the UVB spectral index.

$$J_\nu = J_0 \left(\frac{\nu_0}{\nu}\right)^\beta \tag{4.2}$$

Another common form of quoting the UVB strength is with the UVB photoionization rate, Γ. We show this form in Equation 4.3 where h is Planck's constant, $\sigma(\nu)$ is the hydrogen photoionization cross section, and a_ν=$\sigma(\nu_0)$ is the Lyman limit cross section. The final equality in Equation 4.3 comes from the standard power law approximation to the cross section shape (Osterbrock & Ferland 2006).

$$\Gamma = 4\pi \int_{\nu_0}^{\infty} \frac{J_\nu \sigma(\nu)}{h\nu} d\nu = \frac{4\pi a_\nu J_0}{h \times (3+\beta)} \tag{4.3}$$

In Equation 4.4 we equate recombination and ionization rates under a plane parallel approximation. For the radial regions where any self-shielding can take place, we consider the top and bottom of the disk to each see incident flux from only half their total solid angle. We define n_e as the electron density, n_p as the proton density, ξ as the ionization fraction, α_B as the case B recombination coefficient, and $z_c(R)$ as the height above the midplane to which the photoionization front penetrates at radius R. We define ε as the volume filling factor, assumed to be spatially invariant. A clumpy gas distribution can, to first order, be represented by using this term somewhat lower than the nominal value of unity. With the assumption of sharp ionization boundaries, we can equate the gas densities as $n_e = n_p = \xi n_H$ at radii beyond the photoionization front.

$$\alpha_B \int_{z_c(R)}^{\infty} \xi^2 \varepsilon n_H^2(R,z) dz = \int_{\nu_0}^{\infty} \frac{2\pi J_\nu}{h\nu} d\nu = \frac{2\pi J_0}{h\beta} \tag{4.4}$$

We next define a threshold radius, r_c, to which the UVB penetrates fully through the disk plane, so $z_c(r_c) = 0$. The solution of Equation 4.4 leads to Equations 4.5 and 4.6.

$$r_c = (\ln(2\xi^2 \varepsilon \alpha_B a_\nu n_0^2 h_z \beta) - \ln(\Gamma \times (3 + \beta))) \times h_r/2 \tag{4.5}$$

$$z_c(R) = \begin{cases} \pm(r_c - R) \times h_z/h_r & : R \leq r_c \\ 0 : R > r_c \end{cases} \tag{4.6}$$

Next, we define the variable ρ as the distance from the disk's midplane along the line-of-sight, spanning $-\infty$ to the observer and ∞ away from the observer. We also define the major axis position b_1, and minor axis position b_2 as the observed field positions projected onto the sky. Finally, we represent the galaxy's inclination with i. Simple transformations to cylindrical coordinates give the expressions in Equations 4.7 and 4.8.

$$|z| = \sqrt{\rho^2 \cos^2 i + b_2^2 \sin^2 i + 2\rho b_2 \sin i \cos i} \tag{4.7}$$

$$R = \sqrt{\rho^2 \sin^2 i + b_2^2 \cos^2 i + b_1^2 - 2\rho b_2 \sin i \cos i} \tag{4.8}$$

The Hα surface brightness, $\mu(b_1, b_2)$, follows directly from a line-of-sight integration. The full evaluation of $\mu(b_1, b_2)$ involves finding the values of ρ that intersect the photoionization surface described by $z_c(R)$ with field positions b_1 and b_2. The analytic solutions to those intersections are given in Appendix C. The solution for the special case at field position $b_2 = 0$ and $b_1 = r_c$ gives the aforementioned peak surface brightness μ_0, which is itself a useful measurement parameter, as related in Equation 4.9. In Equation 4.9, γ is the generally non-analytic integration of the emissivity along the line of sight, $\alpha_{H\alpha}^{\mathrm{eff}}$ is the case B effective Hα recombination coefficient, and Ω is the full sky solid angle of 4π sr. For the gas density parameters we derive in our target galaxies in §4.2.3 and the areas we observe in §4.3, the face-on column densities of total hydrogen are sufficient ($> 10^{17}$ cm^{-2}) to be everywhere optically thick to Lyman limit photons, let alone Lyman-β and the other important lower energy transitions. We use $\alpha_{H\alpha}^{\text{eff}} = 1.17 \times 10^{-13}$ cm^3 s^{-1} as appropriate for T$= 10^4$K (Osterbrock & Ferland 2006).

$$\mu_0 = \frac{2h\nu_{H\alpha}\alpha_{H\alpha}^{\text{eff}} \int_0^\infty n_e(R,z)n_p(R,z)d\rho}{\Omega} = \frac{2\xi^2\varepsilon\alpha_{H\alpha}^{\text{eff}} n_0^2 h\nu_{H\alpha}\gamma}{\Omega}$$
$$\text{with } \gamma = \int_0^\infty \exp(-\frac{2\rho\cos i}{h_z} - \frac{2\sqrt{r_c^2+\rho^2\sin^2 i}}{h_r})d\rho \tag{4.9}$$

We explain the use of certain constants and assumed values to Equation 4.9. The ionization fraction is assumed to be unity by the earlier discussion of the Lyman limit mean free path. The volume filling factor may approach unity as there is no indication of star formation at extended scales in these galaxies. We will discuss the evidence for the absence of extended star formation in Section 4.4. Furthermore, the deprojection of the HI distribution in Uson & Matthews (2003) gives a peak surface density of only 5.8 $M_\odot$ pc^{-2} at the center of UGC 7321. The surface density drops by over an order of magnitude at the locations we observe. These surface densities are well below the dynamical criterion for efficient star formation (Toomre 1964; Kennicutt 1989) and make a smooth gas distribution plausible. It is not possible to exclude small scale clumpiness, so we retain the volume filling factor. The case B and Hα effective recombination coefficients are dependent on electron temperature. Following Weymann et al. (2001) and the discussion therein, we adopt T=10,000 K and the values of Osterbrock & Ferland (2006). The true electron temperature may plausibly be different by a factor of two, leading to corresponding changes in $\alpha_{H\alpha}^{\text{eff}}$ and α_B of the same order of magnitude. However, the linearization in Γ of Equation 4.9 makes the surface brightness depend on the ratio of these two recombination coefficients, so their similar behavior with electron temperature cancels. For consistency with previous works, we do not propagate the recombination coefficient uncertainties as systematics to the final UVB limit.

Some brief numerical examples set the expected orders of magnitude, quantify the achievable limits under different galaxy geometries, and illustrate the important parameter dependencies under linear expansions. We look at some trial cases with $\varepsilon = 1$, $h_r = 1000$ pc, $h_z = 100$ pc, $\beta = 1.8$, $\Gamma = 4 \times 10^{-14}$ s^{-1}, and $n_0 = 5$ cm^{-3}. For $i = 0°$, $\gamma = \exp(-2r_c/h_r) \times h_z/2$ so $\mu \approx 3.0 \times 10^{-20}$ erg/s/cm^2/$\square''$. For $i = 90°$, $\gamma = r_c K_1(2r_c/h_r)$. $K_1(x)$ is the modified Bessel function. In this case, $\mu \approx 1.3 \times 10^{-18}$ erg/s/cm^2/$\square''$. For this work's applications, the surface brightness profiles are smoothed by seeing and sampled by large fibers. Realistic smoothing and sampling, of order several arseconds, can lower these peak values by several tens of percent. We will assume for all calculations that $\beta = 1.8$ as motivated by previous models (Shull et al. 1999) and to aid the comparison with previous observational work that used the same assumption (Weymann et al. 2001). We note that μ_0 scales exactly linearly with Γ when viewed face-on and nearly linearly for all other inclinations. This is easily demonstrated by taking the large argument asymptotic behavior of the modified Bessel function which yields a linear scaling in Γ after a first order expansion. We show the small error caused by assuming a linear relation between μ_0 and Γ in Figure 4.1 for reasonable geometries. All further estimations of Γ in this work will be made in the linear approximation. The discussed numerical example between $i = 0°$ and $i = 90°$ also shows how the selection of thin, edge-on disks can exploit a particular flux limit to a $(30 - 50\times)$ stronger UVB constraint than for face-on disks. We also emphasize with Equation 4.9 that the first order effects near i=90° on distance, volume filling factor, and gas density cancel out; μ_0 only has first order dependence on i, the ratio of scale lengths, $\frac{3+\beta}{\beta}$, and Γ.

4.2.2 HI bounded limit

While we cannot definitively prove that these galaxies maintain their extrapolated hydrogen profiles over the galactocentric distances we will discuss in §4.2.3, such an assumption is reasonable with the current 21 cm data. There is no evidence for

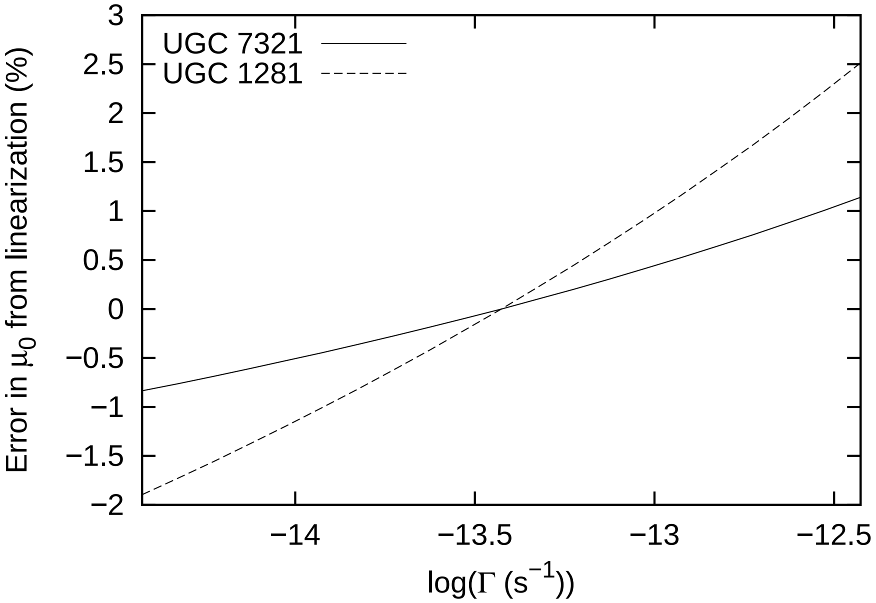

Figure 4.1 The fractional error in a linear relation between the Hα peak surface brightness and the UVB photoionization rate, Γ, under different UVB strengths. The parameters for the two target galaxies are given in Table 4.1 and their derivation described in §4.2.3. The pivot in the linearization at $\Gamma = 4 \times 10^{-14}$ s^{-1} represents the current best estimate from Faucher-Giguère et al. (2009).

flaring in these galaxies, and the superthin shape implies an undisturbed history. In UGC 7321, Uson & Matthews (2003) have searched for low-mass compansions and found none to the limit of $M_{HI} = 2.2 \times 10^6$ $M_\odot$ within $12'$(35 kpc). The nearest optical companions are two dwarf galaxies at minimum distances of 340 kpc, implying minimum times to last encounter of 1.6×10^9 years. So, it is unlikely that gas has been stripped from the regions over which we have extrapolated a density profile. However, we have calculated an alternative limit using data bounded by the HI data in a manner similar to the analysis in Stocke et al. (1991); Vogel et al. (1995); Donahue et al. (1995); Weymann et al. (2001) as an alternative, which is equivalent to assuming that the gas is completely truncated where the 21 cm signal falls below the noise. In those works, a single, simple equation based on global photoionization equilibrium is used and here repeated in Equation 4.10.

$$\Phi = \Gamma \frac{3+\beta}{4a_\nu \beta} = \frac{I_{H\alpha}}{f_a f_{H\alpha}} \frac{A_{proj}}{A_{tot}} \tag{4.10}$$

The variable Φ is the one-sided incident ionizing UVB flux in units of cm^{-2} s^{-1}, $I_{H\alpha}$ is the Hα surface brightness in units of μR, f_a is the fraction of incident photons that become absorbed when passing through the face-on cloud, $f_{H\alpha}$ is the fraction of excited recombinations that produce an Hα photon, A_{proj} is the projected area covered by spectroscopy and 21cm data, and A_{tot} is the total surface area for the regions in projection that can absorb Lyman limit photons. The area aspect ratio is usually determined from 21cm data. This calculation takes no account of the spatial stratification between 21cm and Hα that can realistically occur for very thin gas distributions, as we will see later in §4.2.3 where the predicted Hα surface brightness is derived, and requires Hα searches and interpretations to be restricted to area covered by deep 21cm data. However, for mild aspect ratios ($\sim<$ 10) or large 21cm beams, this method delivers similar predictions as those in §4.2.1.

We now discuss the evaluation of the few terms in this model. The assumption in the HI bounded limit is that the hydrogen resides within some well-defined area represented by the noise floor of the 21cm data. It is not obvious how the area should be defined in a continuous gas distribution, but we adopt the photoionization front we have previously defined in Equations 4.5 and 4.6 as a realistic edge. In §4.2.3 we determine gas geometries for our target galaxies. In particular for the area in UGC 7321 covered by fibers, with $N_{HI} > 10^{19}$ cm^{-2}, and the parameters in Table 4.1, we find $\langle \frac{A_{tot}}{A_{proj}} \rangle = 24.8^{+3.4}_{-1.5}$. This value is in good agreement with the 21cm axis ratio of 29 determined at the 10^{20} cm^{-2} contour in Uson & Matthews (2003, Table 3). By adopting this distribution in face-on column density and a UVB spectral index of $\beta = 1.8$, we can evaluate f_a. We find $\langle \frac{A_{tot} f_a}{A_{proj}} \rangle = 22.8^{+4.4}_{-1.8}$ in UGC 7321. With the same calculations applied to UGC 1281, we find $\langle \frac{A_{tot}}{A_{proj}} \rangle = 19.0^{+5.6}_{-1.8}$ and $\langle \frac{A_{tot} f_a}{A_{proj}} \rangle = 13.6^{+6.2}_{-2.0}$. Identically to Weymann et al. (2001), we adopt $f_{H\alpha} = 0.45$ as appropriate for case B and a 10^4K electron temperature. We also carry out this analysis in Tables 4.1 and 4.2 for continuity with previous work, but we emphasize that our preferred limit comes from the comparisons to the model in §4.2.1 as it incorporates the spatial segregation between the brightest Hα regions and the HI data that is natural in very thin, edge-on geometries.

4.2.3 HI data

Three-dimensional gas distributions must be inferred for individual galaxies to interpret Hα surface brightness and to guide the stacking choices amongst fibers. We will use such fits to extrapolate the density profiles to larger radii where the Hα emission is predicted to reach peak surface brightness. The parameters from stellar distributions could potentially be used, but 21 cm measured HI is the more relevant indicator to ionized hydrogen. We adopt distances of 10 Mpc for UGC 7321 (Uson & Matthews 2003) and 5 Mpc for UGC 1281 (Tully et al. 2006). Low redshift surface brightness is insensitive to distance, so the exact distances are unimportant to this work. Different literature estimations have 50% and 10% rms ranges for the UGC 7321 and UGC 1281 distances respectively. We indicate scale lengths by the terms d_{10} as the actual distance to UGC 7321 in units of 10 Mpc and d_5 as the actual distance to UGC 1281 in units of 5 Mpc. For reference, the scale conversions become $48.5d_{10}$ pc/$''$ for UGC 7321 and $24.2d_5$ pc/$''$ for UGC 1281.

UGC 7321 was observed by Uson & Matthews (2003) using the second most-compact (C) configuration of the VLA[1] which includes some of the shortest spacings available and their full coverage, deep observations yielded spacings down to 28m, close to the dish diameter. Their quasi-naturally weighted ("robust" parameter $\mathcal{R} = +1$) images recovered the full single-dish flux and, moreover, their single-dish equivalent spectrum matched the features of the best single-dish spectrum to within the (higher) uncertainty of the single-dish observations (Uson & Matthews (2003), fig. 6). For this paper, we have used their quasi-uniformly ($\mathcal{R} = -1$) weighted images because of their better resolution ($\sim 12''$) although the somewhat higher (45%) noise level only recovers ~96% of the total flux. However, the five parameter model fits to the zeroth moment maps, described below, recover some of the lost flux and the remaining uncertainties only slightly shift the position of the predicted Hα peak.

For UGC 1281, we have reduced the raw data from the VLA archive. It was observed under proposal AZ097 on 1997 December 26 in the most compact (D) configuration for a total of 3 hours on source with interspersed observations of the strong, primary calibrator J0137+3309 (3C48) for which we have adopted the VLA recommended flux density of 15.9 Jy. The observations were spaced over a range of ±3 hours in H.A. giving excellent uv-coverage and images with 127 channels of width $\sim$ 2.6 km s $^{-1}$ after standard on-line Hanning-smoothing. The angular scale that corresponds to the shortest baseline ($\sim 900''$) is sufficiently larger than the largest

---

[1] The Very Large Array of the National Radio Astronomy Observatory is a facility of the National Science Foundation, operated under cooperative agreement by Associated Universities, Inc.

single-channel galaxy extent ($\sim$285$''$) that the array should have recovered the total HI flux. We followed the same reduction steps as for UGC 7321 (Uson & Matthews 2003) to obtain a "cube" of spectral images using nearly-natural weighting ($\mathcal{R}$ = +1) which gave images with resolution $\sim$51$''$ which were free of artifacts to the rms sensitivity σ $\sim$1.0 mJy/beam per channel. We computed moment maps after applying a standard "1-σ cutoff" evaluated on a cube Gaussian- smoothed spatially to 70$''$ and Hanning-smoothed in frequency, which led to a total HI flux of 41 ± 2 Jy km s^{-1} corresponding to a mass of 2.3×10^8 $d_5^2 M_\odot$. The total flux is in good agreement with the values in the literature, which range from (35.8 to 38.9) Jy km/s from two different single-dish measurements (Huchtmeier 1989) with the spread and uncertainty due in part to some ringing from strong in-band HI emission from the Milky Way as well as to calibration uncertainties. Again, we have obtained a spectral "cube" with nearly-uniform weighting ($\mathcal{R} = -1$) which gave images with resolution of $\sim$42$''$ with rms sensitivity σ $\sim$1.5 mJy/beam per channel. As in UGC 7321, the higher noise level results in a slightly lower total flux, 39 ± 2 Jy km s^{-1}.

Next, we characterize the HI distributions nearest our Hα observations. We have derived five parameter fits in $n_0, h_r, h_z, i,$ and position angle to the zeroth moment maps of UGC 7321 and UGC 1281 through non-linear least squares minimization. The models include convolution to the instrumental beams of $\sim$12$''$ and $\sim$42$''$ FWHM and sampling of Hα appropriate to the fiber data. Both the maps show at least two major axis power law slopes, as Christlein et al. (2010) have found to be common in extended gaseous disk gas. We do not try to model the full gas distributions, but only the large radius trends by restricting the fits heavily to the outermost data regions. Still, the model fits deviate from the data by an amount that exceeds the observational errors. Some minor warps and substructure are visible. The formal errors in the total line intensity images are 15×10^{18} cm^{-2} for UGC 7321 and 5×10^{18} cm^{-2} for UGC 1281, which are both far smaller than the residuals to the best fit models. In order to capture the systematic model errors, we have made Monte Carlo simulations between the data and the best fit models to create 68% confidence intervals as given in Table 4.1 for all disk parameters and Hα observables. The perturbations in the Monte Carlo simulations are made from the residuals of the best fit model, not the statistical errors, to include the influence of systematics. These simulations allow us to create three types of Hα surface brightness prediction, with different scales of spatial co-addition, under an assumed Γ. Note that many of the individual disk parameters in Table 4.1 have large relative uncertainties, but the surface brightness predictions have small relative uncertainties. The disk parameters share degeneracies, as captured in the Monte Carlo simulations, that create highly certain Hα predictions despite the individually uncertain gas parameters. Predictions can be made for individual fibers, but to both mitigate the model uncertainties and improve our limits, we include predictions with a $10'' \times 10''$ FWHM convolution sampled near the peak surface brightness positions. The exact choice of kernel size is not important, but is chosen to combine several neighboring fibers. Finally, we include a prediction for the average surface brightness of all fibers expected to sample $\mu > 10^{-19}$ erg/s/cm^2/$\square''$. These various predictions will be compared to co-added data in §4.3. We give in Figure 4.2 the HI fits along major and minor axis cuts. The fits to UGC 7321 use all the HI data beyond an inner radius cut, which was chosen to avoid a substructure bump near $R \approx 140''$. The fits to UGC 1281 are more constrained with both an inner and outer radius cut. The outer cut is to exclude a known $\sim 8^\circ$ warp (García-Ruiz et al. 2002). The fitting function assumes a single position angle at all radii and does not describe warps well. We have investigated the disk's outer behavior by also deriving fits from the R>220$''$ data alone. A radial scale length compatible with, but noisier than, the Table 4.1 value was found with a significant change in position angle, a reflection of the warp.

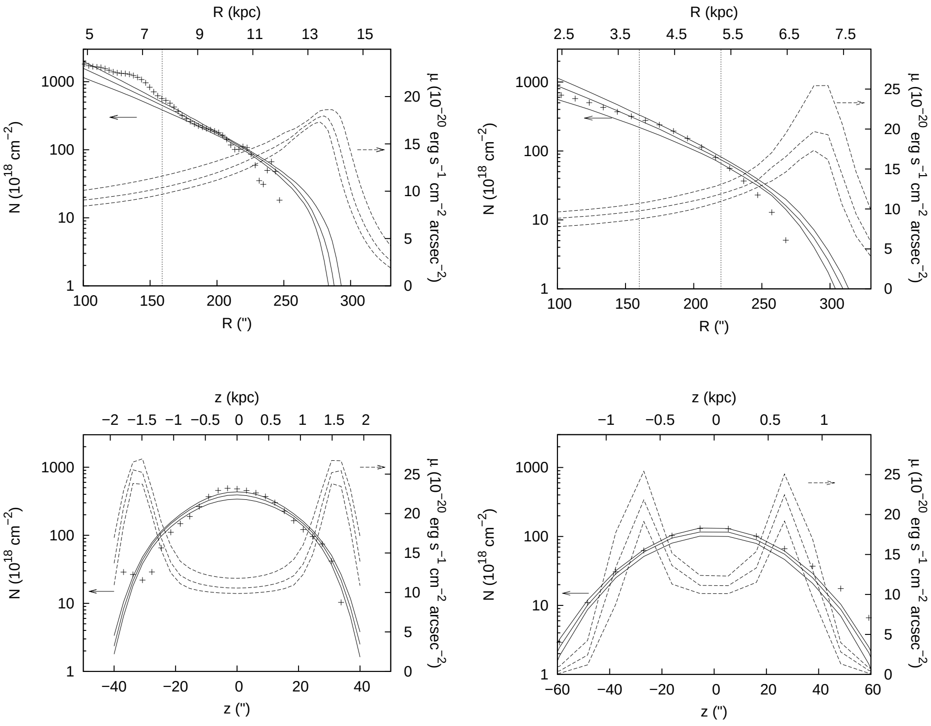

Figure 4.2 The single position angle, parameterized fits to the HI distributions. The predicted Hα surface brightness profiles are also shown against the right side axis. The horizontal arrows indicate the correct axis for each profile. The stratification of Hα emission in these very thin galaxies is not captured in the model predictions of §4.2.2, but is captured in our preferred limit analysis of §4.2.1. The breaks at large radii in the 21 cm profiles are due to intersections with the UVB photoionization fronts. *Top* The data along the major axes. *Bottom* The data along the minor axes at particular offsets. *Left* Cuts along the midplane and normal to it offset by $165''$ with data, models, and 68% confidence intervals in UGC 7321. We restrict the fit to points $> 160''$ from the galaxy's center as indicated by the vertical dotted line. Using the best parameters from Table 4.1, the threshold radius (Equation 4.5) with the nominal value of $\Gamma = 4 \times 10^{-14}$ s^{-1} is predicted to be at $r_c = 13.4$kpc. Our spectroscopic data cover regions from R= 9.5kpc to R= 14.6kpc. *Right* Similarly, data and fits to UGC 1281. The offset here is $200''$ from the minor axis. The points between the dotted lines at $160''$ and $220''$ form the restricted range of the fit as a $\approx 8^\circ$ warp becomes important beyond. This fit appears poorer because of the larger warp, but a fit to all points at R $> 220''$ returns the same radial scale length to within the Monte Carlo errors. Using the best parameters from Table 4.1, the threshold radius (Equation 4.5) is predicted to be at $r_c = 7.4$kpc. Our spectroscopic data cover regions from R= 5.7kpc to R= 9.1kpc.

Table 4.1. HI based model parameters and Hα surface brightness predictions*

Galaxy	n$_0$ (cm^{-3})	h$_z$ (pc)	h$_r$ (kpc)	i (°)	PA (°)	μ_0 †	$(\mu \otimes S)_0$ ‡	$\bar{\mu}$ ††	$\mu_{\rm HI}$ **
UGC 7321	$3.3^{+3.5}_{-1.7}$	$426.^{+120.}_{-88.} d_{10}$	$2.12^{+0.25}_{-0.16} d_{10}$	$82.8^{+0.9}_{-0.6}$	-100.1±0.1	$18.4\ ^{+1.0}_{-0.9}$	$16.7^{+1.1}_{-0.7}$	$16.6^{+1.0}_{-0.3}$	$22.5^{+4.3}_{-1.8}$
UGC 1281	$3.8^{+3.2}_{-2.6}$	$303.^{+70.}_{-58.} d_5$	$1.17^{+0.19}_{-0.14} d_5$	$84.9^{+4.0}_{-1.3}$	-141.3±0.3	$21.4\ ^{+12.1}_{-2.8}$	$19.4^{+5.6}_{-2.4}$	$17.9^{+1.7}_{-1.1}$	$13.4^{+6.1}_{-2.0}$

*Fit under the restricted radial ranges shown in Figure 4.2 assuming $\Gamma = 4 \times 10^{-14}$ s^{-1} and $\beta = 1.8$.

†10^{-20} erg/s/cm^2/□″

‡10^{-20} erg/s/cm^2/□″, smoothed by a circular 10″ FWHM kernel

††10^{-20} erg/s/cm^2/□″, average for all fiber positions with predicted values of $\mu > 10^{-19}$ erg/s/cm^2/□″

**10^{-20} erg/s/cm^2/□″, based on the HI bounded area (Equations 6-8 of Weymann et al. (2001))

4.3 Hα data and analysis

We have obtained new integral field spectroscopy positioned along the major axes of UGC 7321 and UGC 1281 targeting Hα with the Visible Integral-field Replicable Unit Spectrograph Prototype (VIRUS-P, Hill et al. 2008b) on the McDonald 2.7m telescope. We observed UGC 1281 on 2009 October 22-24 with R = 1288 from 4700-6990Å for 21 photometric hours and UGC 7321 on 2010 April 9 and 11 with a resolution of R = 3860 from 6040-6740Å for 15 hours under non-photometric conditions. Between the R = 1288 and R = 3860 observations, made possible by a new grating, we not only gain in sensitivity scaled by the square root of the resolution but resolve the bright skylines, OH λ6568.779 and geocoronal Hα, from our target wavelengths. We have set the controller to bin pixels by two in the wavelength direction which samples the spectra just at the Nyquist criterion and minimizes read noise. The VIRUS-P field covers a $1\farcm6\times1\farcm6$ field with 246 fibers of $2\farcs05$ radius with a one-third fill-factor. We split our observations into three dithers to cover the entire field. In UGC 1281 we split our time further between two overlapping fields to cover the outer plane better in the presence of a possible <8° warp (García-Ruiz et al. 2002) yielding a total of six dithers. Spectrophotometric flux standard stars from Massey et al. (1988) were measured once or twice nightly. We tracked the transparency through the offset guiding camera. Galactic extinction corrections (Schlegel et al. 1998; O'Donnell 1994) were made with A_V=0.09 and A_V=0.15 for UGC 7321 and UGC 1281 respectively. A spectral airmass/extinction curve specifically modelled for the McDonald Observatory site was applied. We estimate its systematic uncertainty by comparing it to the Kitt Peak curve supplied with the IRAF package `onedspec`. We find a 20% rms difference between the wavelengths of 6000-7000Å. The two curves deviate systematically at $\lambda > 5900$Å. We believe the site specific McDonald curve to be more accurate to our data. However, we propagate the difference as a potential, systematic uncertainty. The flux calibration uncertainty due to the airmass/extinction curve at the data's median airmass of 1.09 is ±0.023 magnitudes.

4.3.1 Flux calibration

The $8'$ offset guiding camera is an Apogee Alta with a $20.25\square'$ field-of-view under a B+V ($\lambda_{\mathrm{mean}} = 5000$Å) filter. Guider images were read out and saved every few seconds. Stacks of guider images that overlapped in time with each individual VIRUS-P exposure (20 minutes each on UGC 1281, 30 minutes each on UGC 7321, and 1 minute each on the flux standards) were combined. We make a relative photometry correction to each science frame based on the stack of guider images taken simultaneously with the VIRUS-P data. Typically, ten stars per guider frame were available for photometry.

We have switched from the standard stars to the science targets with gaps of less than 5 minutes and assumed the conditions to be constant over that time and between the standard star and galaxy positions to make the absolute flux calibration. The observations of standard stars were taken during the most photometrically stable periods during each night to mitigate this potential source of error. Even so, the final flux calibration factor we apply may have systematic errors. We assess this error by considering the 5 observations of 2 standards, PG1708+602 and Feige 34, taken along with the UGC 7321 data and the 3 observations of 1 standard, Feige 110, taken along with the UGC 1281 data. The distribution in flux calibrations is wavelength-independent over our observed range with a 6.8% rms and 2.2% rms respectively. These estimates also capture possible variation in transparency with on-sky position. They are reported in Table 4.2 along with the possible error in the extinction curve between the effective wavelength of the guider and the wavelength of Hα. For the non-photometric data on UGC 7321, we measured a median zero-point change, Δzp, of 0.276 magnitudes and a 68% range of 0.171-0.382 magnitudes over the two nights. The more nearly photometric data on UGC 1281 had median Δzp =0.057 magnitudes and a 68% range of 0.043-0.077 magnitudes over the three nights.

4.3.2 Sky background subtraction

The choice of sky subtraction is particularly important for this work which reaches for flux limits far below the average sky brightness. If the science field were covered with source emission, sky nods would be necessary. Then, the time variability of the OH and geocoronal Hα sky lines would form important systematic error sources. Fortunately, the large VIRUS-P field of view and selection of extremely thin, edge-on target galaxies affords a subset of fibers that contain a negligible amount of source flux to serve as simultaneously measured sky fibers. We selected fibers sufficiently far from the major axis such that the models predicted $\mu < 2{\times}10^{-21}$ erg/s/cm^2/$\square''$(with the baseline $\Gamma = 4 \times 10^{-14}$ s^{-1}), or 100× below the expected peak surface brightness, to be used for sky subtraction. This cut left 24% and 44% of the fibers for sky estimation in UGC 7321 and UGC 1281 respectively. We experimented with moving this sky fiber cut up and down by a factor of five and found no difference in the final upper limits to the UVB strength. Depending on the number of fibers co-added, the statistical Hα flux errors presented here reach to 300× dimmer than the sky level. Without simultaneously measured sky background, the systematics of sky nods would quickly dominate the limits.

4.3.3 Data reduction

The data reduction, optimal background subtraction, and search for emission lines were completed with algorithms developed for a Lyman-α emitter survey (Adams et al. 2011). We summarize here the important steps. First, overscans and a master bias frame are subtracted from each frame. The wavelength solution for each fiber is fit as a fourth order polynomial to ~ 30 emission lines from HgCd lamps passing through the entire telescope light path. The residuals to the solution are of order one hundredth of a resolution element. Flat fields precise to $< 1\%$ are made from twilight flats with the solar spectrum removed by a b-spline fit (Dierckx 1993) and division. This fit method is the same as we apply to fitting and subtracting the sky background and has important advantages over data interpolation. By avoiding data resampling, we keep the errors largely uncorrelated. Small distortions of the instrument camera over a regular pixel grid lead to the spectrum from each fiber being sampled at slightly different wavelengths. By considering a collection of fibers together in a fit, the spectrum is oversampled, and we can recover nearly blended features. This method delivers an optimal spectral model robust against cosmic rays and without the residuals that linear interpolation can create. A thorough description of b-spline fits as applied to astronomy datasets can be found in Kelson (2003). The next step in the data reduction is to fit and subtract a b-spline sky background modelled from selected sky fibers. Next, cosmic rays are masked by finding all pixels that deviate from the other pixels in the same fiber by some large threshold value. Some dim cosmic rays are missed by this step, but are rejected when combining multiple frames. We have chosen a threshold that misses the weakest $\sim$20% of cosmic rays for direct masking in this work. The exact threshold does not affect the results. The frame is then flux calibrated with the non-photometric zeropoint correction and airmass correction applied. Finally, a one dimensional final spectrum for each fiber position is created by combining all the frames taken at the same dither position and running across the 5 pixel cross-dispersion aperture. For the final estimate to be immune to remaining cosmic rays we have used the biweight estimator (Beers et al. 1990) at this step. Our pipeline makes no cross-talk correction since we restrict our cross-dispersion apertures to 5 pixels where the fiber separations are typically 8 pixels and the cross-dispersion FWHMs are typically 4 pixels. This leads to, at most, 10% contamination from neighboring fibers and becomes especially trivial when considering large collections of fibers as an aperture. The scattered light properties of the instrument have been characterized in Adams et al. (2008) and, particularly at Hα wavelengths, no scattered light or ghost patterns are found. The spectral resolution varies by $< 5\%$ for all fibers at a common wavelength due to careful design and alignment of the spectrograph camera. We have made no corrections by convolution to a common resolution. The effect of the spectral resolution variation and the background subtraction scheme is to leave residuals under bright skylines. We characterize the spectral resolution systematic in §4.3.5. Given the large number of independent spectral elements in VIRUS-P data (126,000 in each dither), we must choose a high significance cut. At 5σ significance, the chance of noise leading to a detection at a particular wavelength in a particular dither is only 1 in 14,000. We choose to quote this limit as sufficiently conservative.

4.3.4 Emission line detection

We describe here an automated emission line search algorithm to work with a sky background and continuum subtracted spectrum or stacks of spectra. By applying this search, we robustly find all significant emission lines at all redshifts. In practice, we find no significant Hα emission with plausible velocity offsets in any fiber for either galaxy. Plausible velocity offsets are determined by the HI rotation curves. In UGC 7321, for example, the rotation curve is flat over our data range with variations of only ± 10 km s^{-1}. The gas dispersion is measured in the HI data to be near 7 km s^{-1} subject to the limitation of the 5 km s^{-1} resolution (Uson & Matthews 2003). Over a very conservative ± 100 km s^{-1} (2.2Å) range around our target wavelengths, the flux limit is flat. First, spectral pixels at any wavelength that exceed the noise by 1σ are treated as seeds. Around each seed, we fit Gaussian profiles of variable intensity, width, and central wavelength. The S/N of an emission line is then calculated by summing all pixels and errors in quadrature within $\pm 2\sigma_{res}$ for the wavelength of interest where σ_{res} is the instrumental dispersion. In the UGC 7321 data, σ_{res} =33 km s^{-1}, and in the UGC 1281 data, σ_{res} =100 km s^{-1}. When quoting limits on undetected emission lines, we sum in quadrature the errors within the same spectral window. These steps in error combination consider both the statistical errors in the reduced data and the systematic error based on ill-matched spectral resolution between fibers discussed in §4.3.6. A spectral correction factor is divided into the detections and limits to consider the fraction of a Gaussian function's flux that falls outside of the considered window as $f_{spec} = \mathrm{erf}(\sqrt{2}\sigma_{res}/\sqrt{\sigma_{res}^2 + \sigma_{det}^2})$ where σ_{det} is the detected emission line width. This same factor determines the degradation in flux limit for broad line detections. For unresolved limits, σ_{det} is considered to be zero and the spectral correction (f_{spec}^{-1}) evaluates as ×1.05. In practice, we make no significant detections within ±500 km/s of the HI based expected velocity in either galaxy. The average HI heliocentric velocities of UGC 7321 and UGC 1281 are 407 km/s (Uson & Matthews 2003) and 157 km/s (García-Ruiz et al. 2002) with the asymptotic HI velocities nearest our pointings at ∼510 km/s and ∼210 km/s respectively. We observed under topocentric radial velocities of -12 km/s and 3 km/s toward UGC 7321 and UGC 1281 respectively. Therefore, we expect unresolved Hα emission at 6573.7±0.4Å and 6567.5±0.8Å using the asymptotic values just quoted, in the observed frames of UGC 7321 and UGC 1281 respectively. The gas velocity dispersions in the 21 cm data are of the order 7 km s^{-1}. The 21 cm rotation curves change by ±10 km s^{-1} over our fields. These two values form the expected wavelength range, and the flux limits around these lines are flat to ±100 km s^{-1}.

Background galaxies produce the dominant flux in a number of fibers. This is evident where we can measure redshifts through emission lines identifiable as either Lyman-α, [OII]λ3727, Hβ, [OIII]λ4959, or [OIII]λ5007. For most of the background systems with emission lines the redshift is determined by the pattern of multiple emission lines. If the background galaxies have smooth continuum through our wavelength of interest their removal is accomplished in the continuum removal step. However, the possibility of spectral structure in the continuum across the corresponding Hα wavelength range leads us to mask those regions. Operationally, we mask a fiber if it displays a 5σ significant value in its continuum as estimated across all available wavelengths under inverse variance weighting. It is also possible that weak continuum is coming from objects in the halo of the target galaxies, in which case the desirability of a mask is less certain. We have performed all the emission line searches and limits with and without this masking process and found no detections in either case. The values we present as limits were made with the masks applied.

4.3.5 Data co-addition and limits

We show the derived limits in Table 4.2. We find no significant emission lines within the vicinity of the galaxies' velocities (defined as within ± 500 km s^{-1}) in any individual fiber. We next mask out continuum sources and apply a circular spatial filter as a 2D Gaussian function kernel with FWHM=$10''$. Again, we find no significant emission. Finally, we stack all fibers which by the model of §4.2.1 should have $\mu > 10^{-19}$ erg/s/cm^2/$\square''$. The models used to select those fibers are those presented in Table 4.1 with an assumed $\Gamma = 4 \times 10^{-14}$ s^{-1} and $\beta = 1.8$. We use the nearly (Figure 4.1) linear scaling between Γ and μ to determine the true value of Γ. The models predict such averages to yield $1.7{\times}10^{-19}$ erg/s/cm^2/$\square''$ for UGC 7321 and $1.8{\times}10^{-19}$ erg/s/cm^2/$\square''$ for UGC 1281. We again find no significant emission in the stacked spectra. These emission line searches were performed solely with errors based on Poisson noise statistics and yielded no detections. In §4.3.6 we discuss additional systematic errors that degrade the final limits derived from purely Poisson errors in the data. By the models, the peak Hα surface brightness would have fallen in our fields for UVB strengths from 2×10^{-14} s^{-1} $< \Gamma <$ 2×10^{-12} s^{-1} and warps of <12.4° in UGC 7321 and 4×10^{-15} s^{-1} $< \Gamma <$ 3×10^{-13} s^{-1} and warps of <15.8° in UGC 1281. However, a radial displacement of the field would still give significant flux as seen in the contour plots, so we do not expect misalignments to affect the final limits. Figure 4.3 shows the positions of the observations relative to several key features. The 21 cm data contours are overlayed, the locations of masked background galaxies are shown, and the expected spatial profiles of Hα emission is shown. We show in Figure 4.4 the sky spectra and the three types of spectral stacks to background subtracted data in UGC 7321. In Figure 4.5 we show the corresponding ones for UGC 1281. In neither case do we make a significant detection in Hα.

Our selection of fibers for co-addition based on a particular value for Γ leads us in turn to a lower limit on Γ. This may in principle introduce an error into our determination of Γ. However, both a rough estimation and then a detailed analysis show that the non-linearity in this operation is negligible. First, one measure of the spatial scale of the Hα surface brightness profile is the threshold radius, r_c, of Equation 4.5. Since r_c scales only as the natural logarithm of Γ, there is little change over the range of possible UVB strengths that we consider. The shape of the Hα surface brightness profile is also broad and smooth, from Figure 4.3, relative to the possible range of r_c. By selecting wide swaths of fibers for co-addition, the problem is particularly well behaved. Second, we verify these arguments with a numerical example. We simulated the surface brightness profiles for $\Gamma = 8 \times 10^{-15}$ s^{-1}, or five times lower than the nominal modeled value. We sampled the same set of fibers for co-addition as with the previous analysis. The model, average surface brightness was $\mu = 3.1 \times 10^{-20}$ erg/s/cm^2/$\square''$ and $\mu = 3.9 \times 10^{-20}$ erg/s/cm^2/$\square''$ for UGC 7321 and UGC 1281 respectively, or only 6% lower and 10% higher than the linear prediction. We conclude that the selection of co-added fibers based on the nominal UVB strength has negligible impact our final limit.

4.3.6 Error assessment

There are several potential sources of systematic error to the presented spectra. We have already discussed the uncertainties in the model-based conversion of Hα surface brightness to UVB strength in §4.2.3. The uncertainty in the absolute spectral flux calibration due to the applied atmospheric extinction curve is discussed in §4.3. The uncertainty in the absolute spectral flux calibration due to the standard star observations is discussed in §4.3.1. We now analyze a final systematic regarding the relative error determinations in the Hα spectra. We observe that the propagation of the errors from the data's original read noise and shot noise does not fully account for the variation in sky subtracted spectra. This is especially true under bright skylines. We discuss three possible causes with a focus on the variation of spectral resolution across different fibers. In any of the cases, the form of the systematic error will be to add a small percentage of the continuum subtracted sky background spectrum applied linearly with the random error.

First, the instrumental spectral resolution varies by at most 5% in different fibers due to small but detectable optical distortions in the camera. We further measure from arc lamp exposures that the variation is 2.5% between the sky and science fibers in the UGC 7321 data and 1.5% in the UGC 1281 data. These factors are presented in column 3 of Table 4.2 and scaled by the background subtracted sky spectrum and applied as systematic errors in the spectra presented in Figures 4.4 and 4.5. This form of the systematic, as the fractional error in the dispersion times the background subtracted sky spectrum, can be derived simply by taking the first order expansion of a Gaussian function near the line center. Second, the fiber-to-fiber throughput can vary slightly between flat field calibrations. The relative fiber-to-fiber throughput is calibrated with sky flats taken at dawn and dusk. This relative

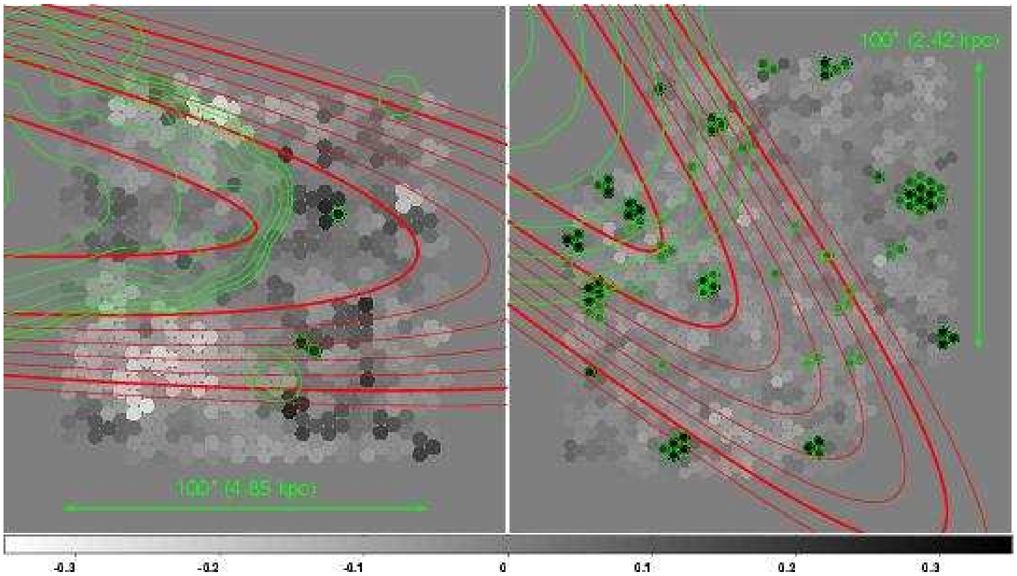

Figure 4.3 *Left* Reconstructed VIRUS-P continuum image of the UGC 7321 outskirts centered at α_{J2000}=12:17:16.4 and δ_{J2000}=+22:31:33 or $\approx$250$''$ off the minor axis. The continuum estimation is made through the entire available spectral range from 6040-6740Å with the colorbar in units of 10^{-17} erg s^{-1} cm^{-2} Å^{-1}. The dark, circled objects are masked as background galaxies, many known to be background by their emission lines at redshifts higher than the target galaxy's redshift. One can see some broad structure in the continuum map due to small residuals in the fiber-to-fiber throughput as described in §4.3.6, especially in the UGC 7321 data. The green contours trace the HI column densities in steps of (10,19,36,67,126,238,448,845) $\times 10^{18}$ cm^{-2}. The red, more extended contours trace the predicted Hα surface brightness assuming $\Gamma = 4 \times 10^{-14}$ s^{-1} and $\beta = 1.8$ in contour levels of (0.1,0.24,0.57,1.4,3.3,7.9,19) $\times 10^{-20}$ erg/s/cm^2/$\square''$. The two innermost red contours enclose the surface brightness maxima. Positions closer to the center again become dimmer in Hα since portions of the gas, in projection, stay neutral at smaller radii. The fibers used in sky subtraction are all those outside the second outermost red contour. We draw the second, seventh, and eighth contours thickly to highlight these regions. As a scale reference, the fiber diameter is $4\overset{''}{.}1$. *Right* The same display for UGC 1281 with central position α_{J2000}=1:49:15.8 and δ_{J2000}=+32:31:46 or $\approx$ 300$''$ off the minor axis. The continuum estimation is made through the entire available spectral range from 4700-6990Å. Here, many more background galaxies are found. In UGC 1281, we took data at two overlapping fields. The central positions covered by both square pointings have the best depth.

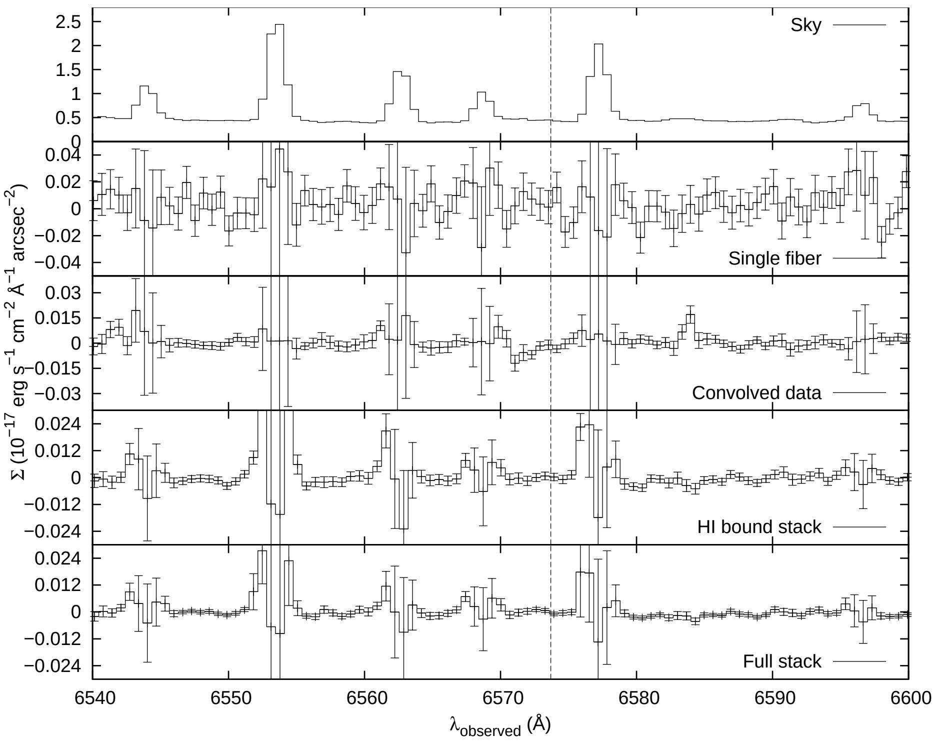

Figure 4.4 Selected spectra around Hα in UGC 7321 presented in units of surface brightness. The expected wavelength for emission is shown with a dotted line. The frames from top to bottom show the background sky, the background subtracted spectrum for a typical fiber that does not display continuum, the spectrum at the same position after being smoothed by a 10″ FWHM circular Gaussian kernel, the data bounded by HI signal, and finally the stack of the 358 fibers predicted to be the brightest by the model. The errorbars consist of the Poisson, observational error and the systematic spectral resolution error of columns two and three in Table 4.2 only. The spectral resolution systematic, discussed in §4.3.6, is most important under the bright skylines and does not dominate at the target wavelength.

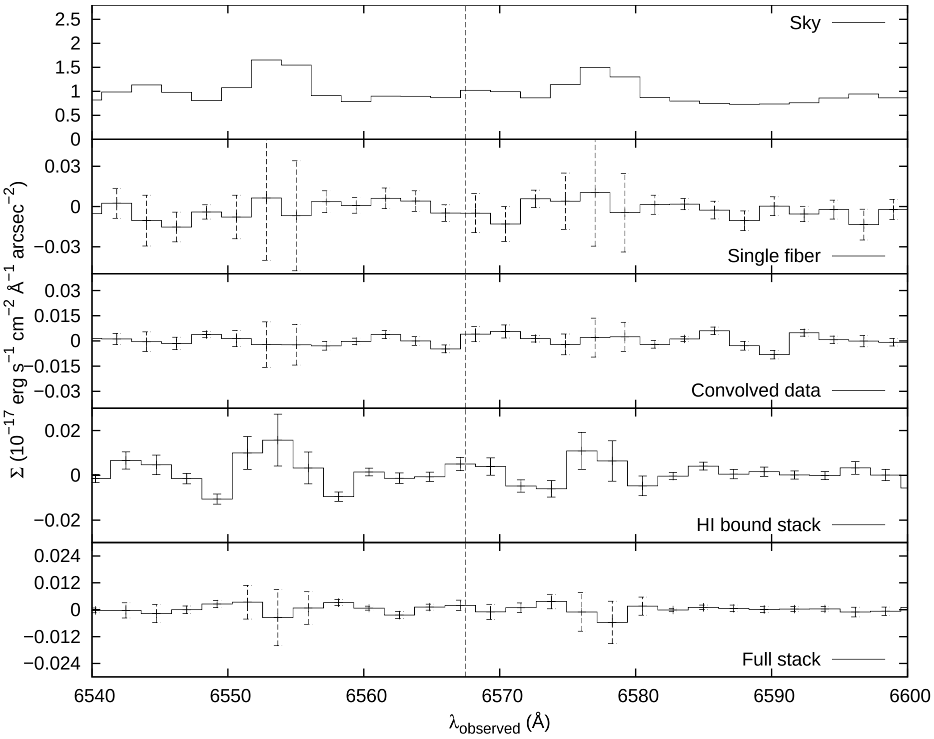

Figure 4.5 Selected surface brightness spectra around Hα in UGC 1281. The format is the same as in Figure 4.4. In this case, 313 of the brightest expected fibers form the final stack.

Table 4.2. Error budget and limits to the UVB strength

Co-addition type (1)	Poisson error (2)	Resolution systematic (3)	Flux calibration (4,%)	SB upper limit (5)	Model systematic (6,%)	$\Gamma(z=0)$ upper limit (7)	χ^2/ν (8)
UGC 7321 each single fiber	11.0	0.8	8.9	64	+5.4/-4.9	15	353/468
UGC 7321 smoothed	2.8	0.4	8.9	17	+6.6/-4.2	4.4	257/454
UGC 7321 radio bound stack	1.8	0.4	8.9	12	+19.3/-7.9	2.3	545/462
UGC 7321 full stack	0.9	0.4	8.9	7.1	+6.0/-1.8	1.7	497/454
UGC 1281 each single fiber	18.6	29.5	4.3	250	+57/-13	53	68/136
UGC 1281 smoothed	6.6	8.9	4.3	81	+29/-12	19	218/136
UGC 1281 radio bound stack	6.0	8.9	4.3	78	+46/-15	27	261/134
UGC 1281 full stack	2.0	8.9	4.3	57	+9.5/-6.1	14	50/134

(1) Detection and model method. Smoothed refers to a $10''$ FWHM Gaussian, circular kernel.

(2) 1σ (10^{-20} erg/s/cm^2/$\square''$) in the spectral data from Poisson noise.

(3) 1σ (10^{-20} erg/s/cm^2/$\square''$) in the spectral data from spectral resolution or sky line variation. See §4.3.6.

(4) 1σ (%) flux calibration systematic including 2.1% for airmass/extinction error.

(5) 5σ (10^{-20} erg/s/cm^2/$\square''$) limit in surface brightness. No detections of significance were found, so this limit derives directly from the error estimates of columns 2, 3, and 4.

(6) 1σ (%) model surface brightness systematic.

(7) 5σ (10^{-14} s^{-1}) total limit assuming $\beta = 1.8$. The achieved Hα surface brightness limit is compared to the low bound of the modeled Hα surface brightness to create this final, linearized estimate from the modeled value of $\Gamma = 4 \times 10^{-14}$ s^{-1}. This limit derives directly from column 5 of this table and the lower bound to one of columns 7, 8, 9, or 10 in Table 4.1 depending on the limit type.

(8) χ^2 of all pixels between 6300-6600Å in the spectrum and the degrees of freedom.

throughput has been measured to be stable to <5% over most nights. However, we find a maximum 15% fiber-to-fiber throughput variation in the UGC 7321 data due to poor fiber cable coiling practices. This error is very evident in the broadband estimate per fiber as shown in Figure 4.3. The error is less important for a continuum subtracted spectral element where most of the fiber-to-fiber throughput error subtracts out. The form of the throughput variation is that a few fibers experience a change with time, but the majority stay stable. We measure the rms throughput variation between all fibers to be far below 1%. Third, sky lines may vary across the $\sim 1'$ separating the sky and science fibers. The UGC 7321 fiducial "signal" is well resolved from all known sky lines and only near OH lines, but the UGC 1281 "signal" is unresolved from an OH line and near the geocoronal Hα. Variations on such small spatial scales have not been observed, and the data are averaged over very long integration times and large ranges in zenith distance, so we do not expect sky variation over our field-of-view to be a dominant error term. It is possible that the geocoronal Hα emission may vary within $\sim 1'$, but small-scale variation is less likely for OH. We choose to parameterize the total effect of these systematics in a conversative manner by deriving from the data themselves the systematic error based on the measured levels of spectral resolution variation seen between fibers.

This systematic error strongly affects the UGC 1281 data since the lower resolution allows blending of night sky lines at the expected wavelength of Hα, but it is a less important component to the UGC 7321 error budget. As data from more fibers are coadded, this systematic error takes on greater importance in relation to the random error. We assess the χ^2 distributions across 6300-6600Å in each coaddition case in Table 4.2. The χ^2 are simply calculated against a flat, zero flux line and can be visually judged in Figures 4.4 and 4.5. The distributions look very symmetric around zero, and the reduced χ^2 values are consistent with noise. The proper χ^2 values validate our systematic noise estimates empirically. In fact, the additional noise estimates may be slightly conservative. One can visually note from Figures 4.4 and 4.5 that the χ^2 values are even lower than the degrees of freedom (ν) in the most important regions near the target wavelengths.

4.3.7 Internal galactic extinctions

Internal extinctions in disk galaxies at these scale lengths are very uncertain despite being a subject of detailed research (e.g. Byun et al. 1994). Matthews et al. (1999) see in UGC 7321 an abrupt truncation of resolved dust clumps beyond r≈80″ and fit a model of radially declining dust where, for our position around 250″, there is no internal extinction. We have taken short VIRUS-P exposures covering Hα and Hβ on the galaxy centers to derive conversative internal extinction upper limit estimates after correction for Galactic extinction. We did not take deep enough exposures to measure accurate stellar populations and photospheric Balmer absorptions ourselves, so we have relied on literature values appropriate to late type galaxies. From the Balmer decrements we measure $A_{H\alpha}$=-0.03±0.09 magnitudes for UGC 7321 and $A_{H\alpha}$=-0.02±0.11 magnitudes for UGC 1281 under the assumption that the absorption equivalent widths satisfy $EW(H\alpha)_{abs}$=$EW(H\beta)_{abs}$=2Å (McCall et al. 1985; Calzetti et al. 1994). As the extinction estimates are consistent with zero, we apply no dust correction to our results.

4.4 Discussion

The flux decrement method is currently the most widely used method to estimate the UVB strength at high redshift. Under the fluctuating Gunn-Peterson approximation (Croft et al. 1998), the Lyman-α forest optical depth distribution should have a normalization that depends only on well constrainted cosmological parameters and the UVB strength. The IGM temperature and density distributions may have some systematic uncertainties that propagate into knowledge of the UVB, but they are not likely the leading uncertainties. The more likely dominant uncertainties in flux decrement modeling are the source emissivities. At $z <\approx 1$, the Lyman limit mean free path becomes larger than the horizon, so the UVB strength at z=0 is influenced by source evolution across this redshift range. AGN and stellar population luminosity functions, both observed and modeled, generally agree to better than an order of magnitude over these redshifts. The least constrained input to flux decrement modeling is the escape fraction for ionizing photons in galaxies, particularly at low redshift and low luminosity. We believe our measurement is best interpreted as an indicator of a low escape fraction.

Our most constraining (5σ) spectral limits are $\Gamma < 1.7 \times 10^{-14}$ s^{-1} in UGC 7321 and $\Gamma < 13.5 \times 10^{-14}$ s^{-1} in UGC 1281 again assuming $\beta = 1.8$. Several benchmarks, both empirical and theoretical, exist with which to compare these limits. Figure 4.6 shows the UVB strength against redshift determined by many groups. The lowest redshift proximity effect limit comes from Kulkarni & Fall (1993) with analysis of 13 quasars from Bahcall et al. (1993) between $0.16 \leq z \leq 1.00$ at $\Gamma(\bar{z} = 0.5) = 2.0^{+10}_{-1.3} \times 10^{-14}$ s^{-1}. However, the proximity effect method has been shown to have a high bias that depends on halo mass (Faucher-Giguère et al. 2008c) and should be interpreted with care. The theoretical model of Faucher-Giguère et al. (2009) gives a drop in the UVB strength by a factor of 3.4 between z=0.5 and z=0.0 leaving this measurement consistent with our current limit. This agreement is interesting and somewhat unexpected given the bias of proximity effect measurements. The only existing low-z flux decrement limit is $\Gamma(\bar{z} = 0.17) = 5.0^{+20.}_{-4.0} \times 10^{-14}$ s^{-1} (Davé & Tripp 2001). The theoretical model itself, normalized by the flux decrement method, predicts $\Gamma(z = 0) = 3.8 \times 10^{-14}$ s^{-1} which is much higher than our new limit. There exists a second set of unpublished theoretical predictions from F. Haardt and P. Madau discussed in Faucher-Giguère et al. (2009) giving $\Gamma(z = 0) = 1 \times 10^{-13}$ s^{-1}. The latter model used a constant 10% escape fraction of ionizing photons and an unspecified star formation history while the former used a completely theoretical and simulation-based star formation history (Hernquist & Springel 2003) and a scaling of the stellar UV emissivity based on high redshift flux decrement measurements that contains the escape fraction. A comparison to Lyman-break galaxy (LBG) luminosity functions led that group to require only $f_{esc,abs} \approx 0.5\%$ (Faucher-Giguère et al. 2008b). The direct measurement of galactic escape fractions is difficult due to the low values involved. While UV bright samples can range up to $\approx 3\%$ in absolute Lyman limit escape fraction (Shapley et al. 2006), a presumably lower-mass sample yielded $(2\pm2)\%$ (Chen et al. 2007). Theoretical work shows a strong decrease in f_{esc} with star formation rate and halo mass (Gnedin et al. 2008) below $M_{tot} \approx 10^{11} M_{\odot}$, and lower redshift observations of populations similar to LBGs show a potential redshift evolution (Siana et al. 2010) with $f_{esc,abs} < 0.8\%$. There is no reason yet to suppose a lower bound to the escape fraction. If we interpret our limit as a scaling of the escape fraction from the models in Faucher-Giguère et al. (2008b) at low redshift, we find $f_{esc,abs} < 0.2\%$.

It is unlikely that systematics from the model assumptions in our analysis can cause the disagreement. Contaminating ionization from the galaxies' forming stars would bias our measurement high, only making the disagreement more severe. We further note that the degree of contamination can be measured by anomalous [NII]λ6548 to Hα ratios (BFQ) and should not, in principle, limit this type of measurement. There has been a large body of work on low strength star formation beyond the optical radii in local galaxy disks, usually labelled extended UV disks (XUV), fostered by far UV (FUV,1350-1750Å) and near UV (1750-2750Å) Galaxy Evolution Explorer (GALEX) data (e.g. Thilker et al. 2007). Narrowband Hα imaging and spectroscopy have revealed that $\sim 10\%$ of gas rich disks (Werk et al. 2010a,b; Herbert-Fort et al. 2010) host outlying Hα emitting complexes as either compact HII regions or dwarf satellite companions. The common Hα fluxes observed so far are of the order of a few times 10^{-16} erg/s/cm^2. Any such systems would have been found in our data as strong detections limited in size to a few fibers. The expectation of large-scale, diffuse UVB Hα emission should discriminate reliably against compact XUV Hα emission. We have also visually inspected the target galaxies' GALEX data which have not yet been analyzed in any XUV focused work. UGC 1281 has only been covered in the rather shallow all-sky survey mode. UGC 7321 has been covered for 2.8ks in the NUV and 1.7 ks in the FUV under guest investigator cycle 4 proposal ID 095 (PI: J. Lee) as part of the 11HUGS project (Lee et al. 2009). In neither system is there evidence for an extended UV disk beyond the DSS2-red[2] limiting contours. Finally, these contamination issues are speculative until a putative UVB Hα detection is made. The only possible systematics that could have made a low bias to our limit are unaccounted for dust or gas distribution parameters, such as inclination, far beyond the range we have constrained. We have made our first analysis under the assumption that the gas distribution extends beyond the HI data limits with the same exponential form as at smaller radii. This assumption, motivated by the thin and regular HI distributions and lack of nearby companions, has the strongest impact on our interpretation. An alternative estimate without this assumption, taking only fibers that overlap with the observed HI signal, yields a very comparable limit of $\Gamma < 2.3 \times 10^{-14}$ s^{-1} at 5σ significance in UGC 7321. This agreement essentially comes about because our original model predicts only a minor Hα contribution at the discarded positions under the modeled UVB strength. Nevertheless, there is no reason to assume the presence of an HI edge since the radio observations detect the gas up to the column densities where the sensitivity runs out. This result raises the question whether a redshift-dependent escape frac-

---

[2] The Digitized Sky Survey was produced at the Space Telescope Science Institute under U.S. Government grant NAG W-2166. The images of these surveys are based on photographic data obtained using the Oschin Schmidt Telescope on Palomar Mountain and the UK Schmidt Telescope. The plates were processed into the present compressed digital form with the permission of these institutions.

tion is manifesting in galaxies. Alternatively, our new limits may be saying that the UVB strength, as estimated through flux decrement measurements, has been overestimated at all redshifts. The latter choice would upset the apparent agreement between current models and reionization constraints. Either case will require some modification to the UVB strength model and its implementation in structure formation simulations. We intend to pursue our measurements of these and other superthin galaxies to greater depth in order to arrive at a detection of $\Gamma(z = 0)$.

Acknowledgements: This work was done in collaboration with Juan M. Uson, Gary J. Hill, and Phillip J. MacQueen.

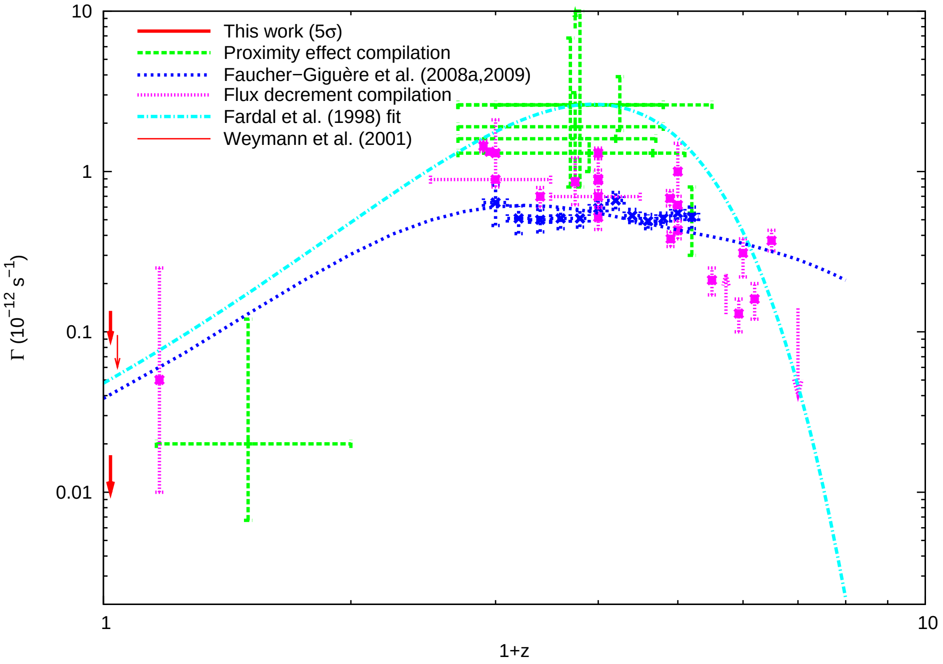

Figure 4.6 A compilation of photoionization rates across redshift. Most of the literature compilations come from Table 2 in Faucher-Giguère et al. (2008c) and Table 1 in Faucher-Giguère et al. (2008b). The flux decrement measurement at $z \sim 0.17$ is from Davé & Tripp (2001). The low redshift, Hα limit from Weymann et al. (2001) (2σ) has been the deepest z=0 limit before this work. The UVB fitting function comes from Fardal et al. (1998) and the newer simulation from Faucher-Giguère et al. (2009). Our work's new limit is well below the flux decrement normalized simulation and challenges one or more of the model assumptions. Some points have been slightly shifted in redshift for visual clarity.

Chapter 5

Conclusions and future work

While the HETDEX LAE pilot survey is complete, there is further analysis being pursued. I am working on constraining the stellar populations of the sample with the pan-chromatic broadband data available. Previous to now, stellar population fits to LAEs have relied on stacking. However, our large survey volume has discovered some of the brightest galaxies selected by their Lyman-α emission of any survey and facilitates individual study.

In the near future, HETDEX will deliver an unparalleled sample of Lyman-α emitting galaxies. I will work to re-observe interesting subsets with additional wavelength coverage. For instance, the interstellar absorption features in Lyman-Break galaxies have been a powerful probe of the kinematic and chemical activity, particularly at very large radii when backlit by quasars or other galaxies (Steidel et al. 2010). HETDEX will discover many such galaxy pairs, and deep re-observations with a high UV throughput multi-object spectrograph will allow the same science in a lower mass range and different evolutionary stage.

The next step regarding the dark matter profiles in late-type dwarfs is simply to observe a statistically relevant sample. We have been awarded eight nights in June, 2011 with VIRUS-W (Fabricius et al. 2008) on the 2.7m at the McDonald

Observatory to expand our sample to five additional galaxies. VIRUS-W delivers σ_{instr}= 20 km s^{-1} around the Mg b region, which will allow tighter dispersion estimates in these low mass systems. We will target UGC 4325, NGC 4395, UGC 5414, DDO 154, and UGC 4499. Analysis will proceed identically to that of NGC 2976 with VIRUS-P. We may attempt Schwarzschild modeling, particularly with triaxial halos, if the S/N warrants, with a goal of measuring dark matter halo ellipiticity.

Finally, we have now acquired deeper data on UGC 7321 using the VIRUS-P instrument on the McDonald Observatory's 2.7m telescope over February 25 through March 4, 2011. Five of the eight nights had excellent transparency (A$_R$ $\sim$<0.2), one night was lost to clouds, and two nights were lost to weather closures forced by dust and high winds. In total, we gathered 30 very high quality hours of pointing on UGC 7321 and an additional 6 hours under medium quality transparency. The final analysis and publication is in work, but the early results look promising toward acquiring a UVB detection. We may have detected very faint, diffuse Hα emission that is best explained as fluorescence from the metagalactic UV background. This has never before been seen, and its measurement permits an estimation of the $z = 0$ metagalactic UV background intensity with implications for the UV escape fraction in galaxies, the global star formation rate density, the quasar luminosity density.

Appendix A

Tests of the resonant scattering code

To provide compatibility between our work and previous authors', we run the same set of four tests on our 3D Monte Carlo resonant scattering code as Dijkstra et al. (2006a). The first test simulates the emergent spectra for centrally created Lyman-α photons in a uniform density spherically symmetric static halo of HI with various line center edge-to-center optical depths at T=10K. We disabled the acceleration scheme for tests 1-3. The second test calculates the redistribution function for single scattering events, which is the probability distribution function for an output frequency given an input frequency and gas temperature. The third test finds the mean number of scatterings prior to escape for a slab of gas of various line center optical depths. The weighting scheme of Avery & House (1968) was used for test 3 where the number of accumulated scatterings and the probability of escape from each scattering site is retained as opposed to solely keeping the properties of each Monte Carlo run's escaping photon. The fourth test gives the emergent spectrum from an infinitely large object under Hubble expansion as originally simulated in Loeb & Rybicki (1999). More details and references are given in Dijkstra et al.

(2006a) Appendix B. We give the four tests in Figure A.1.

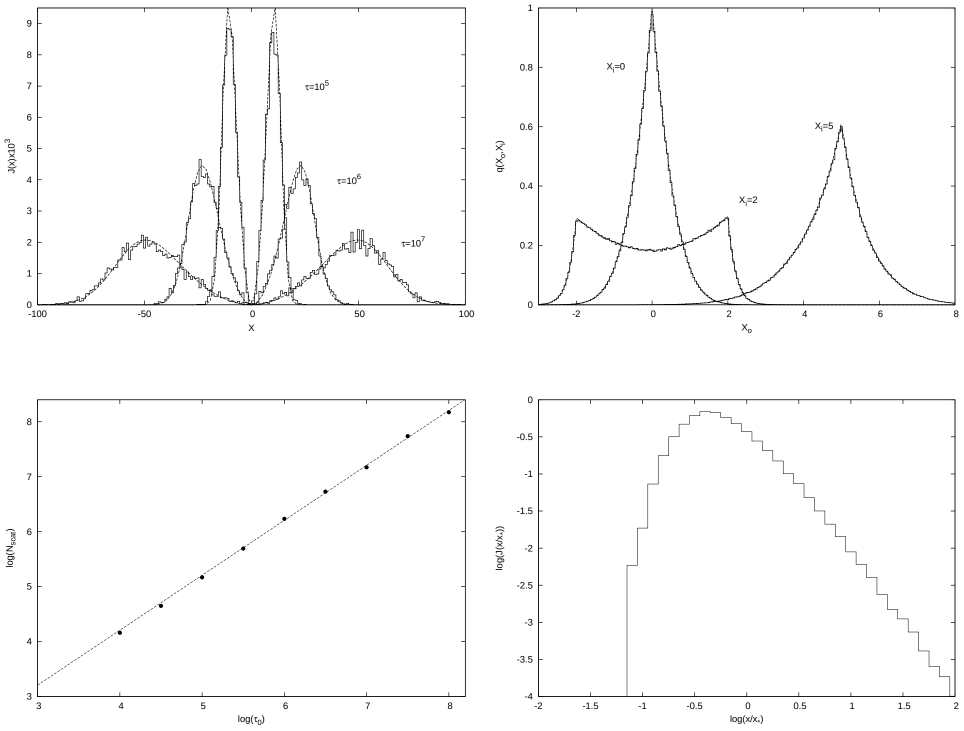

Figure A.1 The four tests of our 3D Monte Carlo resonant scatter code. *Top left* The emergent Lyman-α spectra from uniform density, static halos at T=10K with various line center edge-to-center optical depths. The histograms are from our simulations. The lines are from function 9 in Dijkstra et al. (2006a). *Top right* The redistribution function for Lyman-α scattering with a gas temperature of T=10^4K. The histogram is our code output while the curves are from theory in Hummer (1962); Lee (1974). *Bottom left* The number of scatterings necessary for a Lyman-α photon to escape a neutral, static slab of HI. The points are from our simulations. The line is from theory (Harrington 1973). *Bottom right* The emergent Lyman-α spectrum from an infinite, uniform density HI halo under Hubble expansion at z=10 with T=10K.

Appendix B

Atmospheric differential refraction correction

Atmospheric differential refraction (ADR) effects over this dataset's wavelength and airmass ranges are of the order of the astrometric solution errors, so we have made an astrometry correction to the guider-based positions considering the emission-line source wavelength. There are two ADR effects on the observed fiber positions at any given wavelength: the atmosphere's wavelength-dependent index of refraction at a fixed airmass and the different airmasses between the science and guider FOVs. As we have stated in §1.3.1, the guider's effective wavelength is 5000Å, and we ignore color corrections for different guide stars. In order to retain the ability to stack exposures taken at the same dither position, we average the positional differences over the N exposures and apply Equation B.1 from Smart & Green (1977) as the average positional corrections for an emission-line source at wavelength λ due to ADR where ϕ is the site latitude, δ is the declination, θ_g is the distance angle between the guider and IFU centers, H is the hour angle at the middle of the frame's exposure, and k is the constant of mean refraction calculated (Filippenko 1982) for average 2 km altitude conditions (Allen 1973) and related to the atmosphere's index of refraction. Common corrections derived this way are 0-2$''$ with a median of $0\farcs3$ for our sample.

$$\Delta\alpha = \sum_{i=1}^{N} \frac{k(\lambda)\sec^2\delta\sin H}{N\times(\tan\delta\tan\phi+\cos H)} - \frac{k(5000\mathring{A})\sec^2(\delta+\theta_g)\sin H}{N\times(\tan(\delta+\theta_g)\tan\phi+\cos H)}$$

$$\Delta\delta = \sum_{i=1}^{N} \frac{k(\lambda)\times(\tan\phi-\tan\delta\cos H)}{N\times(\tan\delta\tan\phi+\cos H)} - \frac{k(5000\mathring{A})\times(\tan\phi-\tan(\delta+\theta_g)\cos H)}{N\times(\tan(\delta+\theta_g)\tan\phi+\cos H)} \tag{B.1}$$

Appendix C

Full solution to the general Hα surface brightness

We give here the derivation of the general Hα surface brightness at field positions b_1 and b_2. The special case for b_1=r_c and b_2=0 was derived as Equation 4.9. That case is simplified since the line of sight integration can proceed from zero to infinity without intersecting the photoionization boundary and has symmetry between positive and negative values of ρ. For the general case, the simple task presented in this Appendix is to find the possible geometrical intersections of z from Equation 4.7 and $z_c(R)$ from Equation 4.6 as a function of ρ under inputs i, b_1, and b_2. This may have zero or two intersections labelled as ρ_{r1} and ρ_{r2}. Once found, the general expression for μ then follows Equation C.1.

$$\mu(b_1, b_2) = \frac{\xi^2 \varepsilon \alpha_{H\alpha}^{eff} n_0^2 h \nu_{H\alpha} \gamma}{\Omega}$$

$$\text{with } \gamma = \begin{cases} \int_{-\infty}^{\infty} \exp(-\frac{2\rho \cos i}{h_z} - \frac{2\sqrt{r_c^2+\rho^2 \sin^2 i}}{h_r}) d\rho & : \text{no roots in } \rho \\ \int_{-\infty}^{\rho_{r1}} \exp(-\frac{2\rho \cos i}{h_z} - \frac{2\sqrt{r_c^2+\rho^2 \sin^2 i}}{h_r}) d\rho + & \\ \int_{\rho_{r2}}^{\infty} \exp(-\frac{2\rho \cos i}{h_z} - \frac{2\sqrt{r_c^2+\rho^2 \sin^2 i}}{h_r}) d\rho & : \text{roots in } \rho \end{cases} \qquad \text{(C.1)}$$

The first necessary condition for any intersection to occur is evidently expressed in Equation C.2, as the largest possible distance for an intersection to lie from the galaxy center is r_c while the closest possible approach for a sight line is b_1.

$$b_1 < r_c \tag{C.2}$$

The intersections in ρ can be expanded into simple quadratic equations. Each of the two potential roots from the quadratic solution is double valued when considering intersections with both signs of the $z_c(R)$ surface leading to four possible roots. However, only at most two of the roots will be physical with the rejected two lying on extrapolations of $z_c(R)$ at $R(\rho) > r_c$ or $|z(\rho)| > r_c \times h_z/h_r$. The intersections with these surfaces lead to possible limits ρ_{s1}, ρ_{s2}, ρ_{s3}, and ρ_{s4} expressed in Equations C.3-C.6. The most constraining limits are then the values between these four with the smallest absolute values leading to Equations C.7-C.8 for the active limits ρ_{l1} and ρ_{l2}.

$$\rho_{s1} = \frac{-b_2 \sin i - \frac{h_z}{h_r} r_c}{\cos i} \tag{C.3}$$

$$\rho_{s2} = \frac{b_2 \cos i - \sqrt{r_c^2 - b_1^2}}{\sin i} \tag{C.4}$$

$$\rho_{s3} = \frac{-b_2 \sin i + \frac{h_z}{h_r} r_c}{\cos i} \tag{C.5}$$

$$\rho_{s4} = \frac{b_2 \cos i + \sqrt{r_c^2 - b_1^2}}{\sin i} \tag{C.6}$$

$$\rho_{l1} = \max(\rho_{s1}, \rho_{s2}) \tag{C.7}$$

$$\rho_{l2} = \min(\rho_{s3}, \rho_{s4}) \tag{C.8}$$

The potential intersections with $z_c(R)$ can be directly evaluated as ρ_{p1}, ρ_{p2}, ρ_{p3}, and ρ_{p4} as given in Equations C.9-C.12.

$$\begin{aligned}
\rho_{p1} &= \frac{\left(\frac{h_r}{h_z}\right) r_c \cos i - \left(\frac{h_r}{h_z}\right)^2 b_2 \sin i \cos i - b_2 \sin i \cos i + \sqrt{\beta_{p1}}}{\left(\frac{h_r}{h_z}\right)^2 \cos^2 i - \sin^2 i} \\
\beta_{p1} &= 2\left(\frac{h_r}{h_z}\right)^2 b_2^2 \cos^2 i \sin^2 i - 2\left(\frac{h_r}{h_z}\right) b_2 r_c \cos^2 i \sin i + b_1^2 \left(\frac{h_r}{h_z}\right)^2 \cos^2 i \\
&+ b_2^2 \left(\frac{h_r}{h_z}\right)^2 \sin^2 i + r_c^2 \sin^2 i + \left(\frac{h_r}{h_z}\right)^2 b_2^2 \sin^4 i - 2\left(\frac{h_r}{h_z}\right) r_c b_2 \sin^3 i - b_1^2 \sin^2 i
\end{aligned} \tag{C.9}$$

$$\begin{aligned}
\rho_{p2} &= \frac{\left(\frac{h_r}{h_z}\right) r_c \cos i - \left(\frac{h_r}{h_z}\right)^2 b_2 \sin i \cos i - b_2 \sin i \cos i - \sqrt{\beta_{p1}}}{\left(\frac{h_r}{h_z}\right)^2 \cos^2 i - \sin^2 i} \\
\beta_{p1} &= 2\left(\frac{h_r}{h_z}\right)^2 b_2^2 \cos^2 i \sin^2 i - 2\left(\frac{h_r}{h_z}\right) b_2 r_c \cos^2 i \sin i + b_1^2 \left(\frac{h_r}{h_z}\right)^2 \cos^2 i \\
&+ b_2^2 \left(\frac{h_r}{h_z}\right)^2 \sin^2 i + r_c^2 \sin^2 i + \left(\frac{h_r}{h_z}\right)^2 b_2^2 \sin^4 i - 2\left(\frac{h_r}{h_z}\right) r_c b_2 \sin^3 i - b_1^2 \sin^2 i
\end{aligned} \tag{C.10}$$

$$\begin{aligned}
\rho_{p3} &= -\frac{\left(\frac{h_r}{h_z}\right) r_c \cos i - \left(\frac{h_r}{h_z}\right)^2 b_2 \sin i \cos i - b_2 \sin i \cos i + \sqrt{\beta_{p2}}}{\left(\frac{h_r}{h_z}\right)^2 \cos^2 i - \sin^2 i} \\
\beta_{p2} &= 2\left(\frac{h_r}{h_z}\right)^2 b_2^2 \cos^2 i \sin^2 i + 2\left(\frac{h_r}{h_z}\right) b_2 r_c \cos^2 i \sin i + b_1^2 \left(\frac{h_r}{h_z}\right)^2 \cos^2 i \\
&+ b_2^2 \left(\frac{h_r}{h_z}\right)^2 \sin^2 i + r_c^2 \sin^2 i + \left(\frac{h_r}{h_z}\right)^2 b_2^2 \sin^4 i + 2\left(\frac{h_r}{h_z}\right) r_c b_2 \sin^3 i - b_1^2 \sin^2 i
\end{aligned} \tag{C.11}$$

$$\begin{aligned}
\rho_{p4} &= -\frac{\left(\frac{h_r}{h_z}\right) r_c \cos i - \left(\frac{h_r}{h_z}\right)^2 b_2 \sin i \cos i - b_2 \sin i \cos i - \sqrt{\beta_{p2}}}{\left(\frac{h_r}{h_z}\right)^2 \cos^2 i - \sin^2 i} \\
\beta_{p2} &= 2\left(\frac{h_r}{h_z}\right)^2 b_2^2 \cos^2 i \sin^2 i + 2\left(\frac{h_r}{h_z}\right) b_2 r_c \cos^2 i \sin i + b_1^2 \left(\frac{h_r}{h_z}\right)^2 \cos^2 i
\end{aligned}$$

$$+b_2^2\left(\frac{h_r}{h_z}\right)^2\sin^2 i+r_c^2\sin^2 i+\left(\frac{h_r}{h_z}\right)^2 b_2^2\sin^4 i+2\left(\frac{h_r}{h_z}\right)r_c b_2\sin^3 i-b_1^2\sin^2 i \tag{C.12}$$

The comparisons to the limits ρ_{l1} and ρ_{l2} discard unphysical values in Equations C.13-C.14 where the final limits of integration are found.

$$\rho_{r1}=\min(x\in\{\rho_{p1},\rho_{p2},\rho_{p3},\rho_{p4}\}:\rho_{l1}<x<\rho_{l2}\}) \tag{C.13}$$

$$\rho_{r2}=\max(x\in\{\rho_{p1},\rho_{p2},\rho_{p3},\rho_{p4}\}:\rho_{l1}<x<\rho_{l2}\}) \tag{C.14}$$

With the integration boundaries now well defined, $\mu(b_1,b_2)$ can easily be obtained through numerical integration.

Bibliography

Adams, J. J., Blanc, G. A., Hill, G. J., Gebhardt, K., Drory, N., Hao, L., Bender, R., Byun, J., Ciardullo, R., Cornell, M. E., Finkelstein, S. L., Fry, A., Gawiser, E., Gronwall, C., Hopp, U., Jeong, D., Kelz, A., Kelzenberg, R., Komatsu, E., MacQueen, P. J., Murphy, J., Odoms, P. S., Roth, M., Schneider, D. P., Tufts, J. R., & Wilkinson, C. P. 2011, ApJS, 192, 5

Adams, J. J., Gebhardt, K., Hill, G. J., Blanc, G. A., & van den Bosch, R. 2010, in Astronomical Society of the Pacific Conference Series, Vol. 432, New Horizons in Astronomy: Frank N. Bash Symposium 2009, ed. L. M. Stanford, J. D. Green, L. Hao, & Y. Mao, 175–+

Adams, J. J., Hill, G. J., & MacQueen, P. J. 2008, in Society of Photo-Optical Instrumentation Engineers (SPIE) Conference Series, Vol. 7014, 232

Adelman-McCarthy, J. K., Agüeros, M. A., Allam, S. S., Allende Prieto, C., Anderson, K. S. J., Anderson, S. F., Annis, J., Bahcall, N. A., Bailer-Jones, C. A. L., Baldry, I. K., Barentine, J. C., Bassett, B. A., Becker, A. C., Beers, T. C., Bell, E. F., Berlind, A. A., Bernardi, M., Blanton, M. R., Bochanski, J. J., Boroski, W. N., Brinchmann, J., Brinkmann, J., Brunner, R. J., Budavári, T., Carliles, S., Carr, M. A., Castander, F. J., Cinabro, D., Cool, R. J., Covey, K. R., Csabai, I., Cunha, C. E., Davenport, J. R. A., Dilday, B., Doi, M., Eisenstein, D. J., Evans, M. L., Fan, X., Finkbeiner, D. P., Friedman, S. D., Frieman, J. A., Fukugita, M., Gänsicke, B. T., Gates, E., Gillespie, B., Glazebrook, K., Gray, J., Grebel, E. K., Gunn, J. E., Gurbani, V. K., Hall, P. B., Harding, P., Harvanek, M., Hawley, S. L., Hayes, J., Heckman, T. M., Hendry, J. S., Hindsley, R. B., Hirata, C. M., Hogan, C. J., Hogg, D. W., Hyde, J. B., Ichikawa, S., Ivezić, Ž., Jester, S., Johnson, J. A., Jorgensen, A. M., Jurić, M., Kent, S. M., Kessler, R., Kleinman, S. J., Knapp, G. R., Kron, R. G., Krzesinski, J., Kuropatkin, N., Lamb, D. Q., Lampeitl, H., Lebedeva, S., Lee, Y. S., Leger, R. F., Lépine, S., Lima, M., Lin, H., Long, D. C., Loomis, C. P., Loveday, J., Lupton, R. H., Malanushenko, O., Malanushenko, V., Mandelbaum, R., Margon, B., Marriner, J. P., Martínez-Delgado, D., Matsubara, T., McGehee, P. M., McKay, T. A., Meiksin, A., Morrison, H. L., Munn, J. A., Nakajima, R., Neilsen, Jr., E. H., Newberg, H. J., Nichol, R. C., Nicinski, T., Nieto-Santisteban, M., Nitta, A., Okamura, S., Owen, R., Oyaizu, H., Padmanabhan, N., Pan, K., Park, C., Peoples, Jr., J., Pier, J. R., Pope, A. C., Purger, N., Raddick, M. J., Re Fiorentin, P., Richards, G. T., Richmond, M. W., Riess, A. G., Rix, H., Rockosi, C. M., Sako, M., Schlegel, D. J., Schneider, D. P., Schreiber, M. R., Schwope, A. D., Seljak, U., Sesar, B., Sheldon, E., Shimasaku, K., Sivarani, T., Smith, J. A., Snedden, S. A., Steinmetz, M., Strauss, M. A., SubbaRao, M., Suto, Y., Szalay, A. S., Szapudi, I., Szkody, P., Tegmark, M., Thakar, A. R., Tremonti, C. A., Tucker, D. L., Uomoto, A., Vanden Berk, D. E., Vandenberg, J., Vidrih, S., Vogeley, M. S., Voges, W., Vogt, N. P., Wadadekar, Y., Weinberg, D. H., West, A. A., White, S. D. M., Wilhite, B. C., Yanny, B., Yocum, D. R., York, D. G., Zehavi, I., & Zucker, D. B. 2008, ApJS, 175, 297

Ahn, S., & Lee, H. 2002, Journal of Korean Astronomical Society, 35, 175

Ahn, S., Lee, H., & Lee, H. M. 2000, Journal of Korean Astronomical Society, 33, 29

—. 2001, ApJ, 554, 604

—. 2002, ApJ, 567, 922

Alexander, D. M., Bauer, F. E., Brandt, W. N., Schneider, D. P., Hornschemeier, A. E., Vignali, C., Barger, A. J., Broos, P. S., Cowie, L. L., Garmire, G. P., Townsley, L. K., Bautz, M. W., Chartas, G., & Sargent, W. L. W. 2003, AJ, 126, 539

Allen, C. W. 1973, Astrophysical quantities

Allington-Smith, J., Murray, G., Content, R., Dodsworth, G., Davies, R., Miller, B. W., Jorgensen, I., Hook, I., Crampton, D., & Murowinski, R. 2002, PASP, 114, 892

Antonucci, R. 1993, ARA&A, 31, 473

Arnaud, M., & Evrard, A. E. 1999, MNRAS, 305, 631

Avery, L. W., & House, L. L. 1968, ApJ, 152, 493

Bacon, R. 1994, in Astronomy with the CFHT Adaptive Optics Bonnette, ed. R. Arsenault, 115–+

Bacon, R., Copin, Y., Monnet, G., Miller, B. W., Allington-Smith, J. R., Bureau, M., Carollo, C. M., Davies, R. L., Emsellem, E., Kuntschner, H., Peletier, R. F., Verolme, E. K., & de Zeeuw, P. T. 2001, MNRAS, 326, 23

Bahcall, J. N., Bergeron, J., Boksenberg, A., Hartig, G. F., Jannuzi, B. T., Kirhakos, S., Sargent, W. L. W., Savage, B. D., Schneider, D. P., Turnshek, D. A., Weymann, R. J., & Wolfe, A. M. 1993, ApJS, 87, 1

Bahcall, J. N., & Casertano, S. 1984, ApJ, 284, L35

Bajtlik, S., Duncan, R. C., & Ostriker, J. P. 1988, ApJ, 327, 570

Barden, S. C., Sawyer, D. G., & Honeycutt, R. K. 1998, in Presented at the Society of Photo-Optical Instrumentation Engineers (SPIE) Conference, Vol. 3355, Society of Photo-Optical Instrumentation Engineers (SPIE) Conference Series, ed. S. D'Odorico, 892–899

Barden, S. C., & Wade, R. A. 1988, in Astronomical Society of the Pacific Conference Series, Vol. 3, Fiber Optics in Astronomy, ed. S. C. Barden, 113–124

Barger, A. J., Cowie, L. L., & Wang, W. 2008, ApJ, 689, 687

Barkana, R. 2004, MNRAS, 347, 59

Barkana, R., & Loeb, A. 2003, Nature, 421, 341

Barthel, P. D. 1989, ApJ, 336, 606

Becker, T. 2002

Beers, T. C., Flynn, K., & Gebhardt, K. 1990, AJ, 100, 32

Begelman, M. C., & Cioffi, D. F. 1989, ApJ, 345, L21

Bell, E. F., & de Jong, R. S. 2001, ApJ, 550, 212

Bershady, M. A., Andersen, D. R., Harker, J., Ramsey, L. W., & Verheijen, M. A. W. 2004, PASP, 116, 565

Bershady, M. A., Verheijen, M. A. W., Swaters, R. A., Andersen, D. R., Westfall, K. B., & Martinsson, T. 2010a, ApJ, 716, 198

Bershady, M. A., Verheijen, M. A. W., Westfall, K. B., Andersen, D. R., Swaters, R. A., & Martinsson, T. 2010b, ApJ, 716, 234

Bertin, E., & Arnouts, S. 1996, A&AS, 117, 393

Best, P. N. 2000, MNRAS, 317, 720

Binney, J. 1977, ApJ, 215, 483

Birnboim, Y., & Dekel, A. 2003, MNRAS, 345, 349

Blanc, G., et al. 2010, ApJ, in prep.

Bland-Hawthorn, J., Freeman, K. C., & Quinn, P. J. 1997, ApJ, 490, 143

Bochkarev, N. G., & Sunyaev, R. A. 1977, Astronomicheskii Zhurnal, 54, 957

Bond, N. A., Feldmeier, J. J., Matković, A., Gronwall, C., Ciardullo, R., & Gawiser, E. 2010, ApJ, 716, L200

Bongiovanni, É., Oteo, I., Cepa, J., Pérez García, A. M., Sánchez-Portal, M., Ederoclite, A., Aguerri, J. A. L., Alfaro, E. J., Altieri, B., Andreani, P., Aparicio-Villegas, M. T., Aussel, H., Benítez, N., Berta, S., Broadhurst, T., Cabrera-Caño, J., Castander, F. J., Cava, A., Cerviño, M., Chulani, H., Cimatti, A., Cristóbal-Hornillos, D., Daddi, E., Dominguez, H., Elbaz, D., Fernández-Soto, A., Förster Schreiber, N., Genzel, R., Gómez, M. F., González Delgado, R. M., Grazian, A., Gruppioni, C., Herreros, J. M., Iglesias Groth, S., Infante, L., Lutz, D., Magnelli, B., Magdis, G., Maiolino, R., Márquez, I., Martínez, V. J., Masegosa, J., Moles, M., Molino, A., Nordon, R., Del Olmo, A., Perea, J., Poglitsch, A., Popesso, P., Pozzi, F., Prada, F., Quintana, J. M., Riguccini, L., Rodighiero, G., Saintonge, A., Sánchez, S. F., Santini, P., Shao, L., Sturm, E., Tacconi, L., & Valtchanov, I. 2010, A&A, 519, L4+

Bonnet, H., Abuter, R., Baker, A., Bornemann, W., Brown, A., Castillo, R., Conzelmann, R., Damster, R., Davies, R., Delabre, B., Donaldson, R., Dumas, C., Eisenhauer, F., Elswijk, E., Fedrigo, E., Finger, G., Gemperlein, H., Genzel, R., Gilbert, A., Gillet, G., Goldbrunner, A., Horrobin, M., Ter Horst, R., Huber, S., Hubin, N., Iserlohe, C., Kaufer, A., Kissler-Patig, M., Kragt, J., Kroes, G., Lehnert, M., Lieb, W., Liske, J., Lizon, J.-L., Lutz, D., Modigliani, A., Monnet, G., Nesvadba, N., Patig, J., Pragt, J., Reunanen, J., Röhrle, C., Rossi, S., Schmutzer, R., Schoenmaker, T., Schreiber, J., Stroebele, S., Szeifert, T., Tacconi, L., Tecza, M., Thatte, N., Tordo, S., van der Werf, P., & Weisz, H. 2004, The Messenger, 117, 17

Bottema, R. 1989a, A&A, 225, 358

—. 1989b, A&A, 221, 236

—. 1990, A&A, 233, 372

—. 1992, A&A, 257, 69

Bottema, R., van der Kruit, P. C., & Freeman, K. C. 1987, A&A, 178, 77

Bottema, R., van der Kruit, P. C., & Valentijn, E. A. 1991, A&A, 247, 357

Bouwens, R. J., Illingworth, G. D., Franx, M., Chary, R., Meurer, G. R., Conselice, C. J., Ford, H., Giavalisco, M., & van Dokkum, P. 2009, ApJ, 705, 936

Bower, R. G., Morris, S. L., Bacon, R., Wilman, R. J., Sullivan, M., Chapman, S., Davies, R. L., de Zeeuw, P. T., & Emsellem, E. 2004, MNRAS, 351, 63

Brammer, G. B., van Dokkum, P. G., & Coppi, P. 2008, ApJ, 686, 1503

Bromm, V., & Loeb, A. 2003, ApJ, 596, 34

Bruzual, G., & Charlot, S. 2003, MNRAS, 344, 1000

Bruzual A, G. 2007, ArXiv Astrophysics e-prints

Burgh, E. B., Bershady, M. A., Westfall, K. B., & Nordsieck, K. H. 2007, PASP, 119, 1069

Byun, Y. I., Freeman, K. C., & Kylafis, N. D. 1994, ApJ, 432, 114

Calzetti, D., Armus, L., Bohlin, R. C., Kinney, A. L., Koornneef, J., & Storchi-Bergmann, T. 2000, ApJ, 533, 682

Calzetti, D., Kinney, A. L., & Storchi-Bergmann, T. 1994, ApJ, 429, 582

Capak, P., Aussel, H., Ajiki, M., McCracken, H. J., Mobasher, B., Scoville, N., Shopbell, P., Taniguchi, Y., Thompson, D., Tribiano, S., Sasaki, S., Blain, A. W., Brusa, M., Carilli, C., Comastri, A., Carollo, C. M., Cassata, P., Colbert, J., Ellis, R. S., Elvis, M., Giavalisco, M., Green, W., Guzzo, L., Hasinger, G., Ilbert, O., Impey, C., Jahnke, K., Kartaltepe, J., Kneib, J., Koda, J., Koekemoer, A., Komiyama, Y., Leauthaud, A., Le Fevre, O., Lilly, S., Liu, C., Massey, R., Miyazaki, S., Murayama, T., Nagao, T., Peacock, J. A., Pickles, A., Porciani, C., Renzini, A., Rhodes, J., Rich, M., Salvato, M., Sanders, D. B., Scarlata, C., Schiminovich, D., Schinnerer, E., Scodeggio, M., Sheth, K., Shioya, Y., Tasca, L. A. M., Taylor, J. E., Yan, L., & Zamorani, G. 2007, ApJS, 172, 99

Capak, P., Cowie, L. L., Hu, E. M., Barger, A. J., Dickinson, M., Fernandez, E., Giavalisco, M., Komiyama, Y., Kretchmer, C., McNally, C., Miyazaki, S., Okamura, S., & Stern, D. 2004, AJ, 127, 180

Cappellari, M. 2002, MNRAS, 333, 400

—. 2008, MNRAS, 390, 71

Cappellari, M., Bacon, R., Bureau, M., Damen, M. C., Davies, R. L., de Zeeuw, P. T., Emsellem, E., Falcón-Barroso, J., Krajnović, D., Kuntschner, H., McDermid, R. M., Peletier, R. F., Sarzi, M., van den Bosch, R. C. E., & van de Ven, G. 2006, MNRAS, 366, 1126

Cappellari, M., & Copin, Y. 2003, MNRAS, 342, 345

Cappelluti, N., Brusa, M., Hasinger, G., Comastri, A., Zamorani, G., Finoguenov, A., Gilli, R., Puccetti, S., Miyaji, T., Salvato, M., Vignali, C., Aldcroft, T., Böhringer, H., Brunner, H., Civano, F., Elvis, M., Fiore, F., Fruscione, A., Griffiths, R. E., Guzzo, L., Iovino, A., Koekemoer, A. M., Mainieri, V., Scoville, N. Z., Shopbell, P., Silverman, J., & Urry, C. M. 2009, A&A, 497, 635

Cappelluti, N., Hasinger, G., Brusa, M., Comastri, A., Zamorani, G., Böhringer, H., Brunner, H., Civano, F., Finoguenov, A., Fiore, F., Gilli, R., Griffiths, R. E., Mainieri, V., Matute, I., Miyaji, T., & Silverman, J. 2007, ApJS, 172, 341

Carignan, C., & Purton, C. 1998, ApJ, 506, 125

Carilli, C. L. 1995, A&A, 298, 77

Carilli, C. L., Roettgering, H. J. A., van Ojik, R., Miley, G. K., & van Breugel, W. J. M. 1997, ApJS, 109, 1

Carswell, R. F., Whelan, J. A. J., Smith, M. G., Boksenberg, A., & Tytler, D. 1982, MNRAS, 198, 91

Cassata, P., Le Fevre, O., Garilli, B., Maccagni, D., Le Brun, V., Scodeggio, M., Tresse, L., Ilbert, O., Zamorani, G., Cucciati, O., Contini, T., Bielby, R., Mellier, Y., McCracken, H. J., Pollo, A., Zanichelli, A., Bardelli, S., Cappi, A., Pozzetti, L., Vergani, D., & Zucca, E. 2010, ArXiv e-prints

Cen, R., Miralda-Escudé, J., Ostriker, J. P., & Rauch, M. 1994, ApJ, 437, L9

Chambers, K. C., & Miley, G. K. 1990, in Astronomical Society of the Pacific Conference Series, Vol. 10, Evolution of the Universe of Galaxies, ed. R. G. Kron, 373–388

Charlot, S., & Fall, S. M. 1993, ApJ, 415, 580

Chen, H., Prochaska, J. X., & Gnedin, N. Y. 2007, ApJ, 667, L125

Christlein, D., & Zaritsky, D. 2008, ApJ, 680, 1053

Christlein, D., Zaritsky, D., & Bland-Hawthorn, J. 2010, MNRAS, 641

Cody, A. M., & Braun, R. 2003, A&A, 400, 871

Cooke, J., Barton, E. J., Bullock, J. S., Stewart, K. R., & Wolfe, A. M. 2008, ApJ, 681, L57

Copin, Y., Cretton, N., & Emsellem, E. 2004, A&A, 415, 889

Corbelli, E., Schneider, S. E., & Salpeter, E. E. 1989, AJ, 97, 390

Corbelli, E., & Walterbos, R. A. M. 2007, ApJ, 669, 315

Corsini, E. M., Pizzella, A., Sarzi, M., Cinzano, P., Vega Beltrán, J. C., Funes, J. G., Bertola, F., Persic, M., & Salucci, P. 1999, A&A, 342, 671

Cowie, L. L., & Hu, E. M. 1998, AJ, 115, 1319

Croft, R. A. C., Weinberg, D. H., Katz, N., & Hernquist, L. 1998, ApJ, 495, 44

Croton, D. J., Springel, V., White, S. D. M., De Lucia, G., Frenk, C. S., Gao, L., Jenkins, A., Kauffmann, G., Navarro, J. F., & Yoshida, N. 2006, MNRAS, 365, 11

Daddi, E., Cimatti, A., Renzini, A., Fontana, A., Mignoli, M., Pozzetti, L., Tozzi, P., & Zamorani, G. 2004, ApJ, 617, 746

Dalcanton, J. J., Williams, B. F., Seth, A. C., Dolphin, A., Holtzman, J., Rosema, K., Skillman, E. D., Cole, A., Girardi, L., Gogarten, S. M., Karachentsev, I. D., Olsen, K., Weisz, D., Christensen, C., Freeman, K., Gilbert, K., Gallart, C., Harris, J., Hodge, P., de Jong, R. S., Karachentseva, V., Mateo, M., Stetson, P. B., Tavarez, M., Zaritsky, D., Governato, F., & Quinn, T. 2009, ApJS, 183, 67

Dale, D. A., Gil de Paz, A., Gordon, K. D., Hanson, H. M., Armus, L., Bendo, G. J., Bianchi, L., Block, M., Boissier, S., Boselli, A., Buckalew, B. A., Buat, V., Burgarella, D., Calzetti, D., Cannon, J. M., Engelbracht, C. W., Helou, G., Hollenbach, D. J., Jarrett, T. H., Kennicutt, R. C., Leitherer, C., Li, A., Madore, B. F., Martin, D. C., Meyer, M. J., Murphy, E. J., Regan, M. W., Roussel, H., Smith, J. D. T., Sosey, M. L., Thilker, D. A., & Walter, F. 2007, ApJ, 655, 863

Davé, R., & Tripp, T. M. 2001, ApJ, 553, 528

de Blok, W. J. G., Walter, F., Brinks, E., Trachternach, C., Oh, S., & Kennicutt, R. C. 2008, AJ, 136, 2648

De Breuck, C., Neri, R., Morganti, R., Omont, A., Rocca-Volmerange, B., Stern, D., Reuland, M., van Breugel, W., Röttgering, H., Stanford, S. A., Spinrad, H., Vigotti, M., & Wright, M. 2003, A&A, 401, 911

de Vaucouleurs, G., de Vaucouleurs, A., Corwin, Jr., H. G., Buta, R. J., Paturel, G., & Fouque, P. 1991, Third Reference Catalogue of Bright Galaxies

Dekel, A., & Birnboim, Y. 2006, MNRAS, 368, 2

Dekel, A., Birnboim, Y., Engel, G., Freundlich, J., Goerdt, T., Mumcuoglu, M., Neistein, E., Pichon, C., Teyssier, R., & Zinger, E. 2009, Nature, 457, 451

Dickinson, M., Giavalisco, M., & GOODS Team. 2003, in The Mass of Galaxies at Low and High Redshift, ed. R. Bender & A. Renzini, 324–+

Diemand, J., Kuhlen, M., Madau, P., Zemp, M., Moore, B., Potter, D., & Stadel, J. 2008, Nature, 454, 735

Dierckx, P. 1993, Curve and surface fitting with splines

Dijkstra, M., Haiman, Z., & Spaans, M. 2006a, ApJ, 649, 14

—. 2006b, ApJ, 649, 37

Dijkstra, M., & Loeb, A. 2008, MNRAS, 386, 492

Djorgovski, S. G., Volonteri, M., Springel, V., Bromm, V., & Meylan, G. 2008, in The Eleventh Marcel Grossmann Meeting On Recent Developments in Theoretical and Experimental General Relativity, Gravitation and Relativistic Field Theories, ed. H. Kleinert, R. T. Jantzen, & R. Ruffini, 340–367

Donahue, M., Aldering, G., & Stocke, J. T. 1995, ApJ, 450, L45+

Dove, J. B., & Shull, J. M. 1994, ApJ, 423, 196

Drory, N., Feulner, G., Bender, R., Botzler, C. S., Hopp, U., Maraston, C., Mendes de Oliveira, C., & Snigula, J. 2001, MNRAS, 325, 550

Eddington, A. S. 1913, MNRAS, 73, 359

Eddington, Sir, A. S. 1940, MNRAS, 100, 354

Efstathiou, G. 1992, MNRAS, 256, 43P

Eisenhauer, F., Abuter, R., Bickert, K., Biancat-Marchet, F., Bonnet, H., Brynnel, J., Conzelmann, R. D., Delabre, B., Donaldson, R., Farinato, J., Fedrigo, E., Genzel, R., Hubin, N. N., Iserlohe, C., Kasper, M. E., Kissler-Patig, M., Monnet, G. J., Roehrle, C., Schreiber, J., Stroebele, S., Tecza, M., Thatte, N. A., & Weisz, H. 2003, in Presented at the Society of Photo-Optical Instrumentation Engineers (SPIE) Conference, Vol. 4841, Society of Photo-Optical Instrumentation Engineers (SPIE) Conference Series, ed. M. Iye & A. F. M. Moorwood, 1548–1561

Eisenstein, D. J., & Loeb, A. 1995, ApJ, 443, 11

Elvis, M., Civano, F., Vignali, C., Puccetti, S., Fiore, F., Cappelluti, N., Aldcroft, T. L., Fruscione, A., Zamorani, G., Comastri, A., Brusa, M., Gilli, R., Miyaji, T., Damiani, F., Koekemoer, A. M., Finoguenov, A., Brunner, H., Urry, C. M., Silverman, J., Mainieri, V., Hasinger, G., Griffiths, R., Carollo, M., Hao, H., Guzzo, L., Blain, A., Calzetti, D., Carilli, C., Capak, P., Ettori, S., Fabbiano, G., Impey, C., Lilly, S., Mobasher, B., Rich, M., Salvato, M., Sanders, D. B., Schinnerer, E., Scoville, N., Shopbell, P., Taylor, J. E., Taniguchi, Y., & Volonteri, M. 2009, ApJS, 184, 158

Fabian, A. C. 1994, ARA&A, 32, 277

Fabian, A. C., Nulsen, P. E. J., & Canizares, C. R. 1984, Nature, 310, 733

Fabricius, M. H., Barnes, S., Bender, R., Drory, N., Grupp, F., Hill, G. J., Hopp, U., & MacQueen, P. J. 2008, in Presented at the Society of Photo-Optical Instrumentation Engineers (SPIE) Conference, Vol. 7014, Society of Photo-Optical Instrumentation Engineers (SPIE) Conference Series

Fan, X., Strauss, M. A., Schneider, D. P., Becker, R. H., White, R. L., Haiman, Z., Gregg, M., Pentericci, L., Grebel, E. K., Narayanan, V. K., Loh, Y., Richards, G. T., Gunn, J. E., Lupton, R. H., Knapp, G. R., Ivezić, Ž., Brandt, W. N., Collinge, M., Hao, L., Harbeck, D., Prada, F., Schaye, J., Strateva, I., Zakamska, N., Anderson, S., Brinkmann, J., Bahcall, N. A., Lamb, D. Q., Okamura, S., Szalay, A., & York, D. G. 2003, AJ, 125, 1649

Fardal, M. A., Giroux, M. L., & Shull, J. M. 1998, AJ, 115, 2206

Fardal, M. A., Katz, N., Gardner, J. P., Hernquist, L., Weinberg, D. H., & Davé, R. 2001, ApJ, 562, 605

Fathi, K., van de Ven, G., Peletier, R. F., Emsellem, E., Falcón-Barroso, J., Cappellari, M., & de Zeeuw, T. 2005, MNRAS, 364, 773

Faucher-Giguère, C., Lidz, A., Hernquist, L., & Zaldarriaga, M. 2008a, ApJ, 682, L9

—. 2008b, ApJ, 688, 85

Faucher-Giguère, C., Lidz, A., Zaldarriaga, M., & Hernquist, L. 2008c, ApJ, 673, 39

—. 2009, ApJ, 703, 1416

Felten, J. E., & Bergeron, J. 1969, Astrophys. Lett., 4, 155

Fernández-Soto, A., Lanzetta, K. M., & Yahil, A. 1999, ApJ, 513, 34

Ferrarese, L., & Merritt, D. 2000, ApJ, 539, L9

Filippenko, A. V. 1982, PASP, 94, 715

Finkelstein, S. L., Rhoads, J. E., Malhotra, S., & Grogin, N. 2009, ApJ, 691, 465

Francis, P. J., Williger, G. M., Collins, N. R., Palunas, P., Malumuth, E. M., Woodgate, B. E., Teplitz, H. I., Smette, A., Sutherland, R. S., Danks, A. C., Hill, R. S., Lindler, D., Kimble, R. A., Heap, S. R., & Hutchings, J. B. 2001, ApJ, 554, 1001

Furusawa, H., Kosugi, G., Akiyama, M., Takata, T., Sekiguchi, K., Tanaka, I., Iwata, I., Kajisawa, M., Yasuda, N., Doi, M., Ouchi, M., Simpson, C., Shimasaku, K., Yamada, T., Furusawa, J., Morokuma, T., Ishida, C. M., Aoki, K., Fuse, T., Imanishi, M., Iye, M., Karoji, H., Kobayashi, N., Kodama, T., Komiyama, Y., Maeda, Y., Miyazaki, S., Mizumoto, Y., Nakata, F., Noumaru, J., Ogasawara, R., Okamura, S., Saito, T., Sasaki, T., Ueda, Y., & Yoshida, M. 2008, ApJS, 176, 1

Gallego, J., García-Dabó, C. E., Zamorano, J., Aragón-Salamanca, A., & Rego, M. 2002, ApJ, 570, L1

Gallego, J., Zamorano, J., Aragon-Salamanca, A., & Rego, M. 1995, ApJ, 455, L1+

García-Ruiz, I., Sancisi, R., & Kuijken, K. 2002, A&A, 394, 769

Gawiser, E., Francke, H., Lai, K., Schawinski, K., Gronwall, C., Ciardullo, R., Quadri, R., Orsi, A., Barrientos, L. F., Blanc, G. A., Fazio, G., Feldmeier, J. J., Huang, J., Infante, L., Lira, P., Padilla, N., Taylor, E. N., Treister, E., Urry, C. M., van Dokkum, P. G., & Virani, S. N. 2007, ApJ, 671, 278

Gawiser, E., van Dokkum, P. G., Gronwall, C., Ciardullo, R., Blanc, G. A., Castander, F. J., Feldmeier, J., Francke, H., Franx, M., Haberzettl, L., Herrera, D., Hickey, T., Infante, L., Lira, P., Maza, J., Quadri, R., Richardson, A., Schawinski, K., Schirmer, M., Taylor, E. N., Treister, E., Urry, C. M., & Virani, S. N. 2006, ApJ, 642, L13

Gaylord, T. K., & Moharam, M. G. 1985, in Proc. IEEE, Vol. 73, 894–937

Gebhardt, K., Bender, R., Bower, G., Dressler, A., Faber, S. M., Filippenko, A. V., Green, R., Grillmair, C., Ho, L. C., Kormendy, J., Lauer, T. R., Magorrian, J., Pinkney, J., Richstone, D., & Tremaine, S. 2000a, ApJ, 539, L13

Gebhardt, K., Richstone, D., Kormendy, J., Lauer, T. R., Ajhar, E. A., Bender, R., Dressler, A., Faber, S. M., Grillmair, C., Magorrian, J., & Tremaine, S. 2000b, AJ, 119, 1157

Giavalisco, M., Ferguson, H. C., Koekemoer, A. M., Dickinson, M., Alexander, D. M., Bauer, F. E., Bergeron, J., Biagetti, C., Brandt, W. N., Casertano, S., Cesarsky, C., Chatzichristou, E., Conselice, C., Cristiani, S., Da Costa, L., Dahlen, T., de Mello, D., Eisenhardt, P., Erben, T., Fall, S. M., Fassnacht, C., Fosbury, R., Fruchter, A., Gardner, J. P., Grogin, N., Hook, R. N., Hornschemeier, A. E., Idzi, R., Jogee, S., Kretchmer, C., Laidler, V., Lee, K. S., Livio, M., Lucas, R., Madau, P., Mobasher, B., Moustakas, L. A., Nonino, M., Padovani, P., Papovich, C., Park, Y., Ravindranath, S., Renzini, A., Richardson, M., Riess, A., Rosati, P., Schirmer, M., Schreier, E., Somerville, R. S., Spinrad, H., Stern, D., Stiavelli, M., Strolger, L., Urry, C. M., Vandame, B., Williams, R., & Wolf, C. 2004, ApJ, 600, L93

Gilbank, D. G., Balogh, M. L., Glazebrook, K., Bower, R. G., Baldry, I. K., Davies, G. T., Hau, G. K. T., Li, I. H., & McCarthy, P. 2010, MNRAS, 405, 2419

Gnedin, N. Y., Kravtsov, A. V., & Chen, H. 2008, ApJ, 672, 765

Governato, F., Brook, C., Mayer, L., Brooks, A., Rhee, G., Wadsley, J., Jonsson, P., Willman, B., Stinson, G., Quinn, T., & Madau, P. 2010, Nature, 463, 203

Greisen, E. W., & Calabretta, M. 1993, in Bulletin of the American Astronomical Society, Vol. 25, Bulletin of the American Astronomical Society, 808–+

Gronwall, C., Ciardullo, R., Hickey, T., Gawiser, E., Feldmeier, J. J., van Dokkum, P. G., Urry, C. M., Herrera, D., Lehmer, B. D., Infante, L., Orsi, A., Marchesini, D., Blanc, G. A., Francke, H., Lira, P., & Treister, E. 2007, ApJ, 667, 79

Guaita, L., Gawiser, E., Padilla, N., Francke, H., Bond, N. A., Gronwall, C., Ciardullo, R., Feldmeier, J. J., Sinawa, S., Blanc, G. A., & Virani, S. 2010, ApJ, 714, 255

Haardt, F., & Madau, P. 1996, ApJ, 461, 20

Haiman, Z., Spaans, M., & Quataert, E. 2000, ApJ, 537, L5

Hammer, F., Flores, H., Lilly, S. J., Crampton, D., Le Fevre, O., Rola, C., Mallen-Ornelas, G., Schade, D., & Tresse, L. 1997, ApJ, 481, 49

Hansen, M., & Oh, S. P. 2006, MNRAS, 367, 979

Harrington, J. P. 1973, MNRAS, 162, 43

Hayashino, T., Matsuda, Y., Tamura, H., Yamauchi, R., Yamada, T., Ajiki, M., Fujita, S. S., Murayama, T., Nagao, T., Ohta, K., Okamura, S., Ouchi, M., Shimasaku, K., Shioya, Y., & Taniguchi, Y. 2004, AJ, 128, 2073

Hayes, M., Östlin, G., Atek, H., Kunth, D., Mas-Hesse, J. M., Leitherer, C., Jiménez-Bailón, E., & Adamo, A. 2007, MNRAS, 382, 1465

Heckman, T. M., Lehnert, M. D., Miley, G. K., & van Breugel, W. 1991, ApJ, 381, 373

Henault, F., Bacon, R., Bonneville, C., Boudon, D., Davies, R. L., Ferruit, P., Gilmore, G. F., Le Fèvre, O., Lemonnier, J.-P., Lilly, S., Morris, S. L., Prieto, E., Steinmetz, M., & de Zeeuw, P. T. 2003, in Presented at the Society of Photo-Optical Instrumentation Engineers (SPIE) Conference, Vol. 4841, Society of Photo-Optical Instrumentation Engineers (SPIE) Conference Series, ed. M. Iye & A. F. M. Moorwood, 1096–1107

Herbert-Fort, S., Zaritsky, D., Christlein, D., & Kannappan, S. J. 2010, ApJ, 715, 902

Hernquist, L., & Springel, V. 2003, MNRAS, 341, 1253

Herrmann, K. A., & Ciardullo, R. 2009, ApJ, 705, 1686

Hill, G. J., Gebhardt, K., Komatsu, E., Drory, N., MacQueen, P. J., Adams, J., Blanc, G. A., Koehler, R., Rafal, M., Roth, M. M., Kelz, A., Gronwall, C., Ciardullo, R., & Schneider, D. P. 2008a, in Astronomical Society of the Pacific Conference Series, Vol. 399, Astronomical Society of the Pacific Conference Series, ed. T. Kodama, T. Yamada, & K. Aoki, 115–+

Hill, G. J., Gebhardt, K., Komatsu, E., & MacQueen, P. J. 2004, in American Institute of Physics Conference Series, Vol. 743, The New Cosmology: Conference on Strings and Cosmology, ed. R. E. Allen, D. V. Nanopoulos, & C. N. Pope, 224–233

Hill, G. J., Lee, H., Vattiat, B. L., Adams, J. J., Marshall, J. L., Drory, N., Depoy, D. L., Blanc, G., Bender, R., Booth, J. A., Chonis, T., Cornell, M. E., Gebhardt, K., Good, J., Grupp, F., Haynes, R., Kelz, A., MacQueen, P. J., Mollison, N., Murphy, J. D., Rafal, M. D., Rambold, W. N., Roth, M. M., Savage, R., & Smith, M. P. 2010, in Society of Photo-Optical Instrumentation Engineers (SPIE) Conference Series, Vol. 7735, 21

Hill, G. J., & Lilly, S. J. 1991, ApJ, 367, 1

Hill, G. J., MacQueen, P. J., Smith, M. P., Tufts, J. R., Roth, M. M., Kelz, A., Adams, J. J., Drory, N., Grupp, F., Barnes, S. I., Blanc, G. A., Murphy, J. D., Altmann, W., Wesley, G. L., Segura, P. R., Good, J. M., Booth, J. A., Bauer, S., Popow, E., Goertz, J. A., Edmonston, R. D., & Wilkinson, C. P. 2008b, in Society of Photo-Optical Instrumentation Engineers (SPIE) Conference Series, Vol. 7014, Society of Photo-Optical Instrumentation Engineers (SPIE) Conference Series

Ho, L. C., Greene, J. E., Filippenko, A. V., & Sargent, W. L. W. 2009, ApJS, 183, 1

Hogg, D. W., Cohen, J. G., Blandford, R., & Pahre, M. A. 1998, ApJ, 504, 622

Hopkins, A. M. 2004, ApJ, 615, 209

Hopkins, P. F., Richards, G. T., & Hernquist, L. 2007, ApJ, 654, 731

Hu, E. M., Cowie, L. L., Capak, P., McMahon, R. G., Hayashino, T., & Komiyama, Y. 2004, AJ, 127, 563

Hu, E. M., Cowie, L. L., Kakazu, Y., & Barger, A. J. 2009, ApJ, 698, 2014

Hu, E. M., & McMahon, R. G. 1996, Nature, 382, 231

Huchtmeier, R. 1989, A General Catalog of HI Observations of Galaxies. The Reference Catalog.

Hui, L., & Gnedin, N. Y. 1997, MNRAS, 292, 27

Hummer, D. G. 1962, MNRAS, 125, 21

Humphrey, A., Villar-Martín, M., Fosbury, R., Binette, L., Vernet, J., De Breuck, C., & di Serego Alighieri, S. 2007, MNRAS, 375, 705

Ilbert, O., Capak, P., Salvato, M., Aussel, H., McCracken, H. J., Sanders, D. B., Scoville, N., Kartaltepe, J., Arnouts, S., Floc'h, E. L., Mobasher, B., Taniguchi, Y., Lamareille, F., Leauthaud, A., Sasaki, S., Thompson, D., Zamojski, M., Zamorani, G., Bardelli, S., Bolzonella, M., Bongiorno, A., Brusa, M., Caputi, K. I., Carollo, C. M., Contini, T., Cook, R., Coppa, G., Cucciati, O., de la Torre, S., de Ravel, L., Franzetti, P., Garilli, B., Hasinger, G., Iovino, A., Kampczyk, P., Kneib, J., Knobel, C., Kovac, K., Le Borgne, J. F., Le Brun, V., Fèvre, O. L., Lilly, S., Looper, D., Maier, C., Mainieri, V., Mellier, Y., Mignoli, M., Murayama, T., Pellò, R., Peng, Y., Pérez-Montero, E., Renzini, A., Ricciardelli, E., Schiminovich, D., Scodeggio, M., Shioya, Y., Silverman, J., Surace, J., Tanaka, M., Tasca, L., Tresse, L., Vergani, D., & Zucca, E. 2009, ApJ, 690, 1236

Inoue, S., & Sasaki, S. 2001, ApJ, 562, 618

Jeong, D., & Komatsu, E. 2006, ApJ, 651, 619

—. 2009, ApJ, 691, 569

Kaastra, J. S., Ferrigno, C., Tamura, T., Paerels, F. B. S., Peterson, J. R., & Mittaz, J. P. D. 2001, A&A, 365, L99

Kaiser, N. 1986, MNRAS, 222, 323

Kakazu, Y., Cowie, L. L., & Hu, E. M. 2007, ApJ, 668, 853

Karachentsev, I. D., Dolphin, A. E., Geisler, D., Grebel, E. K., Guhathakurta, P., Hodge, P. W., Karachentseva, V. E., Sarajedini, A., Seitzer, P., & Sharina, M. E. 2002, A&A, 383, 125

Kauffmann, G., Heckman, T. M., White, S. D. M., Charlot, S., Tremonti, C., Brinchmann, J., Bruzual, G., Peng, E. W., Seibert, M., Bernardi, M., Blanton, M., Brinkmann, J., Castander, F., Csábai, I., Fukugita, M., Ivezic, Z., Munn, J. A., Nichol, R. C., Padmanabhan, N., Thakar, A. R., Weinberg, D. H., & York, D. 2003, MNRAS, 341, 33

Keel, W. C., Cohen, S. H., Windhorst, R. A., & Waddington, I. 1999, AJ, 118, 2547

Kelson, D. D. 2003, PASP, 115, 688

Kelz, A., Verheijen, M. A. W., Roth, M. M., Bauer, S. M., Becker, T., Paschke, J., Popow, E., Sánchez, S. F., & Laux, U. 2006, PASP, 118, 129

Kennicutt, R. C. 1989, ApJ, 344, 685

Kennicutt, Jr., R. C. 1992, ApJ, 388, 310

Kennicutt, Jr., R. C., Armus, L., Bendo, G., Calzetti, D., Dale, D. A., Draine, B. T., Engelbracht, C. W., Gordon, K. D., Grauer, A. D., Helou, G., Hollenbach, D. J., Jarrett, T. H., Kewley, L. J., Leitherer, C., Li, A., Malhotra, S., Regan, M. W., Rieke, G. H., Rieke, M. J., Roussel, H., Smith, J., Thornley, M. D., & Walter, F. 2003, PASP, 115, 928

Kenworthy, M. A., Parry, I. R., & Taylor, K. 1998, in Presented at the Society of Photo-Optical Instrumentation Engineers (SPIE) Conference, Vol. 3355, Society of Photo-Optical Instrumentation Engineers (SPIE) Conference Series, ed. S. D'Odorico, 926–931

Kereš, D., Katz, N., Fardal, M., Davé, R., & Weinberg, D. H. 2009, MNRAS, 395, 160

Kereš, D., Katz, N., Weinberg, D. H., & Davé, R. 2005, MNRAS, 363, 2

Koehler, R. S., Schuecker, P., & Gebhardt, K. 2007, A&A, 462, 7

Koester, B. P., McKay, T. A., Annis, J., Wechsler, R. H., Evrard, A., Bleem, L., Becker, M., Johnston, D., Sheldon, E., Nichol, R., Miller, C., Scranton, R., Bahcall, N., Barentine, J., Brewington, H., Brinkmann, J., Harvanek, M., Kleinman, S., Krzesinski, J., Long, D., Nitta, A., Schneider, D. P., Sneddin, S., Voges, W., & York, D. 2007, ApJ, 660, 239

Kogelnik, H. 1969, in Bell System Tech. J., Vol. 48, 2909–2947

Kornei, K. A., Shapley, A. E., Erb, D. K., Steidel, C. C., Reddy, N. A., Pettini, M., & Bogosavljević, M. 2010, ApJ, 711, 693

Koushiappas, S. M., Bullock, J. S., & Dekel, A. 2004, MNRAS, 354, 292

Krajnović, D., Cappellari, M., Emsellem, E., McDermid, R. M., & de Zeeuw, P. T. 2005, MNRAS, 357, 1113

Kron, R. G. 1980, ApJS, 43, 305

Kulkarni, V. P., & Fall, S. M. 1993, ApJ, 413, L63

Kunth, D., Mas-Hesse, J. M., Terlevich, E., Terlevich, R., Lequeux, J., & Fall, S. M. 1998, A&A, 334, 11

Kurtz, M. J., & Mink, D. J. 1998, PASP, 110, 934

Kurucz, R. L., Furenlid, I., Brault, J., & Testerman, L. 1984, Solar flux atlas from 296 to 1300 nm

Kuzio de Naray, R., McGaugh, S. S., & de Blok, W. J. G. 2008, ApJ, 676, 920

Larkin, J. E., Quirrenbach, A., Krabbe, A., Aliado, T., Barczys, M., Brims, G., Canfield, J., Gasaway, T. M., LaFreniere, D., Magnone, N., Skulason, G., Spencer, M., Sprayberry, D., & Weiss, J. 2003, in Presented at the Society of Photo-Optical Instrumentation Engineers (SPIE) Conference, Vol. 4841, Society of Photo-Optical Instrumentation Engineers (SPIE) Conference Series, ed. M. Iye & A. F. M. Moorwood, 1600–1610

Laursen, P., Razoumov, A. O., & Sommer-Larsen, J. 2009, ApJ, 696, 853

Le Fèvre, O., Saisse, M., Mancini, D., Brau-Nogue, S., Caputi, O., Castinel, L., D'Odorico, S., Garilli, B., Kissler-Patig, M., Lucuix, C., Mancini, G., Pauget, A., Sciarretta, G., Scodeggio, M., Tresse, L., & Vettolani, G. 2003, in Presented at the Society of Photo-Optical Instrumentation Engineers (SPIE) Conference, Vol. 4841, Society of Photo-Optical Instrumentation Engineers (SPIE) Conference Series, ed. M. Iye & A. F. M. Moorwood, 1670–1681

Lee, H., & Ahn, S. 1998, ApJ, 504, L61+

Lee, J. 1974, ApJ, 192, 465

Lee, J. C., Gil de Paz, A., Tremonti, C., Kennicutt, R. C., Salim, S., Bothwell, M., Calzetti, D., Dalcanton, J., Dale, D., Engelbracht, C., Funes, S. J. J. G., Johnson, B., Sakai, S., Skillman, E., van Zee, L., Walter, F., & Weisz, D. 2009, ApJ, 706, 599

Lemaux, B. C., Lubin, L. M., Sawicki, M., Martin, C., Lagattuta, D. J., Gal, R. R., Kocevski, D., Fassnacht, C. D., & Squires, G. K. 2009, ApJ, 700, 20

Li, Y., Hernquist, L., Robertson, B., Cox, T. J., Hopkins, P. F., Springel, V., Gao, L., Di Matteo, T., Zentner, A. R., Jenkins, A., & Yoshida, N. 2007, ApJ, 665, 187

Lilly, S. J. 1988, ApJ, 333, 161

Lilly, S. J., Le Brun, V., Maier, C., Mainieri, V., Mignoli, M., Scodeggio, M., Zamorani, G., Carollo, M., Contini, T., Kneib, J., Le Fèvre, O., Renzini, A., Bardelli, S., Bolzonella, M., Bongiorno, A., Caputi, K., Coppa, G., Cucciati, O., de la Torre, S., de Ravel, L., Franzetti, P., Garilli, B., Iovino, A., Kampczyk, P., Kovac, K., Knobel, C., Lamareille, F., Le Borgne, J., Pello, R., Peng, Y., Pérez-Montero, E., Ricciardelli, E., Silverman, J. D., Tanaka, M., Tasca, L., Tresse, L., Vergani, D., Zucca, E., Ilbert, O., Salvato, M., Oesch, P., Abbas, U., Bottini, D., Capak, P., Cappi, A., Cassata, P., Cimatti, A., Elvis, M., Fumana, M., Guzzo, L., Hasinger, G., Koekemoer, A., Leauthaud, A., Maccagni, D., Marinoni, C., McCracken, H., Memeo, P., Meneux, B., Porciani, C., Pozzetti, L., Sanders, D., Scaramella, R., Scarlata, C., Scoville, N., Shopbell, P., & Taniguchi, Y. 2009, ApJS, 184, 218

Lilly, S. J., & Longair, M. S. 1984, MNRAS, 211, 833

Loeb, A., & Eisenstein, D. J. 1995, ApJ, 448, 17

Loeb, A., & Rasio, F. A. 1994, ApJ, 432, 52

Loeb, A., & Rybicki, G. B. 1999, ApJ, 524, 527

Longair, M. S., & Seldner, M. 1979, MNRAS, 189, 433

Lowenthal, J. D., Koo, D. C., Guzman, R., Gallego, J., Phillips, A. C., Faber, S. M., Vogt, N. P., Illingworth, G. D., & Gronwall, C. 1997, ApJ, 481, 673

Luo, B., Brandt, W. N., Xue, Y. Q., Brusa, M., Alexander, D. M., Bauer, F. E., Comastri, A., Koekemoer, A., Lehmer, B. D., Mainieri, V., Rafferty, D. A., Schneider, D. P., Silverman, J. D., & Vignali, C. 2010, ApJS, 187, 560

Ly, C., Malkan, M. A., Kashikawa, N., Shimasaku, K., Doi, M., Nagao, T., Iye, M., Kodama, T., Morokuma, T., & Motohara, K. 2007, ApJ, 657, 738

Madau, P., Haardt, F., & Rees, M. J. 1999, ApJ, 514, 648

Madau, P., & Rees, M. J. 2001, ApJ, 551, L27

Madsen, G. J., Reynolds, R. J., Haffner, L. M., Tufte, S. L., & Maloney, P. R. 2001, ApJ, 560, L135

Magorrian, J., Tremaine, S., Richstone, D., Bender, R., Bower, G., Dressler, A., Faber, S. M., Gebhardt, K., Green, R., Grillmair, C., Kormendy, J., & Lauer, T. 1998, AJ, 115, 2285

Maloney, P. 1993, ApJ, 414, 41

Maraston, C. 2005, MNRAS, 362, 799

Markevitch, M. 1998, ApJ, 504, 27

Martin, C. L., Sawicki, M., Dressler, A., & McCarthy, P. 2008, ApJ, 679, 942

Martin, D. C., Fanson, J., Schiminovich, D., Morrissey, P., Friedman, P. G., Barlow, T. A., Conrow, T., Grange, R., Jelinsky, P. N., Milliard, B., Siegmund, O. H. W., Bianchi, L., Byun, Y., Donas, J., Forster, K., Heckman, T. M., Lee, Y., Madore, B. F., Malina, R. F., Neff, S. G., Rich, R. M., Small, T., Surber, F., Szalay, A. S., Welsh, B., & Wyder, T. K. 2005, ApJ, 619, L1

Martin-Mirones, J. M., Martinez-Gonzalez, E., Gonzalez-Serrano, J. I., & Sanz, J. L. 1995, ApJ, 440, 191

Massey, P., Strobel, K., Barnes, J. V., & Anderson, E. 1988, ApJ, 328, 315

Matsuda, Y., Yamada, T., Hayashino, T., Tamura, H., Yamauchi, R., Ajiki, M., Fujita, S. S., Murayama, T., Nagao, T., Ohta, K., Okamura, S., Ouchi, M., Shimasaku, K., Shioya, Y., & Taniguchi, Y. 2004, AJ, 128, 569

Matsuda, Y., Yamada, T., Hayashino, T., Yamauchi, R., & Nakamura, Y. 2006, ApJ, 640, L123

Matthews, L. D., Gallagher, III, J. S., & van Driel, W. 1999, AJ, 118, 2751

McCall, M. L., Rybski, P. M., & Shields, G. A. 1985, ApJS, 57, 1

McCarthy, P. J. 1993, ARA&A, 31, 639

McCarthy, P. J., & van Breugel, W. 1989, in NATO ASIC Proc. 264: The Epoch of Galaxy Formation, ed. C. S. Frenk, R. S. sEllis, T. Shanks, A. R. Heavens, & J. A. Peacock , 57–+

McGregor, P. J., Hart, J., Conroy, P. G., Pfitzner, M. L., Bloxham, G. J., Jones, D. J., Downing, M. D., Dawson, M., Young, P., Jarnyk, M., & Van Harmelen, J. 2003, in Presented at the Society of Photo-Optical Instrumentation Engineers (SPIE) Conference, Vol. 4841, Society of Photo-Optical Instrumentation Engineers (SPIE) Conference Series, ed. M. Iye & A. F. M. Moorwood, 1581–1591

Menéndez-Delmestre, K., Sheth, K., Schinnerer, E., Jarrett, T. H., & Scoville, N. Z. 2007, ApJ, 657, 790

Meurer, G. R., Tsvetanov, Z. I., Gronwall, C., Capak, P., Blakeslee, J. P., Benítez, N., Ford, H. C., Illingworth, G. D., Bradley, L. D., Pirzkal, N., Walsh, J., Bouwens, R. J., & Srinivasan, S. 2007, AJ, 134, 77

Miley, G., & De Breuck, C. 2008, A&A Rev., 15, 67

Monet, D. G., Levine, S. E., Canzian, B., Ables, H. D., Bird, A. R., Dahn, C. C., Guetter, H. H., Harris, H. C., Henden, A. A., Leggett, S. K., Levison, H. F., Luginbuhl, C. B., Martini, J., Monet, A. K. B., Munn, J. A., Pier, J. R., Rhodes, A. R., Riepe, B., Sell, S., Stone, R. C., Vrba, F. J., Walker, R. L., Westerhout, G., Brucato, R. J., Reid, I. N., Schoening, W., Hartley, M., Read, M. A., & Tritton, S. B. 2003, AJ, 125, 984

Murphy, J. D., Gebhardt, K., & Adams, J. J. 2011, ApJ, 729, 129

Murphy, J. D., MacQueen, P. J., Hill, G. J., Grupp, F., Kelz, A., Palunas, P., Roth, M., & Fry, A. 2008, in Society of Photo-Optical Instrumentation Engineers (SPIE) Conference Series, Vol. 7018, 2

Navarro, J. F., Eke, V. R., & Frenk, C. S. 1996a, MNRAS, 283, L72

Navarro, J. F., Frenk, C. S., & White, S. D. M. 1996b, ApJ, 462, 563

—. 1997, ApJ, 490, 493

Nesvadba, N. P. H., Lehnert, M. D., De Breuck, C., Gilbert, A. M., & van Breugel, W. 2008, A&A, 491, 407

Neufeld, D. A. 1991, ApJ, 370, L85

Nilsson, K. K., Fynbo, J. P. U., Møller, P., Sommer-Larsen, J., & Ledoux, C. 2006, A&A, 452, L23

Nilsson, K. K., Møller, P., Möller, O., Fynbo, J. P. U., Michałowski, M. J., Watson, D., Ledoux, C., Rosati, P., Pedersen, K., & Grove, L. F. 2007, A&A, 471, 71

Nilsson, K. K., Östlin, G., Møller, P., Möller-Nilsson, O., Tapken, C., Freudling, W., & Fynbo, J. P. U. 2010, ArXiv e-prints

Nilsson, K. K., Tapken, C., Møller, P., Freudling, W., Fynbo, J. P. U., Meisenheimer, K., Laursen, P., & Östlin, G. 2009, A&A, 498, 13

Ocvirk, P., Pichon, C., & Teyssier, R. 2008, MNRAS, 390, 1326

O'Donnell, J. E. 1994, ApJ, 422, 158

Oh, S., de Blok, W. J. G., Brinks, E., Walter, F., & Kennicutt, Jr, R. C. 2010, ArXiv e-prints

Oh, S., de Blok, W. J. G., Walter, F., Brinks, E., & Kennicutt, R. C. 2008, AJ, 136, 2761

Ohyama, Y., Taniguchi, Y., Kawabata, K. S., Shioya, Y., Murayama, T., Nagao, T., Takata, T., Iye, M., & Yoshida, M. 2003, ApJ, 591, L9

Oke, J. B., & Gunn, J. E. 1983, ApJ, 266, 713

Oosterloo, T., Fraternali, F., & Sancisi, R. 2007, AJ, 134, 1019

Osterbrock, D. E., & Ferland, G. J. 2006, Astrophysics of gaseous nebulae and active galactic nuclei

Ouchi, M., Shimasaku, K., Akiyama, M., Simpson, C., Saito, T., Ueda, Y., Furusawa, H., Sekiguchi, K., Yamada, T., Kodama, T., Kashikawa, N., Okamura, S., Iye, M., Takata, T., Yoshida, M., & Yoshida, M. 2008, ApJS, 176, 301

Ouchi, M., Shimasaku, K., Furusawa, H., Miyazaki, M., Doi, M., Hamabe, M., Hayashino, T., Kimura, M., Kodaira, K., Komiyama, Y., Matsuda, Y., Miyazaki, S., Nakata, F., Okamura, S., Sekiguchi, M., Shioya, Y., Tamura, H., Taniguchi, Y., Yagi, M., & Yasuda, N. 2003, ApJ, 582, 60

Palunas, P., Teplitz, H. I., Francis, P. J., Williger, G. M., & Woodgate, B. E. 2004, ApJ, 602, 545

Pentericci, L., McCarthy, P. J., Röttgering, H. J. A., Miley, G. K., van Breugel, W. J. M., & Fosbury, R. 2001, ApJS, 135, 63

Peterson, J. R., Paerels, F. B. S., Kaastra, J. S., Arnaud, M., Reiprich, T. H., Fabian, A. C., Mushotzky, R. F., Jernigan, J. G., & Sakelliou, I. 2001, A&A, 365, L104

Pickles, A. J. 1998, PASP, 110, 863

Pierre, M., Valtchanov, I., Altieri, B., Andreon, S., Bolzonella, M., Bremer, M., Disseau, L., Dos Santos, S., Gandhi, P., Jean, C., Pacaud, F., Read, A., Refregier, A., Willis, J., Adami, C., Alloin, D., Birkinshaw, M., Chiappetti, L., Cohen, A., Detal, A., Duc, P., Gosset, E., Hjorth, J., Jones, L., Le Fèvre, O., Lonsdale, C., Maccagni, D., Mazure, A., McBreen, B., McCracken, H., Mellier, Y., Ponman, T., Quintana, H., Rottgering, H., Smette, A., Surdej, J., Starck, J., Vigroux, L., & White, S. 2004, Journal of Cosmology and Astro-Particle Physics, 9, 11

Pirzkal, N., Xu, C., Malhotra, S., Rhoads, J. E., Koekemoer, A. M., Moustakas, L. A., Walsh, J. R., Windhorst, R. A., Daddi, E., Cimatti, A., Ferguson, H. C., Gardner, J. P., Gronwall, C., Haiman, Z., Kümmel, M., Panagia, N., Pasquali, A., Stiavelli, M., di Serego Alighieri, S., Tsvetanov, Z., Vernet, J., & Yan, H. 2004, ApJS, 154, 501

Portinari, L., Sommer-Larsen, J., & Tantalo, R. 2004, MNRAS, 347, 691

Prescott, M. K. M., Kennicutt, Jr., R. C., Bendo, G. J., Buckalew, B. A., Calzetti, D., Engelbracht, C. W., Gordon, K. D., Hollenbach, D. J., Lee, J. C., Moustakas, J., Dale, D. A., Helou, G., Jarrett, T. H., Murphy, E. J., Smith, J., Akiyama, S., & Sosey, M. L. 2007, ApJ, 668, 182

Press, W. H., Teukolsky, S. A., Vetterling, W. T., & Flannery, B. P. 1992, Numerical recipes in FORTRAN. The art of scientific computing

Prestage, R. M., & Peacock, J. A. 1988, MNRAS, 230, 131

Prugniel, P., & Soubiran, C. 2001, A&A, 369, 1048

Ramsay Howat, S. K., Todd, S., Leggett, S., Davis, C., Strachan, M., Borrowman, A., Ellis, M., Elliot, J., Gostick, D., Kackley, R., & Rippa, M. 2004, in Presented at the Society of Photo-Optical Instrumentation Engineers (SPIE) Conference, Vol. 5492, Society of Photo-Optical Instrumentation Engineers (SPIE) Conference Series, ed. A. F. M. Moorwood & M. Iye, 1160–1171

Ramsey, L. W., Adams, M. T., Barnes, T. G., Booth, J. A., Cornell, M. E., Fowler, J. R., Gaffney, N. I., Glaspey, J. W., Good, J. M., Hill, G. J., Kelton, P. W., Krabbendam, V. L., Long, L., MacQueen, P. J., Ray, F. B., Ricklefs, R. L., Sage, J., Sebring, T. A., Spiesman, W. J., & Steiner, M. 1998, in Society of Photo-Optical Instrumentation Engineers (SPIE) Conference Series, Vol. 3352, Society of Photo-Optical Instrumentation Engineers (SPIE) Conference Series, ed. L. M. Stepp, 34–42

Rauch, M., Haehnelt, M., Bunker, A., Becker, G., Marleau, F., Graham, J., Cristiani, S., Jarvis, M., Lacey, C., Morris, S., Peroux, C., Röttgering, H., & Theuns, T. 2008, ApJ, 681, 856

Rauch, M., Haehnelt, M. G., & Steinmetz, M. 1997a, ApJ, 481, 601

Rauch, M., Miralda-Escude, J., Sargent, W. L. W., Barlow, T. A., Weinberg, D. H., Hernquist, L., Katz, N., Cen, R., & Ostriker, J. P. 1997b, ApJ, 489, 7

Rawlings, S., & Jarvis, M. J. 2004, MNRAS, 355, L9

Rees, M. J., & Ostriker, J. P. 1977, MNRAS, 179, 541

Reuland, M., van Breugel, W., de Vries, W., Dopita, M. A., Dey, A., Miley, G., Röttgering, H., Venemans, B., Stanford, S. A., Lacy, M., Spinrad, H., Dawson, S., Stern, D., & Bunker, A. 2007, AJ, 133, 2607

Reuland, M., van Breugel, W., Röttgering, H., de Vries, W., Stanford, S. A., Dey, A., Lacy, M., Bland-Hawthorn, J., Dopita, M., & Miley, G. 2003, ApJ, 592, 755

Rhoads, J. E., Malhotra, S., Dey, A., Stern, D., Spinrad, H., & Jannuzi, B. T. 2000, ApJ, 545, L85

Richling, S. 2003, MNRAS, 344, 553

Ricotti, M., & Ostriker, J. P. 2004, MNRAS, 350, 539

Rogstad, D. H., Lockhart, I. A., & Wright, M. C. H. 1974, ApJ, 193, 309

Rogstad, D. H., Wright, M. C. H., & Lockhart, I. A. 1976, ApJ, 204, 703

Roth, M. M., Kelz, A., Fechner, T., Hahn, T., Bauer, S.-M., Becker, T., Böhm, P., Christensen, L., Dionies, F., Paschke, J., Popow, E., Wolter, D., Schmoll, J., Laux, U., & Altmann, W. 2005, PASP, 117, 620

Saito, T., Shimasaku, K., Okamura, S., Ouchi, M., Akiyama, M., Yoshida, M., & Ueda, Y. 2008, ApJ, 675, 1076

Sakai, S., Mould, J. R., Hughes, S. M. G., Huchra, J. P., Macri, L. M., Kennicutt, Jr., R. C., Gibson, B. K., Ferrarese, L., Freedman, W. L., Han, M., Ford, H. C., Graham, J. A., Illingworth, G. D., Kelson, D. D., Madore, B. F., Sebo, K., Silbermann, N. A., & Stetson, P. B. 2000, ApJ, 529, 698

Sánchez, S. F. 2006, Astronomische Nachrichten, 327, 850

Sandin, C., Becker, T., Roth, M. M., Gerssen, J., Monreal-Ibero, A., Böhm, P., & Weilbacher, P. 2010, A&A, 515, A35

Santos, M. R., Ellis, R. S., Kneib, J., Richard, J., & Kuijken, K. 2004, ApJ, 606, 683

Saunders, W., Bridges, T., Gillingham, P., Haynes, R., Smith, G. A., Whittard, J. D., Churilov, V., Lankshear, A., Croom, S., Jones, D., & Boshuizen, C. 2004, in Presented at the Society of Photo-Optical Instrumentation Engineers (SPIE) Conference, Vol. 5492, Society of Photo-Optical Instrumentation Engineers (SPIE) Conference Series, ed. A. F. M. Moorwood & M. Iye, 389–400

Savage, R., et al. 2010, in Society of Photo-Optical Instrumentation Engineers (SPIE) Conference Series, Vol. 7733, 149

Sawicki, M., Lemaux, B. C., Guhathakurta, P., Kirby, E. N., Konidaris, N. P., Martin, C. L., Cooper, M. C., Koo, D. C., Newman, J. A., & Weiner, B. J. 2008, ApJ, 687, 884

Schechter, P. 1976, ApJ, 203, 297

Schirber, M., & Bullock, J. S. 2003, ApJ, 584, 110

Schlegel, D. J., Finkbeiner, D. P., & Davis, M. 1998, ApJ, 500, 525

Schwarzschild, M. 1979, ApJ, 232, 236

Scoville, N., Aussel, H., Brusa, M., Capak, P., Carollo, C. M., Elvis, M., Giavalisco, M., Guzzo, L., Hasinger, G., Impey, C., Kneib, J., LeFevre, O., Lilly, S. J., Mobasher, B., Renzini, A., Rich, R. M., Sanders, D. B., Schinnerer, E., Schminovich, D., Shopbell, P., Taniguchi, Y., & Tyson, N. D. 2007, ApJS, 172, 1

Severgnini, P., Della Ceca, R., Braito, V., Saracco, P., Longhetti, M., Bender, R., Drory, N., Feulner, G., Hopp, U., Mannucci, F., & Maraston, C. 2005, A&A, 431, 87

Seymour, N., Stern, D., De Breuck, C., Vernet, J., Rettura, A., Dickinson, M., Dey, A., Eisenhardt, P., Fosbury, R., Lacy, M., McCarthy, P., Miley, G., Rocca-

Volmerange, B., Röttgering, H., Stanford, S. A., Teplitz, H., van Breugel, W., & Zirm, A. 2007, ApJS, 171, 353

Shapley, A. E., Steidel, C. C., Pettini, M., & Adelberger, K. L. 2003, ApJ, 588, 65

Shapley, A. E., Steidel, C. C., Pettini, M., Adelberger, K. L., & Erb, D. K. 2006, ApJ, 651, 688

Sharples, R. M., Bender, R., Lehnert, M. D., Ramsay Howat, S. K., Bremer, M. N., Davies, R. L., Genzel, R., Hofmann, R., Ivison, R. J., Saglia, R., & Thatte, N. A. 2004, in Presented at the Society of Photo-Optical Instrumentation Engineers (SPIE) Conference, Vol. 5492, Society of Photo-Optical Instrumentation Engineers (SPIE) Conference Series, ed. A. F. M. Moorwood & M. Iye, 1179–1186

Shoji, M., Jeong, D., & Komatsu, E. 2009, ApJ, 693, 1404

Shull, J. M., Roberts, D., Giroux, M. L., Penton, S. V., & Fardal, M. A. 1999, AJ, 118, 1450

Siana, B., Teplitz, H. I., Ferguson, H. C., Brown, T. M., Giavalisco, M., Dickinson, M., Chary, R., de Mello, D. F., Conselice, C. J., Bridge, C. R., Gardner, J. P., Colbert, J. W., & Scarlata, C. 2010, ArXiv e-prints

Silk, J. 1977, ApJ, 211, 638

Silk, J., & Rees, M. J. 1998, A&A, 331, L1

Simon, J. D., Bolatto, A. D., Leroy, A., & Blitz, L. 2003, ApJ, 596, 957

Simon, J. D., Bolatto, A. D., Leroy, A., Blitz, L., & Gates, E. L. 2005, ApJ, 621, 757

Smart, W. M., & Green, R. M. 1977, Textbook on Spherical Astronomy

Smith, D. J. B., & Jarvis, M. J. 2007, MNRAS, 378, L49

Smith, M. P., Hill, G. J., MacQueen, P. J., Altmann, W., Goertz, J. A., Good, J. M., Segura, P. R., & Wesley, G. L. 2008, in Society of Photo-Optical Instrumentation Engineers (SPIE) Conference Series, Vol. 7014, Society of Photo-Optical Instrumentation Engineers (SPIE) Conference Series, 233

Somerville, R. S., Lee, K., Ferguson, H. C., Gardner, J. P., Moustakas, L. A., & Giavalisco, M. 2004, ApJ, 600, L171

Spano, M., Marcelin, M., Amram, P., Carignan, C., Epinat, B., & Hernandez, O. 2008, MNRAS, 383, 297

Spekkens, K., & Sellwood, J. A. 2007, ApJ, 664, 204

Steidel, C. C., Adelberger, K. L., Giavalisco, M., Dickinson, M., & Pettini, M. 1999, ApJ, 519, 1

Steidel, C. C., Adelberger, K. L., Shapley, A. E., Pettini, M., Dickinson, M., & Giavalisco, M. 2000, ApJ, 532, 170

—. 2003, ApJ, 592, 728

Steidel, C. C., Erb, D. K., Shapley, A. E., Pettini, M., Reddy, N., Bogosavljević, M., Rudie, G. C., & Rakic, O. 2010, ApJ, 717, 289

Steidel, C. C., Giavalisco, M., Dickinson, M., & Adelberger, K. L. 1996, AJ, 112, 352

Stern, D., Bunker, A., Spinrad, H., & Dey, A. 2000, ApJ, 537, 73

Stetson, P. B. 1990, PASP, 102, 932

Stil, J. M., & Israel, F. P. 2002a, A&A, 389, 29

—. 2002b, A&A, 389, 42

Stocke, J. T., Case, J., Donahue, M., Shull, J. M., & Snow, T. P. 1991, ApJ, 374, 72

Sullivan, M., Treyer, M. A., Ellis, R. S., Bridges, T. J., Milliard, B., & Donas, J. 2000, MNRAS, 312, 442

Sunyaev, R. A. 1969, Astrophys. Lett., 3, 33

Sutherland, W., & Saunders, W. 1992, MNRAS, 259, 413

Swaters, R. A. 1999, PhD thesis, , Rijksuniversiteit Groningen, (1999)

Swaters, R. A., Madore, B. F., van den Bosch, F. C., & Balcells, M. 2003, ApJ, 583, 732

Tamura, T., Kaastra, J. S., Peterson, J. R., Paerels, F. B. S., Mittaz, J. P. D., Trudolyubov, S. P., Stewart, G., Fabian, A. C., Mushotzky, R. F., Lumb, D. H., & Ikebe, Y. 2001, A&A, 365, L87

Tasitsiomi, A. 2006, ApJ, 645, 792

Teplitz, H. I., Collins, N. R., Gardner, J. P., Hill, R. S., & Rhodes, J. 2003, ApJ, 589, 704

Thilker, D. A., Bianchi, L., Meurer, G., Gil de Paz, A., Boissier, S., Madore, B. F., Boselli, A., Ferguson, A. M. N., Muñoz-Mateos, J. C., Madsen, G. J., Hameed, S., Overzier, R. A., Forster, K., Friedman, P. G., Martin, D. C., Morrissey, P., Neff, S. G., Schiminovich, D., Seibert, M., Small, T., Wyder, T. K., Donas, J., Heckman, T. M., Lee, Y., Milliard, B., Rich, R. M., Szalay, A. S., Welsh, B. Y., & Yi, S. K. 2007, ApJS, 173, 538

Tilvi, V., Rhoads, J. E., Hibon, P., Malhotra, S., Wang, J., Veilleux, S., Swaters, R., Probst, R., Krug, H., Finkelstein, S. L., & Dickinson, M. 2010, ApJ, 721, 1853

Toomre, A. 1964, ApJ, 139, 1217

Tremonti, C. A., Heckman, T. M., Kauffmann, G., Brinchmann, J., Charlot, S., White, S. D. M., Seibert, M., Peng, E. W., Schlegel, D. J., Uomoto, A., Fukugita, M., & Brinkmann, J. 2004, ApJ, 613, 898

Treyer, M. A., Ellis, R. S., Milliard, B., Donas, J., & Bridges, T. J. 1998, MNRAS, 300, 303

Tufts, J. R., MacQueen, P. J., Smith, M. P., Segura, P. R., Hill, G. J., & Edmonston, R. D. 2008a, in Proc. SPIE, Vol. 7021-10, Astronomical Telescopes and Instrumentation

Tufts, J. R., MacQueen, P. J., Smith, M. P., Segura, P. R., Hill, G. J., & Edmonston, R. D. 2008b, in Society of Photo-Optical Instrumentation Engineers (SPIE) Conference Series, Vol. 7021, 9

Tull, R. G., MacQueen, P. J., Sneden, C., & Lambert, D. L. 1995, PASP, 107, 251

Tully, R. B., Rizzi, L., Dolphin, A. E., Karachentsev, I. D., Karachentseva, V. E., Makarov, D. I., Sakai, S., & Shaya, E. J. 2006, AJ, 132, 729

Turner, J. E. H., Miller, B. W., Beck, T. L., Song, I., Cooke, A. J., Seaman, R. L., & Valdés, F. G. 2006, New Astronomy Reviews, 49, 655

Urbaniak, J. J., & Wolfe, A. M. 1981, ApJ, 244, 406

Uson, J. M., & Matthews, L. D. 2003, AJ, 125, 2455

Valageas, P., & Silk, J. 1999, A&A, 350, 725

Valdes, F. 1992, in Astronomical Society of the Pacific Conference Series, Vol. 25, Astronomical Data Analysis Software and Systems I, ed. D. M. Worrall, C. Biemesderfer, & J. Barnes, 417–+

van Breukelen, C., Jarvis, M. J., & Venemans, B. P. 2005, MNRAS, 359, 895

van den Bosch, R. C. E., van de Ven, G., Verolme, E. K., Cappellari, M., & de Zeeuw, P. T. 2008, MNRAS, 385, 647

van der Kruit, P. C., & Freeman, K. C. 1984, ApJ, 278, 81

—. 1986, ApJ, 303, 556

van Gorkom, J. 1993, in Astrophysics and Space Science Library, Vol. 188, The Environment and Evolution of Galaxies, ed. J. M. Shull & H. A. Thronson, 345–+

van Ojik, R., Roettgering, H. J. A., Miley, G. K., & Hunstead, R. W. 1997, A&A, 317, 358

Venemans, B. P., Röttgering, H. J. A., Miley, G. K., Kurk, J. D., De Breuck, C., Overzier, R. A., van Breugel, W. J. M., Carilli, C. L., Ford, H., Heckman, T., Pentericci, L., & McCarthy, P. 2005, A&A, 431, 793

Verhamme, A., Schaerer, D., Atek, H., & Tapken, C. 2007, in Astronomical Society of the Pacific Conference Series, Vol. 380, Deepest Astronomical Surveys, ed. J. Afonso, H. C. Ferguson, B. Mobasher, & R. Norris, 97–+

Verhamme, A., Schaerer, D., Atek, H., & Tapken, C. 2008, A&A, 491, 89

Verhamme, A., Schaerer, D., & Maselli, A. 2006, A&A, 460, 397

Verheijen, M. A. W., Bershady, M. A., Andersen, D. R., Swaters, R. A., Westfall, K., Kelz, A., & Roth, M. M. 2004, Astronomische Nachrichten, 325, 151

Vernet, J., Fosbury, R. A. E., Villar-Martín, M., Cohen, M. H., Cimatti, A., di Serego Alighieri, S., & Goodrich, R. W. 2001, A&A, 366, 7

Villar-Martín, M., Sánchez, S. F., Humphrey, A., Dijkstra, M., di Serego Alighieri, S., De Breuck, C., & González Delgado, R. 2007, MNRAS, 378, 416

Vogel, S. N., Weymann, R., Rauch, M., & Hamilton, T. 1995, ApJ, 441, 162

Walsh, W., Staveley-Smith, L., & Oosterloo, T. 1997, AJ, 113, 1591

Walter, F., Brinks, E., de Blok, W. J. G., Bigiel, F., Kennicutt, R. C., Thornley, M. D., & Leroy, A. 2008, AJ, 136, 2563

Watson, M. G., Schröder, A. C., Fyfe, D., Page, C. G., Lamer, G., Mateos, S., Pye, J., Sakano, M., Rosen, S., Ballet, J., Barcons, X., Barret, D., Boller, T., Brunner, H., Brusa, M., Caccianiga, A., Carrera, F. J., Ceballos, M., Della Ceca, R., Denby, M., Denkinson, G., Dupuy, S., Farrell, S., Fraschetti, F., Freyberg, M. J., Guillout, P., Hambaryan, V., Maccacaro, T., Mathiesen, B., McMahon, R., Michel, L., Motch, C., Osborne, J. P., Page, M., Pakull, M. W., Pietsch, W., Saxton, R., Schwope, A., Severgnini, P., Simpson, M., Sironi, G., Stewart, G., Stewart, I. M., Stobbart, A., Tedds, J., Warwick, R., Webb, N., West, R., Worrall, D., & Yuan, W. 2009, A&A, 493, 339

Weijmans, A.-M., Cappellari, M., Bacon, R., de Zeeuw, P. T., Emsellem, E., Falcón-Barroso, J., Kuntschner, H., McDermid, R. M., van den Bosch, R. C. E., & van de Ven, G. 2009, MNRAS, 398, 561

Weinberg, M. D., & Katz, N. 2002, ApJ, 580, 627

Werk, J. K., Putman, M. E., Meurer, G. R., Ryan-Weber, E. V., Kehrig, C., Thilker, D. A., Bland-Hawthorn, J., Drinkwater, M. J., Kennicutt, R. C., Wong, O. I., Freeman, K. C., Oey, M. S., Dopita, M. A., Doyle, M. T., Ferguson, H. C., Hanish, D. J., Heckman, T. M., Kilborn, V. A., Kim, J. H., Knezek, P. M., Koribalski, B., Meyer, M., Smith, R. C., & Zwaan, M. A. 2010a, AJ, 139, 279

Werk, J. K., Putman, M. E., Meurer, G. R., Thilker, D. A., Allen, R. J., Bland-Hawthorn, J., Kravtsov, A., & Freeman, K. 2010b, ApJ, 715, 656

Weymann, R. J., Vogel, S. N., Veilleux, S., & Epps, H. W. 2001, ApJ, 561, 559

Williams, B. F., Dalcanton, J. J., Stilp, A., Gilbert, K. M., Roškar, R., Seth, A. C., Weisz, D., Dolphin, A., Gogarten, S. M., Skillman, E., & Holtzman, J. 2010, ApJ, 709, 135

Williams, R. E., Blacker, B., Dickinson, M., Dixon, W. V. D., Ferguson, H. C., Fruchter, A. S., Giavalisco, M., Gilliland, R. L., Heyer, I., Katsanis, R., Levay, Z., Lucas, R. A., McElroy, D. B., Petro, L., Postman, M., Adorf, H., & Hook, R. 1996, AJ, 112, 1335

Wilman, R. J., Gerssen, J., Bower, R. G., Morris, S. L., Bacon, R., de Zeeuw, P. T., & Davies, R. L. 2005, Nature, 436, 227

Wirth, G. D., Willmer, C. N. A., Amico, P., Chaffee, F. H., Goodrich, R. W., Kwok, S., Lyke, J. E., Mader, J. A., Tran, H. D., Barger, A. J., Cowie, L. L., Capak, P., Coil, A. L., Cooper, M. C., Conrad, A., Davis, M., Faber, S. M., Hu, E. M., Koo, D. C., Le Mignant, D., Newman, J. A., & Songaila, A. 2004, AJ, 127, 3121

Worthey, G., Faber, S. M., Gonzalez, J. J., & Burstein, D. 1994, ApJS, 94, 687

Xu, C., Pirzkal, N., Malhotra, S., Rhoads, J. E., Mobasher, B., Daddi, E., Gronwall, C., Hathi, N. P., Panagia, N., Ferguson, H. C., Koekemoer, A. M., Kümmel, M., Moustakas, L. A., Pasquali, A., di Serego Alighieri, S., Vernet, J., Walsh, J. R., Windhorst, R., & Yan, H. 2007, AJ, 134, 169

Yang, Y., Zabludoff, A., Eisenstein, D., & Davé, R. 2010, ApJ, 719, 1654

Zacharias, N., Monet, D. G., Levine, S. E., Urban, S. E., Gaume, R., & Wycoff, G. L. 2005, VizieR Online Data Catalog, 1297, 0

Zanichelli, A., Garilli, B., Scodeggio, M., Franzetti, P., Rizzo, D., Maccagni, D., Merighi, R., Picat, J. P., Le Fèvre, O., Foucaud, S., Bottini, D., Le Brun, V., Scaramella, R., Tresse, L., Vettolani, G., Adami, C., Arnaboldi, M., Arnouts, S., Bardelli, S., Bolzonella, M., Cappi, A., Charlot, S., Ciliegi, P., Contini, T., Gavignaud, I., Guzzo, L., Ilbert, O., Iovino, A., McCracken, H. J., Marano, B., Marinoni, C., Mathez, G., Mazure, A., Meneux, B., Paltani, S., Pellò, R., Pollo, A., Pozzetti, L., Radovich, M., Zamorani, G., & Zucca, E. 2005, PASP, 117, 1271

Zheng, Z., & Miralda-Escudé, J. 2002, ApJ, 578, 33

Zibetti, S., Charlot, S., & Rix, H.-W. 2009, MNRAS, 400, 1181

Vita

Joshua Jesse Adams attended Ankeny High School in Ankeny, Iowa from 1996-2000. He earned a Bachelor of Science degree with dual-majors in Aerospace Engineering and Physics from Iowa State University at Ames, Iowa in 2005. He worked as an engineering intern at the Boeing Space and Communications Division in Seal Beach, California in 2002 and a research assistant in the Astronomy Department of Indiana University in the summer of 2004. In September of 2005, he entered the Graduate School in the Astronomy Department at The University of Texas at Austin. Joshua begins a post-doctoral research position at the Observatories of the Carnegie Institute of Washington in Pasadena, California starting in September of 2011.

Permanent Address: 2508 W. 12th St., #203
Austin, TX 78703

This dissertation was typeset with LaTeX 2_ε[1] by the author.

---

[1] LaTeX 2_ε is an extension of LaTeX. LaTeX is a collection of macros for TeX. TeX is a trademark of the American Mathematical Society. The macros used in formatting this dissertation were written by Dinesh Das, Department of Computer Sciences, The University of Texas at Austin, and extended by Bert Kay, James A. Bednar, and Ayman El-Khashab.